

IMPERIAL COLLEGE LONDON
DEPARTMENT OF CHEMICAL ENGINEERING

**Developing a Hydrogen Impurity
Enrichment Device for Measuring
Impurities in Fuel-Grade Hydrogen**

Marc Plunkett

A thesis presented for the degree of Doctor of Philosophy

December 28, 2020

Declaration of Originality

I hereby declare that the work reported in this thesis was composed and originated entirely by me. Information derived from published and unpublished results of others has been acknowledged in the text and in the relevant references included within the thesis.

Marc Plunkett

September, 2020

The copyright of this thesis rests with the author and is made available under a 'Creative Commons Attribution Non-Commercial No Derivatives' licence. Researchers are free to copy, distribute or transmit the thesis on the condition that they attribute it, that they do not use it for commercial purposes and that they do not alter, transform or build upon it. For any reuse or redistribution, researchers must make clear to others the licence terms of this work.

Executive summary

As government entities around the world seek to further develop their hydrogen economies with the aim of reducing their CO₂ emissions from the transport sector further adoption of fuel cell electric vehicles is expected. This thesis focused on developing a hydrogen impurity enrichment device using an optimised palladium based membrane as a method for low cost measurement of impurities to ISO 14687 standards. The composition of the palladium membrane was first optimised by screening of compositions using density functional theory. Compositions are simulated by placing ISO 14687 impurities on the surface and measuring their final energy level, with compositions which have a lower energy level with the impurity being deemed unsuitable. The best membrane compositions were then fabricated using a number of thin film deposition techniques including electroless plating and magnetron sputtering. The resulting micron thick palladium membranes were then subjected to two varieties of hydrogen impurities, carbonaceous and sulphurous, and their reactivity measured by using XPS and the change in hydrogen permeability when subjected to impurities. The result from this was that PdCuZr membranes were the least reactive and therefore the most suitable for hydrogen impurity enrichment where a membrane with low reactivity to impurities is required. Finally the resulting membrane was tested in an improved hydrogen impurity enrichment device which was set up with improved process control systems. The membrane was benchmarked against a commercial PdAgAu membrane and tested using an inert sample, sulphurous sample and for the first time a sample taken from a hydrogen refuelling station.

Acknowledgements

Throughout the writing of this dissertation I have received a great deal of support and assistance. I would first like to thank my supervisors, Dr. A. Murugan and Prof. K. Li, whose insights and knowledge into the subject matter steered me through this research.

I would like to acknowledge my colleagues from my National Physical Laboratory and Imperial College London for their wonderful collaboration. You supported me greatly and were always willing to help me. I would particularly like to thank Dr. B. Wang and Dr. T. Li at Imperial College and Dr. T. Bacquart, Dr. S. Bartlett and Ms. A. Morris, and Ms. N. Moore at National Physical Laboratory. I want to thank you for your excellent guidance and for taking the time to teach me the techniques, methodologies and providing me with the tools that I needed to choose the right direction and successfully complete my dissertation.

And my biggest thanks to my friends and family for all the support you have shown me through this research. I would like to thank my brother, David, for his wise counsel and sympathetic ear and my parents who are always there for me. Finally, there are my dear friends; Dr. Iain Hyndman, Emma Abraham, David McKechnie, Bradley Hannah, Anthony Houghton, and Chen Chen for seeing me through the highs and lows and for creating so many unforgettable moments outside of my research.

List of Figures

1.1	Schematic presentation of the thesis structure	24
2.1	Schematic of fuel cell [2]	28
2.2	Schematic of a PEMFC stack [4]	29
2.3	Simplified block diagram of a typical modern Steam Methane Reforming (SMR) and Water Gas Shift (WGS) plant. CO ₂ concentrations are in mol.%. [8]	30
2.4	Illustration of the five membrane separation mechanisms (i) Poiseuille Flow/Knudsen diffusion, (ii) Molecular Sieving, (iii) Surface diffusion (iV) Capillary condensation (V) Solution diffusion (Vi) Facilitated transport .	51
2.5	Palladium-Hydrogen phase diagram adapted from [52]	61
2.6	Metals which can be deposited using electro less plating [149]	97
2.7	Total energies (per atom) for bulk Cu calculated as a function of M for calculations using MxMxM kpoints [154]	101
2.8	Schematic representation of (111) face Pd showing the high-symmetry adsorption sites fcc, hcp, bridge, and top [156]	103
3.1	Schematic representation of the sequential baths for sensitisation/activation process.	148
3.2	Example of ELP procedure when manufacturing a PdCu membrane on YSZ substrate	149

3.3	Experimental set up used during hydrogen permeation and enrichment experiments, TC: Temperature controller, PI: Pressure indicator, V: Valve, TV: Three-way valve, FI: Flow indicator.	152
3.4	Total energy as a function of $M \times M \times M$ k-points across a Pd(111) fcc slab	156
4.1	Adsorption energy of H for each site on a 2x2x5 Pd slab	167
4.2	Average binding energy of H_2 on the surface of palladium and palladium alloy slabs	169
4.3	Average binding energy of He on the surface of palladium and palladium alloy slabs	171
4.4	Average binding energy of N_2 on the surface of palladium and palladium alloy slabs	172
4.5	Average binding energy of CO_2 on the surface of palladium and palladium alloy slabs	173
4.6	Average binding energy of Ar on the surface of palladium and palladium alloy slabs	174
4.7	binding energy of H and CO for each site on a 2x2x5 Pd slab	176
4.8	Average binding energy of CO on the surface of palladium and palladium alloy slabs	177
4.9	Average binding energy of NH_3 on the surface of palladium and palladium alloy slabs	178
4.10	Average binding energy of O_2 on the surface of palladium and palladium alloy slabs	181
4.11	Average binding energy of H_2O on the surface of palladium and palladium alloy slabs	182
4.12	binding energy of H and CH_4 for each site on a 2x2x5 Pd slab	185

4.13 Average binding energy of Methane on the surface of palladium and palladium alloy slabs	186
4.14 Average binding energy of formaldehyde on the surface of palladium and palladium alloy slabs	188
4.15 Average binding energy of Formic Acid on the surface of palladium and palladium alloy slabs	189
4.16 binding energy of H and H ₂ S for each site on a 2x2x5 Pd slab	191
4.17 Average binding energy of H ₂ S on the surface of palladium and palladium alloy slabs	192
5.1 SEM images of fabricated membranes (a) PdCu (fcc) (Sputtering) (b) PdAg (ELP) (c)PdAu (ELP) (d) PdCuZr (Sputtering) (e) PdAgAu (ELP) (f) PdCuAg (ELP) (g) PdCu (bcc) (Sputtering) (h) typical cross section	205
5.2 Permeability data for pure hydrogen, non-sulphur, and sulphur permeation tests	213
6.1 Predicted concentration of krypton within hydrogen samples in; 1L cylinder (30.8 mg Kr), 10L cylinder (300.79 mg Kr), 50L cylinder (1484 mg Kr)	223
6.2 P&ID for the redesigned hydrogen impurity enrichment device	226
6.3 Disconnected transportable unit	229
6.4 Comparison of the On/Off temperature controller and PID temperature controller over a 1 hour period	231
6.5 Diagrammatic representation of the data processing algorithm used to provide real time enrichment factor	233
7.1 <i>CEF_{NI}</i> over the 180 hour enrichment of the inert hydrogen sample shown in table 7.1	241

7.2	GC-PDHID data of the inert sample both before and after enrichment with N ₂ peaks shown at Time=3.25, and Kr peaks shown at Time=3.92 .	243
7.3	GC-SCD data of the sulphurous sample both before and after enrichment with commercial membrane	244
7.4	<i>CEF_{NI}</i> over the 40 hour enrichment of the sulphurous hydrogen sample shown in table 3.2	246
7.5	<i>CEF_{NI}</i> over the 120 hour enrichment of the HRS hydrogen sample	248
7.6	GC-PDHID data of the HRS sample both before and after enrichment with commercial membrane	250
8.1	Theoretical manufacturing process for a bespoke dense metal membrane with optimal composition calculated by a research provider, manufactured to specification, and delivered to the customer	254
8.2	Proposed solution for automatic quality assurance of fuel cell hydrogen at HRS's	257
8.3	The calculated Ag-Pd phase diagram with experimental points [1]	264
8.4	The calculated (dashed) Au-Pd phase diagram with experimental points [2]	265
8.5	Cu-Pd phase diagram	266
8.6	Zr-Pd phase diagram [3]	266
8.7	Enrichment device control panel	295
8.8	Enrichment device chassis layout	296
8.9	Example of connecting thermocouples using TE3	297
8.10	Information based views on eurotherm control panel (a) System Summary (b) Vertical trend over time (c) Vertical bar chart (d) Horizontal bar chart	297
8.11	Temperature control views	298
8.12	Heating switch	298
8.13	Disconnected transportable unit	299

List of Tables

1.1	Concentration limits for ISO-14687 impurities	21
2.1	Summary of impurities in the hydrogen supply chain and their effects on fuel cell operation adapted from [22]	36
2.2	Types of hydrogen separation membrane	54
2.3	Metals which show the ability for hydrogen permeation [47]	58
2.4	Review of palladium alloys and their interactions with impurities	68
2.5	Hydrogen permeable non-palladium metallic membranes	80
2.6	Hydrogen permeable ceramic and cermet membranes which show resistance to common hydrogen impurities	86
2.7	Review of DFT studies for adsorption of ISO 14687-2 impurites and hydrogen on palladium membrane surfaces	108
3.1	Gas mixture composition of the non-sulphur sample (Cylinder NG353R) used during impurity tests	145
3.2	Gas mixture composition of the sulphur sample (Cylinder 2380) used during impurity tests	145
3.3	Compositions used for activation of YSZ substrate prior to palladium deposition	147
3.4	Compositions used for preparation of palladium based membranes on YSZ substrate through electroless plating and immersion plating	148

3.5	Conditions used during magnetron sputtering of palladium membranes on YSZ tubular substrate	150
4.1	Simulated total energy values of alloy slabs	165
4.2	Simulated total energy values of ISO 14687-2 impurities	165
4.3	Correlation coefficient of Ag, Au, Cu, Zr addition to Pd with binding energy of H	168
4.4	Best performing alloys for each environment with respect to the different between the binding energies with relevant impurities, and the binding energy of hydrogen	193
5.1	Membrane compositions analysed by EDS and their thickness measured using FIB-SEM	204
5.2	Pure hydrogen permeability of studied alloy membranes under pure hydrogen at 300°C and 1 bar pressure differential	207
5.3	Permeability results for all membranes under both impurity conditions .	207
5.4	XPS composition analysis of the palladium alloy membrane surfaces after impurity tests	210
7.1	Gas mixture composition of the inert sample used during enrichment tests	239

List of Acronyms, Abbreviations and Symbols

AHF Asymmetric Hollow Fibre

ATR Autothermal Reforming

ASTM American Society for Testing and Materials

BCC Body Centered Cubic

CEF Calculated Enrichment Factor

CRDS Cavity Ring Down Spectroscopy

CTE Coefficient of thermal expansion

CVD Chemical Vapour Deposition

DFT Density Functional Theory

DIN Deutsches Institut für Normung

EDS Energy-dispersive X-ray spectroscopy

EDP Electroplating Deposition

ELP Electroless Plating

EU European Union

FCC Face-centred cubic

FCEV Fuel Cell Electric Vehicle

FTIR Fourier-transform infrared spectroscopy

GC Gas Chromatography

GGA Generalized Gradient Approximation

GUI Graphical User Interface

HCP Hexagonal close packed

HEMS Hydrogen Elimination Mass Spectrometry

HIED Hydrogen Impurity Enrichment Device

HF Hollow Fibre

HPC High-performance computing

HRS Hydrogen Refuelling Station

IEA International Energy Agency

ISO International Standards Organisation

kWh Kilo watt hour

LDA Local Density Approximation

LOHC Liquid Organic Hydrogen Carrier

MEA Membrane Electrode Assembly

MS Mass Spectrometry

NPL National Physical Laboratory

NPT National Pipe Thread

PDHID Pulsed discharge helium ionization detector

PEMFC Proten Exchange Membrane Fuel Cell

PID Proportional–integral–derivative

PPB Parts-Per-Billion

PPM Parts-Per-Million

PSA Pressure Swing Adsorption

PSS Porous Stainless Steel

PVD Physical Vapour Deposition

QE Quantum Espresso

SCD Sulfur chemiluminescence detector

SEM Scanning Electron Microscopy

SMR Steam Methane Reforming

UK United Kingdom

VOC Volatile Organic Compound

WGS Water Gas Shift

XRD X-ray diffraction

XPS X-ray photoelectron spectroscopy

YSZ Yttrium stabilized zirconium

Ag Silver

Ar Argon

Au Gold

CH₄ Methane

Cu Copper

CO Carbon Monoxide

CO₂ Carbon Dioxide

He Helium

H₂ Hydrogen

HCHO Formaldehyde

HCOOH Formic Acid

H₂O Water

N₂H₄ Hydrazine

HCl Hydrochloric Acid

H₂S Hydrogen Sulphide

NaOH Ammonium hydroxide

Pd Palladium

PdNH₃4Cl₂H₂O Tetra-amminepalladium (II) chloride monohydrate

SnCl₂ Tin(ii)Chloride

Zn Zinc

Contents

1	Introduction	19
1.1	Problem statement	19
1.2	Research Objectives	22
1.3	Thesis structure and presentation	24
2	Literature review	27
2.1	Fuel cell electric vehicles	27
2.2	Hydrogen Production	29
2.2.1	Hydrogen from fossil fuels and hydrocarbons	30
2.2.2	Hydrogen from water	33
2.3	Hydrogen impurities in the supply chain	35
2.4	Hydrogen impurity enrichment using metal membranes	45
2.4.1	Other enrichment methods	48
2.5	Review of hydrogen selective membranes	49
2.5.1	Criteria for a hydrogen impurity enrichment material	54
2.5.2	Membrane manufacture	90
2.6	Density functional theory for screening of membrane alloy compositions .	98
2.6.1	Key concepts	99
2.6.2	Use cases, and limitations	105
2.7	Conclusion	111

3 Experimental methods	142
3.1 Introduction	142
3.2 Preparation of gas standards	142
3.3 Hydrogen sampling	144
3.4 Membrane preparation	146
3.4.1 Support fabrication	146
3.4.2 Membrane deposition	146
3.4.3 Materials testing	150
3.5 Membrane Characterization	151
3.5.1 Membrane testing rig	151
3.6 Hydrogen impurity enrichment	153
3.6.1 Krypton spiking	153
3.6.2 Performing enrichment	154
3.7 Density functional theory	155
3.7.1 ISO 14687 Impurities and Hydrogen	155
3.7.2 Palladium and Palladium alloy slab models	156
4 Density functional theory as a screening method for dense metal membranes	161
4.1 Introduction	162
4.2 Results and discussion	164
4.2.1 Stability of palladium alloy compositions and ISO 14687-2 impurities	164
4.2.2 Hydrogen and Impurity adsorption on palladium alloy membranes	166
4.3 Conclusion	193
5 Impurity resistance of dense metal membranes under hydrogen impurities	201
5.1 Introduction	202

5.2	Results and Discussion	204
5.2.1	Membrane characterisation	204
5.2.2	Hydrogen permeation	206
5.2.3	Impurity reactivity	207
5.2.4	Relationship to DFT results	214
5.3	Conclusion	215
6	Designing an improved hydrogen impurity measurement device for measuring ISO 14687 impurities	219
6.1	Introduction	220
6.2	Addition of krypton for tracer enrichment	220
6.3	Improvements	224
6.3.1	Safety	227
6.3.2	Usability	228
6.3.3	Automation	229
6.4	Conclusion	232
7	Enriching impurities in hydrogen refuelling station samples	237
7.1	Introduction	238
7.2	Enrichment of hydrogen samples	239
7.2.1	Inert components	240
7.2.2	Sulphur containing compounds	243
7.2.3	HRS sample	247
7.3	Conclusion	250
8	Conclusions and future work	252
8.1	Membranes for hydrogen separation	252
8.1.1	DFT for screening impurity resistant alloys	252

8.1.2	Use for dense metal membranes in the hydrogen economy	253
8.2	Impurity enrichment devices	255
8.2.1	Commercialisation and optimisation	256
8.2.2	Additional use cases	259
8.3	Other hydrogen impurity measurement challenges	259
8.4	Closing remarks	260

Chapter 1

Introduction

1.1 Problem statement

Due to the damaging environmental effects of using fossil fuels in the transport sector, national and international targets have been set in order to reduce global CO₂ emissions. In the UK for example, there is a plan to completely ban the sale of new conventional petroleum vehicles by as early as 2040. [1] One proposed solution is further adoption of fuel cells and other energy generation methods which utilize hydrogen as a carbon free energy source.

Despite the fact that the technology for hydrogen powered fuel vehicles has existed since the early 1960's, their application has been limited to providing power for space missions and other niche applications. In the late 90's developments in lowering the platinum catalyst loading and breakthroughs in the production of thin film electrodes drove the cost of fuel cells down to a level where they were commercially viable for other applications. As of 2017, a number of automobile manufacturers including Toyota,[2] Hyundai, [3] Honda [4] and Daimler [5] now offer hydrogen vehicles commercially. It is also possible to retrofit a petroleum vehicle to run off hydrogen.[6] Many countries both in the EU, and globally have ambitious hydrogen infrastructure plans over the next 10

years. This is in an effort to become less reliant on importing fossil fuels, increase their energy security, and transition to a carbon free energy system.

The development of the hydrogen economy is still in its infancy, however several countries are aiming to deploy sizable hydrogen fuelling infrastructures over the next few decades. National reports state that Europe's position in 2030 will be: UK - 1,100 hydrogen refuelling stations and 1.6 million fuel cell vehicles [7] France – 600 hydrogen refuelling stations and 0.8 million fuel cell vehicles [8], Germany – 1,180 hydrogen refuelling stations [9] and 1.8 million fuel cell vehicles and the Netherlands – 200 hydrogen refuelling stations and 0.2 million fuel cell vehicles. [9] Although this report seems to have overestimated the development, for example as of 2020 the UK only has 17 HRS's [10], compared to the 65 estimated by the report.

The fuel cell system in a hydrogen vehicle can easily degrade if even parts-per-billion to parts-per-million level of some impurities are present in the hydrogen. Therefore, it is imperative that hydrogen purity, and techniques for verifying purity, are adequate to ensure customers vehicles are not inadvertently damaged by fluctuations in hydrogen composition. International standards advise that all hydrogen suppliers should prove that their product is pure enough to prevent degradation of fuel cell components. ISO 14687 [11], shown in Table 1.1 specifies the maximum impurity levels of 13 impurities that are permissible in fuel cell hydrogen. ISO 14687 includes some challenging hydrogen purity specifications mainly due to the impurity limits being below the limits of detection of the standard techniques commonly used to measure the concentration of these compounds.

Commercial hydrogen purity laboratories are unable to perform traceable analysis to ISO 14687 specifications because appropriate methods and standards have not been developed. The consequence of this is that hydrogen suppliers cannot provide evidence that their fuel meets these specifications and therefore are not permitted to supply

Table 1.1: Concentration limits for ISO-14687 impurities

Characteristics	Regulation
Minimum mole fraction of hydrogen	99.97%
Total non-hydrogen gases	300 $\mu\text{mol mol}^{-1}$
Maximum concentration of individual components	
Total Hydrocarbons (Methane basis)	5 $\mu\text{mol mol}^{-1}$
Water	2 $\mu\text{mol mol}^{-1}$
Oxygen	5 $\mu\text{mol mol}^{-1}$
Helium	300 $\mu\text{mol mol}^{-1}$
Carbon dioxide	2 $\mu\text{mol mol}^{-1}$
Carbon monoxide	0.2 $\mu\text{mol mol}^{-1}$
Total sulphur compounds (H_2S basis)	0.004 $\mu\text{mol mol}^{-1}$
Formaldehyde	0.01 $\mu\text{mol mol}^{-1}$
Formic acid	0.2 $\mu\text{mol mol}^{-1}$
Ammonia	0.1 $\mu\text{mol mol}^{-1}$
Total halogenated compounds	0.05 $\mu\text{mol mol}^{-1}$
Maximum particulate concentration	1 mg/kg

hydrogen. Of the 13 gaseous impurities listed in ISO 14687 there is no single method for measuring all impurities. Laboratories must therefore use several instruments to perform such an analysis. In 2015 Murugan et al published a review of methods for analysing the purity of fuel grade hydrogen [12]. They concluded that in order for a single laboratory to provide full hydrogen analysis to ISO 14687 specifications it would require a number of instruments including Gas Chromatography (GC), Fourier-transform infrared spectroscopy (FTIR) and Cavity ring-down spectroscopy (CRDS). The capital cost of purchasing the gas analysers to perform analysis on the measurable impurities in a hydrogen sample can amount to >€500,000 [12] and hence performing analysis would be out of reach for many laboratories.

While the impurities listed in ISO 14687 are specified at extremely low amount fractions, many can be analysed at higher amount fractions through the use of cheap and routine gas analysers such as Gas Chromatography - Mass Spectrometry (GC-MS). A potential solution is, instead of measuring the concentration of each impurity directly us-

ing costly and specialised pieces of equipment, to increase the concentration of impurities above the limit of detection of a cheaper, more widespread analyser. These techniques are referred to as enrichment or pre-concentration. The most commonly used technique for pre-concentration of hydrogen fuel samples is referred to as ‘Hydrogen Impurity Enrichment’. This method involves passing the sample through a semi permeable membrane material, such as palladium, which only allows the passage of hydrogen.[13] As hydrogen leaves the system, the impurities remain, increasing in concentration with time as more hydrogen permeates through the membrane. This increase in concentration is referred to as the enrichment factor and once the enrichment is complete the sample can then be analysed at these higher concentrations, and using the enrichment factor, the original composition of the sample can be found.

The accuracy, cost and time taken for a hydrogen enrichment device is highly dependent on the membrane material. Different materials will allow hydrogen to permeate at different rates and will interact differently with impurities that may be present in hydrogen.[13] While hydrogen enrichment is a promising technology for hydrogen impurity measurement, more research must be done to properly understand how different membrane materials interact with common hydrogen impurities, and therefore identify the most appropriate material.

1.2 Research Objectives

The issue with past enrichment studies are mainly due to the membrane used. Current commercial membranes suffer from low flux values, driving up the enrichment time, and are highly reactive with hydrogen impurities which throws off the results. This thesis will focus on developing and improving hydrogen impurity enrichment as a method for measuring the impurities in fuel grade hydrogen to ISO 14687. Studies will revolve around the membrane materials used to concentrate the impurities in hydrogen samples,

optimisation of process parameters, and improvements of the enrichment device. The final aims are as follows:

- Perform a literature review in order to identify available membrane types suitable for performing hydrogen impurity enrichment, the nature of impurity reactivity with membranes, and ways to reduce it's severity
- Use density functional theory (DFT) in order to theoretically screen membrane compositions for their suitability as a enrichment material
- Lab test the candidate membranes through lab tests using flux tests to determine the best performing materials based on minimising the degree of interaction and reactivity with the impurities shown in Table 1 using the loss of permeability and surface analysis results as indicators
- A protocol for national measurement institutions to follow when enriching a hydrogen sample.
- Perform full enrichment on a real sample taken from a hydrogen refuelling station

In order to determine suitable enrichment material ‘Density Functional Theory (DFT) will be used to screen a number of materials for their suitability as an impurity enrichment membrane on their simulated interaction strength with ISO 14687 impurities.

The best performing membrane materials simulated in Chapter 3 will then be synthesised in Chapter 4. The hydrogen permeability of each material under a number of ISO 14687 impurities will be measured to validate the simulation results and further narrow down the most suitable membrane composition. Following from this the best membrane will be used in Chapter 5 which will describe the design and commercialisation of the final hydrogen impurity enrichment device. The design of the enrichment device will include an uncertainty budget of the technique, automation of the device, and compliance to European standards.

Finally the new device, featuring the most suitable membrane, redesigned process, and protocols for tracer enrichment will be tested using a real sample taken from a hydrogen refuelling station.

1.3 Thesis structure and presentation

This thesis consists of 8 chapters, which includes the ‘Introduction’, ‘Literature Review’, experimental chapters and ‘Conclusion’. The thesis structure is visualised in figure 1.1. The experimental chapters address different aspects of development of hydrogen metrology techniques as described above.

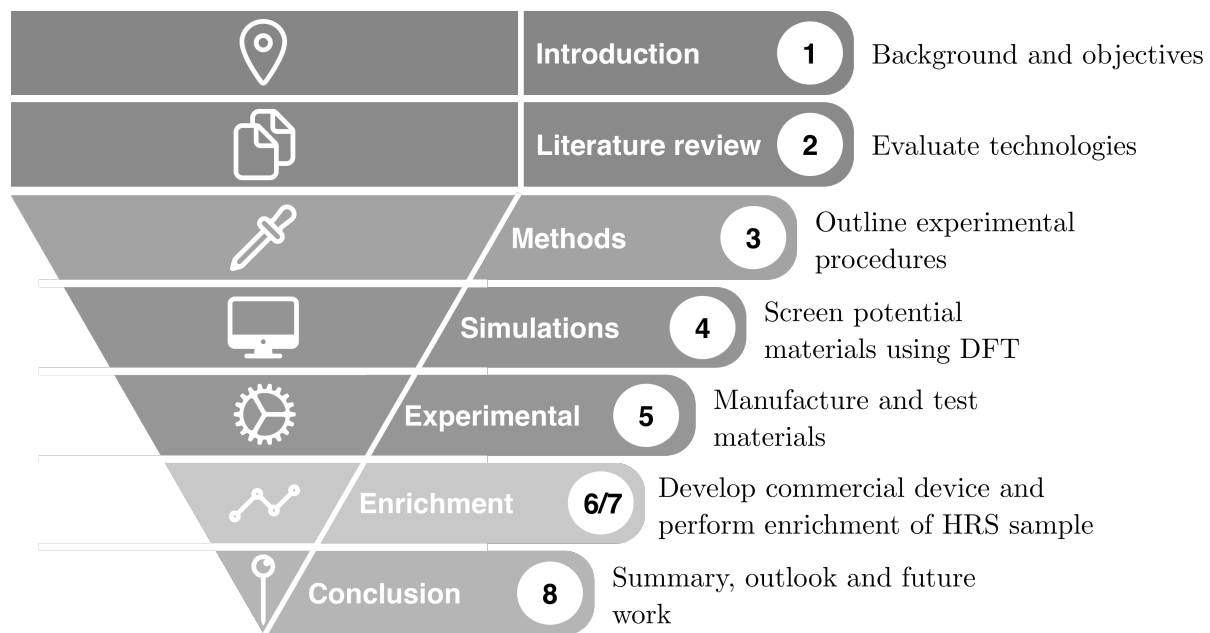


Figure 1.1: Schematic presentation of the thesis structure

References

- [1] Food & Rural Affairs Department for Environment and Department for Transport. Air quality plan for nitrogen dioxide (NO₂) in UK, 2017.
- [2] Toyota. The Toyota Mirai, 2015. URL <https://www.toyota.co.uk/new-cars/new-mirai/landing.json>.
- [3] Hyundai. Hyundai ix35 Hydrogen Fuel Cell Vehicle, 2015. URL <https://www.hyundai.co.uk/about-us/environment/hydrogen-fuel-cell>.
- [4] Honda. Honda Clarity Fuel Cell. URL <http://www.honda.co.uk/cars/new-coming-soon/clarity-fuel-cell/overview.html>.
- [5] C Mohrdieck. Daimler's road to FCEV market introduction. In *7th Stakeholder Forum of the FCH JU*, Brussels, 2014.
- [6] Symbio FCell. Zero emission mobility solutions, 2016. URL <https://www.symbio.one/en/>.
- [7] UK H2 Mobility. UK H2 Mobility: Phase 1 Results. Technical report, 2013.
- [8] Phil Summerton, Sophie Billington, Alex Stewart, Element Energy, Pierre Bidet, and Nathalie Faure. Fuelling France. Technical report, 2015.
- [9] Dennis Hayter and Intelligent Energy. Global H2Mobility initiatives – what they mean for FCEV introduction. Technical Report September, 2014.

- [10] Stephen Errity. Where can i buy hydrogen and where is my nearest hydrogen filling station? *Driving Electric*, Feb 2020. URL <https://www.drivingelectric.com/your-questions-answered/1363/where-can-i-buy-hydrogen-and-where-my-nearest-hydrogen-filling-station>.
- [11] International Standard ISO 14687: 2019. Hydrogen Fuel - Product Specification, 2019.
- [12] Arul Murugan and Andrew S Brown. Review of purity analysis methods for performing quality assurance of fuel cell hydrogen. *International Journal of Hydrogen Energy*, 40(11):4219–4233, 2015. doi: 10.1016/j.ijhydene.2015.01.041.
- [13] Tina M Nenoff Nathan W. Ockwig. Membranes for Hydrogen Separation. *Chemical Reviews*, 107:4078–4110, 2007.

Chapter 2

Literature review

2.1 Fuel cell electric vehicles

A Fuel Cell Electric Vehicle (FCEV) refers to a vehicle which uses a solid state electrochemical device to convert chemical energy into electrical energy for motor power. The most common fuel source for FCEV's is hydrogen, where energy is produced using oxygen from air and compressed hydrogen stored on board.

A fuel cell is made up from an electrolyte and two electrocatalysts at both the anode and cathode sides of the cell. The electrolyte separates the two electrodes and usually defines the type of fuel cell. At the anode side the fuel is oxidised as shown in equation 2.1, creating a positively charged ion and an electron. The electrolyte is designed to only allow the passage of ions, and prevents the passage of electrons. The free electron travels through a circuit, creating an electric current to provide power for it's desired use. The ions travel through the electrolyte to the cathode side of the fuel cell where they are reunited with the freed electrons, and oxygen to produce water as shown in equation 2.2. The overall process for a hydrogen fuel cell is shown in equation 2.3 and visualised in figure 2.1.

Fuel cells are typically categorised based on the material used as an electrolyte. This

classification determines the electro chemical reactions which take place, the type of electrocatalysts, fuels which can be used, and operating conditions. Some examples are Solid Oxide Fuel Cells (SOFC) which uses a proton conducting metal oxide heated to a high temperature (500-1000°C), proton exchange membrane fuel cells (PEMFC) uses a proton conducting polymer membrane as an electrolyte material, typically nafion. And alkaline fuel cells which use a uses an aqueous solution of potassium hydroxide.

While a number of fuel cell technologies can use hydrogen as a fuel source, the most suitable for FCEV's, and in particular mass production of affordable vehicles, are proton exchange membrane fuel cells. This is due to their high power density, low start up time, and low operating temperatures. [1]

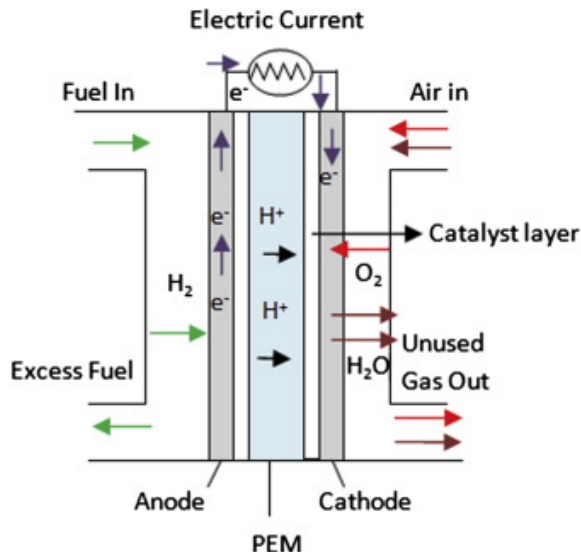
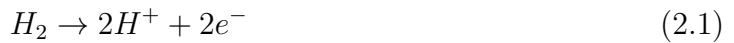


Figure 2.1: Schematic of fuel cell [2]



A PEMFC cell consists of two metal bipolar plates which act to distribute the fuel

and oxidant within the cell, aid water management within the cell, separate individual cells in a fuel cell stack, and carry current away from the cell. [1] A Membrane electrode assembly (MEA) which consists of the polymer membrane (usually nafion [3]), two dispersed noble metal catalyst layers to enable the anode and cathode reactions (Pt or Pt-alloys supported on porous carbon [3]), and two gas diffusion layers (graphite paper or cloth proofed with polytetrafluoroethylene [3]) to ensure uniform access of fuel and oxidant to the catalyst layer. The components are wedged between two rubber seals to ensure the cell is gas tight. Individual cells are combined in series to form a fuel cell stack which can provide the desired power as shown in 2.2

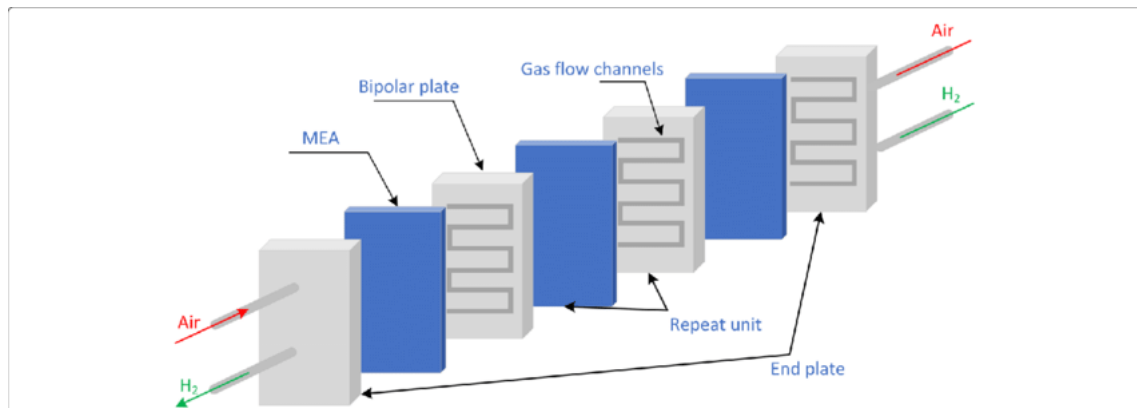


Figure 2.2: Schematic of a PEMFC stack [4]

2.2 Hydrogen Production

Hydrogen production refers to a range of industrial processes for generating hydrogen. Since there are no natural reserves of hydrogen, it must be obtained through one of these methods. The most important factor for determining the feasibility of a hydrogen production process is the primary source of energy that is used. Currently the options for this are nuclear energy in the form of heat; renewable energy in the form of heat, electricity, light; or fossil fuels either through decomposition of the hydrocarbons present in the fuel, or through heat. Currently the primary sources of hydrogen are from fossil

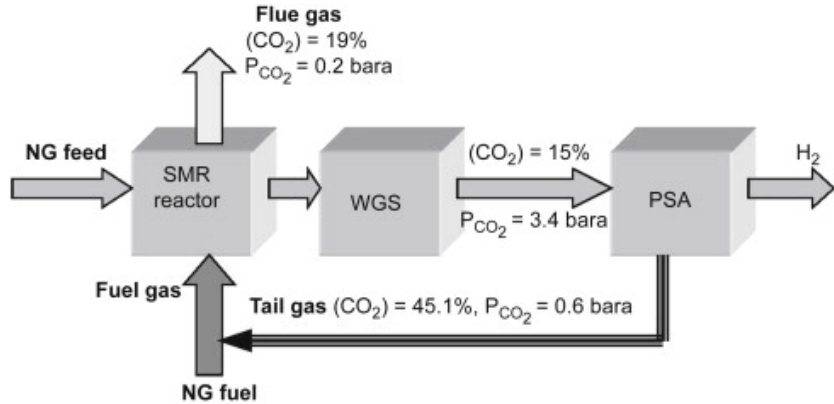


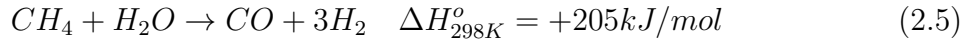
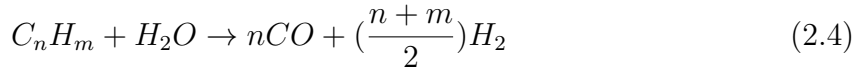
Figure 2.3: Simplified block diagram of a typical modern Steam Methane Reforming (SMR) and Water Gas Shift (WGS) plant. CO₂ concentrations are in mol.%. [8]

fuels: steam reforming of methane accounts for 48% and other hydrocarbons account for 30% of global hydrogen production; gasification of coal accounts for 18%; and electrolysis of water accounting for the remaining 4%. [5] Electrolysis and SMR will be discussed since these are expected to be the most dominant production methods in the future. [6]

2.2.1 Hydrogen from fossil fuels and hydrocarbons

Fossil fuels are the most dominant source of hydrogen production [5] and there are a number of processes which are commonly utilized in industry. The most popular and therefore the ones which will be discussed are steam methane reforming and hydrocarbon decomposition.

Steam Methane reforming is the conventional and most economical method for producing hydrogen, and it has been predicted by the IEA that this trend will continue despite the emergence of other hydrogen production methods. [7] Steam methane reforming occurs through a two-step chemical process. If another hydrocarbon other than methane is being used it must first be pre-reformed into methane as shown in equation 2.4. A schematic representation of the process can be seen in figure 2.3

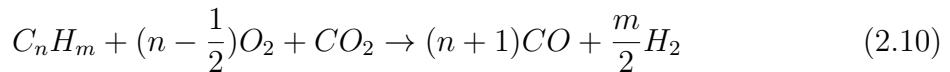
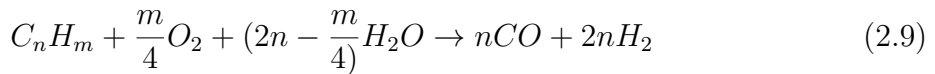
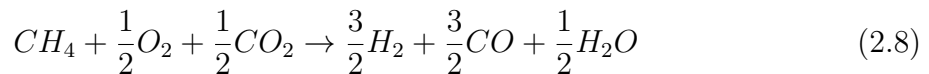
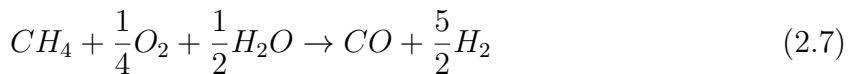


Equation 2.5 takes place in a reactor operating at 700-850°C, at pressures of 3-25 bar, and in the presence of a nickel based catalyst. [8] The result of this step is a mixture of CO and H₂, commonly referred to as syngas. This syngas is further used as a feedstock for the reaction shown in equation 2.6 known as water gas shift in order to produce greater hydrogen yields. This step is carried out in a two-step reaction. An initial high temperature stage at 350°C which converts majority of the syngas to CO₂ and H₂, and a final low-temperature step which operates at 250°C which utilizes a catalyst with higher activity to minimise the remaining CO₂. [8] The final product will be a mixture of CO₂ and H₂.

A number of separation steps are used in order to prevent impurities from contaminating the resulting gas mixture. The traditional separation step is pressure swing adsorption (PSA) which takes advantage of adsorption of gaseous molecules onto a molecular sieve at high pressures. Hydrogen purities of around 99.9% are achievable using this method however the cost is high and typically contributes to around 20-30% of the total production cost. [8] The other main separation step is desulphurization which uses a combination of CoMo and ZnO catalysts in series at 450-550°C to remove sulphur. [8] This step is essential to ensure sulphur is not present and to ensure catalyst poisoning does not occur at any point in the process.

The cost of producing hydrogen through SMR varies but averages at around £2 per kg of hydrogen and therefore costs around £2000 per tonne of hydrogen produced. [9]

Autothermal Reforming (ATR) combines SMR and fuel oxidation into a single unit. [10] Oxygen, sometimes CO₂, and steam is used in a reaction with the selected hydrocarbon to produce syngas (H₂ and CO). Two different types of catalysts are commonly used for ATR: Group VIII transition metals (e.g. platinum, rhodium or nickel) supported on an ion-conducting oxide (e.g. ceria, gadolinium-doped ceria), and mixed non-noble metal oxides with the ABO₃ stoichiometry and a perovskite structure. [11] The full reaction is a combination of steam reforming and partial oxidation reactions, these are shown in equations 2.7 to 2.10[11]



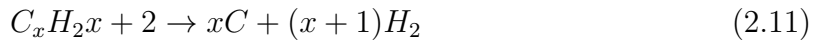
The key element for determining the H₂/CO ratio of the produced syngas is the feed composition. When carbon dioxide is present in the feed the H₂/CO ratio achieved is around 1:1, whereas when steam is present ratios of around 2.5:1 are possible. On an industrial scale the process is usually performed at temperatures between 900-1100 °C, using a feed with an O₂/hydrocarbon ratio between 0.55-0.6.[12] ATR can be used to produce hydrogen from natural gas, however it has recently been studies for production of hydrogen from biofuels. [13]

By taking advantage of this the heat produced from the exothermic oxidation of fuel can be used to power the endothermic reforming process. ATR has become popular in recent years for small, distributed generation of hydrogen, demonstrating faster start up times than SMR. The process also features a compact design with a small footprint, and is soot free, offering clear potential economic and operational benefits over SMR. [11]

Most ATR plants do not suffer from soot formation, due to optimised design inhibiting these reactions.[11]

Despite this ATR is more favourable towards producing exit compositions with low H₂/CO ratios, making SMR the better choice for producing hydrogen in large capacities. [11] As smaller, more distributed hydrocarbon production technologies, such as biogas production, become more widespread, ATR would be a beneficial companion due to it's modular, small scale nature.

Hydrocarbon decomposition is a process by which hydrocarbon molecules are converted into solid carbon and hydrogen. [14] This reaction is typically operated either thermally or by creating a plasma. A metallic catalyst such as nickel or iron is required. The reaction is shown in equation 2.11 [15]

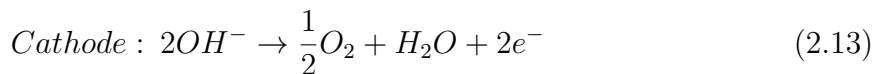
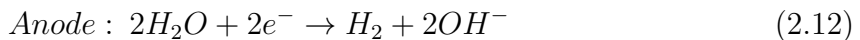


An advantage of this process is that the only feedstock is the hydrocarbon, so presuming that the feedstock is sufficiently pure this method of hydrogen production should remove the needs for further downstream processing. [14] The main disadvantage of this method is since solid carbon is the main by-product the catalyst will be easily deactivated and will require regular maintenance to ensure carbon build up is managed. [14]

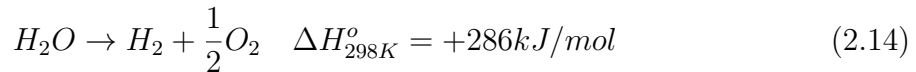
2.2.2 Hydrogen from water

Electrolysis uses an electric current to split water into hydrogen and oxygen using separate anode and cathode chambers isolated using an ion exchange membrane. The anode and cathode reactions are shown in equations 2.12 and 2.13. The main competitive advantage of electrolysis is that reactors are modular and highly scalable, allowing

hydrogen to be produced in a distributed manner. [16] The main input to the process is electricity and if this electricity is produced using renewable sources then the process can be considered carbon neutral. However if a non-renewable source of energy is used the net carbon produced per mole of hydrogen would be higher than that produced by SMR. [17] Electrolysis is incentivised by the increasing price of natural gas and the decreasing price of electricity, which some predict will result in electrolysis becoming more economically feasible than SMR in the future. [16] Currently most commercial electrolyzers operate at efficiencies of around 80% and therefore requires around 55000 kWh per tonne of hydrogen produced. The average price of industrial electricity in the UK in 2020 is around £0.13 per kWh [18] and therefore the average price of hydrogen produced through electrolysis is around £7150 per tonne. [9]



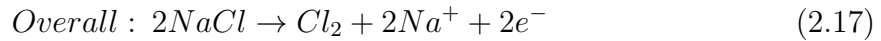
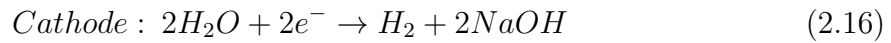
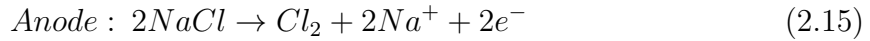
Thermal decomposition of water is the process of splitting water into hydrogen and oxygen at temperatures of 2000°C as shown in equation 2.14. [6] The operating temperature of the reaction can be lowered under the presence of a nickel or iron based catalyst. [6] Due to the high energy demand for this production method water splitting is not a feasible method of commercial hydrogen production.



Chloro Alkali process

The chloro alkali process is an electrolysis process which involves the electrolysis of sodium chloride solutions. The process is already performed on an industrial scale in

the production of chlorine and sodium hydroxide. Hydrogen is a by-product of the cathode reaction in the electrolytic cell shown in equation



It is estimated that around 0.4 million tonnes of hydrogen per year and this could potentially contribute to annual demand. [19] The process is extremely energy intensive however, requiring 2500 kWh per tonne of NaOH produced or 99200 kWh per tonne of H₂ produced. [20] Therefore it is unlikely that this process will be used to solely produce hydrogen. As with many waste gases, producers often reuse the gas to power parts of their process, typically through consumption. It may also be the case that producers would rather find more efficient methods for performing this rather than selling their hydrogen on the open market. A recent example of this is in 2019 when a chloro alkali plant in Jordan reused their waste hydrogen in a fuel cell situated on site to power their process. [21]

2.3 Hydrogen impurities in the supply chain

The method used to manufacture hydrogen will affect which potential impurities can be present in the final product. While steps are taken in both electrolysis and SMR to ensure a pure product is produced, there is still the chance of impurities reaching the customers fuel cell. This section will explore how impurities can enter the hydrogen

supply chain, and their effect on the operation of a PEMFC. A summary is shown in table 2.1

Table 2.1: Summary of impurities in the hydrogen supply chain and their effects on fuel cell operation adapted from [22]

Impurity	Production sources	Contamination source	Contamination barriers	Effect on fuel cell operation
N ₂	SMR	Raw material PSA malfunction Maintenance	PSA	
	Electrolysis	Leakage Air intake into water tank	Maintainance PEM membrane H ₂ pressure > N ₂ pressure supply	Reduced energy density of fuel
Ar He	SMR	Raw materials	PSA	
	Electrolysis	Generation at the anode Membrane cross over TSA malfunction	TSA operating condition Oxygen sensor	Potential damage to hydrogen storage
O ₂	SMR	By-product Raw materials	PSA	Temporary electrocatalyst poisoning
	Electrolysis	By-product Raw materials	CO sensor on line	
CO	SMR	Raw materials	PSA	Damage to hydrogen storage medium Could cause formation of CO
	SMR	Raw materials	CO ₂ filter	
CO ₂	Electrolysis	Water at anodic side Air into the pure water tank	Anodic separator tank Ion exchange resin in closed water loop PEM membrane	
	SMR	Raw material	PSA	Reduced energy density of fuel
CH ₄	SMR	Raw material	Methane sensor on line	
	SMR	Raw material Reactant	PSA	Ice formation during refilling K ⁺ and Na ⁺ contamination reducing cathode side conductivity
H ₂ O	Electrolysis	Through PEM membrane Hydrogen output water saturated	TSA dryer Dew point monitor Operating procedure	
	SMR	TSA malfunction	Desulfuration unit	
Total sulphur compounds	SMR	Raw material	Sulphur trap in reforming system PSA	Permanent electrocatalyst poisoning
NH ₃	SMR	Raw material	Stainless steel pipe and vessel PSA	
	Electrolysis	Water at anodic side	Reverse osmosis PEM membrane	Reduced ion exchange capacity
Formaldehyde Formic acid	SMR	Raw material	PSA	Temporary electrocatalyst poisoning
	SMR	Raw material	PSA	Temporary electrocatalyst poisoning
Halogenated compounds	SMR	Raw material	Desulfuration unit Chlorinated trap in reforming system PSA	
	Electrolysis	Raw material contamination	Stainless steel pipe and vessel Reverse osmosis	Permanent electrocatalyst poisoning
Monitoring Cl ₂ concentration				

Water

Water can be present from both SMR and electrolysis due to it being a main by-product of SMR reactions, and the main reactant in electrolysis.

The PSA process used in SMR is an appropriate barrier to prevent water contaminating the end product. This is due to the molecular sieves commonly used having a high selectivity for water. [8] When a PSA system is designed to produce an output of CO below 0.2 µmol/mol, the concentration of water will be less than 0.1 µmol/mol. [22] This makes it unlikely for H₂O to be present in hydrogen produced using this method.

There are three potential pathways for water to contaminate hydrogen through electrolysis. These are:

- Electro-osmosis through the proton exchange membrane
- Hydrogen water saturated at 60°C
- Drier malfunction

Modern electrolysers are fitted with a drier, which is the main barrier for water vapour exiting the process with hydrogen. [22] In the event of drier failure, most systems feature a dew point analyser that will trip, shutting off production until the issue can be fixed. [22]

Water can also contaminate produced hydrogen in the chloro alkali process since, similar to electrolysis, it is present in the process. Typically the process contains a drier which ensures that a dew point of -20°C is maintained which should prevent any water in the exit stream.

Water generally does not affect the function of a fuel cell, however; it provides a transport mechanism for water-soluble contaminants such as K^+ and Na^+ [23] to pass through the electrolyte and have a negative long-term effect on the conductivity of the cathode side of the membrane. In addition, water may increase the risk of ice formation within vehicle fuel storage and hydrogen dispensing systems under certain conditions.

Total hydrocarbon content

The presence of hydrocarbons are most likely to result from the SMR process. Hydrocarbons are not expected to be present at all in electrolysis or chloro alkali however could potentially contaminate the system if hydrocarbons are present in any components such as compressors. Similar to water contamination through SMR, the most likely reason

for hydrocarbon contamination is due to malfunction of the PSA system used to purify the product hydrogen.

A PSA system designed to deliver hydrogen with a CO concentration <0.2 $\mu\text{mol/mol}$ should be sufficient to reduce the amount fraction of hydrocarbons to below the 5 $\mu\text{mol/mol}$ required by ISO 14687. [22]

Different hydrocarbons have different effects on fuel cell performance. Generally aromatic hydrocarbons adsorb more strongly on the catalyst surface than other hydrocarbons, inhibiting access to hydrogen.[23] Methane (CH_4) is generally considered an inert constituent and its main effect on fuel cell performance is diluting the hydrogen fuel stream. [23]

Oxygen

In SMR processes oxygen is not used as a raw material, nor is it stable during the process conditions, readily reacting with hydrogen to produce water. In addition to this the oxygen content of the feedstock to the PSA separation stage must be below a certain level for safety reasons. Therefore oxygen contamination from hydrogen produced from SMR is unlikely.

Oxygen is a main by-product of electrolysis, although is generated at the anode side of the electrolysis stack. Likely methods of contamination are through cross over through the PEM membrane. Due to the danger of high oxygen levels in hydrogen streams, most electrolysis systems have an oxygen sensor that trips the system if the concentration of oxygen in the hydrogen stream surpasses 5 $\mu\text{mol/mol}$. [22]

Oxygen can also contaminate the exit stream in the chloro alkali process due to it's presence in ambient air. There are no safeguards in place to prevent oxygen contaminating the hydrogen stream so it is likely that oxygen can be present in any produced hydrogen if given the opportunity.[22]

Oxygen in low concentrations does not adversely affect the function of the fuel cell system; however, it may be a concern for some on-board vehicle storage systems, for example, by reaction with metal hydride storage materials. [23]

Helium, nitrogen and argon

Helium may be as a feed material in through SMR as is can be present in low concentrations in natural gas. It is unlikely that helium will be present in the feed for electrolysis. There is also no barrier to Helium in the exit stream and therefore any helium that enters a SMR or electrolysis process will not be removed.

Argon is similar to helium, however it is more likely for Argon to be present in the natural gas feedstock for SMR. Argon is also present in low concentrations in air. Unlike helium, the PSA step in SMR can act as a barrier for Argon, however this will depend on the specific molecular sieve used in the system. [22]

Nitrogen is the most likely inert impurity to be present in fuel cell hydrogen, this is due to the abundance of nitrogen in the air which the system could be exposed to, and the frequency at which nitrogen is used as a functional gas in processes for purging chambers, actuating valves etc.

Inert constituents, such as helium (He), nitrogen (N_2) and argon (Ar) do not adversely affect the function of fuel cell components or a fuel cell system. However, they dilute the hydrogen gas. N_2 and Ar especially can affect system operation and efficiency and can also affect the accuracy of mass metering instruments used for hydrogen dispensing. [23]

Carbon dioxide

Like most other impurities which are present in SMR, CO_2 is likely to be removed from the SMR process at the PSA step, with most commonly used molecular sieves being

able to remove carbon dioxide during normal operation. [8]

CO₂ can be present in the water used for electrolysis although there are several interlocks to prevent it reaching the exit stream. Most electrolysis systems have a CO₂ filter on the inlet and a reverse osmosis unit to ensure the purity of the inlet water. An anodic separation tank which features an ion exchange resin in a closed water loop also acts as an additional barrier, and finally CO₂ has a low crossover potential through the PEM membrane and therefore is unlikely to cross into the cathode side of the system.[22]

Carbon dioxide is not likely to be in the product stream from hydrogen produced in chloro alkali as it remains in the caustic soda lye that is produced. CO₂ could also be formed from oxidation of the membrane material when degraded however no quantitative assessment has been made on this. [22]

CO₂ does not typically affect the function of fuel cells. However, CO₂ may adversely effect on board hydrogen storage systems using metal hydride alloys. With CO₂, at levels higher than the specification, a reverse water gas shift reaction can occur under certain conditions in fuel cell systems to create carbon monoxide. [23]

Carbon monoxide

Carbon monoxide is a main byproduct of SMR which is separated from the exit gas stream through PSA. [8] If this fails SMR processes are fitted with a CO sensor to ensure the concentration in the product does not pass a certain threshold. [22] It is unlikely for CO to be present from electrolysis.

Carbon monoxide (CO) is a severe catalyst poison that adversely effects fuel cell performance by inducing a competitive adsorption effect between itself and hydrogen on the electrocatalyst surface. The result is a temporary reduction in operating efficiency. [23] Although its effect can be reversed through mitigating strategies, such as material selection of membrane electrode assembly (MEA), system design, and operating condi-

tions, its effect on operation is still a concern. Lower catalyst loadings are particularly susceptible to catalyst poisoning contaminants.

Total sulfur compounds

Sulphur contamination is most likely to come from hydrogen produced from hydrocarbon sources. Since the SMR process also uses catalysts that are susceptible to poisoning from sulphur compounds all plants feature a desulphurisation unit upstream from the main process. [8] This is designed to reduce the concentration of sulphurous compounds to <50 nmol/mol. [22]

Should the desulphurisation unit fail the catalysts used in both reforming steps will be deactivated, preventing the process from operating and will likely result in shut down of the plant. PSA also acts as a final barrier, since H₂S will adsorb onto the molecular sieves more strongly than CO. [22]

The other potential source of sulphur contamination is the potential release from any gasket materials used in the process. This can be easily prevented by ensuring only materials that do not contain sulphur are used. [23]. It is unlikely that sulphur contamination will arise from electrolysis.

Sulfur containing compounds are severe catalyst poisons that at even very low levels can cause irreversible degradation of fuel cell performance due to a permanent reaction taking place between sulphur and the platinum catalyst. The specific sulfur compounds addressed in particular are: hydrogen sulfide (H₂S), carbonyl sulfide (COS), carbon disulfide(CS₂), methyl mercaptan (CH₃SH). [23]

Formaldehyde and formic acid

Formaldehyde (HCHO) and formic acid (HCOOH) are produced through a side reaction in SMR depending on the specific operating conditions of the process.[8] PSA is the

main barrier for preventing contamination of the product. [22]

Formaldehyde and formic acid have a similar effect on fuel cell performance as CO and are thus considered as reversible contaminants. The effect of HCHO and HCOOH on fuel cell performance can be more severe than that of CO due to slower recovery kinetics and their specifications are lower than that for CO. [23] Lower catalyst loadings are particularly susceptible to catalyst poisoning contaminants.

Ammonia

Hydrogen could be contaminated with ammonia through either SMR or electrolysis. Ammonia is a by-product of the reforming steps and PSA should be sufficient to remove ammonium from the exit stream of SMR. Ammonia can also be present in water used in electrolysis however the reverse osmosis step used to purify the water before the process is normally sufficient in removing all ammonia before it is used in the process. [22]

Ammonia is also researched as a potential hydrogen storage and transport medium, where ammonia is decomposed into nitrogen and hydrogen prior to use in a fuel cell. [24] Therefore in the future there may also be concerns regarding ammonia entering the fuel cell through this medium.

Ammonia (NH_3) causes some irreversible fuel cell performance degradation by affecting the ion exchange capacity of the ionomer of the proton exchange membrane. [23]

Total halogenated compounds

Halogenated compounds can contaminate hydrogen by entering either SMR or electrolysis through the process input, or leaking into the process at other points where they are used. Potential sources include chlor-alkali production processes, refrigerants used in processing, and cleaning agents. [22]

In the chlor-alkali process, the presence of chlorine and hydrochloric acid in hydrogen gas could be likely since they are main feedstocks in the process. Both HCl and Cl₂ are highly soluble in water and are likely to leave the process in solution. Cl₂ and H₂ are also contained from each other and not expected to cross contaminate. Cross contamination could occur in the event that there is not enough liquid water in the system. This would likely be detected as the system would quickly fill with hydrogen gas which is continuously monitored due to risk of explosion, shutting down the system and preventing contaminated hydrogen leaving. Therefore it is unlikely that Cl will be present in the produced hydrogen. Halogenated compounds cause irreversible performance degradation similar to sulphur, reacting with the platinum electrocatalysts to form platinum-halides such as PtCl₄. [25] However the concentrations required to cause this damage has not been well documented in literature.

Other impurities

While ISO 14687 does a good job of providing guidance on current impurities which can affect the use of hydrogen, in the future as new sources of hydrogen become more widespread, and new storage mediums are commercialised, more impurities will have to be considered.

An example is Siloxanes, which are a group of chemical compounds which feature an Si-O-Si group. Siloxanes are commonly found in consumer goods and are a common byproduct of biogas when they find their way into a landfill. Burning siloxanes results in the formation of solid SiO₂. These deposits are extremely abrasive and result in a large efficiency reduction in power generation equipment. As biogas and biomethane production is further adopted it is reasonable to foresee its utilization as a hydrogen feedstock. For SOFC's siloxanes pose a clear risk due to their high operating temperature making it extremely susceptible to SiO₂ formation. Past studies have shown that 1

ppm of siloxanes can greatly effect the operation of a SOFC, while 10ppm will result in complete failure after 30 minutes of operation. [26] While PEMFC's will be less susceptible to this degradation due to their lower operating temperature, there is still evidence of siloxane build up in the pores of the catalyst layer. [27] The siloxane compounds were mobile within the polymer membrane, and while not hindering the proton conductivity, resulted in their accumulation at the anode side. [27] This will result in decreased fuel cell performance due to increased gas transfer resistance of oxygen. The impact of siloxanes on the operation of a fuel cell is clear and in the future it is reasonable for siloxane content to be included in the standard for fuel grade hydrogen.

VOC's are another class of impurity which, while not directly mentioned in the ISO standard, are also likely to have a large effect on the operation of a fuel cell. Alcohols, alkenes, and other aromatic compounds can be found in waste derived hydrocarbons. If not checked these impurities could potentially form acidic gases which can corrode catalytic surfaces the fuel cell in a similar manner to halogenated compounds and sulphur containing compounds. [26] VOC's could also potentially react with the electrolyte in a fuel cell, also leading to a greatly reduced cell performance. [28]

Finally, while much thought has been put into the effect of impurities on the performance of the fuel cell, much less has gone into their potential effects on auxillary components. In particular in the future it is likely that we will see novel hydrogen storage technologies on board FCEV's, examples being Liquid Organic Hydrogen Carriers (LOHC) and metal hydride storage. The above mentioned impurities, along with other ISO 14687 impurities, are likely to have an effect on metal hydride storage systems and should also be studied and the standard adjusted to factor for potentially greater effects on these systems than in fuel cells. [29] For LOHC systems there is some evidence that these can act as a sourec of impurities themselves, with some LOHC's releasing VOC's alongside the stored hydrogen when released.[30] The precise impurities released by dif-

ferent types of LOHC's, their expected concentration, and their further effect on the operation of the FCEV should be further researched and factored into their suitability for use in hydrogen vehicles.

2.4 Hydrogen impurity enrichment using metal membranes

'Hydrogen impurity enrichment' is a term for any technique which involves increasing the concentration of impurities within a hydrogen sample by means of removing the hydrogen matrix gas. There are two previous reports of impurity enrichment being used as a technique for hydrogen impurity analysis. The first report by Papadis et al at Argonne National Laboratory used a Pd/Cu [31] coated Pd/Ag membrane for non-sulphur containing hydrogen samples and a Pd/Au coated Pd/Ag membrane for sulphur containing hydrogen samples to enrich impurities in a 50 bar sample. The analyte gas used contained N₂, CH₄ and CO₂ at 100 μmol/mol and an additional 2 μmol/mol of H₂S during sulphur tests. The enrichment was calculated by using measured values of temperature and pressure along with the non-ideal gas law this was represented through a 'calculated enrichment factor' as shown in equations 2.18 and 2.19.

$$CEF_{NI} = \frac{\frac{P_{1,a}V_1}{Z_{1,a}RT_{1,a}} \frac{P_{2,a}V_2}{Z_{2,a}RT_{2,a}} - \frac{P_{1,b}V_1}{Z_{1,b}RT_{1,b}}}{\frac{P_{2,b}V_2}{Z_{2,b}RT_{2,b}}} \quad (2.18)$$

$$y_{i,a} = \frac{y_{i,b}}{CEF} \quad (2.19)$$

For equation 2.18 CEF_{NI} is the Calculated Enrichment Factor for the non-ideal gas law method, P_{1,a} P_{1,b} refer to the pressures in the gas cylinder and enrichment vessel before enrichment, P_{2,a} P_{2,b} refer to the pressures in the gas cylinder and enrichment vessel after

enrichment, V_1 refers to the volume of the gas cylinder which is generally 10L, V_2 is the volume of the enrichment vessel, R is the gas constant $8.3145\text{Jmol}^{-1}\text{K}^{-1}$, $T_{1,a}$ and $T_{1,b}$ is the temperature of the gas cylinder and enrichment vessel before enrichment, $T_{2,a}$ and $T_{2,b}$ is the temperature of the gas cylinder and enrichment vessel after enrichment. Z is the compressability factor of the hydrogen in either the gas cylinder (a) or enrichment vessel (b) before (1), or after (2) enrichment.

For equation 2.19 $y_{i,a}$ is the concentration of component i before enrichment, $y_{i,b}$ is the concentration of component i after enrichment, and CEF is the calculated enrichment factor determined in equation 2.18

The set-up was able to reach enrichment factors of around 32 for non-sulphur tests and 15 for sulphur tests. The non-sulphur tests closely matched with the actual component concentrations, however in the second set of tests there was some loss of sulphur observed, most likely due to the formation of palladium sulphide on the surface of the membrane, or through wall catalysed reactions.

A similar experiment was performed by National Physical Laboratory with the aim of decreasing the uncertainty of using such a device. [32] The non-ideal gas law method used in the previous paper [31] was compared to a novel tracer enrichment method developed by NPL. [32] The tracer enrichment method involves spiking the hydrogen sample with a known quantity of krypton prior to enrichment. The enrichment factor is then calculated using the change in concentration of the krypton as shown in equation 2.20.

$$CEF_{Tracer} = \frac{y_{kr_b}}{y_{Kr_a}} = \frac{1}{A_{Kr_b}} \frac{A_{Kr_b}}{A_{Kr_a}} y_{Kr_{st}} \quad (2.20)$$

For equation 2.20 CEF_{Tracer} is the Calculated Enrichment Factor determined using tracer enrichment, y_{kr_a} and y_{kr_b} is the concentration of krypton in the enrichment vessel before and after enrichment respectivley, $y_{Kr_{st}}$ is the concentration of krypton in the

standard used to determine the concentration of krypton in the sample. A is a corerlation factor for the detector used find the concentration of Krypton, this is usually 1 but is added in order to account for the uncertainty of thye detector.

The set-up was similar to the one used by Papadias et al [31] and was used to enrich a 50 bar 10L hydrogen sample containing 1.5-2 $\mu\text{mol/mol}$ of CO, Kr, CH₄ and N₂. Use of the tracer enrichment method reduced the associated uncertainty from 2.6% to 1%. Two tests were performed, with the second test resulting in membrane failure.

When operating the hydrogen impurity enrichment device it was found that both methods should be used to calculate the CEF.[32, 33] While the tracer enrichment method has a lower uncertainty due to it being dependant on fewer variables, it is impossible to tell if a leak has occurred in the device due to the covariance phenomena. [32] The co-varience phemonena refers to the fact that any leaks from the system will effect the concentration of the tracer in an identical way to other impurities in the sample, therefore preventing leaks from spoiling results. Leaks in the enrichment device could occur due to thermal expansion of components due to heating to the required operating temperature or cracks forming in the membrane. The stability of membranes used in such a device will be discussed in the following section. During a leak it will be expected that the ratio of krypton, along with other impurities which are not naturally present in air, will remain constant, resulting in no change in the CEF. A leak will allow oxygen and nitrogen to enter the system and throw off the measurement of these two impurities. While the tracer enrichment method could still be used to calculate the amount fraction of other impurities, the non-ideal gas law method would have to be used to provide an accurate measurement for Oxygen and Nitrogen.

A device similar to the HIED is the Hydrogen Elimination Mass Spectrometer (HEMS) designed by Power + Energy USA. [34] The principle behind the HEMS is the same as the HIED, where a palladium membrane is used to selectively remove the hydrogen

matrix gas and thus concentrate the impurities within the hydrogen sample. The output is directly fed into a mass spectrometer which allows in-situ measurements to be performed. The limit of detection specified by the manufacturer claims to be in the range of pmol/mol however there is no published information regarding the accuracy or uncertainty associated with the device. As of 2016 the device was discontinued by the manufacturer.

2.4.1 Other enrichment methods

Sorbent tubes

The use of traps and sorbent tubes to pre-concentrate impurities in gases is very common in gas analysis, but only two hydrogen purity analysis standards have incorporated this technique to facilitate purity analysis. A method for concentrating the impurities in a sample of hydrogen using a zeolite- packed chromatographic column has been described in a paper by Hille [35]. The method involves flowing the gas sample into the column using a pump and cooling the column to a temperature that allows the impurities to remain trapped whilst the matrix gas passes through. The sample is then transferred to Gas Chromatography Mass Spectrometer (GC-MS) for analysis. The enrichment factor for this method is determined by the flowrate and amount of time that the gas is sampled into the column. The method was validated by analysing gas mixtures of hydrogen containing 8.7 mmol/mol of silane. By enriching the sample, the signal- to-noise for the same measurement was increased by a factor of 2000 indicating that levels in the range of 4 nmol/mol of silane would easily be measured using this method whereas the usual limit of detection (without pre-concentration) would have been 1 $\mu\text{mol/mol}$

Cryo-focusing

A method for performing pre-concentration by cryo-focusing has been detailed in ASTM WK34574 where the device is used to concentrate the impurities in a sample of hydrogen before analysing the gas using Gas Chromatography Mass Spectrometry (GC-MS) [33]. The pre-concentration method involves trapping the impurities onto a glass bead trap at -150°C. By increasing the temperature of the trap all of the impurities apart from water are transferred to a separate Tenax trap which is cooled to -170°C. Upon heating once again the enriched sample is introduced to the analyser. Very high enrichment factors can be achieved using this method by flowing a high volume of the sample gas through the pre-concentration device to allow capture of the impurities whilst the hydrogen is removed. No information was provided in the standard to indicate the accuracy or limitations of this method.

2.5 Review of hydrogen selective membranes

The term membrane is used to describe a semipermeable barrier which selectively allows certain species to pass through it, while preventing or inhibiting the passage of others. The driving force for gas separation through a membrane is the pressure and component concentration gradients across the chosen material. In the context of hydrogen separation, the trans-membrane pressure and hydrogen concentration gradient across the feed and permeate, combined with the unique properties of the chosen separation material, will allow hydrogen to pass through the membrane, while preventing or inhibiting the transport of impurities which the membrane is not selective or less selective towards. A large number of materials have been studied for hydrogen separation. For the purpose of this review they will be split into four broad categories based on their material type and separation mechanism which is related to their pore structure (dense or porous);

these categories are shown in Table 2.2 and visualized in Figure 5.1.

The material, its structure with regards to pore size and pore size distribution, and surface chemistry, all contribute to the separation mechanism for removing hydrogen from its constituent gas mixture. The six main membrane separation mechanisms are visualised in Figure 5.1, with (i) – (iv) showing the four separation mechanisms for gases in porous media, and (V)- (Vi) showing gas separation through dense media. For porous materials typically a combination of these mechanisms dictates the overall separation performance due to imperfections in the membranes structure. All dense membranes should be dictated by the solution diffusion mechanism and the presence of any other mechanisms are evidence of imperfections in the membrane.

For most porous media, the separation mechanism is dominated by Poiseuille flow or Knudsen Diffusion. The precise separation mechanism can be determined by calculating the ratio between the mean free path of the gas molecules (λ) and the pore radius (r) as shown in Equation 2.21 where η is the viscosity of the gas, P is the pressure, T is the temperature, M_w is the molecular weight of the gas, and R is the universal gas constant.

$$\frac{r}{\lambda} = \frac{2P}{3\eta} \sqrt{\left(\frac{2M_w}{\pi RT}\right)} \quad (2.21)$$

This ratio determines the contribution of Knudsen and Poiseuille flow. If $r/\lambda > 1$ it would indicate that the main gas transport rate limiting step is due to molecule-molecule collisions indicating that Poiseuille flow is the dominant transport mechanism. Likewise if $r/\lambda < 1$ it indicates that molecule-wall collisions govern the rate limiting step showing that Knudsen diffusion is the dominant mechanism. If the transport is purely Knudsen diffusion the H_2/CO_2 selectivity of the membrane will be equal to around 4.7. Since this value is relatively low, it has pushed researchers into fabricating membranes with smaller pore structures, and to modify their membranes to take advantage of specific surface interactions. Both of these developments allow researchers to surpass the selectivity

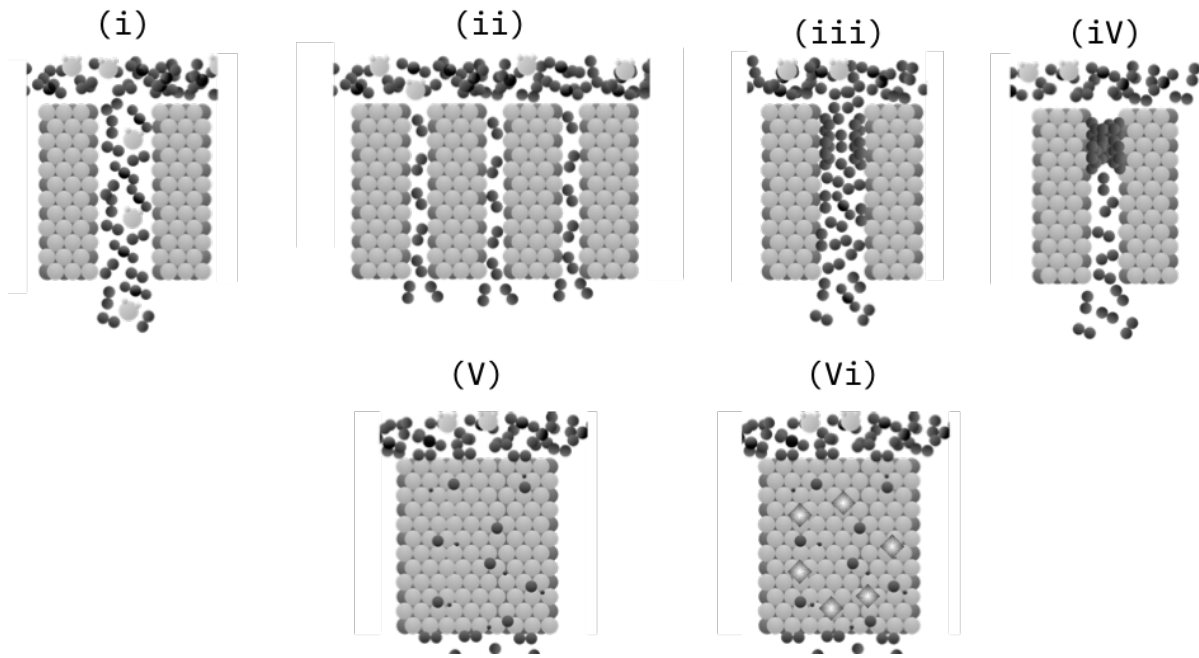


Figure 2.4: Illustration of the five membrane separation mechanisms (i) Poiseuille Flow/Knudsen diffusion, (ii) Molecular Sieving, (iii) Surface diffusion (iV) Capillary condensation (V) Solution diffusion (Vi) Facilitated transport

achievable with purely Knudsen diffusion.

Molecular sieve materials can be classed as macroporous ($>50\text{nm}$), mesoporous (2- 50nm) and microporous ($<2\text{nm}$) with microporous materials being the most relevant for hydrogen separation processes. These membranes are fabricated in such a way that the passageways are small enough that the entrance of molecules with large kinetic diameters is not possible. This results in higher permeation of smaller components in a gas mixture such as H_2 or He while slowing, or completely preventing the passage of bulkier molecules. This mechanism, while effective for some gas mixtures, may not be feasible when looking to perform separation on similar sized gas pairs; selectivity is often hindered by competitive adsorption between the species due to the surface chemistry of the material. Fabrication of these membranes can also be difficult and manufacturing large scale membranes with a tight enough pore size distribution to ensure molecular sieving still proves to be a difficult task. Common microporous materials which

are able to be fabricated into molecular sieving membranes are zeolites, metal organic frameworks, activated carbon, and amorphous silica.

Surface diffusion and capillary condensation are similar in that the surface chemistry of the pores in the membrane has a large effect on the separation efficiency. Surface diffusion occurs when the walls of the pore either intrinsically, or following modification, provides adsorption sites for the desired gas molecule. The gas molecule will adsorb onto the walls resulting in faster diffusion through the pore structure than other gases in the mixture. Similarly, capillary condensation typically follows on from surface diffusion and involves the gas species condensing within the pore of the membrane, either due to stronger molecule-wall interactions, or a smaller pore radius. The condensation of the molecule results in further selectivity improvements towards this component by providing an added transport barrier to other gas species.

Gas transport in dense media is typically harder to categorise due to the unique material chemistry present in each material, however all dense membranes perform separation through some variation of the solution diffusion mechanism. Typically, the following steps are always present in some form:

1. Adsorption of gas species onto the surface of the membrane
2. Diffusion of gas species through the bulk of the membrane
3. Desorption and diffusion of the gas species in the downstream.

More details will be provided on the precise features of solution diffusion in each material in the following sections. Facilitated transport is a sub section of solution diffusion and occurs in dense membranes which have a selected chemical species added into the bulk of the membrane. These materials are chosen based on the presence of a particular interaction with components of a gas species. These interactions are typically reversible reactions between the added species and the gas intended for separation and

is intended to enhance the diffusion of the selected gas, this additive could either be fixed species (solid) or mobile (liquid).

The most commonly reported metrics for membrane performance is the flux or permeability coefficient and selectivity. The flux (J) of a membrane is a measure of the amount of gas the membrane is allowing to pass per unit time per unit surface area and is typically used as a measure for how effective the fabricated membrane performs. The permeability coefficient (P) can be derived from the flux and is a quantitative expression which gives a specific measure of the separation properties of a material independent of operational and manufacturing constraints such as operating pressure and membrane thickness. While flux and permeability are similar and tied to each other they are both useful in their own way. The permeability coefficient is typically tied to the material and is useful for comparing different materials to each other, while the flux offers a measure on how effective a specific membrane is.

The selectivity ($\alpha_{i/j}$) represents the separating ability of the membrane for a specific gas species (i) with respect to another gas species (j). This is common notation for porous membranes and membranes which are not completely selective towards one component. For membranes which are only selective towards one component such as dense metal and dense ceramic, the selectivity is not reported since any presence of another component in the exit stream is generally an indication of a manufacturing defect.

While these values are reported for all membranes in order to allow for a direct comparison of performance, this is where the similarities end. The fundamental separation mechanism, manufacturing techniques, and unique material chemistry are often different for each material. In addition to this there are other important metrics for the usefulness of a membrane such as mechanical stability, lifespan, and chemical resistance which are more difficult to quantify.

Table 2.2: Types of hydrogen separation membrane

Material	Separation mechanism	Mechanical stability	Chemical Stability	Operating temperature	Selectivity
Polymer (Dense)	Solution diffusion, Facilitated transport	Susceptible to Compaction [36] and Swelling [37]	Low chemical stability, Degrades under H ₂ S, HCl, CO ₂ , SO _x [38]	< 100°C	2.5 [39] – 960 [40]
Nano-porous	Knudsen diffusion, Poiseuille flow, Capillary condensation, Surface diffusion, Molecular sieving	Brittle	Good[41]	Ambient -500°C	2.4 [42] - 1000 [41] (H ₂ /N ₂ selectivity)
Dense Metal	Solution Diffusion	Phase transition [43] Dependant on support [43] Surface segregation[43]	Negative interaction with CO, CH ₄ , and H ₂ O. Reacts with H ₂ S and SO _x [43]	300-600 [44]	∞
Dense Ceramic	Solution Diffusion	Brittle Difficult to seal due to high operating temperature	Degrades under CO ₂ [45]	500-1000 [45]	∞

2.5.1 Criteria for a hydrogen impurity enrichment material

In order for a membrane to be suitable for hydrogen impurity enrichment material it must be able to increase the concentration of low-level impurities in a hydrogen sample. Although all past examples of hydrogen impurity enrichment have used dense membranes with an infinite selectivity towards hydrogen, it is theoretically possible to use a membrane which has a lower selectivity to perform enrichment. This would have the advantage of allowing membranes with faster flux to be used, greatly reducing the amount of time required for an enrichment run, while allowing cheaper materials to be used in place of the palladium membranes used in past studies. In order to perform this calculation, the following must be known:

- Selectivity of the membrane must be known to a high accuracy
- Total number of moles leaving the system

- Concentration of enriched impurities

Since the selectivity shows the ratio of substances passing through the membrane (i.e. H₂/N₂ selectivity of 2 represents 2 moles of hydrogen for every 1 mole of nitrogen passing through the membrane) if both quantities are known the number of moles of impurity leaving the system through permeation could be easily estimated.

$$n_{i_{exit}} = n_{exit_{total}} / \alpha^{H_2/i} \quad (2.22)$$

Where $n_{i_{exit}}$ is the number of moles of impurity i leaving the system, $n_{exit_{total}}$ is the total number of moles leaving the system, and $\alpha^{H_2/i}$ is the selectivity of hydrogen relative to impurity i .

The concentration, and therefore the number of moles of impurity on the retentate side of the membrane could then be analysed using suitable instrumentation. These values could then be added together and divided by the enrichment factor in order to give the original number of moles that would be in the vessel.

$$y_i = \frac{(n_{i_{ret}} + n_{i_{exit}})/n_{tot_{ret}}}{CEF} \quad (2.23)$$

Where y_i is the concentration of component i in the gas sample, $n_{i_{ret}}$ is the number of moles of i on the retentate side of the membrane, $n_{tot_{ret}}$ is the number of moles of gas remaining on the retentate side of the membrane. In practice however this may not be feasible due to the low concentrations of impurities expected to be present in these hydrogen samples. In order for an enrichment calculation to work there must be an analysable concentration of impurity remaining in order to back calculate. Since the level of expected impurities in a hydrogen sample is so low, and the selectivity of many membranes also low, there is a high risk of either all impurities simply leaving the sample during the enrichment run, or only achieving a lower enrichment factor. Take

the example of enriching a sample containing 0.2 $\mu\text{mol/mol}$ of CO by 100 in order to analyse its composition on a GC-MS. If the sample is a standard 10L cylinder containing 100 bar a H₂/CO selectivity of around 4950000 is required to simply prevent all of the CO leaving the enrichment device, which is effectively the same as the selectivity's seen in dense metal membranes. However, for the same sample containing 0.3 $\mu\text{mol/mol}$ of Helium a H₂/He selectivity of 330 is the minimum required which is more feasible. However, both these values are the exact values required by the standard, in reality they would be much lower. The highest reported selectivity of a non-infinitely selective membrane was Liquid crystalline polyester which had a H₂/N₂ selectivity of 2632 [46] which indicates that this is not a solution for enriching low concentration impurities. It is also unlikely that the selectivity of a membrane material will stay constant throughout its lifespan. Any drift in selectivity would throw off the calculation and either require regular changing of the membrane, driving up cost, or regular calibration to recalculate the selectivity of the membrane at a given time, which would be time consuming. It is however likely that infinitely selective membranes are the only feasible enrichment material due to their ability to enrich every impurity in hydrogen, whereas non-infinitely selective membranes may be applied to analysis of individual impurities, it is unlikely such a scenario would occur in reality which makes them a non-ideal solution.

The common thread with all the micro-porous materials discussed here is that they are currently difficult and expensive to synthesise on a large scale, particularly in membrane form. Due to the separation mechanism of micro-porous materials they are not suitable for use in hydrogen impurity enrichment as their selectivity will not produce a viable enrichment medium. However, due to their high surface areas and ability to be modified to promote integration with specific gas species, they may find use in sensor applications for detecting the ISO-14687 impurities. There is a wealth of work on the use of many of these materials as chemical sensors however much of this work has been

performed using the gases in non-hydrogen matrix gases and therefore much work is required before their true potential in this area can be realised.

Polymer membranes have a similar issue to micro porous materials in that their selectivity is too low to be effective at enriching impurities in hydrogen samples. The mechanical strength and impurity resistance of polymer membranes also limits their use as hydrogen impurity enrichment mediums. While again there are some successful applications of polymers as sensor materials, the same issues as micro porous materials regarding lack of information of their effectiveness in a hydrogen matrix crops up again. It is likely that polymer membranes will continue to be most effective in industrial separation and will be limited in their use as an analytical material.

Therefore this section will only concern itself with membranes which show permselectivity towards hydrogen therefore making them viable as hydrogen impurity enrichment materials. This section will discuss the performance of dense metallic and dense ceramic membranes, and by comparing their reported metrics, their suitability for hydrogen impurity enrichment will be determined.

Dense metallic

Metallic membranes are comprised of dense metal or alloy sheets which allow the permeation of hydrogen through its constituent electrons and protons. While this is the same separation mechanism seen in dense polymer membranes the hydrogen selectivity is typically a lot higher in these systems since molecules which are not hydrogen are unable to dissociate and permeate through the membrane surface, giving a theoretically infinite selectivity towards hydrogen. The minimum requirement for a dense metal membrane for hydrogen separation is the ability to dissociate and permeate hydrogen. There are a number of metals which have shown varying degrees of suitability for hydrogen separation and these are shown in Table 2.3.

The flux of a dense metal membrane is given by Eqn 2.24 and is a function of the

Table 2.3: Metals which show the ability for hydrogen permeation [47]

Structure	Metal	Activation energy for hydrogen permeation (kJ/mol)	Heat of hydride formation (kJ/mol)	Hydrogen permeability at 500°C (mol/ m s pa ^{1/2})
fcc	Ni	40.0	-6	7.8 × 10 ⁻¹¹
	Cu	38.9	-	4.9 × 10 ⁻¹²
	Pd	24.0	20	1.9 × 10 ⁻⁸
	Pt	24.7	26	2.0 × 10 ⁻¹²
bcc	V	5.6	-54	1.9 × 10 ⁻⁷
	Fe	44.8	14	1.8 × 10 ⁻¹⁰
	Nb	10.2	-60	1.6 × 10 ⁻⁶
	Ta	14.5	-78	1.3 × 10 ⁻⁷

metals permeability to hydrogen, the concentration and pressure gradient across the membrane, and the thickness of the dense layer.

$$J = \frac{\phi}{l} (P_{H,ret}^{0.5} - P_{H,perm}^{0.5}) \quad (2.24)$$

Where J is the flux of the membrane, l is the thickness of the membrane separation layer, ϕ is the permeability of hydrogen in the membrane material, and P is the partial pressure of hydrogen on the retentate and permeate sides of the membrane.

From the metals shown in Table 2.3 palladium and its alloys are by far the most popular choice due to a combination of high hydrogen permeability, favourable catalytic activity towards hydrogen dissociation and re-association, and aversion towards hydride formation compared to other metals.[47, 48, 49]

For other metals there is often a trade-off, V, Nb and Ta exhibit higher permeability than palladium but are limited by their low catalytic activity for hydrogen dissociation and typically must be combined with another metal to compensate for this. A common strategy is to deposit palladium particles on both sides of membranes made from these metals to provide this catalytic activity. Embrittlement of pure metal membranes is also an issue, even for metals with a high heat of hydride formation. Embrittlement is a side effect of hydrogen passing through the crystal lattice. During transport a H-M

phase will form which has a higher lattice parameter than the original crystal lattice. This change in lattice parameter can cause stress in the overall structure of the dense membrane layer and cause the formation of pin holes, cracks, and eventually membrane failure. Metals with a low heat of hydride formation in Table 2.3 will readily embrittle within hydrogen containing atmospheres.

This section will discuss developments in both palladium and non-palladium membranes and the issues still surrounding the technology.

As previously mentioned palladium is typically the material of choice for dense metallic membranes due to its combination of high stability, permeability, and catalytic activity. Palladium based membranes have been successfully used to provide ultrapure hydrogen for a number of applications including electronics, industrial gas, and fuel cell industries for a number of years. One of the main downside to the use of palladium is its high cost of around \$25 per gram. [50] Although for our application of hydrogen impurity enrichment this is of secondary importance as the membrane cost only represents around 20% of the total device cost. The high cost of palladium has pushed researchers into focusing on reducing the amount of palladium used in the membrane in order to find a more economical solution. This is done either by using a traditional membrane approach, whereby the thickness of the membrane layer is reduced as much as possible to maximise the flux while decreasing the overall amount of palladium used, or by alloying palladium with a cheaper metal to reduce the amount of bulk palladium in the manufacturing process.

During operation of a pure palladium membrane at temperatures lower than 300°C, hydrogen embrittlement can occur due to the aforementioned phase transition between interstitial hydrogen within palladium (α phase) and palladium hydride (β phase). The β phase (0.4025 nm) has a lattice parameter bigger than the α phase (0.389nm). [51] The formation of this α - β phase will cause the membrane to distort, become brittle,

and eventually results in membrane failure when a leak occurs. [52] The behaviour of hydrogen embrittlement is shown in figure 2.5 Aside from this pure palladium has poor chemical stability, it can be poisoned by a number of impurities which are commonly found in hydrogen. Some of these impurities simply inhibit permeation of hydrogen but do not have a permanent interaction and thus their effects can be mitigated by optimising the operating conditions. Others such as H₂S and CH₄ are known to interact with the membrane through chemisorption and permanently damage the membrane through the formation of compounds with palladium, breaking the crystalline lattice resulting in membrane failure.

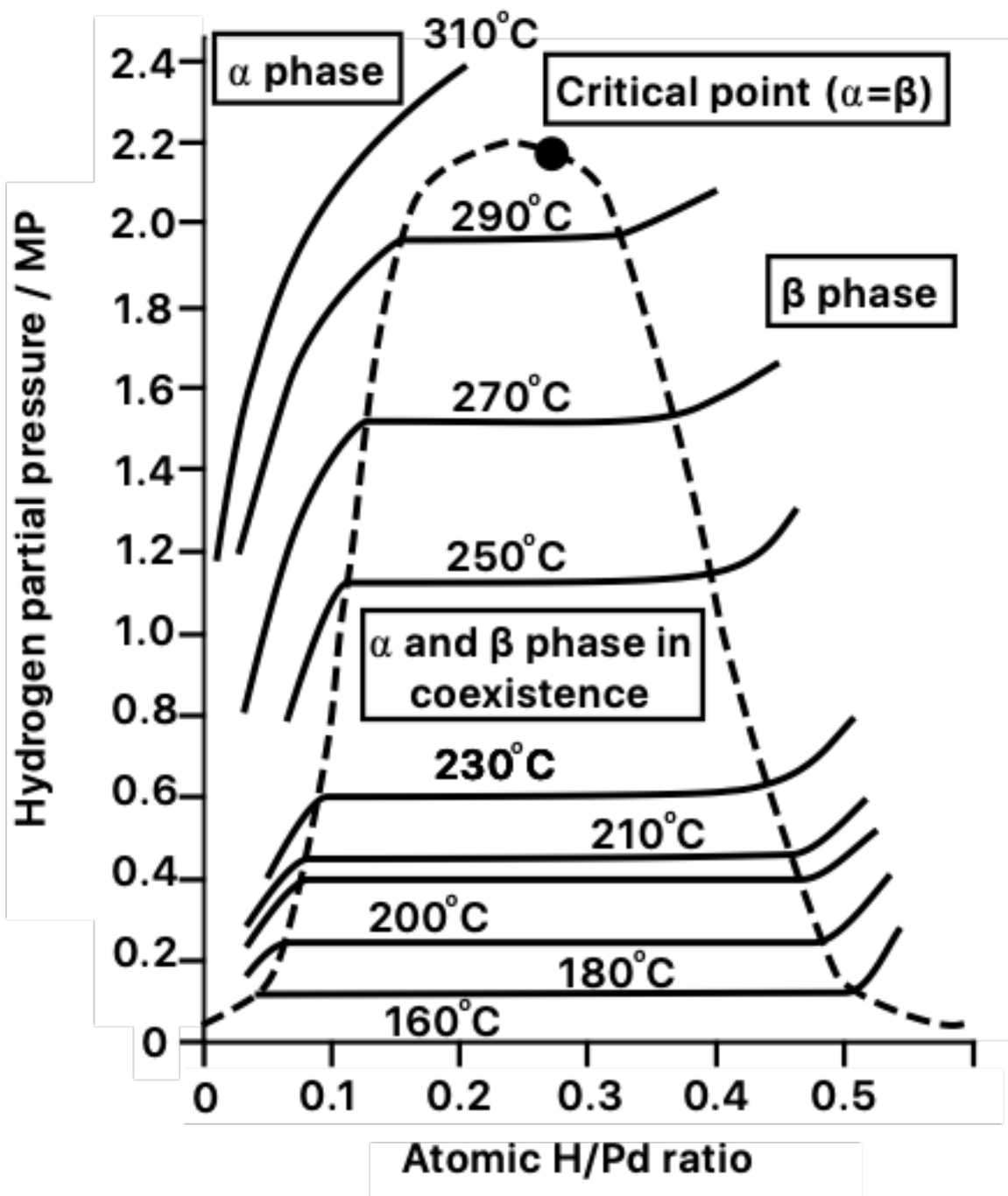


Figure 2.5: Palladium-Hydrogen phase diagram adapted from [52]

From the impurities listed in ISO 14687 CO, H₂O, Hydrocarbons and sulphur containing compounds are known to have a physisorption interaction with palladium. Physisorption based poisoning occurs by the impurity inducing a competitive adsorption

with hydrogen, blocking active sites for hydrogen dissociation, and hence reducing the active area available for hydrogen permeation.[43] The ultimate effect of this is a temporary flux reduction which has no long lasting damage on the membrane. Compounds such as H₂S have a more extreme effect on the membrane as adsorption leads to a reaction between palladium and the metal permanently changing the membrane composition and structure. The most commonly studied interaction is the interaction between palladium and H₂S to form palladium sulphide. Palladium sulphide, while still permeable to hydrogen, has an extremely low permeability, drastically reducing the efficiency of the membrane. Palladium sulphide also has a larger lattice constant than that of pure palladium which can lead to membrane failure by creating gaps in the crystal lattice resulting in pinholes. Some of these impurities, in particular those which only exhibit physisorption, can be mitigated by altering the operating conditions. It has been reported that the effects of CO and H₂O poisoning can be completely eliminated by operating at temperatures above 300°C. Another example where this is shown is with H₂S related poisoning. Since the reaction between palladium and H₂S is exothermic, and produces hydrogen as a side product, it can be inhibited by increasing the H₂:H₂S ratio and increasing the temperature.

A combination of cost, easy formation of phase transitions [51, 52] and its low tolerance for common impurities found in hydrogen processes limits pure palladium's use as a hydrogen separation material. Many of these effects however, can be completely mitigated through alloying palladium with another metal. By forming an alloy with a metal which has a lattice parameter similar to that of the β -phase the average difference between the sizes of the two phases is effectively decreased and thus the hydrogen embrittlement effect can be effectively mitigated. The effect of impurities on palladium membranes can also be partially mitigated by alloying with another metal and oftentimes an increase in permeability is reported with certain alloy compositions.

Both binary and ternary alloys of palladium have been reported and is a mature topic in literature. By far the three most popular alloying compounds with palladium are silver, copper and gold. The current literature landscape of palladium alloy membranes are summarised in Table 2.4 and for the purpose of this review studies which looked at the impurity resistance, which is currently the most pressing issue in the field, were focused on.

Silver is the most popular dopant for palladium membranes and forms a stable alloy with palladium at concentrations greater than 20wt %, with the optimal composition occurring at 23%. On top of mitigating the effects of hydrogen embrittlement, a 60% increase in permeability is observed when compared to pure Pd membranes. Despite having enhanced permeation properties, PdAg is still susceptible to poisoning, in particular from sulphurous compounds which can form both Pd_4S and $\text{Ag}_5\text{Pd}_{10}\text{S}_5$. Several studies exposing PdAg membranes to sulphurous compounds have been performed and in most cases the membranes suffer a large decrease in flux, and are permanently damaged as shown by a permanent decrease in flux when sulphide is removed from the inlet. [53] It has been observed that exposure to $5 \mu\text{mol mol}^{-1} \text{H}_2\text{S}$ in the feed stream is enough to induce Pd_4S formation [53] and therefore this composition is only suitable for atmospheres and applications which do not contain any sulphur.

Copper is another widely studied binary alloy which is known to suppress hydrogen embrittlement. Alloying with copper also has the advantage that it reduces the cost of the membrane by a larger amount than most other metals and through improving the membranes sulphur resistance. The maximum permeability of a palladium copper membrane occurs at the composition $\text{Pd}_{60}\text{Cu}_{40}$ and this is due to the formation of a bcc lattice rather than the fcc lattice commonly seen in pure palladium and most binary alloys. [54] Temperature cycling has been performed on this alloy composition and it has been found that the bcc crystalline configuration has a higher permeability than the

fcc phase. [55] This behaviour is due to the increased number of hcp adsorption sites which hydrogen has a slight preference for.[56] Conversely the fcc structure has a higher impurity resistance than the bcc structure, particularly for H₂S. This has been theorised to be because adsorption of H₂S on a palladium membranes surface is largely controlled by electronic factors.[57] There have been several studies reporting an increased resistance to sulphur poisoning by alloying palladium with copper. A Pd₈₀Cu₂₀ membrane exposed to 20 $\mu\text{mol mol}^{-1}$ of H₂S for 90 hours results in a 22% drop in flux, performing much better than Pd₇₅Ag₂₅ reported in the same paper which became impermeable after 65 hours of exposure in the same conditions.[53] In a similar study, the performance of bcc and fcc alloys in response to H₂S Pd₂₀Cu₈₀, Pd₄₀Cu₆₀ and Pd₅₃Cu₄₇ foils at varying temperatures was tested in hydrogen containing 1000 $\mu\text{mol mol}^{-1}$ H₂S.[58] It was found that when the alloys were in the fcc phase the reduction in flux was only round 10%, while in the bcc phase the membrane loses around 99% of its permeance. The H₂S concentration required to make a Pd₆₀Cu₄₀ membrane completely impermeable was found to be around 300 $\mu\text{mol mol}^{-1}$ [59].

PdAu alloys see a slight increase in permeability, up to 30% more than pure Pd, with gold additions up to 20%, after which the permeability rapidly decreases. While alloying with gold does not improve the permeability much compared to silver or copper, gold alloys show greatly improved sulphur resistance. Several studies have been performed which show that PdAu membranes show no permanent permeability loss after exposed to ppm levels of sulphurous compounds implying that permeability decline is only due to H₂S adsorption. It has been reported that a Pd₉₂Au₈ membrane exposed to 54.8 $\mu\text{mol mol}^{-1}$ of H₂S was able to resist reaction with H₂S and its permeability was completely recoverable. [60]. When tested higher temperatures it was also found that the adsorption effect of H₂S was reduced which is evidence that dissociative adsorption of H₂S on metals is exothermic. [60] In the original patent for palladium membranes by

McKinley [61] in 1964 Pd₆₀Au₄₀ was found to be the composition which performed best under sulphur containing atmospheres, losing only 9.44% of its flux compared to the 99% and 95% lost by PdAg and PdCu membranes respectively.[61] However under recovery the flux increased to 120% of its original value while the PdCu membrane was fully recovered under the same conditions. This may be evidence that the Pd₆₀Au₄₀ membrane used is not completely stable. [61] When comparing the performance of PdCu and PdAu membranes under a number of gases which commonly result from the water gas shift reaction it was found that the PdAu resisted . [62] It was found that from the four membranes tested, the PdAu membranes show no permeability loss under an atmosphere containing CO, CO₂ and H₂O while the PdCu membranes showed considerable permeability loss. [62] The biggest downside to alloying with gold is that due to its high price in recent years alloying palladium with gold drives up the price higher than that of a pure palladium membrane and is one of the less economic options. [63]

Other metals have been alloyed with palladium although outside of these three metals, studies evaluating the impurity resistance of other binary alloys are rare. The adsorption of CO on Pd₉₂Y₈ membranes under various concentrations has been studied using TDS and XPS and found that CO can react with the Pd-Y allow at 623K, forming YO and solid carbon. [64] Bryden et al studied the poisoning resistance of nanostructured palladium-iron alloys compared to polycrystalline membranes of the same composition. [65] They found that nanostructured membranes not only display higher fluxes, but also exhibit a higher resistance to hydrogen sulphide poisoning. When exposed to ~60 $\mu\text{mol mol}^{-1}$, of H₂S for 2.2 hours there was no permanent reduction in flux. Howard et al studied the performance of PdPt₂₀ membranes under 1000 $\mu\text{mol mol}^{-1}$ H₂S at temperatures between 350°C and 450 °C. [66] The alloy had decent performance on the lower end of the temperature, only losing about 5% of permanent permeability. At higher temperatures the membrane lost around 25% of its permeability, much of this attributed

to platinum segregation to the surface of the membrane.[66] The impurity resistance of PdPt membranes has also been studied under common WGS compositions which concluded that small additions of Pt (Between 5-9%) can decrease the flux decline caused by WGS mixtures from 39% for pure Pd, to anywhere between 7%-22%. [66] Platinum however does not appear to be as effective at mitigating the effects of WGS mixtures as alloying with Au which can completely mitigate the flux decline. [67] The use of Pd₉₅Ru₅ membranes in syngas mixtures has been tested in WGS conditions and also showed good resistance to adsorbing compounds, losing only 6% of their flux compared to the 11% lost by a pure Pd membrane under the same conditions.[68]

Ternary alloys are a newly emerging field which aims at utilizing the strengths of a binary alloy while mitigating its weaknesses with another component. Research in this area has mainly focused on ternary alloys based on copper, gold and silver however there are theoretically infinite combinations possible. A Pd₈₀Au₁₀Pt₁₀ membrane manufactured through magnetron sputtering was found to be completely resistant to H₂S poisoning, recovering 100% of its flux prior to exposure to impurity containing gas streams. [69] However after long term testing, the purity of the permeate decreased which implies that pinholes had started to form on the membrane surface. [69] This is most likely due to segregation of the individual components, destabilising the structure. This was not confirmed in the papers analysis however. [69] The most in depth study of PdAgAu membranes under H₂S was performed by Braun et al, who studied the performance of Pd, Pd₉₀Ag₁₀, Pd₇₈Ag₉Au₁₃, Pd₇₅Ag₁₆Au₉, and Pd₉₁Au₉. While all the tested membranes saw a permanent permeability loss under 100 $\mu\text{mol mol}^{-1}$ of H₂S the Pd₉₁Au₉, Pd₇₈Ag₉Au₁₃, and Pd₇₅Ag₁₆Au₉ all resisted bulk corrosion as proven by Energy-dispersive X-ray spectroscopy (EDS), with the Pd₉₁Au₉ sample having the highest resistance to H₂S atmospheres. [70, 71] While this study shows that ternary alloys do offer an increase in impurity resistance over pure Pd and PdAg membranes,

the original flux values are not provided so it is difficult to see if there are any inherent advantages over simply using a PdAu alloy. [70, 71] The Materials and Chemistry group at SINTEF have performed the most extensive study into ternary alloys, [72, 73] testing by far the widest range of alloys and using a combination of X-ray Diffraction (XRD) and X-ray photoelectron spectroscopy to analyse the segregation behaviour of the ternary alloys. [72, 73] Through alloying PdCu alloys with a third transition metal they found that the addition of 1% of a transition metal component always resulted in an increase in permeability, likely due to a phenomenon where the activation energy for hydrogen permeation decreases with increasing fcc lattice constant. [74] In particular the addition of 1% Ta, 1% Y and 14% Ag resulted in an increase in permeability of 10, 45 and 65% respectively when compared with Pd₇₃Cu₂₇ membranes for Y and Ta, and Pd₆₅Cu₃₅ membranes for Ag additions. [74] In the follow up paper Pd₇₅Ag₂₂Au₃, Pd₇₆Ag₂₁Mo₃ and Pd₆₉Ag₂₇Y₄ membranes were exposed to 20 $\mu\text{mol mol}^{-1}$ of H₂S for 500 hours. The Pd₇₅Ag₂₂Au₃ membrane was the only membrane which showed no bulk sulphur formation, with the other two membrane compositions showing large levels of oxidation and segregation when analysed using XPS. [75] The PdAgAu composition has been further studied by Braun et al, [71] who backed up that small additions of Au to PdAg membranes can reduce the membranes reactivity with sulphides and would be suitable for application in a hydrogen impurity enrichment device. Tarditi et al, have done a similar study on the impurity resistance of PdCuAu membranes. [76] While XRD and EDS of this alloy showed no formation of bulk sulphides, the XPS depth profile showed low, but measurable levels of sulphur showing that this composition has some reactivity with impurities. [76]

Table 2.4: Review of palladium alloys and their interactions with impurities

Membrane composition	Support	Susceptability to poisoning compounds				Pressure (bar)	Permeability $molm^{-1}s^{-1}pa^{-\frac{1}{2}}$	Temperature °C	Fabrication technique	Membrane thickness (μm)	Ref
		Compound	Exposure time	Percentage flux drop	Flux Recovery						
PdAg ₂₃	PSS/Al ₂ O ₃	19.2% CO ₂ ,									
		15.4% H ₂ O,	500h	88.36%	-	990 $cm^3cm^{-2}min^{-1}$	26	2.42×10^{-9}	400	Magnetron Sputtering	2.2 [77]
		4% CO,									
		1.2% CH ₄									
PdAg ₂₃	PSS/Al ₂ O ₃	40.5% CO ₂ ,									
		25% H ₂ O,	500h	94.65%	-	990 $cm^3cm^{-2}min^{-1}$	26	2.42×10^{-9}	400	Magnetron Sputtering	2.2 [77]
		2% CO,									
		2.5% CH ₄									
PdAg ₂₃	PSS/Al ₂ O ₃	60% CO ₂ ,									
		25.5% H ₂ O,	500h	94.65%	-	990 $cm^3cm^{-2}min^{-1}$	26	2.42×10^{-9}	400	Magnetron Sputtering	2.2 [77]
		2% CO,									
		2.5% CH ₄									
Pd	Self-supported	1000 ppm H ₂ S	6h	90%	-	14 $cm^3cm^{-2}min^{-1}$	3.1	1.2×10^{-8}	350	-	25 [58]
PdCu ₅₃	Self-supported	1000 ppm H ₂ S	6h	90%	-	14 $cm^3cm^{-2}min^{-1}$	3.1	1.3×10^{-8}	350	-	25 [58]
Pd	PSS/Al ₂ O ₃	54.8 ppm H ₂ S	24h	93%	0%	-	2.02	-	400	ELP	10.3 [60]
PdAu ₈	PSS/Al ₂ O ₃	54.8 ppm H ₂ S	24h	85%	54%	-	2.02	-	400	ELP/Electroplating	16 [60]
PdAg ₂₃	PSS	2 ppm H ₂ S	10 minutes	7%	100%	66.7 $cm^3cm^{-2}min^{-1}$	-	1.9×10^{-8}	450	Magnetron Sputtering	10 [78]
PdAg ₂₃	PSS	5 ppm H ₂ S	10 minutes	29%	100%	66.7 $cm^3cm^{-2}min^{-1}$	-	1.9×10^{-8}	450	Magnetron Sputtering	10 [78]

PdAg ₂₃	PSS	2-5-2 ppm H ₂ S	10 minutes at 5ppm	25%	99.4%	$51.5 \text{ cm}^3 \text{cm}^{-2} \text{min}^{-1}$	-	1.9×10^{-8}	450	Magnetron Sputtering	10	[78]
PdAg ₂₃	PSS	2-6.6-2 ppm H ₂ S	10 minutes at 6.6ppm	25%	36%	$51.2 \text{ cm}^3 \text{cm}^{-2} \text{min}^{-1}$	-	1.9×10^{-8}	450	Magnetron Sputtering	10	[78]
PdAg ₂₃	PSS	2-10-2 ppm H ₂ S	10 minutes at 10ppm	83%	99.6%	$51.2 \text{ cm}^3 \text{cm}^{-2} \text{min}^{-1}$	-	1.9×10^{-8}	450	Magnetron Sputtering	10	[78]
PdAg ₂₃	PSS	2-20-2 ppm H ₂ S	10 minutes at 20ppm	85%	100%	$51.0 \text{ cm}^3 \text{cm}^{-2} \text{min}^{-1}$	-	1.9×10^{-8}	450	Magnetron Sputtering	10	[78]
PdAg ₂₃	PSS	5-20-5 ppm H ₂ S	10 minutes at 6.6ppm	71%	17.99%	$18.9 \text{ cm}^3 \text{cm}^{-2} \text{min}^{-1}$	-	1.9×10^{-8}	450	Magnetron Sputtering	10	[78]
Pd	PSS/Al ₂ O ₃	14.2% CO, 1.7% CH ₄ 51% N ₂ 11.8% CO ₂ , 5.3% H ₂ O,	48h	11%	-	-	0.1	-	350	ELP	6.5	[79]
Pd	PSS/Al ₂ O ₃	14.2% CO, 1.7% CH ₄ 51% N ₂ 120 mg/m ³ tar	24h	66.7%	-	-	0.1	-	350	ELP	6.5	[79]

Pd	PSS/Al ₂ O ₃	14.2% CO, 1.7% CH ₄	24h	100%	-	-	0.1	-	350	ELP	6.5	[79]
		5.3% H ₂ O, 51% N ₂										
		240 mg/m ³ tar										
PdRu ₅	PSS	14.2% CO, 1.7% CH ₄	48h	6%	-	-	0.1	-	350	ELP	7.3	[79]
		5.3% H ₂ O, 51% N ₂										
		11.8% CO ₂ ,										
PdRu ₅	PSS	14.2% CO, 1.7% CH ₄	24h	66.7%	-	-	0.1	-	350	ELP	7.3	[79]
		5.3% H ₂ O, 51% N ₂										
		120 mg/m ³ tar										
PdRu ₅	PSS	14.2% CO, 1.7% CH ₄	24h	93%	-	-	0.1	-	350	ELP	7.3	[79]
		5.3% H ₂ O, 51% N ₂										
		240 mg/m ³ tar										
Pd	YSZ	50% NH ₃	75h	0%	-	0.056.0 mol m ⁻² s ⁻¹	2-7	-	400	ELP	1.6	[80]
PdAg ₂₅	PSS	0.5%CO	Until stable	80%	-	-	-	-	400	-	100	[81]
PdAg ₂₅	PSS	0.5%CO	Until stable	4%	-	-	-	-	573	-	100	[81]

PdAg ₂₅	PSS	0.5%CO	Until stable	0%	-	-	-	-	773	-	100	[81]
PdAg ₂₅	PSS	1.5%CO	Until stable	91%	-	-	-	-	400	-	100	[81]
PdAg ₂₅	PSS	1.5%CO	Until stable	7%	-	-	-	-	573	-	100	[81]
PdAg ₂₅	PSS	1.5%CO	Until stable	0%	-	-	-	-	773	-	100	[81]
PdAg ₂₅	PSS	10%CO	Until stable	98%	-	-	-	-	400	-	100	[81]
PdAg ₂₅	PSS	10%CO	Until stable	50%	-	-	-	-	573	-	100	[81]
PdAg ₂₅	PSS	10%CO	Until stable	0%	-	-	-	-	773	-	100	[81]
PdAg ₂₅	PSS	20%CO	Until stable	99.8%	-	-	-	-	400	-	100	[81]
PdAg ₂₅	PSS	20%CO	Until stable	50.5%	-	-	-	-	573	-	100	[81]
PdAg ₂₅	PSS	20%CO	Until stable	0%	-	-	-	-	773	-	100	[81]
Pd	PSS	0.1%H ₂ S	120h	75%	-	$8.5\text{cm}^3\text{cm}^{-2}\text{min}^{-1}$	-	4×10^{-8}	350	-	100	[82]
Pd	PSS	0.1%H ₂ S	120h	82%	-	$13.5\text{cm}^3\text{cm}^{-2}\text{min}^{-1}$	-	4×10^{-8}	450	-	100	[82]
Pd	PSS	0.1% H ₂ S	120h	81%	-	$27.5\text{cm}^3\text{cm}^{-2}\text{min}^{-1}$	-	4×10^{-8}	550	-	100	[82]
Pd	PSS	12% CO, 12% N ₂	Until stable	22%	-	$8.5\text{cm}^3\text{cm}^{-2}\text{min}^{-1}$	3	-	380	ELP	10	[83]
Pd	PSS	1.6% Steam, 1.6% N ₂	Until stable	17%	-	$12.87\text{cm}^3\text{cm}^{-2}\text{min}^{-1}$	3	-	380	ELP	10	[83]
Pd	-	20 ppm H ₂ S, 40% N ₂	115h	71.88%	-	-	31	1.5×10^{-8}	320	-	100	[53]
PdAg ₂₅	-	10 ppm H ₂ S, 20% N ₂	65h	100%	-	$27.5\text{cm}^3\text{cm}^{-2}\text{min}^{-1}$	31	1.4×10^{-8}	320	-	130	[53]
PdCu ₂₀	-	20 ppm H ₂ S, 40% N ₂	90h	22%	-	-	31	-	320	-	130	[53]
PdCu ₈	PSS	42.7 ppm H ₂ S	2.5h	82%	86.67%	-	2	-	450	ELP	14	[84]
PdAg ₂₇	-	4.4 ppm H ₂ S	48h	99%	67%	$3.7\text{cm}^3\text{cm}^{-2}\text{min}^{-1}$	5.17	-	350	-	920	[61]
PdCu ₄₀	-	4.5 ppm H ₂ S	72h	95%	100%	$2.9\text{cm}^3\text{cm}^{-2}\text{min}^{-1}$	5.17	-	350	-	1030	[61]

PdAu ₄₀	-	4.7 ppm H ₂ S	72h	9.4%	120%	$0.99 \text{ cm}^3 \text{cm}^{-2} \text{min}^{-1}$	5.17	-	350	-	820	[61]
Pd	-	4.7 ppm H ₂ S	96h	70.1%	10%	$1.8 \text{ cm}^3 \text{cm}^{-2} \text{min}^{-1}$	5.17	-	350	-	900	[61]
PdAu ₄₀	-	20.6 ppm H ₂ S	168h	56.6%	120%	$0.99 \text{ cm}^3 \text{cm}^{-2} \text{min}^{-1}$	5.17	-	350	-	790	[61]
PdAu ₄₀	-	6.6% H ₂ S	6h	99%	120%	$0.99 \text{ cm}^3 \text{cm}^{-2} \text{min}^{-1}$	5.17	-	350	-	810	[61]
PdFe ₆	PSS	59.1 ppm H ₂ S	2.2h	75%	100%	$8.8 \text{ cm}^3 \text{cm}^{-2} \text{min}^{-1}$	1	-	200	Electroplating	10	[65]
PdFe ₆	PSS	59.1 ppm H ₂ S	2.2h	95%	100%	$6.4 \text{ cm}^3 \text{cm}^{-2} \text{min}^{-1}$	1	-	200	Electroplating	10	[65]
PdFe ₅	PSS	1% CO	4.2h	83.3%	-	$5.5 \text{ cm}^3 \text{cm}^{-2} \text{min}^{-1}$	1	-	200	Electroplating	18	[65]
PdFe ₅	PSS	1% CO	4.2h	79%	-	$3.9 \text{ cm}^3 \text{cm}^{-2} \text{min}^{-1}$	1	-	200	Electroplating	18	[65]
PdCu ₄	Accusep	20% CO ₂ , 8% CO 26% CO ₂ ,	2h	17%	-	$5.85 \text{ cm}^3 \text{cm}^{-2} \text{min}^{-1}$	1.38	-	350	-	7	[62]
PdAu ₁₃	Accusep	21% H ₂ O, 50 ppm H ₂ S	13h	0%	-	$35.56 \text{ cm}^3 \text{cm}^{-2} \text{min}^{-1}$	4.96	-	350	-	7	[62]
PdCu ₄	Accusep	26% CO ₂ , 21% H ₂ O, 2% CO 50 ppm H ₂ S	2h	70%	100%	$5.85 \text{ cm}^3 \text{cm}^{-2} \text{min}^{-1}$	4.96	-	350	-	7	[62]
PdAu ₁₃	Accusep	26% CO ₂ , 21% H ₂ O, 2% CO 30% CO ₂ ,	2h	0%	-	$35.56 \text{ cm}^3 \text{cm}^{-2} \text{min}^{-1}$	4.96	-	350	-	7	[62]
PdAu ₁₀	Self-supported	19% H ₂ O, 1% CO	43h	32%	-	$0.28 \text{ molm}^{-2} \text{s}^{-1}$	12.7	-	400	Magnetron Sputtering	-	[69]

PdAu ₁₀	Self-supported	30% CO ₂ , 19% H ₂ O, 1% CO 20 ppm H ₂ S	100h	70%	-	0.28 mol m ⁻² s ⁻¹	12.7	-	400	Magnetron Sputtering	-	[69]
PdAu ₂₀ Pt ₁₀	Self-supported	30% CO ₂ , 19% H ₂ O, 1% CO 30% CO ₂ ,	43h	30%	-	0.212 mol m ⁻² s ⁻¹	12.7	-	400	Magnetron Sputtering	-	[69]
PdAu ₂₀ Pt ₁₀	Self-supported	19% H ₂ O, 1% CO 20 ppm H ₂ S 30% CO ₂ ,	100h	100%	-	0.28 mol m ⁻² s ⁻¹	12.7	-	400		33	[69]
PdAu _{10.2}	PSS	19% H ₂ O, 1% CO 30% CO ₂ ,	350h	36%	-	0.21 mol m ⁻² s ⁻¹	6.27	-	400	Cold working	25	[67]
PdAu _{10.2}	PSS	19% H ₂ O, 1% CO 20 ppm H ₂ S 30% CO ₂ ,	350h	72%	-	0.21 mol m ⁻² s ⁻¹	6.27	-	400	Cold working	25	[67]
PdAu ₁₉	PSS	19% H ₂ O, 1% CO 30% CO ₂ ,	350h	0%	-	0.25 mol m ⁻² s ⁻¹	6.27	-	400	Cold working	25	[67]
PdAu ₁₉	PSS	19% H ₂ O, 1% CO 20 ppm H ₂ S	350h	0%	-	0.25 mol m ⁻² s ⁻¹	6.27	-	400	Cold working	25	[67]

PdAu ₇	PSS	30% CO ₂ , 19% H ₂ O, 1% CO	350h	32%	-	0.47 molm ⁻² s ⁻¹	6.27	-	400	Cold working	11	[67]
PdAu ₇	PSS	30% CO ₂ , 19% H ₂ O, 1% CO	350h	68%	-	0.47 molm ⁻² s ⁻¹	6.27	-	400	Cold working	11	[67]
PdAu _{10.1}	PSS	20 ppm H ₂ S 30% CO ₂ , 19% H ₂ O, 1% CO	350h	24%	-	0.36 molm ⁻² s ⁻¹	6.27	-	400	Cold working	31	[67]
PdAu _{10.1}	PSS	20 ppm H ₂ S 30% CO ₂ , 19% H ₂ O, 1% CO	350h	62%	-	0.36 molm ⁻² s ⁻¹	6.27	-	400	Cold working	31	[67]
Pd	ZrO ₃ /PSS	100 ppm H ₂ S	24h	85%	16%	-	-	1.21×10 ⁻⁸	400	ELP	-	[71]
PdAg ₁₀	ZrO ₃ /PSS	100 ppm H ₂ S	24h	75.7%	33%	-	-	1.65×10 ⁻⁸	400	ELP	-	[71]
PdAg ₁₆ Au ₉	ZrO ₃ /PSS	100 ppm H ₂ S	24h	73%	64.5%	-	-	1.18×10 ⁻⁸	400	ELP	-	[71]
PdAg ₉ Au ₁₃	ZrO ₃ /PSS	100 ppm H ₂ S	24h	66.67%	81%	-	-	1.34×10 ⁻⁸	400	ELP	-	[71]
PdAu ₉	ZrO ₃ /PSS	100 ppm H ₂ S	24h	60%	80%	-	-	0.99×10 ⁻⁸	400	ELP	-	[71]
PdAg ₂₃	Micro channel stainless steel	10% N ₂ , 20 ppm H ₂ S	1h	97.5%	67.5%	170 cm ³ cm ⁻² min ⁻¹	-	1.3×10 ⁻⁸	450	Magnetron Sputtering	2.2	[73]
PdAg ₂₂ Au ₃	Micro channel stainless steel	10% N ₂ , 20 ppm H ₂ S	1h	87.5%	80%	145 cm ³ cm ⁻² min ⁻¹	-	9.3×10 ⁻⁹	450	Magnetron Sputtering	1.9	[73]
PdAg ₂₇ Y ₄	Micro channel stainless steel	10% N ₂ , 20 ppm H ₂ S	1h	92.5%	65%	140 cm ³ cm ⁻² min ⁻¹	-	1.3×10 ⁻⁸	450	Magnetron Sputtering	2.4	[73]

PdAg ₂₁ Mo ₃	Micro channel stainless steel	10% N ₂ , 20 ppm H ₂ S	1h	97.5%	98%	75 cm ³ cm ⁻² min ⁻¹	-	5.8×10 ⁻⁸	450	Magnetron Sputtering	2.3	[73]
PdAg ₁₁ Mo ₄	Micro channel stainless steel	10% N ₂ , 20 ppm H ₂ S	1h	97.5%	96%	125 cm ³ cm ⁻² min ⁻¹	-	8.8×10 ⁻⁸	450	Magnetron Sputtering	2.2	[73]
PdAg ₂ Au ₁₅	Al ₂ O ₃ /PSS	1000 ppm H ₂ S	30h	-	-	-	-	1.3×10 ⁻⁸	350	ELP	-	[70]
PdAg ₁₄ Au ₁₂	Al ₂ O ₃ /PSS	1000 ppm H ₂ S	30h	-	-	-	-	-	350	ELP	-	[70]
Pd	PSS	1000 ppm H ₂ S	30h	-	-	-	-	1.2×10 ⁻⁸	350	ELP	25	[70]
PdCu ₆₅	ZrO ₂ /PSS	Varying	Varying	-	-	-	-	-	450	ELP	10	[59]
PdCu ₇₃	ZrO ₂ /PSS	Varying	Varying	-	-	-	-	-	450	ELP	8	[59]
Pd	ZrO ₂ /PSS	Varying	Varying	-	-	-	-	-	450	ELP	4	[59]
Pd	ZrO ₂ /PSS	Varying	Varying	-	-	-	-	-	450	ELP	3	[59]
PdCu ₃₂	ZrO ₂ /PSS	Varying	Varying	-	-	-	-	-	450	ELP	2	[59]
PdCu ₂₀	ZrO ₂ /PSS	Varying	Varying	-	-	-	-	-	450	ELP	3	[59]
PdCu ₄₀	ZrO ₂ /PSS	Varying	Varying	-	-	-	-	-	450	ELP	15	[59]
PdCu ₄₀	ZrO ₂ /PSS	Varying	Varying	-	-	-	-	-	450	Cast rolled	25	[59]
PdPt ₂₀	Self-supported	1000 ppm H ₂ S	150h	50%	95%	1.85 mLcm ⁻² min ⁻¹	6.2	-	350	Metalurgical	100	[66]
PdPt ₂₀	Self-supported	1000 ppm H ₂ S	125h	80%	75%	2.95 mLcm ⁻² min ⁻¹	6.2	-	400	Metalurgical	100	[66]
PdPt ₂₀	Self-supported	1000 ppm H ₂ S	125h	25%	75%	3.55 mLcm ⁻² min ⁻¹	6.2	-	450	Metalurgical	100	[66]
PdY ₈	-	2-26% CO SO ₂	-	-	-	-	0.06	-	Varying	-	-	[64]
Pd	-	CS ₂ H ₂ S	-	-	-	-	0.07 mBar	-	Varying	-	-	[85]
PdCu ₂₀	Inconel	1000 ppm H ₂ S	-	-	-	-	-	-	Varying	Vacuum arc welding	100	[86]
PdCu ₄₀	Inconel	1000 ppm H ₂ S	-	-	-	-	-	-	Varying	Vacuum arc welding	100	[86]

PdCu ₄₇	Inconel	1000 ppm H ₂ S	-	-	-	-	-	-	Varying	Vacuum arc welding	100	[86]
Pd	PSS	100 ppm H ₂ S	24h	36%	80%	0.0475 mol m ⁻² s ⁻¹	0.5	1.2 × 10 ⁻⁸	400	ELP	4	[87]
PdAu ₉	PSS	100 ppm H ₂ S	24h	59%	75%	0.05 mol m ⁻² s ⁻¹	0.5	9.9 × 10 ⁻⁹	400	ELP	4	[87]
PdCu ₂₅ Au ₅	PSS	100 ppm H ₂ S	24h	50%	74%	0.01 mol m ⁻² s ⁻¹	0.5	1.9 × 10 ⁻⁹	400	ELP	4	[87]
PdCu ₃₇ Au ₃	PSS	100 ppm H ₂ S	24h	54%	70%	0.015 mol m ⁻² s ⁻¹	0.5	2.9 × 10 ⁻⁹	400	ELP	4	[87]
PdAu ₂₃	Accusep	20 ppm H ₂ S	96h	29%	97%	1.4 mol m ⁻² s ⁻¹	11	1.55 × 10 ⁻⁸	500	ELP	4.8	[88]
PdAu ₂₀ Ag ₁₃	Accusep	20 ppm H ₂ S	96h	50%	89%	0.9 mol m ⁻² s ⁻¹	11	1.65 × 10 ⁻⁸	500	ELP	9.3	[88]

Non-palladium

Due to the high cost of palladium there is a particular interest to use alternative materials which still give the high selectivity intrinsic to dense metallic membranes, while reducing the cost, for example, by switching to a cheaper, non-platinum group metal. Non-palladium alloy membranes in the form of amorphous, or crystalline structures generally attract the most research interest.

Crystalline non-palladium membranes are generally based on Group IV based alloys and follow a similar philosophy to the previously discussed palladium membranes. Group IV metals are alloyed with other metals in order to improve their physical properties while maintaining the bcc structure essential for the material to transport hydrogen. Crystalline metals typically have the same advantages and disadvantages as palladium membranes. Recent research activity has focused mainly on studying how the size of the grain boundary affects the permeability of such a membrane, an area which has been mostly neglected in palladium research. [41] This is likely due to the fact that many of these alloys are manufactured through cold work where the grain size can be more easily tailored than in the traditional electroless and sputtering methods used to manufacture palladium membranes. A key aspect of crystalline alloy research is the effect of nano-crystalline structures. Most research in this area has revolved around the addition of small amounts of elements to alloys based on either Zr or Hf to tailor these nano-crystalline structures and study their effects on permeability. Similarly to palladium alloys, dopants are generally chosen based on their effectiveness at suppressing hydride formation, with Zr, Mo, Ru and Rh being popular choices. [89, 90, 91, 92, 93] Alloying in this context would also likely be useful in reducing the membranes interaction with impurities through surface contamination. However this has not been touched upon much in research outside of palladium. The largest drawback to this technology is that crystalline alloys often do not show the catalytic activity necessary for dissociation of

hydrogen. This requires an additional coating of palladium to be applied to the surface in order for the material to be viable for hydrogen separation. Interestingly when this was done with some commonly used industrial alloys [94] it was found that they showed reasonable hydrogen permeability which further highlights the importance of catalytic dissociation of hydrogen. Crystalline membranes are also mechanically weak and still susceptible to hydrogen embrittlement through hydride formation in a similar manner to palladium membranes. [41]

On the other hand amorphous metal membranes are generally seen as more attractive than crystalline membranes and are often reported to have greater mechanical strength and hydrogen solubility properties than crystalline structures due to their amorphous structure giving them a more open lattice. Unlike crystalline structures, amorphous metallic membranes can also have high catalytic activity towards hydrogen dissociation which reduces the need for an additional layer to induce this catalytic activity. This property is highly composition dependent and is typically shown by Nickel containing alloys. [95] For example $Zr_{36}Ni_{64}$ in its pure form due to the presence of nickel which is catalytically active for hydrogen dissociation, however when researchers started to dope the material with Ti or Hf, the catalytic properties of the material was drastically reduced and required a layer of palladium in order to induce permeability.

Amorphous membranes still show some tendency towards hydrogen embrittlement however this is less prevalent than the crystalline alloys previously discussed. This is due to the differences in mechanisms of hydrogen embrittlement between the two classes of materials. Amorphous alloys do not show the α - β phase transition which is the main suspect of embrittlement in crystalline structures [95] and the embrittlement effect is instead due to the filling of free volume within the amorphous structure.

The main disadvantage of amorphous alloys is that given sufficient energy amorphous metallic membranes may crystallise, drastically changing their structure. This has been

reported when the material is heated to high temperatures above 500°C. [95] This limits the application of amorphous alloys to low-temperatures however if the material is intended to be used at 300°C, like most palladium membranes, and the material shows a high enough permeability, then this would likely not be an issue.

Judging from the current research landscape on non-palladium membranes, the technology is still in its infancy, with most studies focusing on the fundamental properties of these alloys and with little focus on the practical applications of the technology. Non-palladium dense metal membranes are promising due to the drastic reduction in material cost with, in many cases, an increase in permeability. Of these technologies amorphous membranes appear to be the most appealing, in particular compositions such as Zr₃₆Ni₆₄ which require no precious metals to induce catalytic activity. This has the great advantage of reducing cost of the module and bringing dense metallic membranes, and their high associated selectivity, to a wider market by taking advantage of already established industrial production of amorphous alloys. Further practical research must be performed on these membrane compositions, in particular impurity interactions, thermal stability, and long-term stability to bring this technology to market.

Table 2.5: Hydrogen permeable non-palladium metallic membranes

Membrane composition	Structure	Catalytic coating	Feed pressure	Permeability mol m ⁻² m s	Temperature °C	Membrane thickness (μm)	Ref
$(Ni_{0.6}Nb_{0.4})_{70}Zr_{30}$	Amorphous	Pd	7	1.8×10^{-8}	400	40	[96]
$(Ni_{0.6}Nb_{0.4})_{60}Zr_{40}$	Amorphous	Pd	7	6×10^{-9}	400	40	[96]
$Ni_{65}Nb_{25}Zr_{10}$	Amorphous	Pd	7	5×10^{-9}	400	40	[96]
$Ni_{45}Nb_{45}Zr_{10}$	Amorphous	Pd	7	3×10^{-9}	400	40	[96]
$Ni_{60}Nb_{40}$	Amorphous	Pd	7	2×10^{-9}	400	40	[96]
$Ni_{44}Nb_{43}Zr_{10}Pd_3$	Amorphous	Pd	7	1×10^{-9}	400	40	[96]
$Zr_{36}Ni_{64}$	Amorphous	None	1	1.2×10^{-9}	350	30	[97]
$(Ni_{0.6}Nb_{0.4})_{45}Zr_{50}Al_5$	Amorphous	Pd	3	1.9×10^{-8}	400	50	[98]
$(Ni_{0.6}Nb_{0.4})_{45}Zr_{50}Co_5$	Amorphous	Pd	3	2.46×10^{-8}	400	50	[98]
$(Ni_{0.6}Nb_{0.4})_{45}Zr_{50}Cu_5$	Amorphous	Pd	3	2.34×10^{-8}	400	50	[98]
$(Ni_{0.6}Nb_{0.4})_{45}Zr_{50}Pd_5$	Amorphous	Pd	3	1.36×10^{-8}	400	50	[98]
$V_{85}Ni_{15}$	Crystalline	Pd	0.8	5×10^{-8}	300	300-400	[99]

$V_{95}Ni_{15}$	Crystalline	Pd	0.1-2.0	4×10^{-7}	400	2000	[100]
$V_{85}Ni_{14.91}Al_{0.09}$	Crystalline	Pd	0.1-2.0	4.5×10^{-7}	400	2000	[100]
$V_{85}Ni_{14.1}Al_{0.9}$	Crystalline	Pd	0.1-2.0	4.5×10^{-7}	400	2000	[100]
$V_{85}Ni_{12.4}Al_{2.6}$	Crystalline	Pd	0.1-2.0	6×10^{-7}	400	2000	[100]
$V_{85}Ni_{10.5}Al_{4.5}$	Crystalline	Pd	0.1-2.0	7×10^{-7}	400	2000	[100]
$V_{90}Al_{10}$	Crystalline	Pd	0.2 – 2.0	2×10^{-7}	900	800-2300	[101]
$V_{70}Al_{30}$	Crystalline	Pd	0.2 – 2.0	1.8×10^{-9}	700	800-2300	[101]
INCOLOY903	Crystalline	Pd	1	1.33×10^{-7}	430	200	[94]
WASPALOY	Crystalline	Pd	1	2.99×10^{-7}	430	200	[94]
JBK-75	Crystalline	Pd	1	4.36×10^{-7}	430	200	[94]
GH85A	Crystalline	Pd	1	2.73×10^{-7}	430	200	[94]
INCOLOY907	Crystalline	Pd	1	9.67×10^{-8}	430	200	[94]
INCONEL718	Crystalline	Pd	1	2.22×10^{-7}	430	200	[94]

GH761	Crystalline	Pd	1	1.5×10^{-7}	430	200	[94]
$Nb_{20}Zr_{35}Ni_{35}$	Crystalline	Pd	1	2.73×10^{-8}	400	500-700	[102]
$Nb_{10}Zr_{45}Ni_{45}$	Crystalline	Pd	1	2.5×10^{-8}	400	500-700	[102]
$Nb_{29}Ti_{31}Ni_{40}$	Crystalline	Pd	2	7×10^{-9}	400	550-750	[103]
Nb17Ti42Ni41	Crystalline	Pd	2	0.6×10^{-8}	400	550-750	[103]
Nb10Ti50Ni40	Crystalline	Pd	2	4.5×10^{-9}	400	550-750	[103]
Nb39Ti31Ni30	Crystalline	Pd	2	2.0×10^{-8}	400	550-750	[103]
Nb28Ti42Ni30	Crystalline	Pd	2	1×10^{-8}	400	550-750	[103]
Nb21Ti50Ni29	Crystalline	Pd	2	1×10^{-8}	400	550-750	[103]
Ta_9W_5	Crystalline	None	1.4	$52 \text{ mol m}^{-2}\text{s}^{-1}$	500	650	[104]

Dense Ceramic

Dense ceramic membranes operate in a similar manner to metallic membranes, with the key difference being that they are made from ion conducting ceramics rather than metals. Dense ceramic membranes have a selectivity comparable to dense metal membranes since they only allow hydrogen to permeate, however at a lower cost than Pd-based membranes. Unlike dense metallic membranes, most ion conducting materials claim to be intrinsically inert to common hydrogen impurities and hence are stable in CO, CO₂ and H₂S containing atmospheres. [41] The major drawback to ion conducting ceramic membranes is that generally high temperatures are required to achieve any form of H₂ flux. While palladium membranes can achieve a high flux at temperatures between 300-400°C, most Perovskite membranes require temperatures between 700-900°C and generally only achieve a hydrogen permeability <10% compared to a palladium membrane of the same thickness.

The hydrogen separation process in a dense ceramic membrane is near identical to that which occurs in a dense metal membrane with the main driving forces being the pressure and concentration gradients. This is primarily controlled by the catalytic surface effects and bulk diffusion rather than thickness due to ceramic materials intrinsically low catalytic activity for such a process. For practical purposes both sides of the membrane should have sufficient catalytic activity to dissociate hydrogen atoms and the bulk should have high enough proton and electron conductivities to ensure a reasonably high flux can be achieved. More information on the precise mechanism behind proton conducting membranes can be found in the following reviews [105, 106]. The bulk diffusion of a dense ceramic membrane can be described through the Wagner equation written as Eq 2.25

$$J_{H_2} = \frac{RT}{4F^2 L} \frac{\theta_H \theta_e}{\theta_H + \theta_e} \ln \left(\frac{P'_{H_2}}{P''_{H_2}} \right) \quad (2.25)$$

Where J is the flux of the membrane, R is the gas constant, T is the operating temperature of the membrane in K, L is the thickness of the membrane layer, F is the faraday constant. θ is the permeability of electrons and protonic hydrogen, and P is the partial pressure of hydrogen on the retentate ('') and permeate ('") sides of the membrane.

Dense ceramic membranes can be split into two broad categories; single phase ceramic membranes are composed of a single material which has the ability to conduct both protons and electrons, and multi-phase ceramic membranes which are normally composed of two or more phases which when combined show proton and electron conductivity. The most common type of multi-phase ceramic membranes is known as ‘cermet’ which combines a proton conducting ceramic and a metal, such as palladium or nickel, as the electron conducting phase.

Single phase ceramic membranes must be given proton conductivity by doping a single phase ceramic material (typically perovskite) in order to create a proton hole within the material. This combined with catalytic dissociation of hydrogen on the surface allows uptake of a certain number of protons, which then diffuse through the material using the proton holes within the material. [105, 106]

Extensive efforts have been placed into developing proton-electron conducting ceramic materials for hydrogen separation however there are still many technical hurdles which must be overcome before the technology can be applied on a useful scale. The main problem holding back the technology is the incredibly low flux values reported despite operating at such high temperatures. Until this is solved there will be no point in using the technology over faster porous materials, or even dense metal membranes which offer the same selectivity’s, at much faster permeation rates. This stems back to a lack of understanding behind the surface kinetics of hydrogen dissociation (which is also an issue for non-palladium dense membranes). Despite claims that ceramic membranes

are inert to impurities there is contradictory evidence showing that the materials cannot withstand acidic conditions and degrade under atmospheres containing CO₂ and H₂S. Finally, since such high temperatures are required there will be difficulties forming a hermetic seal with ceramic membranes which can withstand the high temperature environments. This is already an issue with ceramic supported metallic membranes which operate at much more mild conditions.

From this it can be concluded that dense ceramic membranes for hydrogen separation are still at a research level and a better understanding of the material science behind the surface interactions with hydrogen and other gases, along with research into new classes of ceramics which can either permeate hydrogen at faster rates, at lower temperatures, or both are key to bringing this technology to market.

Table 2.6: Hydrogen permeable ceramic and cermet membranes which show resistance to common hydrogen impurities

Material	Class	Feed	Temperature °C	Flux	Thickness (μm)	Stability	Notes	Ref
$SrCe_{0.75}Zr_{0.2}Tm_{0.05}O_{3-\alpha}$	Perovskite	100 $mLmin^{-1}$ 50% H ₂ + He	900	0.042 $mLcm^{-2}min^{-1}$	1200	-	-	[107]
$Nd_{5.5}WO_{12-\alpha}$	Lanthanide tungstate	80% He + 20 % H ₂	1000	0	900	Stable under 115 ppm H ₂ S, 4.43% CO ₂ , 2.12% CO	No flux due to dry conditions	[108]
$La_{5.5}WO_{11.25}$	Lanthanide tungstate	80% He + 20 % H ₂	1000	< 0.005 $mLmin^{-1}cm^{-2}$	900	Stable in 15% CO ₂ for 3 days	Requires humidification for faster permeation	[109]
Nd_6Wo_{12}	Lanthanide tungstate	He + H ₂	1000	0.012 $mLmin^{-1}cm^{-2}$	510	Stable in CO ₂ and CH4 after 3 days	Humidified atmosphere	[110]
$La_{5.5}W_{0.8}Re_{0.2}O_{11.25-\alpha}$	Lanthanide tungstate	2.5% H ₂ , 2.5% H ₂ O, H ₂ balance	1000	0.095 $mLmin^{-1}cm^{-2}$	760	Stable in 5% CO ₂ 1000 ppm COS 100 ppm HCN 46% CO	Humidified atmosphere	[111]
$(La_{5/6}Nd_{1/6})_{5.5}WO_{12-\alpha}$	Lanthanide tungstate	80% He + 20 %H ₂	1000	0.005 $mLmin^{-1}cm^{-2}$	900	Stable in 15% CO ₂ for 3 days	Requires humidification	[112]
$La_{27}Mo_{1.5}W_{3.5}O_{55.5}$	Lanthanide tungstate	10% H ₂ 90% He	700	$0.78 \times 10^4 mLmin^{-1}cm^{-2}$	650	-	-	[113]
$La_{27}Mo_{1.5}W_{3.5}O_{55.5}$	Lanthanide tungstate	10% H ₂ 90% He	700	$0.78 \times 10^4 mLmin^{-1}cm^{-2}$	650	-	-	[113]

$Nd_{5.5}W_{0.5}Mo_{0.5}O_{11.25-\alpha}$	Lanthanide tungstate	50% H ₂ , 50% He	1000	$0.235 \text{ mLcm}^{-2}\text{min}^{-1}$	900	Stable in environments containing 330 ppm H ₂ S and 22% H ₂ in N ₂ . 480 ppm H ₂ S and 32% H ₂ in N ₂ . 705 ppm H ₂ S and 47% H ₂ in N ₂ 1500 ppm H ₂ S and H ₂ .	Values for humidified atmosphere. Stabilised flux value after 3 sets of tests Flux reduction due to Mo reduction	[114]
$Ni - Ba(Zr_{0.7}Pr_{0.1}Y0.2)O_{3-\alpha}$	Cermet	40% H ₂ , 57% N ₂ , 3% H ₂ O	900	$1.36 \times 10^8 \text{ molcm}^{-2}\text{s}^{-1}$	400	Stable under 30% CO ₂	Maximum value achieved for humid atmosphere	[115]
$Ni - Ba(Zr_{0.1}Ce_{0.7}Y_{0.2})O_{3-\alpha}$	Cermet	20% H ₂ , 77% N ₂ , 3% H ₂ O	900	$1.37 \times 10^{-7} \text{ molcm}^{-2}\text{s}^{-1}$	30	-	Maximum value achieved for humid atmosphere	[116]
$La_{27}W_5O_{55.5} - LaCrO_3$	Dual phase ceramic	50% H ₂ (humid)	700	$0.384 \times 10^{-3} \text{ mLcm}^{-2}\text{min}^{-1}$	1210	-	Pt coating	[117]
$La_{5.5}WO_{11.25-\alpha} - La_{0.87}Sr_{0.13}CrO_{3-\alpha}$	Dual phase ceramic	50% H ₂ , 2.5%H ₂ O	700	$0.15 \text{ mLcm}^{-2}\text{min}^{-1}$	360	Stable in 15% CO ₂ after 24 hours.	No dry atmosphere testing	[118]
$Ni - La_{0.5}Ce_{0.5}O_{2-\alpha}$	Cermet	20% H ₂ , 80% N ₂	900	$5.64 \times 10^{-8} \text{ molcm}^{-2}\text{s}^{-1}$	48	Stable in CO ₂	Flux increased in humidified conditions	[119]
$Ni - Ca_{0.0125}La_{0.4875}Ce_{0.5}O_{2-\alpha}$	Cermet	20% H ₂ , 77% N ₂ , 3%H ₂ O	900	$1.88 \times 10^{-8} \text{ molcm}^{-2}\text{s}^{-1}$	600	Stable in CO ₂	No dry atmosphere testing	[120]
$Ni - La_{0.5}Ce_{0.5}O_{2-\alpha}$	Cermet	20% H ₂ , 80% N ₂	900	$1.57 \times 10^{-8} \text{ molcm}^{-2}\text{s}^{-1}$	600	Stable in CO ₂	No dry atmosphere testing	[120]
$Ni - La_{0.5}Ce_{0.5}O_{2-\alpha}$	Cermet	20% H ₂ , 80% N ₂	900	$2.87 \times 10^{-8} \text{ molcm}^{-2}\text{s}^{-1}$	600	-	No dry atmosphere testing	[121]
$BaZr_{0.8}Y_{0.15}Mn_{0.05}O_{3-\alpha}$	Perovskite	50% H ₂ , 50% He	1000	$0.01 - 0.03 \text{ mLcm}^{-2}\text{min}^{-1}$	900	-	No dry atmosphere, Pt coated	[112]
$SrCe_{0.75}Zr_{0.2}Tm_{0.05}O_{3-\alpha}$	Perovskite	10% H ₂ , 90% He	900	$0.025 \text{ mL(STP)}\text{cm}^{-2}\text{min}^{-1}$	1600	Stable in 20% CO ₂ and 11.3% CO	-	[122]

$SrCe_{0.75}Zr_{0.2}Eu_{0.1}O_{3-\alpha}$	Perovskite	100% H ₂	900	$0.35cm^3cm^{-2}min^{-1}$	17	-	Flux improves in humid atmospheres	[123]
$Ni -$	Cermet	100% H ₂	700	$0.49mLcm^{-2}min^{-1}$	44	-	-	[124]
$BaCe_{0.7}Zr_{0.1}Y_{0.1}Yb_{0.1}O_{3-\alpha}$								
$Ni -$	Cermet	100% H ₂	900	$1.12mLcm^{-2}min^{-1}$	44	-	-	234
$BaCe_{0.7}Zr_{0.1}Y_{0.1}Yb_{0.1}O_{3-\alpha}$								
$BaCe_{0.95}Tb_{0.05}O_{3-\alpha}$	Perovskite	50% H ₂ 50% He	1000	$0.422molcm^{-2}s^{-1}$	-	-	Hollow fibre	[124]
$BaCe_{0.85}Tb_{0.05}Co_{0.1}O_{3-\alpha}$	Perovskite	50% H ₂ 50% He	1000	$0.385mLcm^{-2}min^{-1}$	167	Unstable in H ₂	Hollow fibre. Also shows oxygen permeability	[125]
$Ni -$	Cermet	20% H ₂ , 20% CO ₂ ,	1000	$5.5 \times 10^{-8}molcm^{-2}s^{-1}$	44	Unstable in H ₂	Shows reverse WGS	[126,
$BaCe_{0.7}Y_{0.1}Yb_{0.1}Zr_{0.1}O_{3-\alpha}$		60% N2					catalytic activity, Stable in 60% CO ₂ . CO causes Ni corrosion	127]
$BaCe_{0.8}Y_{0.2}O_{3-\alpha}$	Perovskite	25% H ₂ 75% He	1050	$0.38mLcm^{-2}min^{-1}$	1000	Unstable in humid environments and CO ₂	Hollow Fibre	[128]
$La_{28-x}W_{4+x}O_{54+3x/2}(La = W \times 5.6)$	Lanthanum tungstate	10% H ₂ 90% Ar	925	$0.08NmLcm^{-2}min^{-1}$	30	-	-	[129]
$La_{0.87}Sr_{0.13}CrO_{3-\alpha}$	Lanthanum tungstate	10% H ₂ , 2.5% H ₂ O	1000	$10 \times 10^{-4}mLcm^{-2}min^{-1}$	550	Chemically stable under tested conditions	-	[130]
$BaCe_{0.85}Tb_{0.05}Co_{0.1}O_{3-\alpha}$	Perovskite	50% H ₂ , 50% He	700-1000	$0.009 - 0.164mL(STP)cm^{-2}min^{-1}$	132	-	Hollow fibre	[131]
$BaCe_{0.85}Tb_{0.05}Co_{0.1}O_{3-\alpha}$	Perovskite	50% H ₂ , 50% He	700-1000	$0.018 - 0.269mL(STP)cm^{-2}min^{-1}$	132	-	Hollow fibre, Ni Coating	[131]
$BaCe_{0.85}Tb_{0.05}Co_{0.1}O_{3-\alpha}$	Perovskite	50% H ₂ , 50% He	700-1000	$0.1 - 0.42mL(STP)cm^{-2}min^{-1}$	132	-	Hollow fibre, Pd Coating	[131]

$BaCe_{0.95}Tb_{0.05}O_{3-\alpha}$ Perovskite 50% H₂, 50% He 900 0.272 $mLcm^{-2}min^{-1}$ 100 - Hollow fibre, Pd Coating [132]

Viable membrane materials and outlook

While ceramic membranes provide a viable alternative to metallic membranes as an impurity enrichment material, the technology is still in its infancy and the membranes do not show suitable permeabilities to perform impurity enrichment in a reasonable time frame. While many studies on these materials also claim that impurity resistance of these materials outclasses metallic membranes, there is little data proving this.

Of the membranes discussed, metallic membranes are the most suitable for hydrogen impurity enrichment. Palladium membranes are the only current material that has successfully been used for hydrogen impurity enrichment however there is still room for improvement which will be discussed in the following section. Non-palladium dense metallic membranes for hydrogen impurity enrichment are the next logical step in development of these membranes for analytical purposes due to their lower costs however more practical research on the materials must first be performed.

2.5.2 Membrane manufacture

Dense metal membranes can either be supported or unsupported. Unsupported membranes are free standing structures, which usually feature high wall thicknesses in order to achieve the required mechanical strength to withstand use in a process. As a result of this the flux seen through these membranes is typically low due to the high transport resistance of the membrane. Self-supported membranes are also typically expensive due to the large amount of materials required. [41]

A more efficient method is to use a support structure to allow a thinner membrane layer to be deposited, while achieving the mechanical strength required by use of another, cheaper material. This allows thinner membranes to be deposited, thereby increasing the achievable flux, and greatly reducing the cost of such a membrane.[41] Because of these clear advantages this thesis will explore the use of self-supported membranes.

Support selection

When selecting a support material there are a number of considerations which should be taken into account prior to deposition:

- Pore size distribution: If the supporting materials pore size distribution is too small then it will provide an added transfer resistance to permeation. The minimum thickness of a membrane deposited on a porous support has been found to be 3x the size of the smallest pore, [133] meaning there is a trade off between these two values
- Support surface: Adhesion of the deposited membrane to the surface of the support is compromised if the support is too smooth
- Thermal stability: The thermal stability of a support material is defined by the melting temperature, coefficient of thermal expansion (CTE) and intermetallic diffusion potential. If the CTE difference between the deposited membrane and the support is too large it will lead to a difference in the expansion rate which eventually leads to membrane failure. Intermetallic diffusion is defined as the migration of atoms between the membrane and the substrate which can negatively affect its permeability and lead to membrane failure in extreme cases
- Mechanical Stability
- Chemical stability

Of the materials available for use as a support; ceramics, porous stainless steel, and porous glass have been the most widely studied.

Porous glass supports are generally amorphous solids which feature pores ranging in sizes between the nanometre to micrometre range. They are commonly created through

sol-gel synthesis, through metastable phase separation of borosilicate glasses, or by sintering glass powder. Porous glass supports have high thermal stability, and a narrow pore size distribution typically between 4-5 nm [134] [135], theoretically allowing membrane thicknesses of 8-10 nm to be achieved. [133] Despite this they are extremely brittle and highly susceptible to acidic, alkaline or in the presence of metallic solutions. This limits their use in a number of common membrane manufacturing methods.

They are however extremely brittle and are highly susceptible to degradation under acidic, alkaline, or under metallic solutions which limits their use in a number of common membrane synthesis methods. [136]

Porous Stainless Steel (PSS) is widely available in a large number of geometries and mainly see commercial use in a number of filtering applications. A membrane layer can be deposited on top of PSS in order to gain such properties as the high mechanical strength of PSS. PSS also features a similar CTE to palladium which limits the likelihood of membrane failure due to difference in expansion rate. They are however an expensive option, with 70% of the cost in such systems being attributed to the PSS support.

The main problem with using PSS supports revolves around operation during hydrogen separation. Since both the support material, and the membrane materials are metals, at temperatures above 275°C intermetallic diffusion will occur. Intermetallic diffusion is when molecules from the stainless steel support diffuse into the membrane layer and vice versa. The result is a drastic decrease in permeability, and potential compromise of membrane integrity due to the lattice structure of the membrane being changed. A common method for mitigating this effect is to modify the surface of the PSS support with an intermediate layer that is not susceptible to intermetallic diffusion. Common intermetallic diffusion barrier are zirconia, porous silica, and porous Pd-Ag. [44] It is also possible to create an oxide layer on the surface of the PSS support by heating the material to 80°C which achieves the same result. While these methods

are effective at mitigating the effects of intermetallic diffusion; they instead introduce a different problem where, in particular with some ceramic intermetallic diffusion layers, there is a difference in CTE between the material and support. Many of the intermetallic diffusion materials can also be made into supports on their own, at a much lower cost than PSS so it also opens the question of if these materials can be made into satisfactory supports on their own, why bother adding them to costly PSS supports.

Ceramic supports generally consist of porous ceramics manufactured through sintering of ceramic powders. They are a good candidate for supporting metallic membranes due to their uniform pore size distribution (0.1-10 μm) and their high chemical, thermal and mechanical stabilities.

While the materials and processes for manufacturing ceramic supports are cheaper, the overall manufacturing process requires more steps which increases the overall time required. The resulting membranes are also extremely brittle and can easily be damaged during handling.

Al_2O_3 has traditionally been the ceramic support of choice for palladium membranes however in recent years YSZ has become more popular. This is due to the increased mechanical stability of YSZ [137], and the fact that at higher temperatures aluminium can intrude into the active layer from the support through a mechanism similar to intermetallic diffusion.[44] Using ceramic supports solves the problem of intermetallic diffusion with the drawback of increasing the likelihood of delamination occurring due to different CTE values. Ceramic supports also have the advantage of being much cheaper to manufacture the metallic supports. [44]

Membrane deposition methods

There are various methods which can be used to deposit dense metal membranes onto the surface of a support can be carried through a wide number of chemical processes. From

our reviews performed in sections 2.5.1 and 2.5.1 the most commonly used methods for deposition of dense metal membranes are PVD (e.g. magnetron sputtering) and ELP. Other methods including such as chemical vapour deposition (CVD) [138, 139, 140], electroplating deposition, atmospheric plasma [141] and spray pyrolysis [142] exist, however they have been omitted due to the inconsistency in final material, unreliability of the method, or cost. Additionally methods used to manufacture self-supporting membranes will not be discussed.

Chemical vapour deposition (CVD) involves the thermal composition of one or more metal complexes with a high volatility and subsequent deposition through nucleation and on a surface. Commonly used precursor materials are metal carbonyls or organometallic compounds. The method is known for its ability to reliably deposit thin dense membrane layers typically ($<2\text{ }\mu\text{m}$). The method is held back by its high material costs and the expensive operating conditions required.[138, 143]

Physical vapour deposition (PVD) is a coating method in which a solid material, usually a pure metal, is vaporized in a vacuum system in the presence of a inert gas. The generated atoms migrate in all directions and condensate when coming in contact with a lower temperature substrate, forming a metallic film. PVD involves using the desired membrane material as a target', and a 'coating surface' which in the case of membrane fabrication is the support. [144] The target is bombarded with ions or neutral particles which atomise the material. The inert gas, normally argon, is introduced to the sputtering chamber. The sputtering gas is ionized with a positive charge, while the target is subjected to a negative voltage typically around the magnitude of -300V. This potential difference causes the positively charged ions to impact the surface of the target, as this occurs atoms of the target material are removed and are intended to land on the substrate with enough energy to form a thin, dense, and strongly attached

film. Magnetrons are commonly employed in sputtering which use magnetic fields to confine the charged plasma particles as close to the target as possible, which increases the sputter yield.

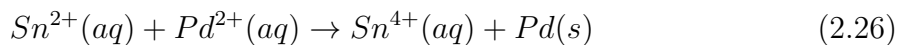
PVD in the form of Magnetron Sputtering is already an industrially widespread deposition method and is used to deposit metallic films for several applications and products. [144] The method can be used to deposit any metal or alloy. This technique can produce extremely thin nanostructured membrane layers while allowing the alloy composition to be accurately controlled and minimising the presence of impurities. [145, 146] However this method can prove to be expensive and complicated when looking to achieve defect free membranes. [147] The quality of the support is also a limiting factor with this fabrication method, the substrate must be extremely smooth in order for the film to properly adhere to the surface. In addition to this some problems arise due to the small grain sizes created by this technique which can cause grain growth and phase transitions at temperatures as low as 200°C. [148]

Electroplating deposition (EDP) is a simple coating process where a thin metal layer is deposited on a substrate by the reduction of metal ions in solution. An electrical potential promotes the transport of the ions through the plating bath on to the desired support material which acts as a cathode. The thickness of the membrane is normally controlled by the electroplating time and the composition of the plating solution. The electrochemical process is simple and only involves simple and low-cost equipment. However, the support must be conductive, which greatly limits your choice. [138, 41].

Electroless Plating (ELP) is an autocatalytic deposition method in which a surface is coated with a metallic film through a two step process. The first step, normally referred to as the activation step, involves preparing the surface by depositing small amounts of a metal with an equal to or higher electropositivity than the metal you desire onto the

surface of the support material. Palladium is commonly used as the seeding material since it has the highest electropositivity of metals capable of being deposited through ELP and hence can be used to catalyse the deposition of any other metallic species. [149] The second step is metallization where the reduction/oxidation reactions occur, catalysed by the deposited seeds and initiated by a reducing agent added to the plating bath.

The activation step is required for all non conductive support materials (i.e. ceramics, glass) otherwise the chemical activity of support will be too low and plating will likely be inefficient or will fail. The most common method used is the stannum route which involves immersing the desired support in an acidic solution of SnCl_2 , and subsequent immersion in a solution of the desired seeding metal in the form of a salt (chloride, nitride). The Sn^{2+} ions are adsorbed on the surface of the substrate in a hydrolytic form. The Sn^{2+} ions are then oxidised and replaced with Pd seeds. [149] The process for seeding a support with palladium is shown in equation 2.26 [149].



The matalization or plating step involves placing the activated support material in a bath of a solution containing a metal source, such as a metallic salt, a complexion agent which stabilizes the metallic ions in the solution, and a stabilizing agent which regulates the pH of the palting bath. The bath is heated to the desired plating conditions before additon of a reducing agent which releases electrons and initiates the reaction. As the reaction proceeds metal is continuously deposited on the seed material, growing until eventually a dense, homogenous layer is formed.

Only a select number of metals can be deposited through electroless plating, these are shown in figure 2.6. [149] These metals can be deposited through electroless plating since they have a high reduction activity. While this is commonly seen as a disadvantage, in practice many of the metals were discussed in section 2.5.1 as having advantageous effects

on the final membrane, and therefore is not as much of a hindrance as often reported. [149] This method also has the advantages of being extremely cheap, easy to perform, can be used to deposit on practically any geometry imaginable, and easily scalable. Due to the nature of this deposition method it is difficult to control the deposition rate and hence the thickness of the membrane deposited. This becomes an even larger problem when plating alloys as the final composition can be difficult to control has a large effect on the properties of the final membrane. Due to the nature of this deposition method the membranes are also susceptible to impurities which may have been present in the plating solutions or entered the solution in other means.

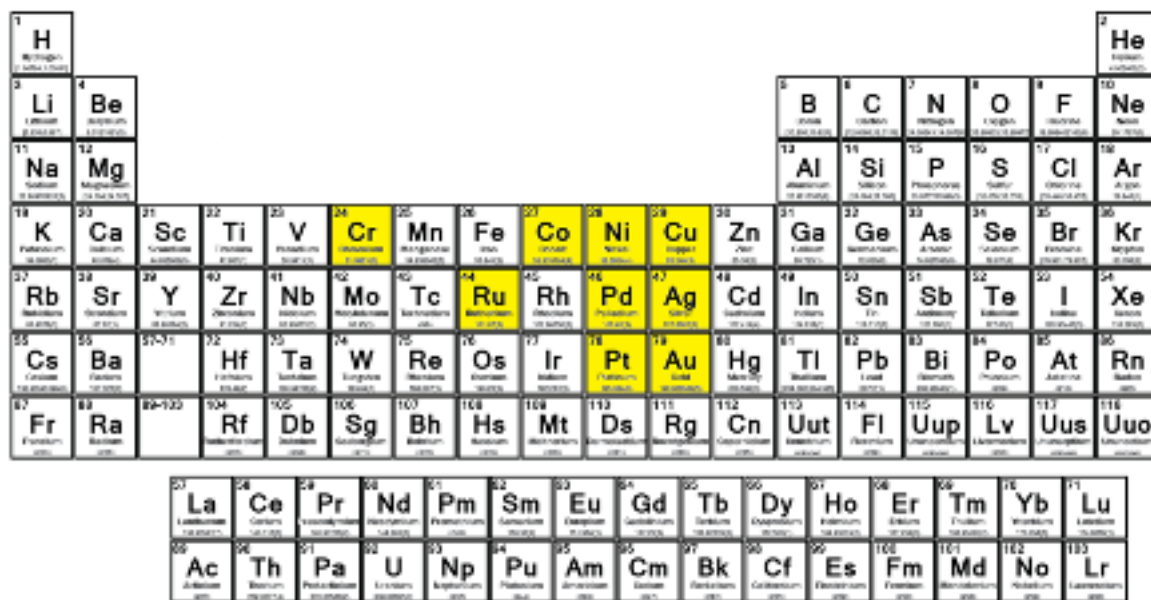


Figure 2.6: Metals which can be deposited using electro less plating [149]

There are two reported ways of creating palladium alloys through electroless plating; co-plating, and sequential plating. Co-plating refers to simultaneously plating each component of the alloy in a single step, as opposed to sequential where each alloy is plated sequentially and turned into an alloy during an additional step. Co-plating has only been reported for Pd-Ag alloys since both palladium and silver have the same reducing agent in the electroless plating reaction and is therefore easier to achieve.[150, 135] Co-plating

may seem like the optimal manufacturing method since it cuts down on the number of steps required it is generally unsuitable for membrane production since the silver content of the bath must be lowered to at least 7% in order to prevent dendritical growth, and even then it is difficult to achieve a defect free layer while maintaining plating bath stability. [149]

Sequential plating involves plating layers on top of each other and forming the alloy in a subsequent step. For example if a Pd-Ag membrane is desired a palladium layer would first be plated followed by a silver layer. [149] The membrane would then be annealed under a high temperature in order to achieve a homogeneous alloy.

2.6 Density functional theory for screening of membrane alloy compositions

Density functional theory (DFT) is a computationa quantum mechanical modelling method which is used to investigate the electronic structure of many body systems, in particular that of atoms, molecules and condensed phases. The method operates by providing an approximate solution to the Schrödinger equation of many body systems. This allows for prediction and calculation of material behaviour based purely on quantum mechanics, eliminating the need for fundamental material properties or experimental data. DFT techniques evaluate the electronic structure of a system by assuming a potential is acting on each of the systems electrons.

DFT-based methods prove to be useful in applications where a large number of elements and compositions must be investigated to optimize the desired material. For our application DFT calculations can be theoretically used to investigate, and quickly screen the suitability of any atomic configuration in the periodic table in combination with any of the ISO 14687 impurities. Much of the work in DFT screening of palladium

membranes has been performed by the group of David S. Scholl who have suggested 5 criteria to ensure the application of DFT to the field of palladium membranes are performed in an optimal manner.[151], [152] These five criteria are:

1. The timescale and/or cost for predictions made using DFT should be shorter than it would take to perform the same tests experimentally
2. There should be minimal input from experimental data
3. Predictions must be made on properties relevant to the end-use application
4. Quantitative data should be sufficient to make confident judgements on whether a material is promising or unpromising
5. The drawbacks and assumptions associated with DFT should be clearly stated to allow judgement on the predictions impact on real-world situations

This section will provide a brief overview into DFT. This will include the key concepts required to perform DFT, different assumptions which can be made along with their advantages and disadvantages, and how these relate to our chosen application, screening of metal alloy membranes. Previous work relating to the use of DFT to predict the performance of palladium alloy membranes will be discussed and finally we will tie our planned work back to Scholl's criteria.

2.6.1 Key concepts

Simulating crystalline structures

DFT is focused on applying calculations to arrangements of atoms that are periodic in space. DFT calculations achieve this by defining the shape of the 'cell' which will be repeated periodically in space. [153]

In crystalline solids, which this thesis will focus on, the atoms are arranged in a periodic fashion which repeats after a certain length. In order to explain the crystal structure in this manner a concept called 'reciprocal space' or 'k space' is used. Using this concept planes can be defined as having coordinates within a crystal lattice. These coordinates are referred to as k-points and allow for the structure of a system to be calculated and therefore solved to it's lowest energy state. [153]

The most effective and widespread solution was developed by Monkhorst and Pack which is implemented into most DFT packages, allowing users to simply define the number of k-points in each direction of reciprocal space. Frequently the same number of k-points are used in each direction. [154]

The number of k-points used is important to the accuracy of the performed calculation, however higher k-points involve a larger number of calculations across the supercell in reciprocal space and therefore will result in higher calculation times for the whole system. [154] Convergence is often used to find the optimal number of k-points. This concept is visualised in figure 2.7

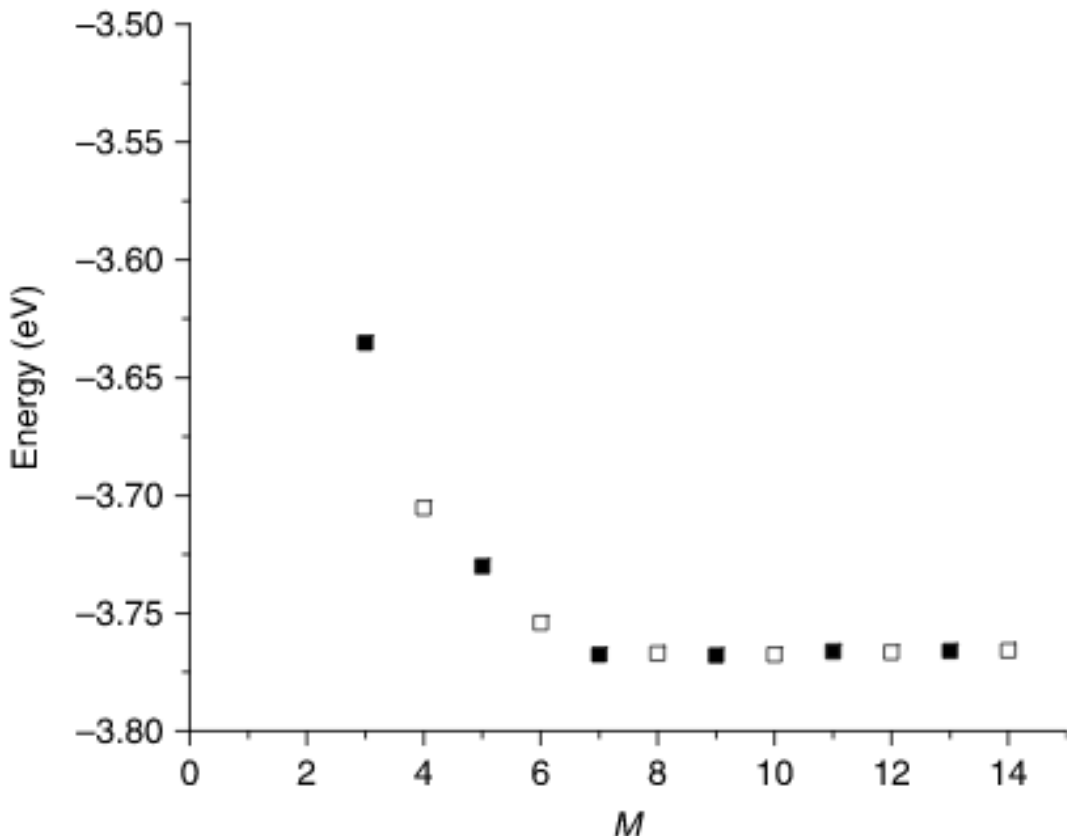


Figure 2.7: Total energies (per atom) for bulk Cu calculated as a function of M for calculations using $M \times M \times M$ kpoints [154]

At lower numbers of k-points the total energy of the system is dependent on the number of k-points used. This value eventually converges and at $M > 8$ k-points becomes completely independent of the number of k-points used. This should be kept in mind when optimising the output values for any simulated system. K-points can be thought of as sampling points within a defined supercell. [153]

Defining the supercell which will be repeated in periodic space is a simple process and involves defining the volume for the supercell, along with the number, and position of the atoms residing within.

Metals are a special case in DFT and require the use of special algorithms to ensure that the energy state of a metallic system can be calculated without a high number of

k-values. The two best methods for doing this are the tetrahedron method, or smearing. The tetrahedron method involves defining a tetrahedron using a discrete set of k-points. This tetrahedron fills the reciprocal space and can be integrated to form at all points in the k space and evaluated. [153]

Smearing involves forcing the function to be continuously integrated to replace any step functions with a smoother function. Ideally the result of the calculation should be a result which can be extrapolated to the limit where smearing is eliminated. [153]

When simulating a membrane often a slab geometry is used in order to avoid 'edge effects' where simulation results are skewed because of unique surface boundaries resulting from being at the edge of a supercell. The geometry of such a model is achieved through the generation of a box containing a multilayer atomic slab representing the membrane material with a vacuum layer in the remaining volume. From literature palladium membranes are normally in the fcc material phase [155] (with the exception being Pd₄₀Cu₆₀ which is in the bcc phase). It is common to represent this using 3-5 atomic layers of palladium. To create alloys random atoms can be substituted for other elements to achieve the desired alloy composition.

In order to determine the adsorption energy of impurities on a palladium membrane using DFT both the slab being used to represent the membrane surface, and the individual gas molecule must first be simulated in order to determine their individual ground energy states. Then the gas molecule must be adsorbed onto the surface of the membrane. In a crystalline structure there are often multiple sites which are available for gas adsorption. In an fcc structure such as Pd there are 4 main sites which can be considered, shown in figure 2.8 [156]. Once the site is chosen the simulation is iterated, slightly changing the distances between molecules until the minimum ground state is found and therefore the ground energy level of the system composed of the palladium membrane, and the adsorbed impurity. The adsorption energy, $E_{i_{ads}}$, for the adsorption

of a gaseous impurity on the surface is calculated equation 2.27. Where E_{slab+i} is the total energy of the relaxed gas-surface system where i is the simulated gas, E_{slab} and E_i are the total energy of relaxed bare surface and gas molecule respectively. Since a system will always tend towards it's lowest energy state, if the total energy of the $E_{i,ads}$ is lower than the sum of it's component energies, it indicates an affinity for the target impurity to adsorb onto the surface of the membrane.

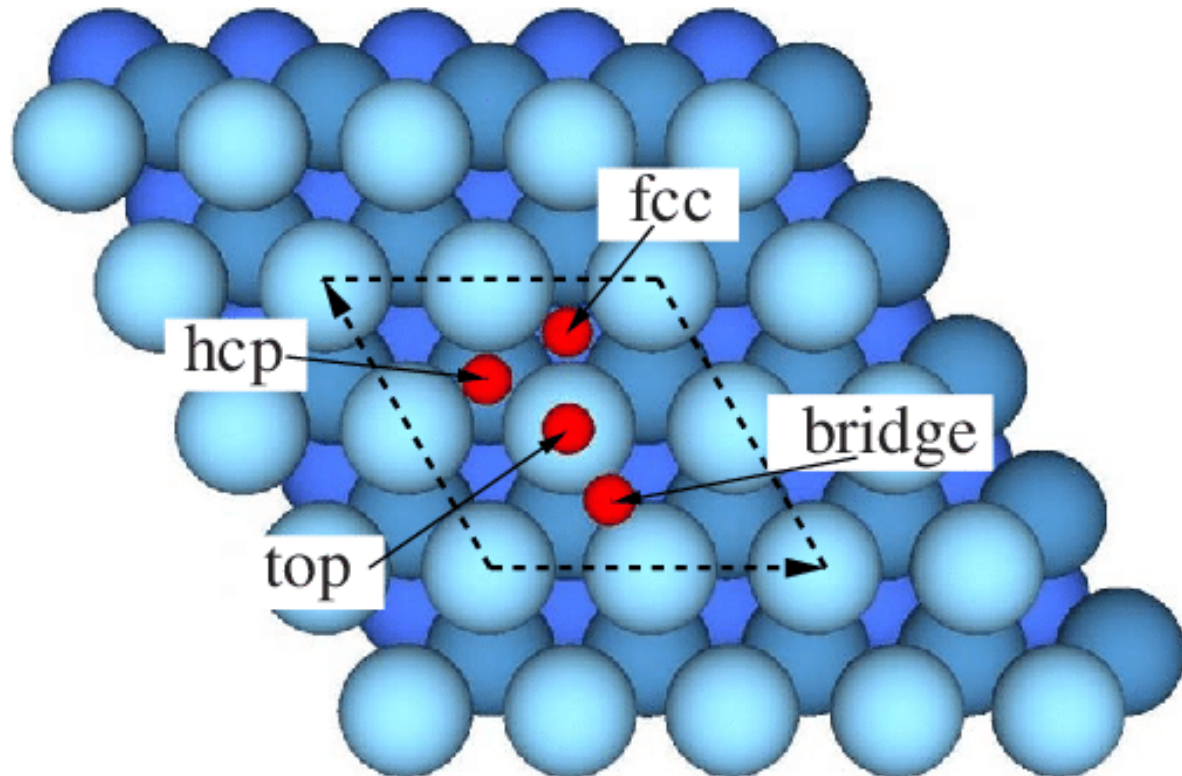


Figure 2.8: Schematic representation of (111) face Pd showing the high-symmetry adsorption sites fcc, hcp, bridge, and top [156]

$$E_{i,ads} = E_{slab} + E_i - E_{slab+i} \quad (2.27)$$

Approximations

The ultimate goal of DFT is to calculate the ground-state energy of the defined system. This was shown by Kohn, Holberg and Sham who discovered that this could be found

by finding a self-consistent solution to a set of single particle equations, as an exchange correlation. A major complication to this however is that a guaranteed exchange correlation function simply does not exist, therefore they must be approximated. Two common methods for approximating exchange correlations are local density approximation (LDA) and generalized gradient approximation (GGA)

LDA is where the energy of the system is assumed to depend on the electron density. LDA is able to predict the energy of a structure to within 1-2% of the experimental value. Unfortunately the method fails when looking to predict magnetic properties of materials and the band gaps calculated generally tend to overshoot the bond strengths. [157]

GGA is an improvement over LDA and takes into account the gradient of electron density as well as the average electron density. This adds an extra layer of computational complexity. It allows for structural properties to be predicted to within 1% of the experimental values and the total energy to be calculated to 1 kJ/mol. [157] This is also claimed in literature [158].

This thesis will mainly focus on the solid state chemistry in the bulk of the material. For this reason GGA functionals have been chosen as they have been shown in numerous publications to perform well.

Pseudopotentials

A pseudopotential is a method used to replace the electron density of a chosen set of core electrons in an atom with a smoothed density chosen to match the physical and mathematical properties of the ionic core of the atom. [157] The use of a pseudopotential is extremely important in reducing computational burden by reducing the number of planes calculated within the atom. This is commonly referred to as the 'frozen core'

assumption whereby only the behaviour of the outer most electrons are calculated, and the inner electrons, whose behaviour has previously been calculated, is considered fixed. [157]

The main differentiating feature between different types of pseudopotentials is the minimum energy cutoff for each atom in an equation. The minimum energy cutoff value refers to the number of plane wave functions which will be used to represent the system, a higher cutoff value means that more plane wave functions are used to represent the behaviour of electrons. The most commonly used pseudopotentials are ultrasoft pseudopotentials which feature a relatively low energy cutoff, making them extremely computationally efficient. A disadvantage of using an ultrasoft pseudopotential is that they require the use of empirical values in defining the properties of the core. However a review of various types of pseudopotentials found that there is virtually no difference in results regardless of what pseudopotential is used and this only becomes a factor when more complex phenomena such as magnetic properties have to be considered. [157]

Calculations that do not use a pseudopotential are called 'all electron' calculations. However their use is limited due to increased computational burden. [157]

2.6.2 Use cases, and limitations

Most work revolving around the use of DFT to predict the adsorption strength of impurities on palladium and palladium alloy surfaces has focused on catalysis of chemical reactions. As a result there are a limited number of papers focusing on quantifying the interaction between these key hydrogen impurities and membranes. Papers which use DFT to predict the behaviour of hydrogen impurities on the surface of palladium membranes are shown in table 2.7 . The most relevant study performed by Ozdogan et al [159] studied the effect of H₂ and H₂S adsorption energies when small additions of Cu and Nb were added to the membrane composition. The results indicated that while

the addition of Cu and Nb hindered hydrogen adsorption, they had a large effect on the adsorption energy of H₂S, concluding that Nb has a higher affinity for H₂S compared to Pd and a lower affinity for Cu. The results were correlated with experimental results and found to be within 1% error which is consistent with results found from using GGA.

Another useful study from Herron et al [160] studied the adsorption of a variety of atomic species (H, O, N, S, and C), molecular species (N₂, HCN, CO, NO, and NH₃), and molecular fragments (CN, NH₂, NH, CH₃, CH₂, CH, HNO, NOH, and OH) on the face of Pd(111) to quantify its effectiveness at catalysing a variety of industrial reactions. Despite its target application not being membranes, the results are still relevant to our desired study since a number of the molecular species and molecular fragments tested can be expected to be found in hydrogen. As well as quantifying the binding energies of all these molecules, the potential energies also indicated that the only reaction thermochemically preferable is the decomposition of NO. Which gives further evidence that reactions such as water gas shift occurring during catalysis are of no concern.

Outside of these the technique has seen use in predicting the stability of palladium and palladium alloy membranes. A number of studies have successfully combined data from density functional theory to calculate the solubility, diffusivity and permeability of PdCu ([161], [162], [163]), PdAg([164], [165], [166]), PdAu([164], [165], [166]), and ternary alloy ([167], [168],[169] membranes. In particular the study by Morreale et al showed that DFT can be used predict experimental data, although to a limited degree as experimental results were approximately 7 times greater than simulated results. [82]. The greatest challenge when attempting to describe the permeation of hydrogen through metallic membranes is frequent disordering of atoms during the simulation runtime, throwing off results. Other methods such as cluster expansion have been employed in order to overcome this.

The fundamental limitation of using DFT to accurately predict the behaviour of materials is that ultimately such calculation usually calculate, at a maximum, interactions between 10-30 of atoms at a time. This is in no way similar to a physical system where the number of atoms is likely to be in the millions.[157] It must be understood that DFT calculations draw results from extremely small numbers of atoms, and while relevant to physical systems, are likely to result in some errors because of this. [157]

DFT is also known to be inaccurate in describing systems where weak van der walls attractions exist between molecules and atoms. [157] This is due to the fact that such attractions are a result of temporary fluctuations in electron density. In order to describe the effect of these interactions on a quantum mechanic level it is necessary to use high level wave function based methods which DFT is unable to accurately predict. This explains why research only focuses on predicting one molecule on a surface at a time, while multiple molecules could theoretically be placed in a simulation, due to the lack of intermolecular forces being taken into account such results are likely to be innacurate. [157]

Despite these drawbacks DFT analysis is a useful tool for screening of potential palladium alloy membrane. The technique is capable of speeding up material development by eliminating options that are unlikely to work, cutting down on trial and error. Due to inaccuracies in the technique however it is unlikely that it will ever become a standalone technique in membrane research and it's findings should always be backed up by experimental data.

Table 2.7: Review of DFT studies for adsorption of ISO 14687-2 impurites and hydrogen on palladium membrane surfaces

Simulated material	Structure	Approximation	Exchange function	K-points	Adsorbed species	Adsorption site	Binding energy (eV)	ref
Pd	4x4x4 unit cell	GGA	PW91	5x5x1	H ₂	hcp	- 0.5485	[159]
Pd	4x4x4 unit cell	GGA	PW91	5x5x1	H ₂	fcc	- 0.5927	[159]
Pd	4x4x4 unit cell	GGA	PW91	5x5x1	H ₂ S	bridge-fcc-top (H-H-S)	- 0.7	[159]
Pd	4x4x4 unit cell	GGA	PW91	5x5x1	H ₂ S	bridge-bridge-top (H-H-S)	- 0.707	[159]
Pd	4x4x4 unit cell	GGA	PW91	5x5x1	H ₂ S	bridge-hcp-top (H-H-S)	- 0.707	[159]
Pd	4x4x4 unit cell	GGA	PW91	5x5x1	H ₂ S	fcc-hcp-top (H-H-S)	- 0.692	[159]
PdNb _{1.6}	4x4x4 unit cell	GGA	PW91	5x5x1	H ₂	hcp	-0.4259	[159]
PdNb _{1.6}	4x4x4 unit cell	GGA	PW91	5x5x1	H ₂	fcc	-0.4740	[159]
PdNb _{1.6}	4x4x4 unit cell	GGA	PW91	5x5x1	H ₂ S	bridge-fcc-top (H-H-S)	- 0.803	[159]
PdNb _{1.6}	4x4x4 unit cell	GGA	PW91	5x5x1	H ₂ S	bridge-bridge-top (H-H-S)	- 0.704	[159]
PdNb _{1.6}	4x4x4 unit cell	GGA	PW91	5x5x1	H ₂ S	bridge-hcp-top (H-H-S)	- 0.735	[159]
PdNb _{1.6}	4x4x4 unit cell	GGA	PW91	5x5x1	H ₂ S	fcc-hcp-top (H-H-S)	- 0.682	[159]

PdNb _{1.6}	4x4x4 unit cell	GGA	PW91	5x5x1	H ₂ S	hcp-bridge-top (H-H-S)	- 0.602	[159]
PdCu _{1.6}	4x4x4 unit cell	GGA	PW91	5x5x1	H ₂	hcp	-0.4946	[159]
PdCu _{1.6}	4x4x4 unit cell	GGA	PW91	5x5x1	H ₂	fcc	-0.5357	[159]
PdNb _{1.6}	4x4x4 unit cell	GGA	PW91	5x5x1	H ₂ S	bridge-fcc-top (H-H-S)	- 0.429	[159]
PdNb _{1.6}	4x4x4 unit cell	GGA	PW91	5x5x1	H ₂ S	bridge-hcp-top (H-H-S)	- 0.431	[159]
Pd	2x2x4 unit cell	GGA	PW91	3x3x1	N ₂	top	- 0.23	[160]
Pd	2x2x4 unit cell	GGA	PW91	3x3x1	N ₂	fcc	- 0.02	[160]
Pd	2x2x4 unit cell	GGA	PW91	3x3x1	N ₂	bridge	- 0.07	[160]
Pd	2x2x4 unit cell	GGA	PW91	3x3x1	NH ₃	top	- 0.62	[160]
Pd	2x2x4 unit cell	GGA	PW91	3x3x1	NH ₂	top	-1.63	[160]
Pd	2x2x4 unit cell	GGA	PW91	3x3x1	NH ₂	bridge	-2.15	[160]
Pd	2x2x4 unit cell	GGA	PW91	3x3x1	NH	fcc	-3.45	[160]
Pd	2x2x4 unit cell	GGA	PW91	3x3x1	NH	hcp	-3.30	[160]
Pd	2x2x4 unit cell	GGA	PW91	3x3x1	CO	top	-1.29	[160]
Pd	2x2x4 unit cell	GGA	PW91	3x3x1	CO	fcc	-1.95	[160]
Pd	2x2x4 unit cell	GGA	PW91	3x3x1	CO	hcp	-1.96	[160]
Pd	2x2x4 unit cell	GGA	PW91	3x3x1	CO	bridge	-1.77	[160]
Pd	2x2x4 unit cell	GGA	PW91	3x3x1	CH ₃	top	-1.67	[160]
Pd	2x2x4 unit cell	GGA	PW91	3x3x1	CH ₂	bridge	-3.56	[160]
Pd	2x2x4 unit cell	GGA	PW91	3x3x1	CH	fcc	-5.91	[160]
Pd	2x2x4 unit cell	GGA	PW91	3x3x1	CH	hcp	-5.89	[160]
Pd	2x2x4 unit cell	GGA	PW91	3x3x1	CH	hcp	-5.89	[160]
Pd	2x2x3 unit cell	GGA	PW91	3x3x1	H ₂	top	-0.07	[158]

Pd	2x2x3 unit cell	GGA	PW91	3x3x1	H ₂	bridge	-0.37	[158]
Pd	2x2x3 unit cell	GGA	PW91	3x3x1	H ₂	fcc	-0.49	[158]
Pd	2x2x3 unit cell	GGA	PW91	3x3x1	H ₂	hcp	-0.45	[158]
PdAg ₂₅	2x2x3 unit cell	GGA	PW91	3x3x1	H ₂	top	0.84	[158]
PdAg ₂₅	2x2x3 unit cell	GGA	PW91	3x3x1	H ₂	bridge	-0.27	[158]
PdAg ₂₅	2x2x3 unit cell	GGA	PW91	3x3x1	H ₂	fcc	-0.22	[158]
PdAg ₂₅	2x2x3 unit cell	GGA	PW91	3x3x1	H ₂	hcp	-0.22	[158]

2.7 Conclusion

In this chapter a number of concepts key to the question of measuring impurities in fuel grade hydrogen were explored. Hydrogen production methods were discussed, identifying key impurities likely to be in fuel cell hydrogen and were therefore suitable to be further researched. It was clear from past literature that the main impurities of note are sulphur containing compounds, due to their low amount fraction required by ISO 14687 and their high reactivity making them the most difficult to measure. It is worthwhile investigating other impurities which, while non-reactive with palladium membranes themselves, still interact with the membrane surface. This interaction could potentially catalyse reactions between the gases in the sample mixture and it is therefore still necessary to investigate the effect of CH₄, CO₂ and CO.

Different methods for enriching hydrogen was discussed with one of the most promising methods identified being hydrogen impurity enrichment using a dense metal membrane. This had an advantage over other methods discussed due to the flexibility it provides. From here a number of membrane materials designed to separate hydrogen from multicomponent mixtures. An extensive summary has been provided on the separation performance and stability of these materials with an emphasis on the complications related to transitioning the use of these materials from laboratory and R&D efforts, to industrially relevant processes. The key observation is that while there is a large research focus on new membrane materials, there is a lack of research looking into the engineering of these membranes into functional systems and products. Out of the hundreds of materials being researched for gas separation, commercially only 4-8 different polymers are used, with some niche applications using palladium membranes. Research focus should shift towards focusing on repeatability, scale up, and creating engineered systems where new membrane materials can be used in order to make progress in bringing these new materials to market. Out of the membrane materials reviewed palladium based alloys

were the most appropriate to be used for hydrogen impurity enrichment and focus in this thesis will be to find a suitable composition for measuring ISO 14687-2 impurities while minimising interaction with reactants.

Different membrane manufacturing techniques and geometries were compared and it was decided that a combination of ELP and magnetron sputtering will be used to create membranes. This is due to the ease and reproducability of these techniques while collectivley being able to produce a wide range of membrane compositions. Ceramic YSZ supports will be used due to their low cost, stability, and ability to achieve a surface on which extremely thin palladium membranes can be deposited.

DFT based theories were identified as a method to save time money and cost when attempting to optimise the palladium alloy composition. There is a gap in research on using this technique for palladium alloys specifically targeting ISO 14687-2 impurities. While limited literature exists since many papers address the use of palladium surfaces as catalysts the research is useful for creating a starting base. Palladium alloy membranes can be screened for materials which exhibit the lowest reactivity with ISO 14687-2 impuruties, and once identified, they can be manufactured and tested. It is important to note however that there are a number of innacuracies involved in the technique and should only be used as a rough guide.

References

- [1] A Alaswad, A Palumbo, M Dassisti, A G B T Reference Module in Materials Science Olabi, and Materials Engineering. Fuel Cell Technologies, Applications, and State of the Art. A Reference Guide. Elsevier, 2016. ISBN 978-0-12-803581-8. doi: <https://doi.org/10.1016/B978-0-12-803581-8.04009-1>. URL <http://www.sciencedirect.com/science/article/pii/B9780128035818040091>.
- [2] Sangeetha Dharmalingam, Vaidhegi Kugarajah, and Moogambigai Sugumar. Chapter 1.7 - Membranes for Microbial Fuel Cells. In S Venkata Mohan, Sunita Varjani, and Ashok B T Microbial Electrochemical Technology Pandey, editors, *Biomass, Biofuels and Biochemicals*, pages 143–194. Elsevier, 2019. ISBN 978-0-444-64052-9. doi: <https://doi.org/10.1016/B978-0-444-64052-9.00007-8>. URL <http://www.sciencedirect.com/science/article/pii/B9780444640529000078>.
- [3] Viral Mehta and Joyce Smith Cooper. Review and analysis of PEM fuel cell design and manufacturing. *Journal of Power Sources*, 114(1):32–53, 2003. ISSN 0378-7753. doi: [https://doi.org/10.1016/S0378-7753\(02\)00542-6](https://doi.org/10.1016/S0378-7753(02)00542-6). URL <http://www.sciencedirect.com/science/article/pii/S0378775302005426>.
- [4] Zhongliang Li, Zhixue Zheng, Liangfei Xu, and Xiaonan Lu. A review of the applications of fuel cells in microgrids: opportunities and challenges. *BMC Energy*, 1, dec 2019. doi: 10.1186/s42500-019-0008-3.

- [5] Klaus-Michael Mangold. Introduction to Hydrogen Technology. By Roman J. Press, K. S. V. Santhanam, Massoud J. Miri, Alla V. Bailey, and Gerald A. Takacs. *ChemSusChem*, 2(8):781, aug 2009. ISSN 1864-5631. doi: 10.1002/cssc.200900109. URL <https://doi.org/10.1002/cssc.200900109>.
- [6] J D Holladay, J Hu, D L King, and Y Wang. An overview of hydrogen production technologies. *Catalysis Today*, 139(4):244–260, 2009. ISSN 0920-5861. doi: <https://doi.org/10.1016/j.cattod.2008.08.039>. URL <http://www.sciencedirect.com/science/article/pii/S0920586108004100>.
- [7] International Energy Agency (IEA). Technology Roadmap Hydrogen and Fuel Cell. Technical report, IEA/OECD Paris., 2015.
- [8] N Muradov. 17 - Low-carbon production of hydrogen from fossil fuels. In Velu Subramani, Angelo Basile, and T Nejat B T Compendium of Hydrogen Energy Veziroğlu, editors, *Woodhead Publishing Series in Energy*, pages 489–522. Woodhead Publishing, Oxford, 2015. ISBN 978-1-78242-361-4. doi: <https://doi.org/10.1016/B978-1-78242-361-4.00017-0>. URL <http://www.sciencedirect.com/science/article/pii/B9781782423614000170>.
- [9] Hydrogen Council. Path to hydrogen competitiveness a cost perspective. Jan 2020.
- [10] J.G. Speight. 6 - gasification processes for syngas and hydrogen production. In Rafael Luque and James G. Speight, editors, *Gasification for Synthetic Fuel Production*, Woodhead Publishing Series in Energy, pages 119 – 146. Woodhead Publishing, 2015. ISBN 978-0-85709-802-3. doi: <https://doi.org/10.1016/B978-0-85709-802-3.00006-0>. URL <http://www.sciencedirect.com/science/article/pii/B9780857098023000060>.
- [11] S. Sui and G.H. Xiu. 14 - fuels and fuel processing in sofc applications.

In Kevin Kendall and Michaela Kendall, editors, *High-Temperature Solid Oxide Fuel Cells for the 21st Century (Second Edition)*, pages 461 – 495. Academic Press, Boston, second edition edition, 2016. ISBN 978-0-12-410453-2. doi: <https://doi.org/10.1016/B978-0-12-410453-2.00014-2>. URL <http://www.sciencedirect.com/science/article/pii/B9780124104532000142>.

- [12] P. Chiesa. 15 - advanced technologies for syngas and hydrogen (h₂) production from fossil-fuel feedstocks in power plants. In Dermot Roddy, editor, *Advanced Power Plant Materials, Design and Technology*, Woodhead Publishing Series in Energy, pages 383 – 411. Woodhead Publishing, 2010. ISBN 978-1-84569-515-6. doi: <https://doi.org/10.1533/9781845699468.3.383>. URL <http://www.sciencedirect.com/science/article/pii/B9781845695156500157>.
- [13] F. Frusteri and G. Bonura. 5 - hydrogen production by reforming of bio-alcohols. In Velu Subramani, Angelo Basile, and T. Nejat Veziroğlu, editors, *Compendium of Hydrogen Energy*, Woodhead Publishing Series in Energy, pages 109 – 136. Woodhead Publishing, Oxford, 2015. ISBN 978-1-78242-361-4. doi: <https://doi.org/10.1016/B978-1-78242-361-4.00005-4>. URL <http://www.sciencedirect.com/science/article/pii/B9781782423614000054>.
- [14] Shakeel Ahmed, Abdullah Aitani, Faizur Rahman, Ali Al-Dawood, and Fahad Al-Muhaish. Decomposition of hydrocarbons to hydrogen and carbon. *Applied Catalysis A: General*, 359(1):1–24, 2009. ISSN 0926-860X. doi: <https://doi.org/10.1016/j.apcata.2009.02.038>. URL <http://www.sciencedirect.com/science/article/pii/S0926860X09001719>.
- [15] Nazim Z Muradov and T Nejat Veziroğlu. “Green” path from fossil-based to hydrogen economy: An overview of carbon-neutral technologies. *International Journal of Hydrogen Energy*, 33(23):6804–6839, 2008. ISSN 0360-3199. doi: <https://doi.org/10.1016/j.ijhydene.2008.07.030>.

doi.org/10.1016/j.ijhydene.2008.08.054. URL <http://www.sciencedirect.com/science/article/pii/S036031990801118X>.

- [16] Canan Acar and Ibrahim Dincer. Comparative assessment of hydrogen production methods from renewable and non-renewable sources. *International Journal of Hydrogen Energy*, 39(1):1–12, 2014. ISSN 0360-3199. doi: <https://doi.org/10.1016/j.ijhydene.2013.10.060>. URL <http://www.sciencedirect.com/science/article/pii/S0360319913025330>.
- [17] C Koroneos, A Dompros, G Roumbas, and N Moussiopoulos. Life cycle assessment of hydrogen fuel production processes. *International Journal of Hydrogen Energy*, 29(14):1443–1450, 2004. ISSN 0360-3199. doi: <https://doi.org/10.1016/j.ijhydene.2004.01.016>. URL <http://www.sciencedirect.com/science/article/pii/S0360319904000655>.
- [18] Energy & Industrial Strategy Department for Business. Prices of fuels purchased by non-domestic consumers in the united kingdom excluding/including ccl (qep 3.4.1 and 3.4.2). Mar 2020. URL <https://www.gov.uk/government/statistical-data-sets/gas-and-electricity-prices-in-the-non-domestic-sector>.
- [19] Argonne National Lab. Life cycle greenhouse gas emissions of by-product hydrogen from chloro-alkali plants. Dec 2017.
- [20] David A. Nelson. Chemical process industries (shreve, r. norris; brink, joseph a.). *Journal of Chemical Education*, 57(9):A270, 1980. doi: 10.1021/ed057pA270.1. URL <https://doi.org/10.1021/ed057pA270.1>.
- [21] Hussam Khasawneh, Motasem N Saidan, and Mohammad Al-Addous. Utilization of hydrogen as clean energy resource in chlor-alkali process. *Energy Exploration*

& Exploitation, 37(3):1053–1072, 2019. doi: 10.1177/0144598719839767. URL <https://doi.org/10.1177/0144598719839767>.

- [22] Thomas Bacquart, Arul Murugan, Martine Carré, Bruno Gozlan, Fabien Auprêtre, Frédérique Haloua, and Thor A Aarhaug. Probability of occurrence of ISO 14687-2 contaminants in hydrogen: Principles and examples from steam methane reforming and electrolysis (water and chlor-alkali) production processes model. *International Journal of Hydrogen Energy*, 43(26):11872–11883, 2018. ISSN 0360-3199. doi: <https://doi.org/10.1016/j.ijhydene.2018.03.084>. URL <http://www.sciencedirect.com/science/article/pii/S0360319918308450>.
- [23] International Standard ISO 14687: 2019. Hydrogen Fuel - Product Specification, 2019.
- [24] Krystina E. Lamb, Michael D. Dolan, and Danielle F. Kennedy. Ammonia for hydrogen storage; a review of catalytic ammonia decomposition and hydrogen separation and purification. *International Journal of Hydrogen Energy*, 44(7):3580 – 3593, 2019. ISSN 0360-3199. doi: <https://doi.org/10.1016/j.ijhydene.2018.12.024>. URL <http://www.sciencedirect.com/science/article/pii/S0360319918339272>.
- [25] Enrico Doná, Michael Cordin, Clemens Deisl, Erminald Bertel, Cesare Franchini, Rinaldo Zucca, and Josef Redinger. Halogen-Induced Corrosion of Platinum. *Journal of the American Chemical Society*, 131(8):2827–2829, mar 2009. ISSN 0002-7863. doi: 10.1021/ja809674n. URL <https://doi.org/10.1021/ja809674n>.
- [26] Papadias D.D., Ahmed S., and Kumar R. Fuel quality issues in stationary fuel cell systems, 2011. URL https://www.energy.gov/sites/prod/files/2014/03/f10/fuel_quality_stationary_fuel_cells.pdf.
- [27] Ji-Sung Seo, Da-Yeong Kim, Sun-Mi Hwang, Min Ho Seo, Dong-Jun Seo, Se-

ung Yong Yang, Chan Hui Han, Yong-Min Jung, Hwanuk Guim, Kee Suk Nahm, Young-Gi Yoon, and Tae-Young Kim. Degradation of polymer electrolyte membrane fuel cell by siloxane in biogas. *Journal of Power Sources*, 316:44 – 52, 2016. ISSN 0378-7753. doi: <https://doi.org/10.1016/j.jpowsour.2016.03.063>. URL <http://www.sciencedirect.com/science/article/pii/S0378775316302762>.

- [28] K. Kortsdottir, F. J. Perez Ferriz, C. Lagergren, and R. W. Lindstrom. Reformate hydrogen fuel in PEM fuel cells: the effect of alkene impurities on anode activity. *ECS Transactions*, 58(1):1857–1865, aug 2013. doi: 10.1149/05801.1857ecst. URL <https://doi.org/10.1149%2F05801.1857ecst>.
- [29] Ki Chul Kim, Mark D. Allendorf, Vitalie Stavila, and David S. Sholl. Predicting impurity gases and phases during hydrogen evolution from complex metal hydrides using free energy minimization enabled by first-principles calculations. *Phys. Chem. Chem. Phys.*, 12:9918–9926, 2010. doi: 10.1039/C001657H. URL <http://dx.doi.org/10.1039/C001657H>.
- [30] A. Bulgarin, H. Jorschick, P. Preuster, A. Bösmann, and P. Wasserscheid. Purity of hydrogen released from the liquid organic hydrogen carrier compound perhydro dibenzyltoluene by catalytic dehydrogenation. *International Journal of Hydrogen Energy*, 45(1):712 – 720, 2020. ISSN 0360-3199. doi: <https://doi.org/10.1016/j.ijhydene.2019.10.067>. URL <http://www.sciencedirect.com/science/article/pii/S0360319919338285>.
- [31] Shabbir Ahmed, Sheldon H D Lee, and Dionissios D Papadias. Analysis of trace impurities in hydrogen: Enrichment of impurities using a H₂ selective permeation membrane . *International Journal of Hydrogen Energy*, 35(22):12480–12490, 2010. doi: 10.1016/j.ijhydene.2010.08.042.
- [32] Arul Murugan and Andrew S Brown. Advancing the analysis of impurities in

hydrogen by use of a novel tracer enrichment method. *Analytical Methods*, 6(15): 5472, 2014. doi: 10.1039/c3ay42174k.

- [33] Arul Murugan and Andrew S Brown. Review of purity analysis methods for performing quality assurance of fuel cell hydrogen. *International Journal of Hydrogen Energy*, 40(11):4219–4233, 2015. doi: 10.1016/j.ijhydene.2015.01.041.
- [34] Peter R Bossard, Jacques Mettes, Luis Breziner, and Emeritus Fred Gornick. New Sensor for Measuring Trace Impurities in Ultra Pure Hydrogen. *Power & Energy, USA*.
- [35] Jürgen Hille. Enrichment and mass spectrometric analysis of trace impurity concentrations in gases. *Journal of Chromatography A*, 502:265–274, 1990. ISSN 0021-9673. doi: [https://doi.org/10.1016/S0021-9673\(01\)89591-1](https://doi.org/10.1016/S0021-9673(01)89591-1). URL <http://www.sciencedirect.com/science/article/pii/S0021967301895911>.
- [36] A Volkov. Membrane Compaction. In Giorno L Drioli E., editor, *Encyclopedia of Membranes*. Springer, Berlin, Heidelberg, 2014.
- [37] A. Gugliuzza. Membrane Swelling. In Drioli E. and Giorno L., editors, *Encyclopedia of Membranes*. Springer, Berlin, Heidelberg, 2015.
- [38] R. Farrauto, S. Hwang, L. Shore, W. Ruettinger, J. Lampert, T. Giroux, Y. Liu, and O. Ilinich. New Material Needs for Hydrocarbon Fuel Processing: Generating Hydrogen for the PEM Fuel Cell. *Annual Review of Materials Research*, 33(1):1–27, 2003. ISSN 1531-7331. doi: 10.1146/annurev.matsci.33.022802.091348. URL <http://www.annualreviews.org/doi/10.1146/annurev.matsci.33.022802.091348>.
- [39] K. Nagai, A. Higuchi, and T. Nakagawa. Gas permeability and stability of poly(1-

trimethylsilyl-1-propyne-co-1-phenyl-1-propyne) membranes. *J. Polym. Sci.: Part B: Polym. Phys.*, 33:289, 1995.

- [40] G. Polotskaya, M. Goikhman, I. Podeshvo, V. Kudryavtsev, Z. Pientka, L. Brozova, and M. Bleha. Gas transport properties of polybenzoxazinoneimides and their prepolymers. *Polymer*, 46(11):3730–3736, 2005. ISSN 00323861. doi: 10.1016/j.polymer.2005.02.111.
- [41] Tina M Nenoff Nathan W. Ockwig. Membranes for Hydrogen Separation. *Chemical Reviews*, 107:4078–4110, 2007.
- [42] Hong Joo Lee, Hiroyuki Suda, Kenji Haraya, and Seung Hyeon Moon. Gas permeation properties of carbon molecular sieving membranes derived from the polymer blend of polyphenylene oxide (PPO)/polyvinylpyrrolidone (PVP). *Journal of Membrane Science*, 296(1-2):139–146, 2007. ISSN 03767388. doi: 10.1016/j.memsci.2007.03.025.
- [43] Huiyuan Gao, Y S Lin, Yongdan Li, and Baoquan Zhang. Chemical Stability and Its Improvement of Palladium-Based Metallic Membranes. *Ind. Eng. Chem. Res.*, 43:6920–6930, 2004.
- [44] K Atsonios, K D Panopoulos, A Doukelis, A K Koumanakos, E Kakaras, T A Peters, and Y C van Delft. Introduction to palladium membrane technology. In A Doukelis, K Panopoulos, A Koumanakos, and E Kakaras, editors, *Palladium Membrane Technology for Hydrogen Production, Carbon Capture and Other Application*, pages 1–21. Woodhead Publishing, 2015. doi: 10.1533/9781782422419.1.
- [45] Truls Norby and Reidar Haugsrud. Dense Ceramic Membranes for Hydrogen Separation, in Membranes for Energy Conversion. *Nonporous inorganic membranes*, pages 169–216, 2008. URL <http://books.google.com/books?>

hl=en{\&}lr={\&}id=gCQjw-cyulAC{\&}oi=fnd{\&}pg=PA1{\&}dq=Dense+
Ceramic+Membranes+for+Hydrogen+Separation{\&}ots=e-3oiNW5EW{\&}sig=
Iv9bFzwJWBTYe7brB66{\&}qq5W{\&}u8.

- [46] D.H. Weinkauf and D.R. Paul. Gas transport properties of thermotropic liquid-crystalline copolyesters. II. The effects of copolymer composition. *J. Polym. Sci.: Part B: Polym. Phys.*, 30:837, 1992.
- [47] Tina M Nenoff Nathan W. Ockwig. Membranes for Hydrogen Separation. *Chemical Reviews*, 107:4078–4110, 2007.
- [48] V. Gryaznov. Metal Containing Membranes for the Production of Ultrapure Hydrogen and the Recovery of Hydrogen Isotopes. *Separation & Purification Reviews*, 29(2):171–187, 2000. ISSN 1542-2119. doi: 10.1081/SPM-100100008.
- [49] N A Al-Mufachi, N V Rees, and R Steinberger-Wilkins. Hydrogen selective membranes: A review of palladium-based dense metal membranes. *Renewable and Sustainable Energy Reviews*, 47:540–551, 2015. doi: 10.1016/j.rser.2015.03.026.
- [50] Johnson Matthey Precious Metals Management. Price Tables, 2016.
- [51] Ted B Flanagan and W A Oates. The Palladium-Hydrogen System. *Annu. Rev. Mater. Sci.*, 21:269–304, 1991.
- [52] Hui Li, Hengyong Xu, and Wenzhao Li. Study of n value and α/β palladium hydride phase transition within the ultra-thin palladium composite membrane. *Journal of Membrane Science*, 324(1-2):44–49, 2008. doi: 10.1016/j.memsci.2008.06.053.
- [53] M V Mundschau, X Xie, C R Evenson Iv, and A F Sammells. Dense inorganic membranes for production of hydrogen from methane and coal with carbon dioxide sequestration. *Catalysis today*, 118:12–23, 2006. doi: 10.1016/j.cattod.2006.01.042.

- [54] Ying She, Sean C Emerson, Neal J Magdefrau, Susanne M Opalka, Catherine Thibaud-Erkey, and Thomas H Vanderspurt. Hydrogen permeability of sulfur tolerant Pd–Cu alloy membranes. *Journal of Membrane Science*, 452:203–211, 2014. doi: 10.1016/j.memsci.2013.09.025.
- [55] M D Dolan. Non-Pd BCC alloy membranes for industrial hydrogen separation. *Journal of Membrane Science*, 362(1-2):12–28, 2010. doi: 10.1016/j.memsci.2010.06.068.
- [56] Ekin Ozdogan Wilcox and Jennifer. Investigation of H₂ and H₂S Adsorption on Niobium- and Copper-Doped Palladium Surfaces. *J. Phys. Chem. B*, pages 12851–12585, 2010. doi: 10.1021/acs.energyfuels.5b01294.
- [57] I R Harris D.T. Hughes. A comparative study of hydrogen permeabilities and solubilities in some palladium solid solution alloys. *Journal of Less Common Metals*, 61:9–21, 1978.
- [58] Casey P O Brien, Bret H Howard, James B Miller, Bryan D Morreale, and Andrew J Gellman. Inhibition of hydrogen transport through Pd and Pd₄₇Cu₅₃ membranes by H₂S at 350C. *Journal of Membrane Science*, 349(1-2):380–384, 2010. doi: 10.1016/j.memsci.2009.11.070.
- [59] A Kulprathipanja, G Alptekin, J Falconer, and J Way. Pd and Pd–Cu membranes: inhibition of H₂ permeation by H₂S. *Journal of Membrane Science*, 254(1-2):49–62, 2005. doi: 10.1016/j.memsci.2004.11.031.
- [60] Chao-Huang Chen and Yi Hua Ma. The effect of H₂S on the performance of Pd and Pd/Au composite membrane. *Journal of Membrane Science*, 362(1-2):535–544, 2010. doi: 10.1016/j.memsci.2010.07.002.
- [61] David L. McKinley. Metal Alloy for Hydrogen Separation and Purification, 1964.

- [62] G. Roa, F., Thoen, P.M., Gade, S.K., Way, J.G., De Voss, S., and Alptekin. Palladium-Copper and Palladium-Gold alloy Composite membranes for hydrogen separations. In *Inorganic Membranes for Energy and Environmental Applications*, page 211. 2009.
- [63] APMEX. Silver Prices, 2016. URL <http://www.apmex.com/spotprices/silver-prices>.
- [64] Lixia Peng, Yongchu Rao, Lizhu Luo, and Chang'An Chen. The poisoning of Pd-Y alloy membranes by carbon monoxide. *Journal of Alloys and Compounds*, 486(1-2):74–77, 2009. doi: 10.1016/j.jallcom.2009.06.158.
- [65] Kenneth J. Bryden and Jackie Y. Ying. Nanostructured palladium-iron membranes for hydrogen separation and membrane hydrogenation reactions. *Journal of Membrane Science*, 203(1-2):29–42, 2002. ISSN 03767388. doi: 10.1016/S0376-7388(01)00736-0.
- [66] B. H. Howard and B. D. Morreale. Effect of H₂S on performance of Pd₄Pt alloy membranes. *Energy Materials*, 3(3):177–185, 2008. ISSN 1748-9237. doi: 10.1179/174892309X12519750237717. URL <http://www.tandfonline.com/doi/full/10.1179/174892309X12519750237717>.
- [67] Sabina K. Gade, Sarah J. DeVoss, Kent E. Coulter, Stephen N. Paglieri, Gökhan O. Alptekin, and J. Douglas Way. Palladium-gold membranes in mixed gas streams with hydrogen sulfide: Effect of alloy content and fabrication technique. *Journal of Membrane Science*, 378(1-2):35–41, 2011. ISSN 03767388. doi: 10.1016/j.memsci.2010.11.044. URL <http://dx.doi.org/10.1016/j.memsci.2010.11.044>.
- [68] Shin Kun Ryi, Anwu Li, C. Jim Lim, and John R. Grace. Novel non-alloy Ru/Pd composite membrane fabricated by electroless plating for hydrogen sep-

aration. *International Journal of Hydrogen Energy*, 36(15):9335–9340, 2011. ISSN 03603199. doi: 10.1016/j.ijhydene.2010.06.014. URL <http://dx.doi.org/10.1016/j.ijhydene.2010.06.014>.

- [69] Kent E. Coulter, J. Douglas Way, Sabina K. Gade, Saurabh Chaudhari, Gökhan O. Alptekin, Sarah J. DeVoss, Stephen N. Paglieri, and Bill Pledger. Sulfur tolerant PdAu and PdAuPt alloy hydrogen separation membranes. *Journal of Membrane Science*, 405-406:11–19, 2012. ISSN 03767388. doi: 10.1016/j.memsci.2012.02.018. URL <http://dx.doi.org/10.1016/j.memsci.2012.02.018>.
- [70] Fernando Braun, James B. Miller, Andrew J. Gellman, Ana M. Tarditi, Benoit Fleutot, Petro Kondratyuk, and Laura M. Cornaglia. PdAgAu alloy with high resistance to corrosion by H₂S. *International Journal of Hydrogen Energy*, 37(23):18547–18555, 2012. ISSN 03603199. doi: 10.1016/j.ijhydene.2012.09.040. URL <http://dx.doi.org/10.1016/j.ijhydene.2012.09.040>.
- [71] Fernando Braun, Ana M Tarditi, James B Miller, and Laura M Cornaglia. Pd-based binary and ternary alloy membranes: Morphological and perm-selective characterization in the presence of H₂S. *Journal of Membrane Science*, 450:299–307, 2014. doi: 10.1016/j.memsci.2013.09.026.
- [72] T. A. Peters, T. Kaleta, M. Stange, and R. Bredesen. Development of thin binary and ternary Pd-based alloy membranes for use in hydrogen production. *Journal of Membrane Science*, 383(1-2):124–134, 2011. ISSN 03767388. doi: 10.1016/j.memsci.2011.08.050. URL <http://dx.doi.org/10.1016/j.memsci.2011.08.050>.
- [73] T A Peters, T Kaleta, M Stange, and R Bredesen. Development of ternary Pd–Ag–TM alloy membranes with improved sulphur tolerance. *Journal of Membrane Science*, 429:448–458, 2013. doi: 10.1016/j.memsci.2012.11.062.

- [74] Xuezhong He and May Britt Hägg. Hollow fiber carbon membranes: From material to application. *Chemical Engineering Journal*, 215-216:440–448, 2013. ISSN 13858947. doi: 10.1016/j.cej.2012.10.051. URL <http://dx.doi.org/10.1016/j.cej.2012.10.051>.
- [75] T A Peters, M Stange, and R Bredesen. Fabrication of palladium-based membranes by magnetron sputtering. In A Doukelis, K Panopoulos, A Koumanakos, and E Kakaras, editors, *Palladium Membrane Technology for Hydrogen Production, Carbon Capture and Other Application*, pages 25–41. Woodhead Publishing, 2015. doi: 10.1533/9781782422419.1.25.
- [76] AM Tarditi, C Imhoff, and F Braun. PdCuAu ternary alloy membranes: Hydrogen permeation properties in the presence of H₂S. *Journal of Membrane ...*, 479: 246–255, 2014. URL <http://www.sciencedirect.com/science/article/pii/S0376738814009338>.
- [77] T A Peters, M Stange, H Klette, and R Bredesen. High pressure performance of thin Pd–23%Ag/stainless steel composite membranes in water gas shift gas mixtures; influence of dilution, mass transfer and surface effects on the hydrogen flux. *Journal of Membrane Science*, 316(1-2):119–127, 2008. doi: 10.1016/j.memsci.2007.08.056.
- [78] T A Peters, M Stange, P Veenstra, A Nijmeijer, and R Bredesen. The performance of Pd–Ag alloy membrane films under exposure to trace amounts of H₂S. *Journal of Membrane Science*, 499:105–115, 2016. doi: 10.1016/j.memsci.2015.10.031.
- [79] Nong Xu, Sung Su Kim, Anwu Li, John R Grace, C Jim Lim, and Tony Boyd. Investigation of the influence of tar-containing syngas from biomass gasification on dense Pd and Pd–Ru membranes. *Powder Technology*, 290:132–140, 2016. doi: 10.1016/j.powtec.2015.08.037.

- [80] Sean-Thomas B Lundin, Taichiro Yamaguchi, Colin A Wolden, S Ted Oyama, and J Douglas Way. The role (or lack thereof) of nitrogen or ammonia adsorption-induced hydrogen flux inhibition on palladium membrane performance. *Journal of Membrane Science*, 514:65–72, 2016. doi: 10.1016/j.memsci.2016.04.048.
- [81] Thu Hoai Nguyen, Shinsuke Mori, and Masaaki Suzuki. Hydrogen permeance and the effect of H₂O and CO on the permeability of Pd0.75Ag0.25 membranes under gas-driven permeation and plasma-driven permeation. *Chemical Engineering Journal*, 155(1-2):55–61, 2009. doi: 10.1016/j.cej.2009.06.024.
- [82] Bryan D Morreale, Bret H Howard, Osemwengie Iyoha, Robert M Enick, Chen Ling, and David S Sholl. Experimental and Computational Prediction of the Hydrogen Transport Properties of Pd 4 S. *Ind. Eng. Chem. Res.*, 46:6313–6319, 2007.
- [83] A Li, W Liang, and R Highes. The effect of carbon monoxide and steam on the hydrogen permeability of a Pd/stainless steel membrane. *Journal of Membrane Science*, 165:135–141, 2000.
- [84] Natalie Pomerantz and Ma Yi Hua. Effect of H₂S on the performance and long-term stability of Pd/Cu membranes. *Industrial and Engineering Chemistry Research*, 48(8):4030–4039, 2009. ISSN 08885885. doi: 10.1021/ie801947a.
- [85] M Saleh. Interaction of Sulphur Compounds with Palladium. pages 242–250, 1969. ISSN 00147672. doi: 10.1039/TF9706600242.
- [86] B. D. Morreale, M. V. Ciocco, B. H. Howard, R. P. Killmeyer, A. V. Cugini, and R. M. Enick. Effect of hydrogen-sulfide on the hydrogen permeance of palladium-copper alloys at elevated temperatures. *Journal of Membrane Science*, 241(2): 219–224, 2004. ISSN 03767388. doi: 10.1016/j.memsci.2004.04.033.

- [87] AM Tarditi, C Imhoff, and F Braun. PdCuAu ternary alloy membranes: Hydrogen permeation properties in the presence of H₂S. *Journal of Membrane science*, 479: 246–255, 2014.
- [88] Amanda E Lewis, Hongbin Zhao, Haseeba Syed, Colin A Wolden, and J Douglas Way. PdAu and PdAuAg composite membranes for hydrogen separation from synthetic water-gas shift streams containing hydrogen sulfide. *Journal of Membrane Science*, 465:167–176, 2014. doi: 10.1016/j.memsci.2014.04.022.
- [89] CO (US); Shane E. Roark, Boulder, CO (US); Richard MacKay, Lafayette, Michael V. Mundscha Longmont S, and s CO (US). DENSE, LAYERED MEMBRANES FOR HYDROGEN SEPARATION, 2006. ISSN 2004001828.
- [90] D.S dos Santos and P.E.V de Miranda. The use of electrochemical hydrogen permeation techniques to detect hydride phase separation in amorphous metallic alloys. *Journal of Non-Crystalline Solids*, 232-234:133–139, 1998. ISSN 00223093. doi: 10.1016/S0022-3093(98)00487-6. URL <http://linkinghub.elsevier.com/retrieve/pii/S0022309398004876>.
- [91] Hiroshi Yukawa, Daisuke Yamashita, Shigeyuki Ito, Masahiko Morinaga, and Shu Yamaguchi. Alloying effects on the phase stability of hydrides formed in vanadium alloys. *Materials Transactions*, 43(11):2757–2762, 2002. ISSN 1345-9678. doi: 10.2320/matertrans.43.2757. URL [\%5Cnpapers2://publication/uuid/3C0A7ADC-9BA8-471E-9CF3-40C116284411\%5Cnhttp://joi.jlc.jst.go.jp/JST.JSTAGE/matertrans/43.2757?from=CrossRef.](http://www.jim.or.jp/journal/e/pdf3/43/11/2757.pdf)
- [92] Hiroshi Yukawa, Akira Teshima, Daisuke Yamashita, Shigeyuki Ito, Masahiko Morinaga, and Shu Yamaguchi. Alloying effects on the hydriding properties of

vanadium at low hydrogen pressures. *Journal of Alloys and Compounds*, 337(1-2): 264–268, 2002. ISSN 09258388. doi: 10.1016/S0925-8388(01)01936-3.

- [93] Hiroshi Yukawa, Daisuke Yamashita, Shigeyuki Ito, Masahiko Morinaga, and Shu Yamaguchi. Compositional dependence of hydriding properties of vanadium alloys at low hydrogen pressures. *Journal of Alloys and Compounds*, 356-357:45–49, 2003. ISSN 09258388. doi: 10.1016/S0925-8388(03)00099-9.
- [94] J. Xu, X. K. Sun, Q. Q. Liu, and W. X. Chen. Hydrogen permeation behavior in IN718 and GH761 superalloys. *Metallurgical and Materials Transactions A*, 25 (3):539–544, 1994. ISSN 10735623. doi: 10.1007/BF02651595.
- [95] S Hara, K Sakaki, N Itoh, H.-M. Kimura, K Asami, and A Inoue. An amorphous alloy membrane without noble metals for gaseous hydrogen separation. *Journal of Membrane Science*, 164:289–294, 2000.
- [96] Shin-ichi Yamaura, Yoichiro (Fukuda Metal Foil & Powder Co. Ltd.) Shimpo, Hitoshi (Fukuda Metal Foil & Powder Co. Ltd.) Okouchi, Motonori (Fukuda Metal Foil & Powder Co. Ltd.) Nishida, Osamu (Fukuda Metal Foil & Powder Co. Ltd.) Kajita, Hisamichi Kimura, and Akihisa Inoue. Hydrogen Permeation Characteristics of Melt-Spun Ni-Nb-Zr Amorphous Alloy Membranes. *Materials Transactions*, 42(9):1885–1890, 2001. ISSN 1345-9678. doi: 10.2320/matertrans.42.1885. URL <http://ci.nii.ac.jp/naid/130004451634/>.
- [97] S Hara, K Sakaki, N Itoh, H.-M. Kimura, K Asami, and A Inoue. An amorphous alloy membrane without noble metals for gaseous hydrogen separation. *Journal of Membrane Science*, 164:289–294, 2000.
- [98] Shin Ichi Yamaura, Yoichiro Shimpo, Hitoshi Okouchi, Motonori Nishida, Osamu Kajita, and Akihisa Inoue. The effect of additional elements on hydrogen

permeation properties of melt-spun Ni-Nb-Zr amorphous alloys. *Nippon Kinzoku Gakkaishi/Journal of the Japan Institute of Metals*, 68(12):1039–1042, 2004. ISSN 00214876. doi: 10.2320/jinstmet.68.1039.

- [99] C Nishimura, M Komaki, S Hwang, and M Amano. V-Ni alloy membranes for hydrogen purification. *Journal of Alloys and Compounds*, 330-332:902–906, 2002.
- [100] Tetsuya Ozaki, Yi Zhang, Masao Komaki, and Chikashi Nishimura. Preparation of Palladium-coated V and V-15Ni membranes for hydrogen purification by electroless plating technique. *International Journal of Hydrogen Energy*, 28:297–302, 2003.
- [101] C. Nishimura, T. Ozaki, M. Komaki, and Y. Zhang. Hydrogen permeation and transmission electron microscope observations of V-Al alloys. *Journal of Alloys and Compounds*, 356-357:295–299, 2003. ISSN 09258388. doi: 10.1016/S0925-8388(02)01273-2.
- [102] T. Takano, K. Ishikawa, T. Matsuda, and K. Aoki. Hydrogen Permeation of Eutectic Nb-Zr-Ni Alloy Membranes Containing Primary Phases. *Materials Transactions*, 45(12):3360–3362, 2004. ISSN 13459678. doi: 10.2320/matertrans.45.3360.
- [103] Kunihiko Hashi, Kazuhiro Ishikawa, Takeshi Matsuda, and Kiyoshi Aoki. Microstructures and Hydrogen Permeability of Nb-Ti-Ni Alloys with High Resistance to Hydrogen Embrittlement. *Materials Transactions*, 46(5):1026–1031, 2005. ISSN 1345-9678. doi: 10.2320/matertrans.46.1026. URL https://www.jstage.jst.go.jp/article/matertrans/46/5/46_1026/_article.
- [104] H. Yukawa, T. Nambu, and Y. Matsumoto. Ta-W Alloy for Hydrogen Permeable Membranes. *Materials Transactions*, 52(4):610–613, 2011. ISSN 1347-5320. doi:

10.2320/matertrans.MA201007. URL <http://joi.jlc.jst.go.jp/JST.JSTAGE/matertrans/MA201007?from=CrossRef>.

- [105] Zetian Tao, Litao Yan, Jinli Qiao, Baolin Wang, Lei Zhang, and Jiujun Zhang. A review of advanced proton-conducting materials for hydrogen separation. *Progress in Materials Science*, 74:1–50, 2015. ISSN 00796425. doi: 10.1016/j.pmatsci.2015.04.002. URL <http://dx.doi.org/10.1016/j.pmatsci.2015.04.002>.
- [106] John W. Phair and Richard Donelson. Developments and design of novel (non-palladium-based) metal membranes for hydrogen separation. *Industrial and Engineering Chemistry Research*, 45(16):5657–5674, 2006. ISSN 08885885. doi: 10.1021/ie051333d.
- [107] Wen Hui Yuan, Ling Ling Mao, and Li Li. Novel SrCe_{0.75}Zr_{0.20}Tm_{0.05}O₃-alpha membrane for hydrogen separation. *Chinese Chemical Letters*, 21(3):369–372, 2010. ISSN 10018417. doi: 10.1016/j.cclet.2009.11.002.
- [108] Sonia Escolástico, Cecilia Solís, and José M. Serra. Hydrogen separation and stability study of ceramic membranes based on the system Nd₅LnWO₁₂. *International Journal of Hydrogen Energy*, 36(18):11946–11954, 2011. ISSN 03603199. doi: 10.1016/j.ijhydene.2011.06.026.
- [109] Sonia Escolástico, Cecilia Solís, Tobias Scherb, Gerhard Schumacher, and Jose M. Serra. Hydrogen separation in La_{5.5}WO_{11.25-δ} membranes. *Journal of Membrane Science*, 444:276–284, 2013. ISSN 03767388. doi: 10.1016/j.memsci.2013.05.005. URL <http://dx.doi.org/10.1016/j.memsci.2013.05.005>.
- [110] Sonia Escolástico, Vicente B. Vert, and José M. Serra. Preparation and characterization of nanocrystalline mixed proton-electronic conducting materials based

on the system Ln₆WO₁₂. *Chemistry of Materials*, 21(14):3079–3089, 2009. ISSN 08974756. doi: 10.1021/cm900067k.

- [111] Sonia Escolástico, Janka Seeger, Stefan Roitsch, Mariya Ivanova, Wilhelm A. Meullenberg, and José M. Serra. Enhanced H₂ separation through mixed proton-electron conducting membranes based on La_{5.5}W_{0.8}M_{0.2}O_{11.25-δ}. *ChemSusChem*, 6(8):1523–1532, 2013. ISSN 18645631. doi: 10.1002/cssc.201300091.
- [112] Sonia Escolástico, Cecilia Solís, and José M. Serra. Study of hydrogen permeation in (La 5/6Nd 1/6) 5.5WO_{12-δ} membranes. *Solid State Ionics*, 216:31–35, 2012. ISSN 01672738. doi: 10.1016/j.ssi.2011.11.004. URL <http://dx.doi.org/10.1016/j.ssi.2011.11.004>.
- [113] Einar Vøllestad, Camilla K. Vigen, Anna Magrasó, and Reidar Haugsrud. Hydrogen permeation characteristics of La₂₇Mo_{1.5}W_{3.5}O_{55.5}. *Journal of Membrane Science*, 461:81–88, 2014. ISSN 18733123. doi: 10.1016/j.memsci.2014.03.011. URL <http://dx.doi.org/10.1016/j.memsci.2014.03.011>.
- [114] Sonia Escolástico, Simona Somacescu, and José M. Serra. Tailoring mixed ionic–electronic conduction in H₂ permeable membranes based on the system Nd 5.5 W 1 x Mo x O 11.25 δ. *J. Mater. Chem. A*, 3(2):719–731, 2015. ISSN 2050-7488. doi: 10.1039/C4TA03699A. URL <http://xlink.rsc.org/?DOI=C4TA03699A>.
- [115] Zhiwen Zhu, Wenping Sun, Yingchao Dong, Zhongtao Wang, Zhen Shi, Qingsheng Zhang, and Wei Liu. Evaluation of hydrogen permeation properties of Ni–Ba(Zr_{0.7}Pr_{0.1}Y_{0.2})O₃ δ cermet membranes. *International Journal of Hydrogen Energy*, 39(22):11683–11689, 2014. ISSN 03603199. doi: 10.1016/j.ijhydene.2014.05.163. URL <http://linkinghub.elsevier.com/retrieve/pii/S0360319914015754>.

- [116] Zhiwen Zhu, Wenping Sun, Litao Yan, Weifeng Liu, and Wei Liu. Synthesis and hydrogen permeation of Ni–Ba(Zr_{0.1}Ce_{0.7}Y_{0.2})O₃ δ metal–ceramic asymmetric membranes. *International Journal of Hydrogen Energy*, 36(10):6337–6342, 2011. ISSN 03603199. doi: 10.1016/j.ijhydene.2011.02.029. URL <http://linkinghub.elsevier.com/retrieve/pii/S0360319911003466>.
- [117] Jonathan M Polfus, Wen Xing, Marie-Laure Fontaine, Christelle Denonville, Partow P Henriksen, and Rune Bredesen. Hydrogen separation membranes based on dense ceramic composites in the La₂₇W₅O_{55.5}-LaCrO₃ system. *Journal of Membrane Science*, 479:39–45, 2015. ISSN 03767388. doi: 10.1016/j.memsci.2015.01.027. URL <http://dx.doi.org/10.1016/j.memsci.2015.01.027>.
- [118] S. Escolástico, C. Solís, C. Kjølseth, and J. M. Serra. Outstanding hydrogen permeation through CO ₂-stable dual-phase ceramic membranes. *Energy Environ. Sci.*, 7(11):3736–3746, 2014. ISSN 1754-5692. doi: 10.1039/C4EE02066A. URL <http://xlink.rsc.org/?DOI=C4EE02066A>.
- [119] Zhiwen Zhu, Wenping Sun, Zhongtao Wang, Jiafeng Cao, Yingchao Dong, and Wei Liu. A high stability Ni-Lainf_{0.5}/infCeinf_{0.5}/infOinf_{2- δ} /inf asymmetrical metal-ceramic membrane for hydrogen separation and generation. *Journal of Power Sources*, 281:417–424, 2015. ISSN 03787753. doi: 10.1016/j.jpowsour.2015.02.005. URL <http://dx.doi.org/10.1016/j.jpowsour.2015.02.005>.
- [120] Shumin Fang, Lei Bi, Litao Yan, and Wenping Sun. CO₂ Resistant Hydrogen Permeation Membranes Based on Doped Ceria and Nickel. *Journal of Physical Chemistry C*, pages 10986–10991, 2010. ISSN 1932-7447. doi: 10.1021/jp102271v. URL <http://pubs.acs.org/doi/abs/10.1021/jp102271v>.
- [121] Litao Yan, Wenping Sun, Lei Bi, Shumin Fang, Zetian Tao, and Wei Liu. Effect of Sm-doping on the hydrogen permeation of Ni-La₂Ce₂O₇ mixed protonic-electronic

conductor. *International Journal of Hydrogen Energy*, 35(10):4508–4511, 2010. ISSN 03603199. doi: 10.1016/j.ijhydene.2010.02.134. URL <http://dx.doi.org/10.1016/j.ijhydene.2010.02.134>.

- [122] Jay Kniep and Y. S. Lin. Effect of zirconium doping on hydrogen permeation through strontium cerate membranes. *Industrial and Engineering Chemistry Research*, 49(6):2768–2774, 2010. ISSN 08885885. doi: 10.1021/ie9015182.
- [123] Tak keun Oh, Heesung Yoon, and E. D. Wachsman. Effect of Eu dopant concentration in SrCe_{1 - x}Eu_xO_{3 - ??} on ambipolar conductivity. *Solid State Ionics*, 180 (23-25):1233–1239, 2009. ISSN 01672738. doi: 10.1016/j.ssi.2009.07.001.
- [124] Wei Liu, Victor G. Ruiz, Guo Xu Zhang, Biswajit Santra, Xinguo Ren, Matthias Scheffler, and Alexandre Tkatchenko. Structure and energetics of benzene adsorbed on transition-metal surfaces: Density-functional theory with van der Waals interactions including collective substrate response. *New Journal of Physics*, 15 (111), 2013. ISSN 13672630. doi: 10.1088/1367-2630/15/5/053046.
- [125] Jian Song, Liping Li, Xiaoyao Tan, and K. Li. BaCe_{0.85}Tb_{0.05}Co_{0.1}O_{3-??} perovskite hollow fibre membranes for hydrogen/oxygen permeation. *International Journal of Hydrogen Energy*, 38(19):7904–7912, 2013. ISSN 03603199. doi: 10.1016/j.ijhydene.2013.04.104.
- [126] Shumin Fang, Kyle Brinkman, and Fanglin Chen. Unprecedented CO ₂-Promoted Hydrogen Permeation in Ni-BaZr _{0.1}Ce _{0.7} Y _{0.1} Yb _{0.1} O _{3δ} Membrane. *ACS Applied Materials & Interfaces*, 6(1):725–730, 2014. ISSN 1944-8244. doi: 10.1021/am405169d. URL <http://pubs.acs.org/doi/abs/10.1021/am405169d>.

- [127] Shumin Fang, Kyle S. Brinkman, and Fanglin Chen. Hydrogen permeability and chemical stability of Ni-BaZr_{0.1}Ce_{0.7}Y_{0.1}Yb_{0.1}O_{3- δ} membrane in concentrated H₂O and CO₂. *Journal of Membrane Science*, 467:85–92, 2014. ISSN 18733123. doi: 10.1016/j.memsci.2014.05.008. URL <http://dx.doi.org/10.1016/j.memsci.2014.05.008>.
- [128] Xihan Tan, Xiaoyao Tan, Naitao Yang, Bo Meng, Kun Zhang, and Shaomin Liu. High performance BaCe_{0.8}Y_{0.2}O₃-A (BCY) hollow fibre membranes for hydrogen permeation. *Ceramics International*, 40(2):3131–3138, 2014. ISSN 02728842. doi: 10.1016/j.ceramint.2013.09.132.
- [129] Vanesa Gil, Jonas Gurauskis, Christian Kjølseth, Kjell Wiik, and Mari-Ann Einarsrud. Hydrogen permeation in asymmetric La_{28-x}W₄ + xO₅₄ + 3x/2 membranes. *International Journal of Hydrogen Energy*, 38(7):3087–3091, 2013. ISSN 03603199. doi: 10.1016/j.ijhydene.2012.12.105. URL <http://linkinghub.elsevier.com/retrieve/pii/S0360319912028406>.
- [130] Camilla K. Vigen and Reidar Haugsrud. Hydrogen flux in La_{0.87}Sr_{0.13}CrO_{3- δ} . *Journal of Membrane Science*, 468:317–323, 2014. ISSN 18733123. doi: 10.1016/j.memsci.2014.06.012.
- [131] Jian Song, Bo Meng, Xiaoyao Tan, and Shaomin Liu. Surface-modified proton conducting perovskite hollow fibre membranes by Pd-coating for enhanced hydrogen permeation. *International Journal of Hydrogen Energy*, 40(18):6118–6127, 2015. ISSN 03603199. doi: 10.1016/j.ijhydene.2015.03.057. URL <http://dx.doi.org/10.1016/j.ijhydene.2015.03.057>.
- [132] Jian Song, Jian Kang, Xiaoyao Tan, Bo Meng, and Shaomin Liu. Proton conducting perovskite hollow fibre membranes with surface catalytic modification for enhanced hydrogen separation. *Journal of the European Ceramic Society*, 36(7):

1669–1677, 2015. ISSN 1873619X. doi: 10.1016/j.jeurceramsoc.2016.01.006. URL <http://dx.doi.org/10.1016/j.jeurceramsoc.2016.01.006>.

- [133] Ivan P. Mardilovich, Erik Engwall, and Yi Hua Ma. Dependence of hydrogen flux on the pore size and plating surface topology of asymmetric Pd-porous stainless steel membranes. *Desalination*, 144(1-3):85–89, 2002. ISSN 00119164. doi: 10.1016/S0011-9164(02)00293-X.
- [134] E.-U. Schlünder, J. Yang, and A. Seidel-Morgenstern. Competitive diffusion and adsorption in vycor glass membranes—a lumped parameter approach. *Catalysis Today*, 118(1):113 – 120, 2006. ISSN 0920-5861. doi: <https://doi.org/10.1016/j.cattod.2005.11.094>. URL <http://www.sciencedirect.com/science/article/pii/S0920586106003488>. Catalysis in Membrane Reactors.
- [135] Shigeyuki Uemiya, Noboru Sato, Hiroshi Ando, Yukinori Kude, Takeshi Matsuda, and Eiichi Kikuchi. Separation of hydrogen through palladium thin film supported on a porous glass tube. *Journal of Membrane Science*, 56(3):303 – 313, 1991. ISSN 0376-7388. doi: [https://doi.org/10.1016/S0376-7388\(00\)83040-9](https://doi.org/10.1016/S0376-7388(00)83040-9). URL <http://www.sciencedirect.com/science/article/pii/S0376738800830409>.
- [136] S. Mukherjee, M.K. Hatalis, and M.V. Kothare. Water gas shift reaction in a glass microreactor. *Catalysis Today*, 120(1):107 – 120, 2007. ISSN 0920-5861. doi: <https://doi.org/10.1016/j.cattod.2006.07.007>. URL <http://www.sciencedirect.com/science/article/pii/S092058610600438X>. The Novel Compact Catalytic Reactor.
- [137] Hideko Hayashi, Tetsuya Saitou, Naotaka Maruyama, Hideaki Inaba, Katsuyuki Kawamura, and Masashi Mori. Thermal expansion coefficient of yttria stabilized zirconia for various yttria contents. *Solid State Ionics*, 176(5-6):613–619, 2005. ISSN 01672738. doi: 10.1016/j.ssi.2004.08.021.

- [138] Samhun Yun and S Ted Oyama. Correlations in palladium membranes for hydrogen separation: A review. *Journal of Membrane Science*, 375(1-2):28–45, 2011. doi: 10.1016/j.memsci.2011.03.057.
- [139] W P Wang, S Thomas, X L Zhang, X L Pan, W S Yang, and G X Xiong. H₂/N₂ gaseous mixture separation in dense Pd/ α -Al₂O₃ hollow fiber membranes: Experimental and simulation studies. *Separation and Purification Technology*, 52(1):177–185, 2006. doi: 10.1016/j.seppur.2006.04.007.
- [140] E David and J Kopac. Development of palladium/ceramic membranes for hydrogen separation. *International Journal of Hydrogen Energy*, 36(7):4498–4506, 2011. doi: 10.1016/j.ijhydene.2010.12.032.
- [141] Yan Huang and Roland Dittmeyer. Preparation of thin palladium membranes on a porous support with rough surface. *Journal of Membrane Science*, 302(1):160 – 170, 2007. ISSN 0376-7388. doi: <https://doi.org/10.1016/j.memsci.2007.06.040>. URL <http://www.sciencedirect.com/science/article/pii/S0376738807004358>.
- [142] Zhong Yan Li, Hideaki Maeda, Katsuki Kusakabe, Shigeharu Morooka, Hiroshi Anzai, and Shigeo Akiyama. Preparation of palladium-silver alloy membranes for hydrogen separation by the spray pyrolysis method. *Journal of Membrane Science*, 78(3):247 – 254, 1993. ISSN 0376-7388. doi: [https://doi.org/10.1016/0376-7388\(93\)80004-H](https://doi.org/10.1016/0376-7388(93)80004-H). URL <http://www.sciencedirect.com/science/article/pii/037673889380004H>.
- [143] Angelo Basile, Fausto Gallucci, and Silvano Tosti. Synthesis, Characterization, and Applications of Palladium Membranes. 13:255–323, 2008. doi: 10.1016/s0927-5193(07)13008-4.

- [144] T A Peters, M Stange, and R Bredesen. Fabrication of palladium-based membranes by magnetron sputtering. In A Doukelis, K Panopoulos, A Koumanakos, and E Kakaras, editors, *Palladium Membrane Technology for Hydrogen Production, Carbon Capture and Other Application*, pages 25–41. Woodhead Publishing, 2015. doi: 10.1533/9781782422419.1.25.
- [145] George Xomeritakis and Y. S. Lin. Fabrication of thin metallic membranes by MOCVD and sputtering. *Journal of Membrane Science*, 133(2):217–230, 1997. ISSN 03767388. doi: 10.1016/S0376-7388(97)00084-7.
- [146] B. McCool, G. Xomeritakis, and Y. S. Lin. Composition control and hydrogen permeation characteristics of sputter deposited palladium-silver membranes. *Journal of Membrane Science*, 161(1-2):67–76, 1999. ISSN 03767388. doi: 10.1016/S0376-7388(99)00087-3.
- [147] Jos T. F. Keurentjes, Frank C. Gielens, H. D. Tong, C. J. M. van Rijn, and Marius a. G. Vorstman. High-Flux Palladium Membranes Based on Microsystem Technology. *Industrial & Engineering Chemistry Research*, 43(16):4768–4772, 2004. ISSN 0888-5885. doi: 10.1021/ie0341202. URL <http://pubs.acs.org/doi/abs/10.1021/ie0341202>.
- [148] Kenneth J. Bryden and Jackie Y. Ying. Nanostructured palladium membrane synthesis by magnetron sputtering. *Materials Science and Engineering A*, 204 (1-2):140–145, 1995. ISSN 09215093. doi: 10.1016/0921-5093(95)09950-6.
- [149] M J den Exter. The use of electroless plating as a deposition technology in the fabrication of palladium-based membranes. In A Doukelis, K Panopoulos, A Koumanakos, and E Kakaras, editors, *Palladium Membrane Technology for Hydrogen Production, Carbon Capture and Other Application*, pages 43–67. Woodhead Publishing, 2015. doi: 10.1533/9781782422419.1.43.

- [150] E Kikuchi and S Uemiya. Preparation of supported thin palladium-silver alloy membranes and their characteristics for hydrogen separation. *Gas Separation and Purification*, 5, 1991.
- [151] David S. Sholl. Using density functional theory to study hydrogen diffusion in metals: A brief overview. *Journal of Alloys and Compounds*, 446-447:462 – 468, 2007. ISSN 0925-8388. doi: <https://doi.org/10.1016/j.jallcom.2006.10.136>. URL <http://www.sciencedirect.com/science/article/pii/S0925838806017439>. Proceedings of the International Symposium on Metal-Hydrogen Systems, Fundamentals and Applications (MH2006).
- [152] Kelly M. Nicholson, Nita Chandrasekhar, and David S. Sholl. Powered by dft: Screening methods that accelerate materials development for hydrogen in metals applications. *Accounts of Chemical Research*, 47(11):3275–3283, 2014. doi: 10.1021/ar500018b. URL <https://doi.org/10.1021/ar500018b>. PMID: 24937509.
- [153] *DFT Calculations for Simple Solids*, chapter 2, pages 35–48. John Wiley & Sons, Ltd, 2009. ISBN 9780470447710. doi: 10.1002/9780470447710.ch2. URL <https://onlinelibrary.wiley.com/doi/abs/10.1002/9780470447710.ch2>.
- [154] *DFT Calculations for Surfaces of Solids*, chapter 4, pages 83–112. John Wiley & Sons, Ltd, 2009. ISBN 9780470447710. doi: 10.1002/9780470447710.ch4. URL <https://onlinelibrary.wiley.com/doi/abs/10.1002/9780470447710.ch4>.
- [155] David Alique, David Martinez-Diaz, Raul Sanz, and Jose Calles. Review of supported pd-based membranes preparation by electroless plating for ultra-pure hydrogen production. *Membranes*, 8(1):5, Jan 2018. ISSN 2077-0375. doi: 10.3390/membranes8010005. URL <http://dx.doi.org/10.3390/membranes8010005>.
- [156] Zhenhua Zeng, Juarez Da Silva, Hui-Qiu Deng, and Wei-Xue Li. Density functional

theory study of the energetics, electronic structure, and core-level shifts of no adsorption on the pt(111) surface. *Phys. Rev. B*, 79, 05 2009. doi: 10.1103/PhysRevB.79.205413.

- [157] *What is Density Functional Theory?*, chapter 1, pages 1–33. John Wiley & Sons, Ltd, 2009. ISBN 9780470447710. doi: 10.1002/9780470447710.ch1. URL <https://onlinelibrary.wiley.com/doi/abs/10.1002/9780470447710.ch1>.
- [158] O. M. Løvvik and R. A. Olsen. Density functional calculations of hydrogen adsorption on palladium–silver alloy surfaces. *The Journal of Chemical Physics*, 118(7):3268–3276, 2003. doi: 10.1063/1.1536955. URL <https://doi.org/10.1063/1.1536955>.
- [159] Ekin Ozdogan and Jennifer Wilcox. Investigation of h₂ and h₂s adsorption on niobium- and copper-doped palladium surfaces. *The Journal of Physical Chemistry B*, 114(40):12851–12858, 2010. doi: 10.1021/jp105469c. URL <https://doi.org/10.1021/jp105469c>. PMID: 20845969.
- [160] Jeffrey A. Herron, Scott Tonelli, and Manos Mavrikakis. Atomic and molecular adsorption on pd(111). *Surface Science*, 606(21):1670 – 1679, 2012. ISSN 0039-6028. doi: <https://doi.org/10.1016/j.susc.2012.07.003>. URL <http://www.sciencedirect.com/science/article/pii/S0039602812002245>.
- [161] Preeti Kamakoti, Bryan D. Morreale, Michael V. Ciocco, Bret H. Howard, Richard P. Killmeyer, Anthony V. Cugini, and David S. Sholl. Prediction of hydrogen flux through sulfur-tolerant binary alloy membranes. *Science*, 307(5709):569–573, 2005. ISSN 0036-8075. doi: 10.1126/science.1107041. URL <https://science.scienmag.org/content/307/5709/569>.
- [162] Preeti Kamakoti and David S. Sholl. A comparison of hydrogen diffusivities in

pd and cupd alloys using density functional theory. *Journal of Membrane Science*, 225(1):145 – 154, 2003. ISSN 0376-7388. doi: <https://doi.org/10.1016/j.memsci.2003.07.008>. URL <http://www.sciencedirect.com/science/article/pii/S0376738803003831>.

- [163] Preeti Kamakoti and David S. Sholl. Ab initio lattice-gas modeling of interstitial hydrogen diffusion in cupd alloys. *Phys. Rev. B*, 71:014301, Jan 2005. doi: 10.1103/PhysRevB.71.014301. URL <https://link.aps.org/doi/10.1103/PhysRevB.71.014301>.
- [164] Chandrashekhar G. Sonwane, Jennifer Wilcox, and Yi Hua Ma. Achieving optimum hydrogen permeability in pdag and pdau alloys. *The Journal of Chemical Physics*, 125(18):184714, 2006. doi: 10.1063/1.2387166. URL <https://doi.org/10.1063/1.2387166>.
- [165] Chandrashekhar G. Sonwane, Jennifer Wilcox, and Yi Hua Ma. Solubility of hydrogen in pdag and pdau binary alloys using density functional theory. *The Journal of Physical Chemistry B*, 110(48):24549–24558, 2006. doi: 10.1021/jp064507t. URL <https://doi.org/10.1021/jp064507t>. PMID: 17134214.
- [166] Shucheng Xu, Parveen Sood, M. L. Liu, and Angelo Bongiorno. First-principles study of hydrogen permeation in palladium-gold alloys. *Applied Physics Letters*, 99(18):181901, 2011. doi: 10.1063/1.3656739. URL <https://doi.org/10.1063/1.3656739>.
- [167] Preeti Kamakoti and David Sholl. Towards first principles-based identification of ternary alloys for hydrogen purification membranes. *Journal of Membrane Science - J MEMBRANE SCI*, 279:94–99, 08 2006. doi: 10.1016/j.memsci.2005.11.035.
- [168] Lymarie Semidey-Flecha, Chen Ling, and David S. Sholl. Detailed first-principles

models of hydrogen permeation through pdcu-based ternary alloys. *Journal of Membrane Science*, 362(1):384 – 392, 2010. ISSN 0376-7388. doi: <https://doi.org/10.1016/j.memsci.2010.06.063>. URL <http://www.sciencedirect.com/science/article/pii/S0376738810005302>.

- [169] Chen Ling, Ly Marie Semidey-Flecha, and David S. Sholl. First-principles screening of pdcuag ternary alloys as h₂ purification membranes. *Journal of Membrane Science*, 371(1):189 – 196, 2011. ISSN 0376-7388. doi: <https://doi.org/10.1016/j.memsci.2011.01.030>. URL <http://www.sciencedirect.com/science/article/pii/S0376738811000494>.

Chapter 3

Experimental methods

3.1 Introduction

This chapter provides an overview of the materials, techniques, and methods used in the experimental work performed in this thesis and outlines the procedures used in the following chapters.

3.2 Preparation of gas standards

Gas standards of hydrogen were prepared gravimetrically in 10 litre cylinders (BOC, UK) in accordance with [1] from pure hydrogen (Air Products, UK), nitrogen (Air Products), carbon monoxide (Scott Speciality Gases, UK), methane (CK Gases, UK) and krypton (BOC, UK). Any impurities that were detected in these pure gases were quantified and these values were then incorporated into the final determination of the gas mixture compositions and uncertainties.

The 10 liter cylinder was evacuated to $1 \times 10^{-6} mBar$ using a scroll pump followed by a turbo pump. This pressure ensures that any residual gas within the cylinder will not contribute towards the uncertainty of the final mixture. [1] The target masses of

each impurity desired in the gas mixture was then calculated using equation 3.1 where m_Ω is calculated using equation 3.2

$$m_j = \frac{y_k \times M_k}{\sum_{i=1}^q y_i \times M_i} \times m_\Omega \quad (3.1)$$

$$m_\Omega = \frac{P_{F,\Omega} \times V_{cyl}}{Z_\Omega \times R \times T_F} \sum_{i=1}^q y_i \times M_i \quad (3.2)$$

Where m_j is the concentration of component j in the gas mixture, y is the mass fraction of each component, M is the molecular weight, V is the volume of the vessel, Z is the compressability factor, R is the gas constant, T is the temperature during fill, P is the fill pressure and Ω denotes the final mixture.

After the target masses have been calculated a preparation procedure is selected taking into account the target composition and uncertainty of the calibration gas mixture; the target filling pressure of the calibration gas mixture; the required tolerance for the preparation; the composition of any available parent gas mixture; and the performance specifications of the balance to be used. For this work it was determined that adding impurities using a 10mL loop weighed using a Mettler Toledo model PR2004 top pan balance, and hydrogen through direct fill weighed using a Mettler Toledo Model XP26003L top pan balance was appropriate for all gas mixtures. For loop addition the loop is weighed before and after the addition of the component to the cylinder. The difference is the mass of the component added to the cylinder.

The uncertainty of each mass added to the cylinder is then calculated taking into account the accuracy of the balance including its calibration and linearity, repeatability of the balance readings including errors caused by the location of the cylinder on the balance, buoyancy effects, effects of moisture adsorption and dust on the outer surface of the cylinder, errors due to the loss of material during transfer into the cylinder. Guidance on these uncertainty values, and methods used for calibration can be found in Appendix

3. All weighing procedures required the use of a tare, which is a vessel made of the same material that nominally has the same internal and external volumes. For all sulphur containing samples the internal surfaces of the cylinders were pretreated by heating a mixture of 5% H₂S in CH₄ in order to prevent the added H₂S reacting with the cylinder walls.

For the purpose of this thesis the gas standards that were used to perform the permeation tests will be referred to as gas mixtures, and the gas standards that were used to calibrate the analytical instruments will be referred to as calibration gas standards. Before use, the gas mixtures were verified against traceable primary reference materials using Gas Chromatography with either a pulsed helium discharge ionisation detector (PDHID) for samples not containing sulphur [2, 3], and sulphur chemiluminescence detector (SCD) for sulphur containing samples [4]. The compositions of the non-sulphur, and sulphur containing gas standards created for the purposes of this thesis are shown in tables 3.1 and 3.2.

3.3 Hydrogen sampling

Hydrogen sampling was performed using the sampling procedure developed by Bacquart et al [5]. The H₂ Qualitizer designed by Linde Australia was used and is designed to operate in line when a hydrogen vehicle is being refuelled. The adaptor is effectively a T piece inserted between the refuelling nozzle and the FCEV (Toyota Mirai). A pressure regulator is installed before the connection to the sampling cylinder and set at 18MPa in order to prevent overpressurisation of the vessel.

The H₂ Qualitizer pressure reducer is fixed and tightened onto the sampling cylinder valve using a DIN 477 N.1 connection. The high-pressure hose leading from the sample cylinder is then connected to the pressure reducer and sample taking connections using quick connect fittings. The sample-taking adapter is then connected on to the FCEV

Table 3.1: Gas mixture composition of the non-sulphur sample (Cylinder NG353R) used during impurity tests

Impurity	Concentration ($\mu\text{mol/mol}$)
O ₂	10.06 ± 0.0242
N ₂	10.04 ± 0.378
CH ₄	10.01 ± 0.0096
CO ₂	10 ± 0.0081
CO	9.98 ± 0.0085
H ₂	Balance

Table 3.2: Gas mixture composition of the sulphur sample (Cylinder 2380) used during impurity tests

Impurity	Concentration ($\mu\text{mol/mol}$)
Kr	1.1 ± 0.0108
H ₂ S	0.41 ± 0.0015
OCS	0.42 ± 0.0013
CS ₂	0.362 ± 0.0012
t-BuSH	0.391 ± 0.0011
THT	0.409 ± 0.0011
H ₂	Balance

receptacle. The system is then purged and is considered ready for sampling.

A number of safety measures are in place when performing this procedure. The sampling bottle is secured using a safety belt at the HRS location and at the suitable distance to perform the sampling. An earthing cable and anti-whip device needs to be connected to both the pressure regulator and sample taking adapter to ensure safe operation.

3.4 Membrane preparation

3.4.1 Support fabrication

The YSZ 3% hollow fibre substrates with a sponge like microstructure were fabricated by an induced phase-inversion process, followed by high temperature sintering. A uniform ceramic suspension, with 60 wt.% solid loading YSZ 3% powder (1 μ m, VWR), was prepared by ball milling. After degassing, the ceramic suspension was transferred into 200 mL stainless steel syringes and extruded through a tube-in-orifice spinneret (outer diameter 3 mm, inner diameter 1.2 mm) into a coagulation bath with no air gap. An extrusion rate of 7 and 5 mL min⁻¹ was adopted for ceramic suspension and bore fluid (15 wt.% 1,4-dioxane in n-hexane) respectively. The formed precursor fibres were kept in deionized water for a minimum of 12 h, in order to remove the excess solvent. After being gently washed with deionized water, the precursor fibres were dried at room temperature and sintered at 1400°C in a tubular furnace (Elite, Model TSH 17/75/450).

3.4.2 Membrane deposition

Electroless Plating

Palladium silver, copper, gold, and ternary alloy compositions (expect for PdCuZr) were deposited onto the surface of the porous YSZ substrate through electroless plating. The process was performed in the two step activation-plating process discussed in section 2.5.2. Palladium was used due to its high electro positivity compared to other metals commonly plated through electroless deposition.

Prior to deposition, the outer surface of the fibre was cleaned by sequential washings with a 1:1 mixture of ethanol and water for 10 min in an ultrasonic bath, and were then dried overnight at 120°C. The substrates were then coated at one end with a gas tight glaze and sintered at 900°C for 1 hour. The outer surfaces of the fibres were cleaned by

Table 3.3: Compositions used for activation of YSZ substrate prior to palladium deposition

Compound	Concentration (g/L)			
	Sensitisation	Washing	Activation	Acid Washing
SnCl ₂	1	-	-	-
PdCl ₂	-	-	0.1	-
HCl	1	-	1	0.01

sequential washings with a 1:1 mixture of ethanol and water for 10 min in an ultrasonic bath, and were then dried overnight at 120 °C.

The substrates were then activated with Pd nuclei via sensitisation in an acidic SnCl₂ solution, followed by activation in an acidic PdCl₂ solution. The sensitisation/activation process was carried out by immersing the glazed hollow fibre substrates sequentially in five chemical baths, i.e. acidic SnCl₂ solution for 5 min; deionised water for 5 min, acidic PdCl₂ solution for 5 min; 0.01 M HCl solution for 2 min; and finally deionised water for 3 mins. All chemical baths were homogenised using compressed air. The sensitisation/activation process was repeated for 8 cycles. The composition of each bath is shown in Table 3.3.

The substrates were then immersed in a Pd electroless plating (ELP) solution, at 60°C, in order to deposit metallic Pd layers onto the activated surface. The Pd ELP solution was prepared according to the composition presented in Table 3.4 taken from [6] for Pd, [7] for Ag, [8] and left to stabilize for 1 h in an ultrasonic bath prior to use. The volume of Pd ELP solution was fixed at 4 mL per cm₂ of substrate surface area. The electroless plating procedure was performed twice, with a total plating time of 60 mins.

After the palladium coating the membranes were then subjected to one, or multiple, other plating steps of silver, gold, or copper. The plating time for silver was 30 minutes for one cycle and the volume of plating solution to substrate was the same as the

Table 3.4: Compositions used for preparation of palladium based membranes on YSZ substrate through electroless plating and immersion plating

Compound	Deposited metal			
	Pd	Ag	Cu	Au
Metal Source (g/L)				
PdCl ₂	4	-	-	-
AgNO ₃	-	3.4	-	-
CuSO ₄	-	-	10	-
AuCl ₃	-	-	-	0.1
Stabilising agent				
NH ₃ -H ₂ O (mL/L)	198	200	-	-
NaOH (g/L)	-	-	8.63	1
Complexing Agent (g/L)				
Na ₂ EDTA-2H ₂ O	40	35	-	-
Persulfate	-	-	30	-
Reducing agent (mL/L)				
N ₂ H ₄	5.6	4.2	-	-
Formaldehyde	-	-	14	-

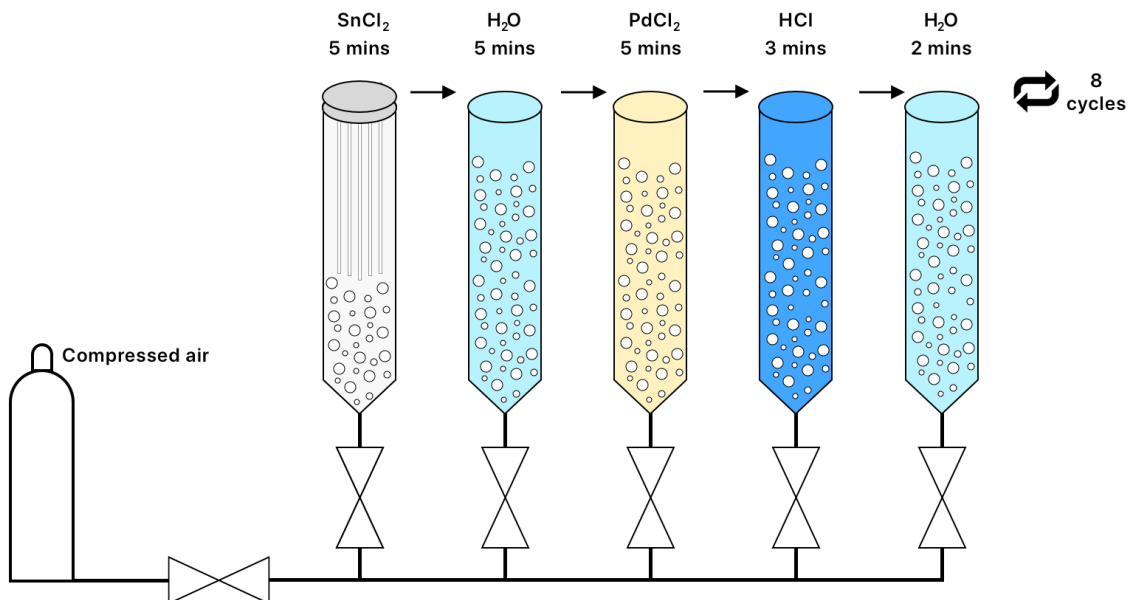


Figure 3.1: Schematic representation of the sequential baths for sensitisation/activation process.

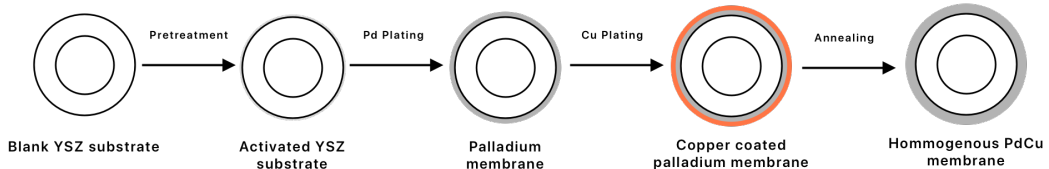


Figure 3.2: Example of ELP procedure when manufacturing a PdCu membrane on YSZ substrate

palladium steps.

It should be noted that the deposition of gold is through immersion plating rather than electroless plating. [9] Immersion plating is the process of applying adhering layers of noble metals to another metal's surface by dipping the material in a heated nobler metal solution ion to produce a replacement reaction. This causes the deposition of a metallic coating on a base metal from solutions that contain coating metal. One metal is typically displaced by metal ions that have lower levels of oxidation potential, relative to the metal ion being displaced. The plating time for gold was 3 hours and the volume of plating solution to substrate was $4\text{mL}/\text{cm}^3$.

The resulting composite membranes consisting of multiple metal layers stacked were then heat treated at 500°C under an environment containing 25% H_2 in Ar balance for 24 hours in order to alloy the layers into a homogenous membrane and reduce any oxides that were present on the surface.

Magnetron Sputtering

Membranes were deposited using a closed field unbalanced magnetron sputter ion plating system produced by Teer Coatings Ltd. The thin film membranes were deposited onto the YSZ 3% hollow fibres by mounting them vertically inside the sputtering system. The system was then evacuated to 1×10^{-6} mBar and subjected to an ion cleaning process with Ar plasma prior to sputtering. Pd, Cu, and Zr targets (99.9% purity) were used

Table 3.5: Conditions used during magnetron sputtering of palladium membranes on YSZ tubular substrate

Alloy	Target current (A)		
	Pd	Cu	Zr
PdCuZr	1.25	0.65	0.4
PdCu (fcc)	1.25	0.8	-
PdCu (bcc)	1.2	1.0	-

to sputter the chosen alloy composition onto the membranes at the target currents shown in. A bias voltage of 50 V was applied to the magnetron during deposition runs. Samples were deposited using pulsed DC, with a constant target to substrate distance and a sample rotation speed of 16 rpm. An Ar flux of 25 (SCC/m) was used during deposition. PdCu membranes in both BCC and FCC phase were manufactured through magnetron sputtering along with PdCuZr ternary alloys.

3.4.3 Materials testing

The thickness of the plated layers was characterised by first using a Focused Ion Beam (FIB) to mill through a section of the hollow fibre to provide a flat, cross sectional surface for analysis. The thickness of the metal later was then measured using high resolution Scanning Electron Microscopy (SEM) and composition analysed using Energy Dispersive x-ray Spectrometry (EDS) on the same sample.

The surface composition of the membrane was further characterised using X-ray Photoelectron Spectroscopy to provide a more accurate compositional analysis for the top 10 nm of the membrane, the depth which is most relevant for catalytic dissociation of hydrogen and adsorption of impurities.

Prior to the H₂ permeation tests, the integrity of the hollow fibre membranes was evaluated by testing the gas-tightness of the membrane under N₂ atmosphere, up to 10 bar and room temperature and using a gas-tightness apparatus developed in house. [6]

3.5 Membrane Characterization

3.5.1 Membrane testing rig

After the membranes were ensured to be gas tight, hydrogen permeation measurements were performed using the experimental apparatus shown in Figure 1. The palladium alloy composite hollow fibre membranes were sealed on to a stainless steel $\frac{1}{4}$ " NPT fitting. The membrane was then placed in a Sulfinert®-treated sample vessel (Thames Restek, UK) with nominal volume of 300 cm^3 . The vessel was then heated using heavy insulated heating tape (OMEGA STH051-020). The heating was controlled using the temperature of the membrane using a PID temperature controller (OMRON). The feed was supplied from a cylinder either containing BIP+ hydrogen (Air Products) for pure hydrogen permeability tests or one of two gravimetrically prepared gas mixtures for impurity testing shown in tables 3.1 and 3.2. Prior to introducing gas to the membrane the system was evacuated down to $1 \times 10^{-6}\text{ mbar}$. The pressure on the retentate side of the membrane is controlled using a tamper proof pressure reducer. The set-up is shown in figure 3.3. After tests the system was vented and purged 7 times with N_2 to ensure an explosive atmosphere could not build up within the equipment.

The flux and permeability of the membrane were automatically calculated using software developed in house. Each membrane sample was made using the same batch of substrate and cut to the same length prior to testing. The permeability (P) of a dense metal membrane is given by Eqn 3.3 [10] and is a function of the hydrogen flux through the membrane (J), the concentration and pressure gradient across the membrane ($P_{ret}^{0.5} - P_{perm}^{0.5}$), and the thickness of the metallic membrane (l).

$$P = \frac{Jl}{P_{ret}^{0.5} - P_{perm}^{0.5}} \quad (3.3)$$

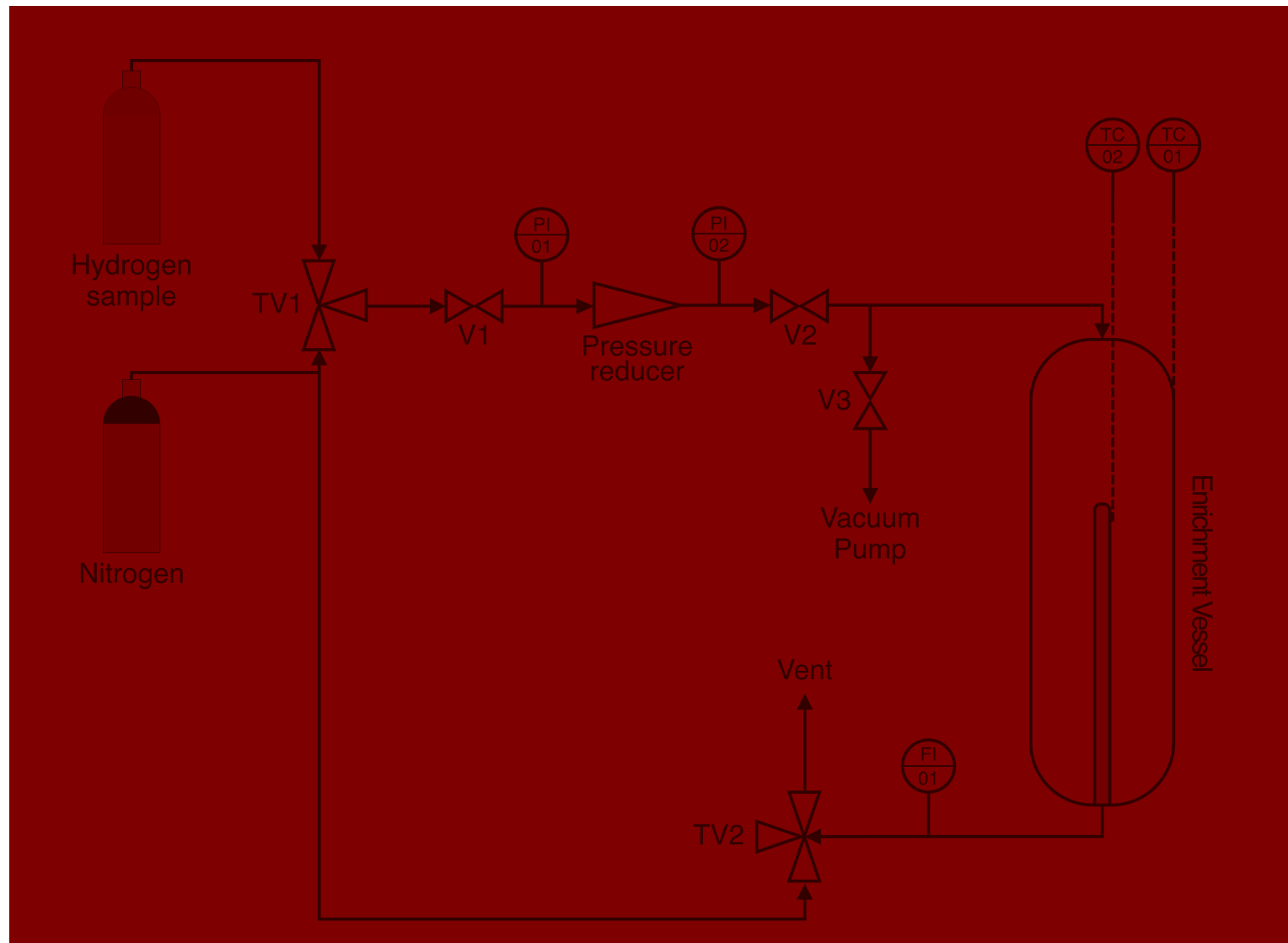


Figure 3.3: Experimental set up used during hydrogen permeation and enrichment experiments, TC: Temperature controller, PI: Pressure indicator, V: Valve, TV: Three-way valve, FI: Flow indicator.

3.6 Hydrogen impurity enrichment

A hydrogen impurity enrichment device was designed and tested, more details on this will be discussed in chapter 6. This section will describe the methodology and testing procedure for the hydrogen impurity enrichment device.

Hydrogen impurity enrichment tests were performed on synthetic samples created using the procedure described in section 3.2 and using a sample taken from a hydrogen refuelling station. Regardless of source all samples were tested using a PDHID in order to calculate it's oxygen level for safety reasons. Since only hydrogen can leave the HIED in normal testing conditions, if not checked the concentration of oxygen could rise above a safe level and create an explosive mixture. For the purpose of these tests the enrichment factor was capped at a value that would ensure the oxygen level in the mixture would not surpass 1%.

The enrichment factor was calculated using both non-ideal gas law (equation ??), and tracer enrichment (equation ??) methods. This was to ensure any leaks in the device could be detected using non-ideal gas law method, while having a low uncertainty on the final value from the tracer enrichment method. Gas composition testing was performed using the same GC procedures discussed in section 3.2

3.6.1 Krypton spiking

In order to perform enrichment using the tracer enrichment method a certain quantity of inert gas, not normally present within a hydrogen sample, must be included in the gas. Krypton was used in this study. For synthetic samples this can be added using loop addition along with other impurities using the procedure in section 3.2. When taking a sample directly from a hydrogen refuelling station, as would have to be done in real sampling, this approach is not effective as the tracer gas cannot be added to an already pressurised container. The krypton must first be added to the evacuated sampling vessel

through loop addition.

Since sampling from a hydrogen refuelling station is dependent on a number of variables, it is difficult to determine the final pressure of the sample. Therefore, a fixed quantity of krypton gas was added to the cylinders. For the purpose of this thesis, since 10L cylinders were used for the purpose of hydrogen sampling, 0.3g of Kr was added through loop addition as this is enough to ensure at a max fill pressure of 100 bar there would be atleast 70 $\mu\text{mol/mol}$, which is well within the range of the GC-PDHID detector, and available gas standards for validation.

3.6.2 Performing enrichment

The protocol for performing hydrogen impurity enrichment is similar to hydrogen permeation tests. After evacuation the gas is introduced to a vessel containing the chosen palladium membrane composition at a set enrichment pressure and the vessel heated to 300°C to begin enrichment. The pressure of the enrichment vessel and sample cylinder were both monitored and their values used to calculate the enrichment factor in real time using equations 2.18 and 2.20.

Once the desired enrichment factor was achieved the heater was switched off and the enrichment vessel isolated. The enrichment vessel was then brought to the desired GC detector and tested in the GC-PDHID as described in section 3.2 in order to determine the krypton composition against the original sample, and gas standards. This krypton concentration is used to calculate the tracer enrichment factor. The concentration of other impurities in the enriched sample can then be quantified by testing the enriched sample against a gas standard containing the target impurity, and it's original composition calculated using this value in conjunction with the tracer enrichment factor.

The uncertainty for both non-ideal gas law, and tracer enrichment factor, and their effect on the final composition calculated using these methods. For non-ideal gas law

method the sources for uncertainty arise from errors associated with the sensors monitoring process variables, namely temperature and pressures, in addition to the uncertainty with the method used to correct for non-ideal gas behaviour, and the uncertainty associated with the gas analysis equipment used to determine the composition of both the enriched, and unenriched samples. For tracer enrichment the only source of uncertainty is from the gas analysis equipment used to determine the composition of the enriched and unenriched gas. Values for these errors can be found in the Appendix.

3.7 Density functional theory

All DFT calculations were performed using the Quantum Espresso (QE) [11, 12, 13] ab initio simulation package using the generalized gradient approximation with the PW91 functional to describe electron-correlation effects. Ion-electron interactions were described using ultra-soft pseudopotentials. A plane-wave expansion with a cut-off energy of 233.73 eV was used in all calculations. Geometry relaxations were performed with a conjugate gradient method until the forces on all unconstrained atoms were less than 0.03 eV/A. A Monkhorst Pack mesh with 5x5x5 k-points was used for all calculations as this was determined to be adequate for achieving convergence from literature in table 2.7 and backed up by initial testing on a Pd system as shown in figure 3.4.

Python with scikit learn, pandas, numpy, and matplotlib packages were used for scripting, data collection and analysis. Sample files can be found in Appendix 3.

3.7.1 ISO 14687 Impurities and Hydrogen

ISO 14687 impurities were simulated using the above parameters and their structure relaxed until convergence was achieved. The resulting structure was then cross checked using bond lengths from literature to ensure the resulting molecule was an accurate representation.

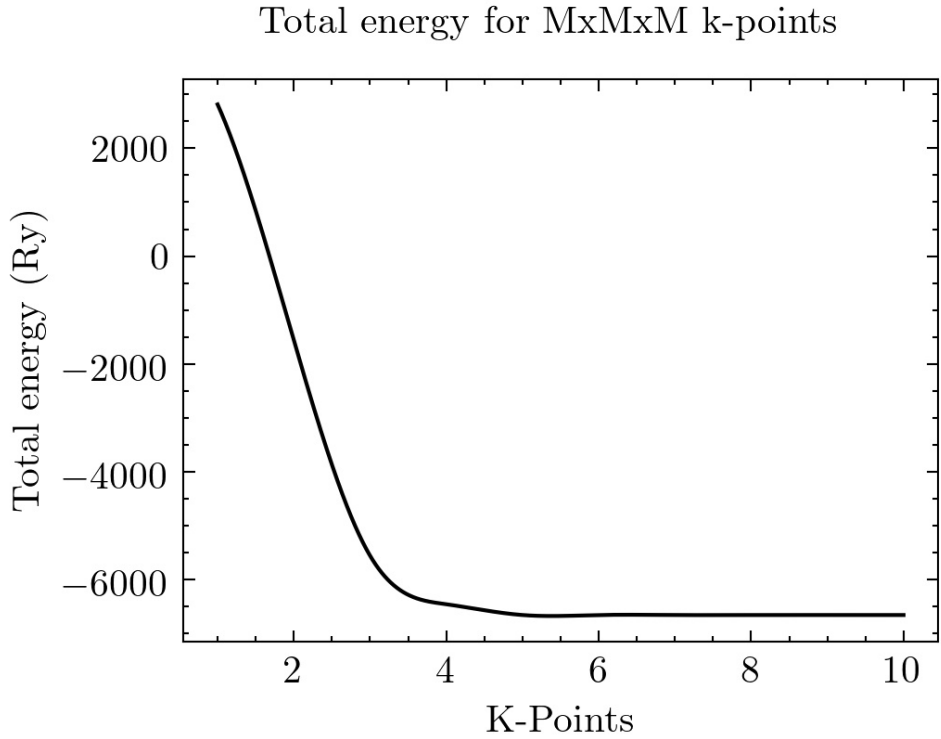


Figure 3.4: Total energy as a function of $M \times M \times M$ k-points across a Pd(111) fcc slab

3.7.2 Palladium and Palladium alloy slab models

The structure of bulk palladium was first created using a lattice parameter of 3.859\AA as reported by D. Wheeler [14]. Initially the pure palladium slab model used to represent the periodic supercell was created using this palladium primitive unit cell cleaved using the miller indices $(h, k, l) = (111)$ which is adequate in describing the surface of a palladium membrane. A 2×2 slab was created in order to ensure minimal in-plane interactions between neighbouring molecules adsorbed onto the surface in the periodic simulations. The slab was extended to 5 atom thickness which is adequate to describe the surface of Pd(111) and a 20\AA vacuum layer was placed on top. The resulting supercell consisted of 20 atoms.

When creating palladium alloy systems it was assumed that alloys adopt a substitutional, random fcc structure. Metal atoms were randomly distributed among the fcc

lattice in the supercell. All atoms were allowed to relax during the calculation, with the volume of the super cell fixed.

Quantum ATK Virtual NanoLab Builder [15] was used to generate these structures and export to QE input files. Each metal composition was simulated with three random distributions of substituted metal. For each alloy, geometry optimization was performed to get the lattice constant and total energy of each alloy prior to adsorption of gaseous molecules.

Adsorption energy

In order to find the adsorption energy of each ISO 14687 impurity on the membrane surfaces the molecules simulated in section 3.7.1 were inserted into the vacuum region of the slab models generated in section 3.7.2. (111) fcc surfaces have 4 available sites for adsorption shown in figure 2.8 A separate system was created for adsorption of each impurity onto each of these sites. Initially the adsorbed molecule was simulated using a rigid constraint to prevent any changes to the impurities molecular structure, and a low cutoff energy in order to get a quick starting point for the basis of the full simulation. Final goemtry relaxation was then performed from this using the parameters described in section 3.7

The adsorption energy, $E_{i_{ads}}$, for the adsorption of a gaseous impurity on the surface is then calculated using equation 2.27 where i is the target ISO 14687 impurity or hydrogen molecule.

References

- [1] International Standards Organisation. ISO/TC 158 Analysis of gases, 2015.
- [2] Thomas Bacquart and Arul Murugan. Desk instruction 34: Methods for performing analysis of impurities in hydrogen. *National Physical Laboratory: Chemical, Medical and Environmental Science Department*, 2019.
- [3] Abigail S Morris and Thomas Bacquart. Desk instruction 34a: Methods for analysing ar, o₂ and n₂ in hydrogen using gc-pdhid. *National Physical Laboratory: Chemical, Medical and Environmental Science Department*, 2019.
- [4] Thomas S Bacquart and Arul Murugan. Desk instruction 34c: Methods for performing total sulphur analysis (total sulphur or h₂s) in hydrogen using gc-scd. *National Physical Laboratory: Chemical, Medical and Environmental Science Department*, 2019.
- [5] Thomas Bacquart, Niamh Moore, Nick Hart, Abigail Morris, Thor A. Aarhaug, Ole Kjos, Fabien Aupretre, Thibault Colas, Frederique Haloua, Bruno Gozlan, and Arul Murugan. Hydrogen quality sampling at the hydrogen refuelling station – lessons learnt on sampling at the production and at the nozzle. *International Journal of Hydrogen Energy*, 45(8):5565 – 5576, 2020. ISSN 0360-3199. doi: <https://doi.org/10.1016/j.ijhydene.2019.10.178>. URL <http://www.sciencedirect.com/science/article/pii/S0360319919340510>. 22nd World Hydrogen Energy Conference.

- [6] Ana Gouveia Gil, Miria Hespanhol M Reis, David Chadwick, Zhentao Wu, and K Li. A highly permeable hollow fibre substrate for Pd/Al₂O₃ composite membranes in hydrogen permeation. *International Journal of Hydrogen Energy*, 40(8):3249–3258, 2015. ISSN 0360-3199. doi: <https://doi.org/10.1016/j.ijhydene.2015.01.021>. URL <http://www.sciencedirect.com/science/article/pii/S0360319915000580>.
- [7] Fernando Braun, Ana M Tarditi, James B Miller, and Laura M Cornaglia. Pd-based binary and ternary alloy membranes: Morphological and perm-selective characterization in the presence of H₂S. *Journal of Membrane Science*, 450:299–307, 2014. doi: 10.1016/j.memsci.2013.09.026.
- [8] Natalie Pomerantz and Ma Yi Hua. Effect of H₂S on the performance and long-term stability of Pd/Cu membranes. *Industrial and Engineering Chemistry Research*, 48(8):4030–4039, 2009. ISSN 08885885. doi: 10.1021/ie801947a.
- [9] M.a. Rabiatul Adawiyah, O. Saliza Azlina, Nor Akmal Fadil, Siti Rabiatull Aisha, and M.a Azmah Hanim. Electroless and immersion plating process towards structures and imc formation. *International Journal of Engineering and Technology*, 8(6):2558–2570, 2016. doi: 10.21817/ijet/2016/v8i6/160806210.
- [10] Tina M Nenoff Nathan W. Ockwig. Membranes for Hydrogen Separation. *Chemical Reviews*, 107:4078–4110, 2007.
- [11] Paolo Giannozzi, Stefano Baroni, Nicola Bonini, Matteo Calandra, Roberto Car, Carlo Cavazzoni, Davide Ceresoli, Guido L Chiarotti, Matteo Cococcioni, Ismaila Dabo, Andrea Dal Corso, Stefano de Gironcoli, Stefano Fabris, Guido Fratesi, Ralph Gebauer, Uwe Gerstmann, Christos Gougaoussis, Anton Kokalj, Michele Lazzeri, Layla Martin-Samos, Nicola Marzari, Francesco Mauri, Riccardo Mazzarello, Stefano Paolini, Alfredo Pasquarello, Lorenzo Paulatto, Carlo Sbraccia, Sandro Scandolo, Gabriele Sclauzero, Ari P Seitsonen, Alexander Smogunov, Paolo Umari, and

- Renata M Wentzcovitch. Quantum espresso: a modular and open-source software project for quantum simulations of materials. *Journal of Physics: Condensed Matter*, 21(39):395502 (19pp), 2009. URL <http://www.quantum-espresso.org>.
- [12] P Giannozzi, O Andreussi, T Brumme, O Bunau, M Buongiorno Nardelli, M Calandra, R Car, C Cavazzoni, D Ceresoli, M Cococcioni, N Colonna, I Carnimeo, A Dal Corso, S de Gironcoli, P Delugas, R A DiStasio Jr, A Ferretti, A Floris, G Fratesi, G Fugallo, R Gebauer, U Gerstmann, F Giustino, T Gorni, J Jia, M Kawamura, H-Y Ko, A Kokalj, E Küçükbenli, M Lazzeri, M Marsili, N Marzari, F Mauri, N L Nguyen, H-V Nguyen, A Otero de-la Roza, L Paulatto, S Poncé, D Rocca, R Sabatini, B Santra, M Schlipf, A P Seitsonen, A Smogunov, I Timrov, T Thonhauser, P Umari, N Vast, X Wu, and S Baroni. Advanced capabilities for materials modelling with quantum espresso. *Journal of Physics: Condensed Matter*, 29(46):465901, 2017. URL <http://stacks.iop.org/0953-8984/29/i=46/a=465901>.
- [13] Paolo Giannozzi, Oscar Baseggio, Pietro Bonfà, Davide Brunato, Roberto Car, Ivan Carnimeo, Carlo Cavazzoni, Stefano de Gironcoli, Pietro Delugas, Fabrizio Ferrari Ruffino, Andrea Ferretti, Nicola Marzari, Iurii Timrov, Andrea Urru, and Stefano Baroni. Quantum espresso toward the exascale. *The Journal of Chemical Physics*, 152(15):154105, 2020. doi: 10.1063/5.0005082. URL <https://doi.org/10.1063/5.0005082>.
- [14] Wheeler P. Davey. Precision measurements of the lattice constants of twelve common metals. *Phys. Rev.*, 25:753–761, Jun 1925. doi: 10.1103/PhysRev.25.753. URL <https://link.aps.org/doi/10.1103/PhysRev.25.753>.
- [15] Inc Synopsys. Quantumatk. *Atomic-Scale Modeling for Semiconductor & Materials Research*. URL <https://www.synopsys.com/silicon/quantumatk.html>.

Chapter 4

Density functional theory as a screening method for dense metal membranes

Abstract

In this chapter 18 different palladium based membrane materials were simulated in order to determine their suitability as a material for hydrogen impurity enrichment. The alloys were represented using $2 \times 2 \times 5$ atomic slab models comprised of palladium, with varying compositions of different metals including common palladium additives (Au, Ag, Cu), and metals known for their resistance against aggressive environments (Zr, Cu). From the alloy compositions tested 16/18 were stable, with Cr containing alloys unable to form a stable system. The 16 remaining alloys were then tested with hydrogen, and each of the ISO 14687-2 impurities adsorbed on the 4 available surface sites for hydrogen adsorption. The results were that the impurities could be split into four broad groups. Inert impurities included NH₃, CO₂, N₂, He, Ar and formic acid, which did not interact with the surface of the alloys. Oxidising impurities included

H_2O and O_2 , which pure palladium alone was completely resistant against. The effect could be amplified through the addition of Au and Ag, with PdAu_{20} being the best performing alloy for resisting these impurities. Carbonaceous impurities included CO and CH_4 where PdAu_{20} was again the best performing alloy, with an average binding energy of CO and CH_4 of around $\times 0.4$ and $\times 0.5$ compared to binding of H. Finally sulphurous atmospheres were tested using H_2S where PdCuZr and PdAuZr alloys were the best performing. These alloys showed an average binding energy of $\times 0.52$ and $\times 0.49$ compared to H. Formaldehyde was a special case where no alloy composition was found to resist binding.

This study shows that DFT can be used to give an indication on the suitability of a palladium alloy membrane for it's desired purpose. It also shows that while the effects of some impurities on the surface of a palladium alloy membrane can be completely mitigated, many cannot be inhibited completely. A number of alloys were identified as the best options for hydrogen impurity detection and will be studied experimentally in the following chapters.

4.1 Introduction

Metal membranes operate by selectively dissociating hydrogen, which then allows the hydrogen atoms to subsequently permeate through the bulk of the separation layer. The problem in using palladium membranes as a material for performing hydrogen impurity enrichment is that many hydrogen impurities are also capable of adsorbing onto, and interacting with palladium membranes. The impact of this adsorption can vary depending the molecule, Carbon monoxide for example will simply adsorb onto the surface and result in competitive adsorption between the hydrogen and impurity. Sulphur containing impurities present more of a problem since they can potentially react with many metals used for hydrogen separation membranes. The impact of these contaminants

can be minimized by designing alloy compositions that have a weaker attraction to the membrane, and therefore will have less of an affect at higher temperatures where these membranes operate.

Physically testing each potential membrane composition would be time consuming and costly due to the high price of palladium, the time required to synthesise specific membrane compositions, and performing the tests. Simulations provide a solution to this, allowing potential alloys to be quickly screened for their interaction strength with each individual ISO 14687-2 impurity, avoiding the costly and time consuming process of manufacturing each alloy composition.

In this chapter, 18 dense metal alloy membranes will be simulated using DFT density functional theory as described in section 3.7 [1, 2, 3]. The metals will first be evaluated in terms their ability to form a stable alloy, with low risk of segregation, or failure. All stable metals will then be simulated with either hydrogen, or an ISO 14687-2 impurity on the surface, and it's binding energy calculated. The results will be evaluated using the ratio of binding energy of adsorbent to binding energy of hydrogen (σ) on the same metal as shown in equation 4.1 where E_{ads} is the binding energy, i is the simulated impurity on the surface of the metal alloy, and H is hydrogen.

$$\sigma = E_{i_{ads}} / E_{H_{ads}} \quad (4.1)$$

The metallic compositions with the lowest value for σ represent the best simulated material for dealing with that impurity. A high value of σ indicates that the metal is more reactive with the impurity molecule, whereas a σ value of 1 or lower indicates that the ability for the impurity to adsorb on the surface is equal to, or lower than that of hydrogen, and therefore has a weaker interaction.

4.2 Results and discussion

4.2.1 Stability of palladium alloy compositions and ISO 14687-2 impurities

In order to perform the simulations, first an appropriate slab model of each alloy must be created. The structure of these slabs is shown in section 3.7.2 and is simulated as (111) face fcc palladium. The metals chosen to substitute into the palladium lattice were common palladium alloys (Au, Cu, and Ag) and metals which have previously shown a resistance to sulphur. Zr[4] and Cr[5] are commonly used additives in steel to improve it's corrosion resistance in acidic environments and were decided to be ideal candidates. Once simulated the total energy of the system was compared to the sum of the energy levels of the component atoms. The results of this analysis are shown in table 4.1. All alloys were stable except for the Cr containing alloys which could not converge to a suitable solution.

Similarly each ISO 14687-2 impurity was simulated and the results of these can be found in table 4.2. The parameters used to simulate these molecules can be found in the appendix.

Table 4.1: Simulated total energy values of alloy slabs

Alloy/Metal Composition	Total Energy (ry)
Pd	-6653.38
PdAg ₂₃	-6774.37
PdAu ₁₀	-7545.53
PdAu ₂₀	-8437.613
Pd ₆₀ Cu ₄₀	-5703.15
Pd ₈₀ Cu ₂₀	-6178.29
Pd ₇₀ Au ₂₀ Zr ₁₀	-8389.61
Pd ₇₀ Cu ₂₀ Zr ₁₀	-6130.29
Pd ₇₀ Ag ₁₀ Zr ₂₀	-6605.75
PdZr ₁₀	-6605.45
PdZr ₂₀	-6557.46
Pd ₇₀ Au ₂₀ Ag ₁₀	-8485.99
Pd ₇₀ Au ₂₀ Cu ₁₀	-8200.05
Pd ₇₀ Cu ₂₀ Ag ₁₀	-6226.71
PdCr ₁₀	-
PdCr ₂₀	-

Table 4.2: Simulated total energy values of ISO 14687-2 impurities

Gas	Total Energy (kJ × 10 ⁻²¹)
H (Atomic)	-2.01
N ₂	-123.91
O ₂	-180.86
CO	-130.93
CO ₂	-221.95
NH ₃	-1933.22
Ar	-208.10
CH ₄	-50.73
Formaldehyde	-136.13
Formic Acid	-227.08
H ₂ S	-150.36
He	-12.62
H ₂ O	-95.99

4.2.2 Hydrogen and Impurity adsorption on palladium alloy membranes

Hydrogen

The binding energy of atomic hydrogen on the surface of palladium is a key value for the purpose of this study. The affinity for a palladium alloy to adsorb on the surface is the initial step for hydrogen permeation, and below a certain thickness becomes the rate limiting step. As expected all alloys had an affinity for hydrogen binding and these values matched what is generally found in literature. These values will be compared to the binding energies of other impurities on the alloys in order to determine their resistance to the impurity. The binding energies of hydrogen on a the Pd slab system is shown in figure 4.1. In a Pd system hydrogen preferentially adsorbs on the FCC and top sites at relativley even energies. At both of these sites hydrogen is able to form a stable system without being affected by other forces. HCP and TOP sites have a lower preference for hydrogen binding and this is likely due to the influence of competition by neighbouring sites which can provide higher stability. The average binding energies of hydrogen on the surface of all palladium alloy slab systems are shown in figure 4.2.

All alloys show a decreased preference towards hydrogen binding compared to pure palladium. This is due to hydrogen adsorption energies being closely related to the catalytic activity for hydrogen dissociation of the individual metal elements. The effect appears to be less prevalent for binary alloys with elements with a larger atomic size such as silver which is likely due to the larger atomic size creating a larger area for hydrogen to adsorb within fcc site of the crystalline lattice, which is one of the preferential sites for H adsorption. Zr and Au do not follow this trend however which indicates that the catalytic activity is affected more by electronic interactions than surface geometry. In all cases reduction in palladium from the surface results in lower catalytic activity for hydrogen adsorption which is also likely to be due to the average reduction in number

Hydrogen adsorption sites on Pd

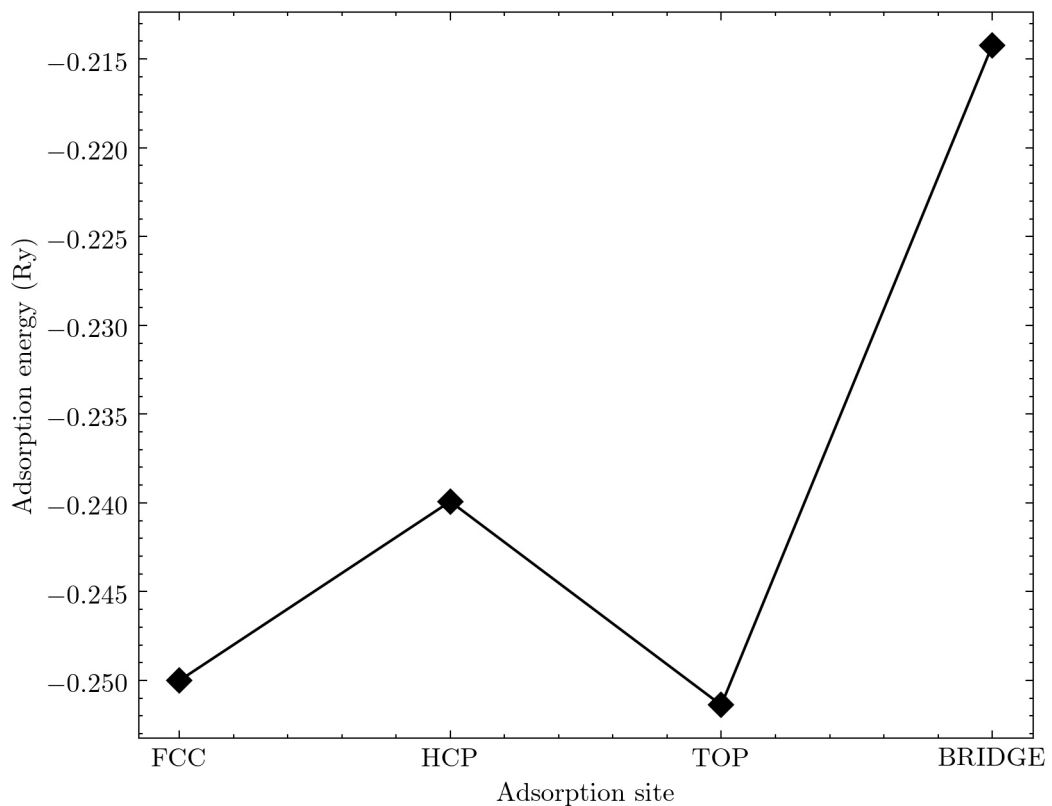


Figure 4.1: Adsorption energy of H for each site on a 2x2x5 Pd slab

Table 4.3: Correlation coefficient of Ag, Au, Cu, Zr addition to Pd with binding energy of H

Metal	Correlation coefficient
Ag	-0.024666
Au	0.259205
Cu	0.019221
Zr	0.347930

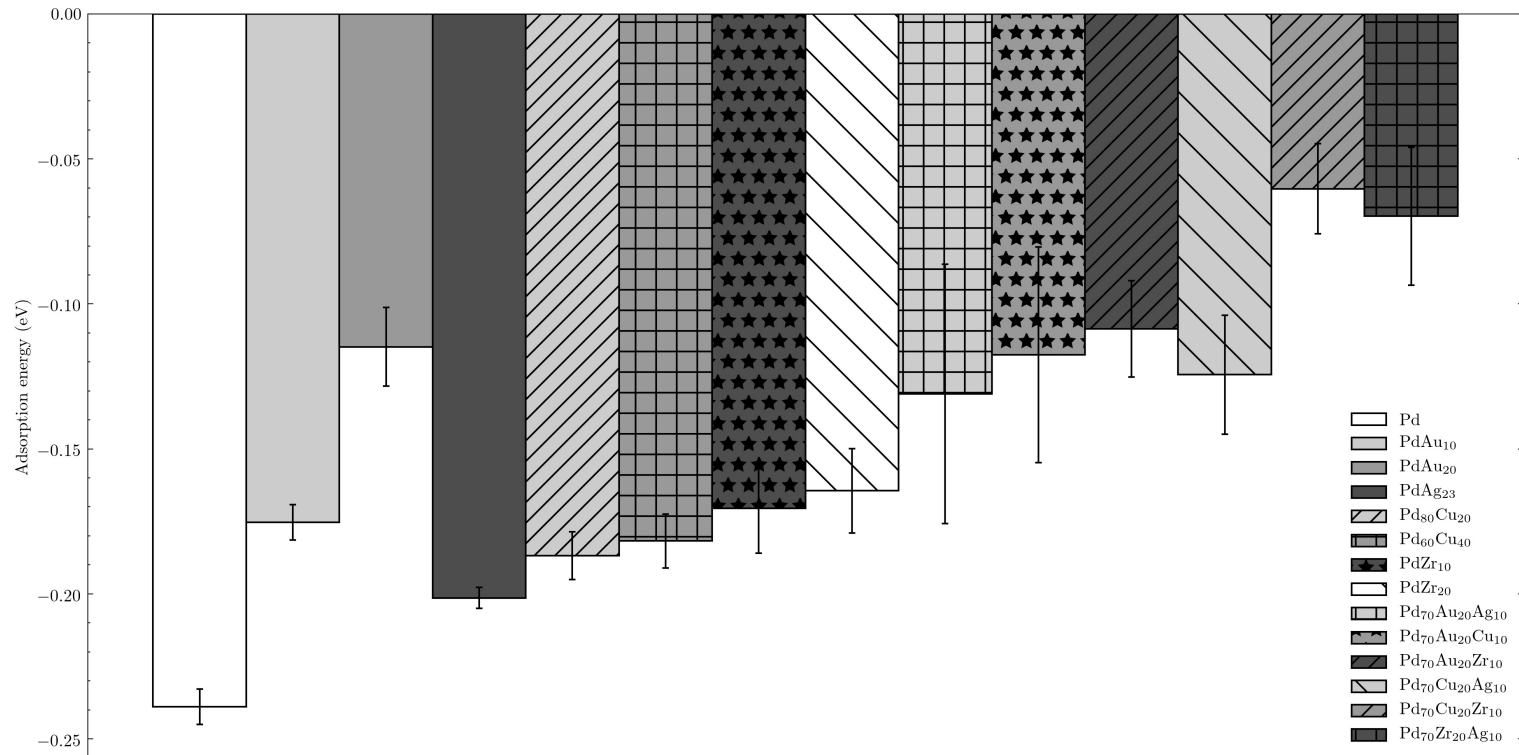
of top sites available for adsorption, which other than FCC is one of the preferential adsorption sites.

The ternary alloys with the highest catalytic activity were PdAuAg and PdCuAg which previous experimental results showing that these alloys have higher permeability than other ternary alloys. All Zr containing alloys had lower catalytic activity showing that for hydrogen permeation Zr has the greatest inhibiting effect. The detrimental effects of Zr to the catalytic activity can be lowered by the addition of Au, Ag, or Cu however all are still lower than binary alloys.

The correlation coefficient for the presence of each metal and it's effect on the resulting adsorption energy was calculated and is shown in table 4.3. It shows that the resulting inhibiting effect of each element follows the order Ag<Cu<Au<Zr.

This binding energy of hydrogen is an important benchmark for the following tests and will be compared to the resulting binding energies for other impurities. If these impurities show a lower binding energy value when compared to hydrogen then they will be preferentially adsorbed and less suitable for use for that type of impurity. It also reveals that the composition of the membrane can largely effect the catalytic activity for dissociation of hydrogen in itself. As membranes become thinner this will result in a shift of the limiting step to catalytic activity and therefore this value must also be optimised to ensure the highest flux can be achieved, however such work is outside the scope of this study.

Hydrogen adsorption

Figure 4.2: Average binding energy of H₂ on the surface of palladium and palladium alloy slabs

Helium, Nitrogen, Carbon Dioxide and Argon

Helium, Nitrogen, Argon, and CO₂ all represent the inert components in fuel cell hydrogen which do not interact with the electrocatalyst and are therefore also likely to be inert to palladium membranes. The binding energies of these molecules on the surface of all the simulated palladium alloy slab systems are shown in figures 4.3 (He), 4.4 (N₂), 4.5 (CO₂) and 4.6 (Ar). All these systems showed a positive binding energy meaning that no competitive adsorption will take place between these gases and hydrogen for the surface adsorption sites.

Carbon Monoxide

CO adsorption was performed by adsorbing the gaseous molecule by the C atom as is normal for CO binding on metallic surfaces [6]. All systems showed binding preference towards CO. The results of the simulations and their binding energies compared to that of hydrogen on the same alloy are shown in figure 4.8. No alloys showed an aversion to CO binding therefore all of the simulated alloys, regardless of their preference to H₂, will likely experience some competitive adsorption and therefore inhibition when CO is present.

The pure Pd system showed a clear preference to CO binding over hydrogen, this matches previous experiments performed to investigate this. [7] Figure 4.7 shows the binding energy on each site compared to that of H calculated in section 4.2.2. The fcc system shows a clear preference for CO on the FCC, HCP and TOP sites, while still preferring to bind to H on the BRIDGE site. This is most prevalent for the FCC site which has a lower binding energy of around -0.55 eV, with HCP and TOP sites showing a drop in around -0.35 and -0.3 eV respectively. However since the top site still shows a preference for H binding which represents around 41% of the binding sites. While this may indicate that these sites are still available for hydrogen permeation,

He adsorption

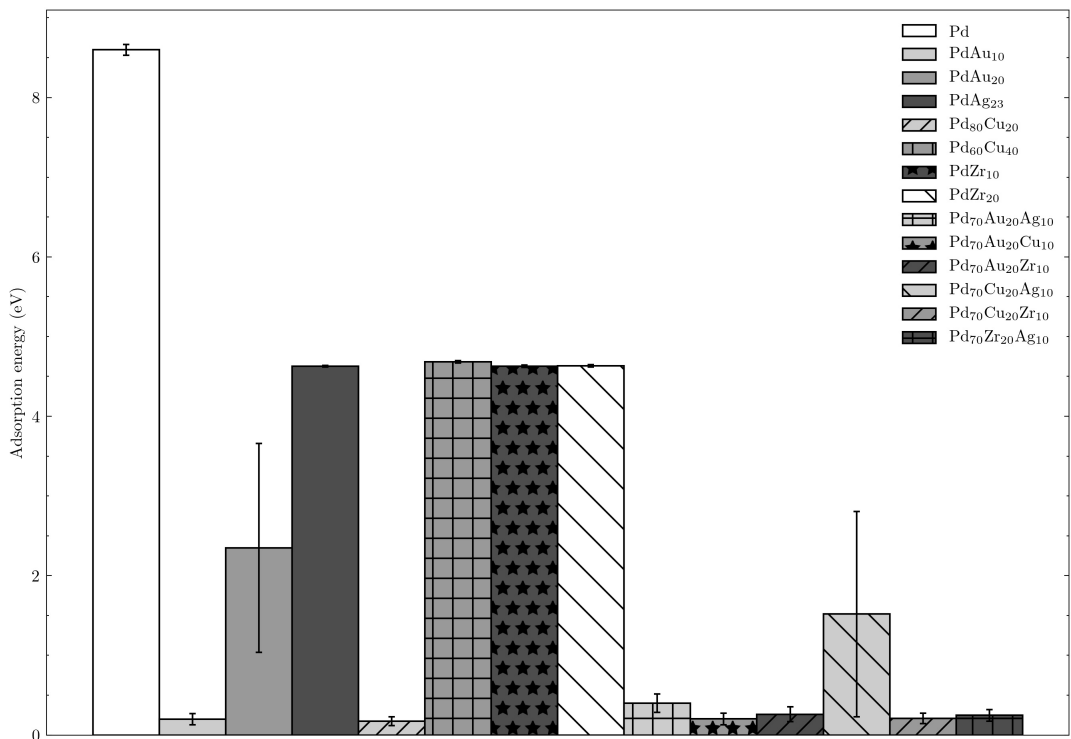


Figure 4.3: Average binding energy of He on the surface of palladium and palladium alloy slabs

N_2 adsorption

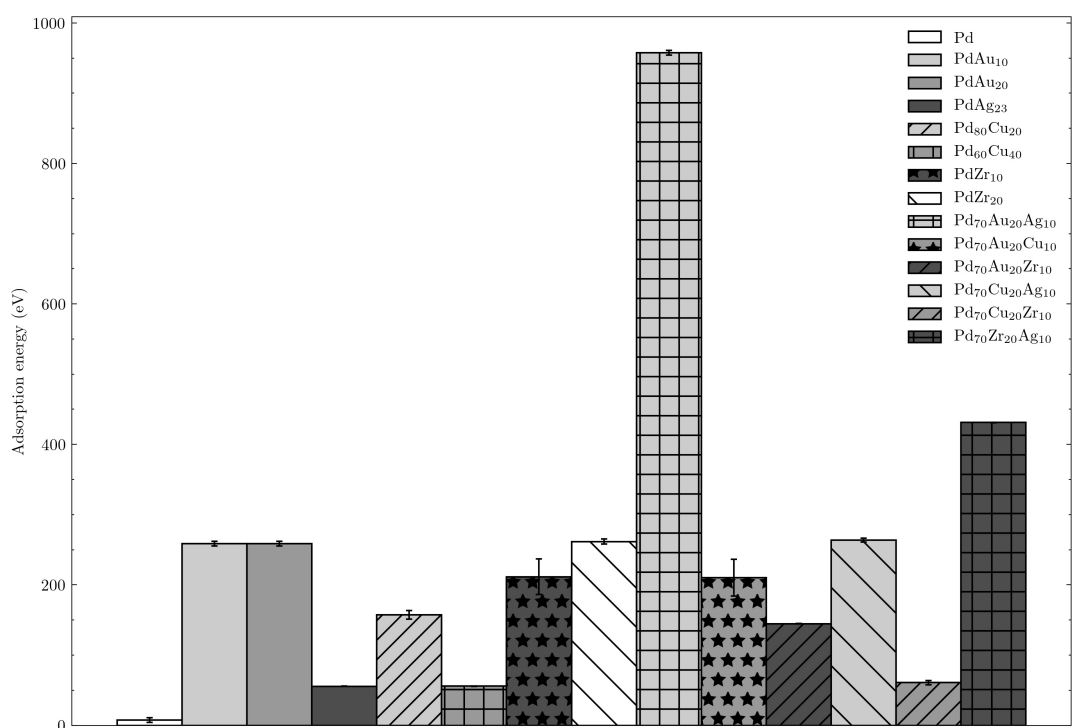


Figure 4.4: Average binding energy of N_2 on the surface of palladium and palladium alloy slabs

CO₂ adsorption

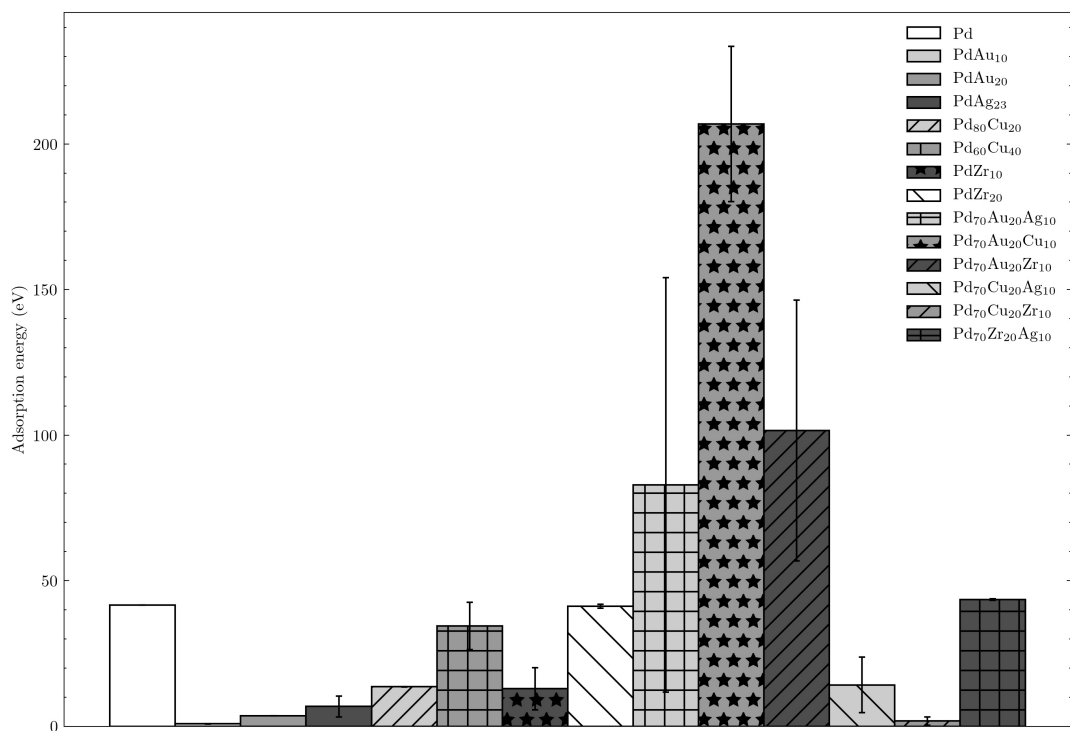


Figure 4.5: Average binding energy of CO₂ on the surface of palladium and palladium alloy slabs

Ar adsorption

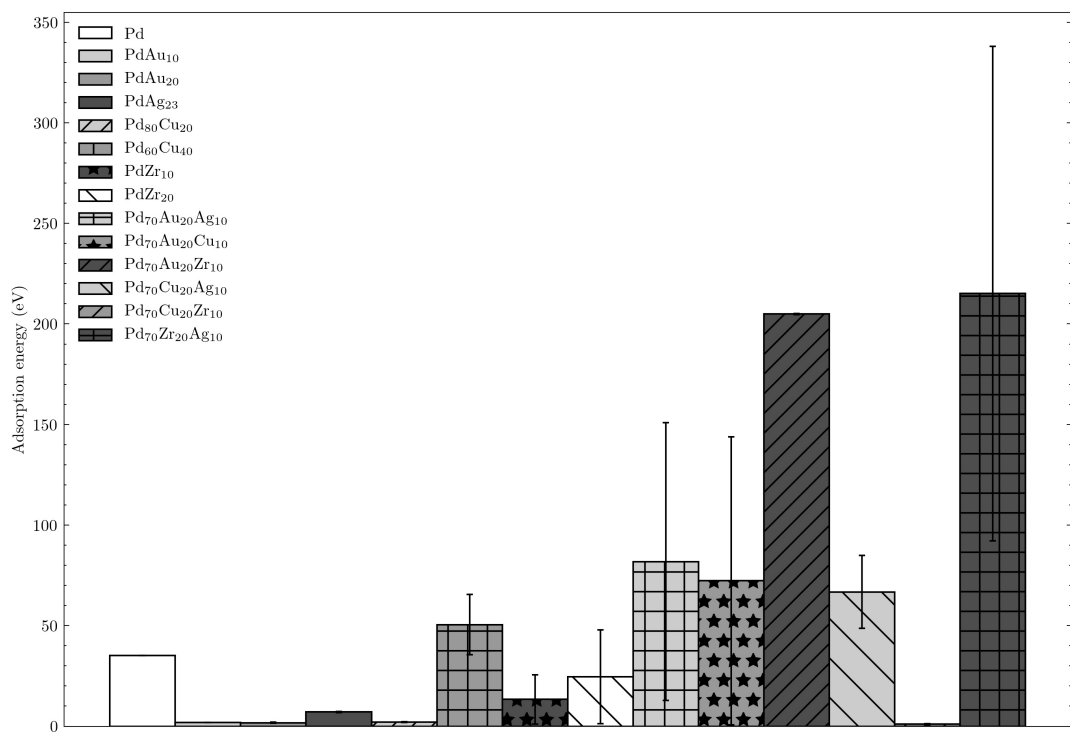


Figure 4.6: Average binding energy of Ar on the surface of palladium and palladium alloy slabs

when bulk diffusion is modelled using kinetic monte carlo simulations that hydrogen travels through the bulk by relaxing the lattice around the fcc and hcp sites to facilitate transport. [8] Therefore the blocking of these sites is likely to have a severe effect on hydrogen permeation.

Of the systems tested PdAu_{20} , PdAg_{23} , and $\text{Pd}_{70}\text{Au}_{20}\text{Cu}_{10}$ all showed marginal preference for hydrogen binding over CO binding. Binding of CO on Au and Ag surfaces has previously been studied and concluded that these metals do not interact with CO under normal circumstances, and will only adsorb through way of material defect or alloying. [9] [10]

By far the worst performing metal for inhibiting the effect of CO were all Zr containing alloys, and $\text{Pd}_{60}\text{Cu}_{40}$. Zr readily forms a bond with C, and even has it's own unique branch of chemistry referring to such compounds.[11] Zirconium is also a common complex used in homogeneous refractory catalysts for reforming hydrocarbon compounds.[12] Therefore the evidence suggests that Zr naturally has a high affinity towards forming carbon bonds and is not a suitable additive for CO resistent membranes.

Similarly Cu has been previously studied and found to readily adsorb CO on it's surface. [9] This does not appear to be an issue for PdCu_{20} alloys indicating that this level of Cu is too low to have such an effect. The $\text{Pd}_{60}\text{Cu}_{40}$ alloy on the other hand has a much higher binding prefernce for CO than it's sister hydrogen system. $\text{Pd}_{60}\text{Cu}_{40}$ is different from other systems in that the crystalline structure transitions to a BCC lattice. [13] BCC structures only have two different sites available for hydrogen binding, BRIDGE and HCP. [14] This change in structure combined with the Cu's availability to bind with C likely accounts for the large discrepancy.

CO adsorption sites on Pd compared to H

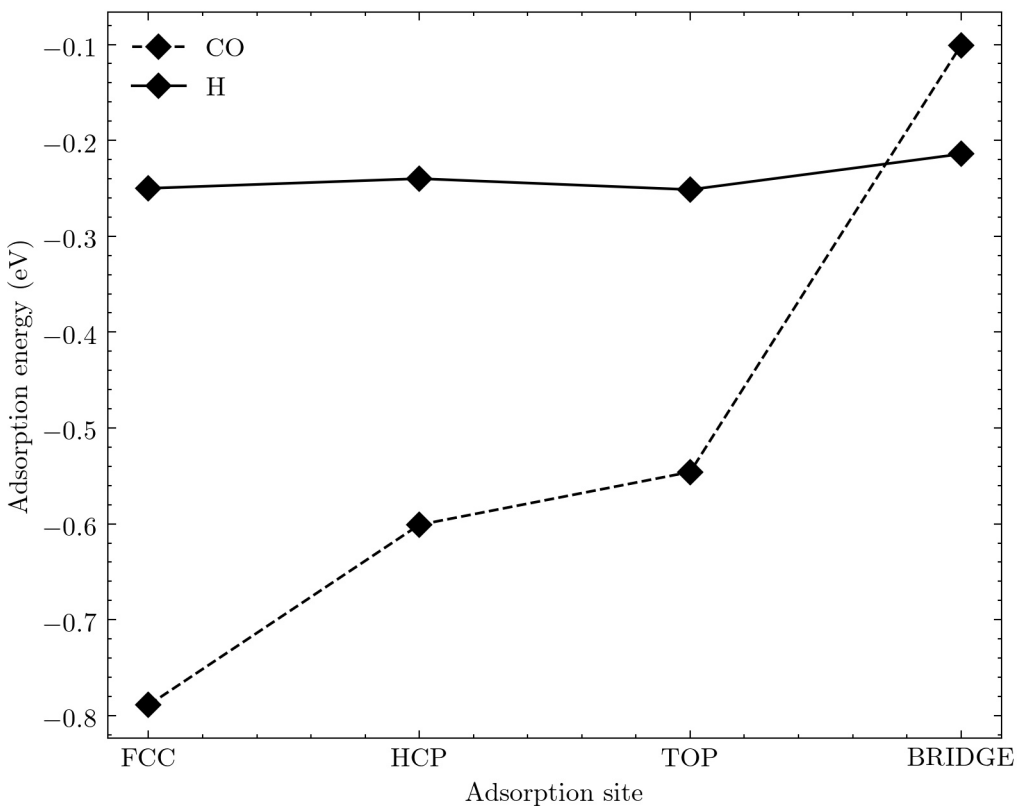


Figure 4.7: binding energy of H and CO for each site on a 2x2x5 Pd slab

CO adsorption

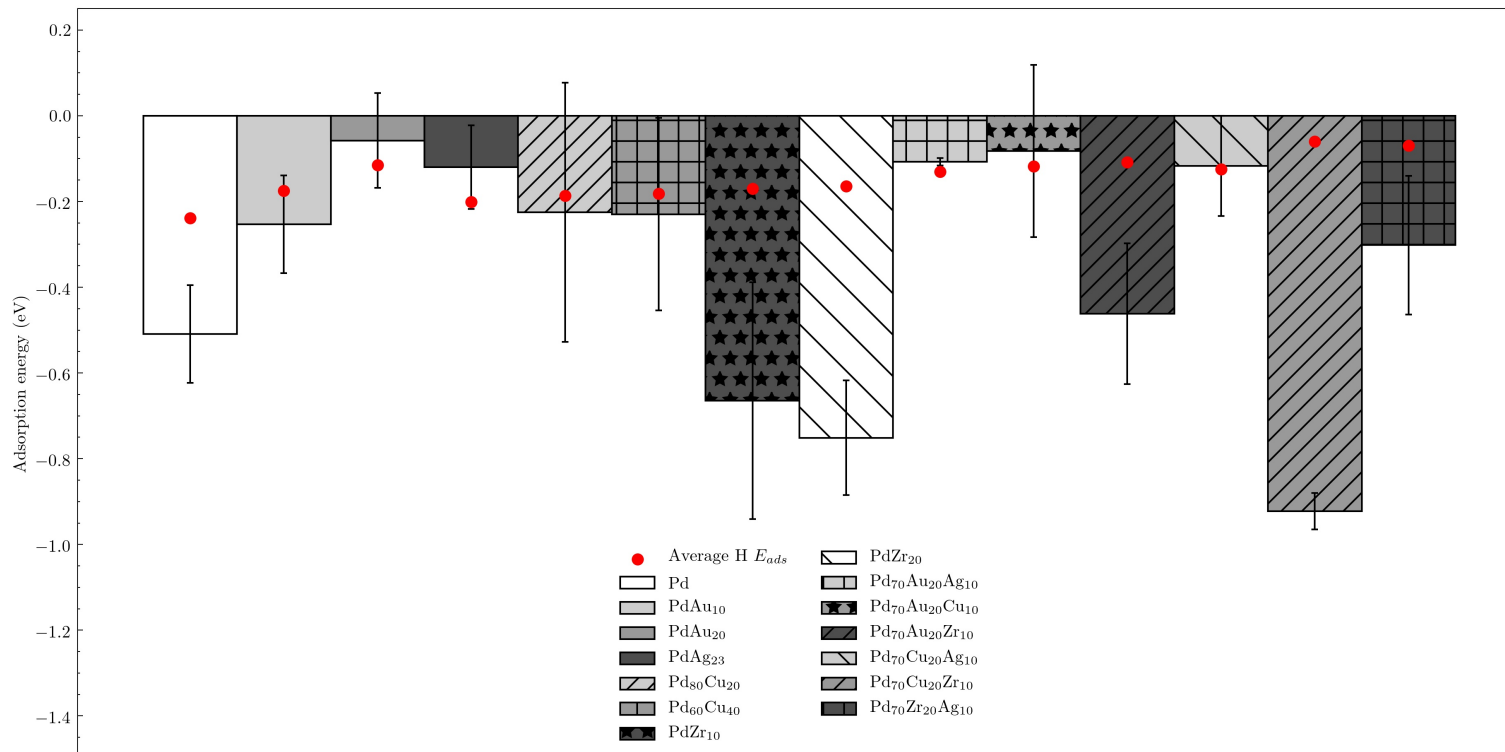


Figure 4.8: Average binding energy of CO on the surface of palladium and palladium alloy slabs

NH₃ adsorption

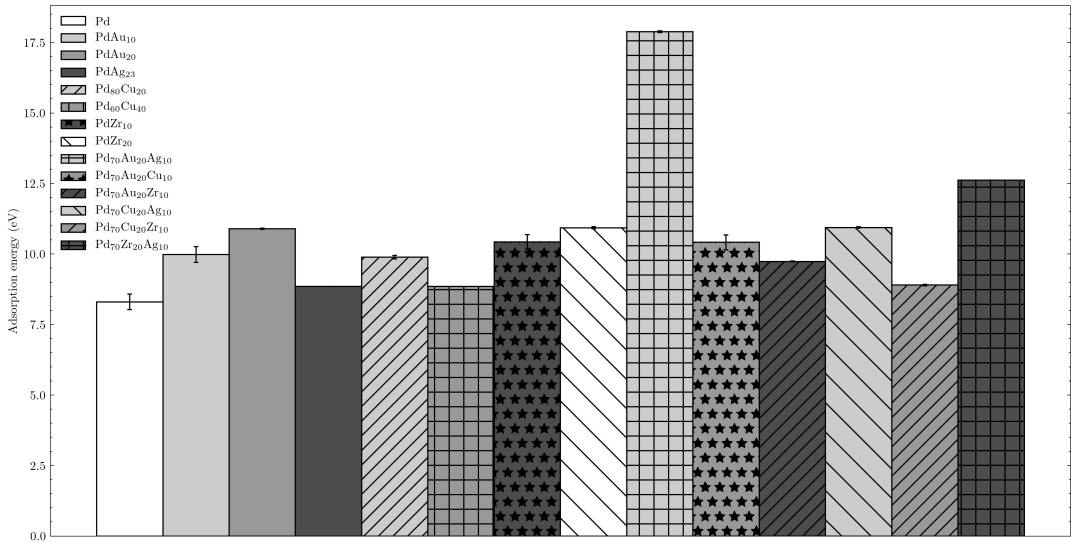


Figure 4.9: Average binding energy of NH₃ on the surface of palladium and palladium alloy slabs

Ammonia

The results of the ammonia simulations are shown in figure 4.9. Of the tested material compositions, neither palladium or any alloy showed an ability to readily bind with Ammonia, this was also true across all sites on the fcc and bcc lattice. This is consistent with the experimental results of Lundin et al [15] and the previous simulations by Herron et al [16]. It should be noted that the paper by Herron [16] found that while ammonia itself did not bind with the surface of palladium, radicals which can be created from ammonia such as imidogen (NH) and azanide (NH₂) will readily form bonds. It is however extremely unlikely that these compounds wil be present in fuel cell hydrogen, and in the unlikely event they are they will likely instantly reform into the more stable NH₃. It can be concluded therfore that NH₃ will create no challenges for the operation of palladium membranes.

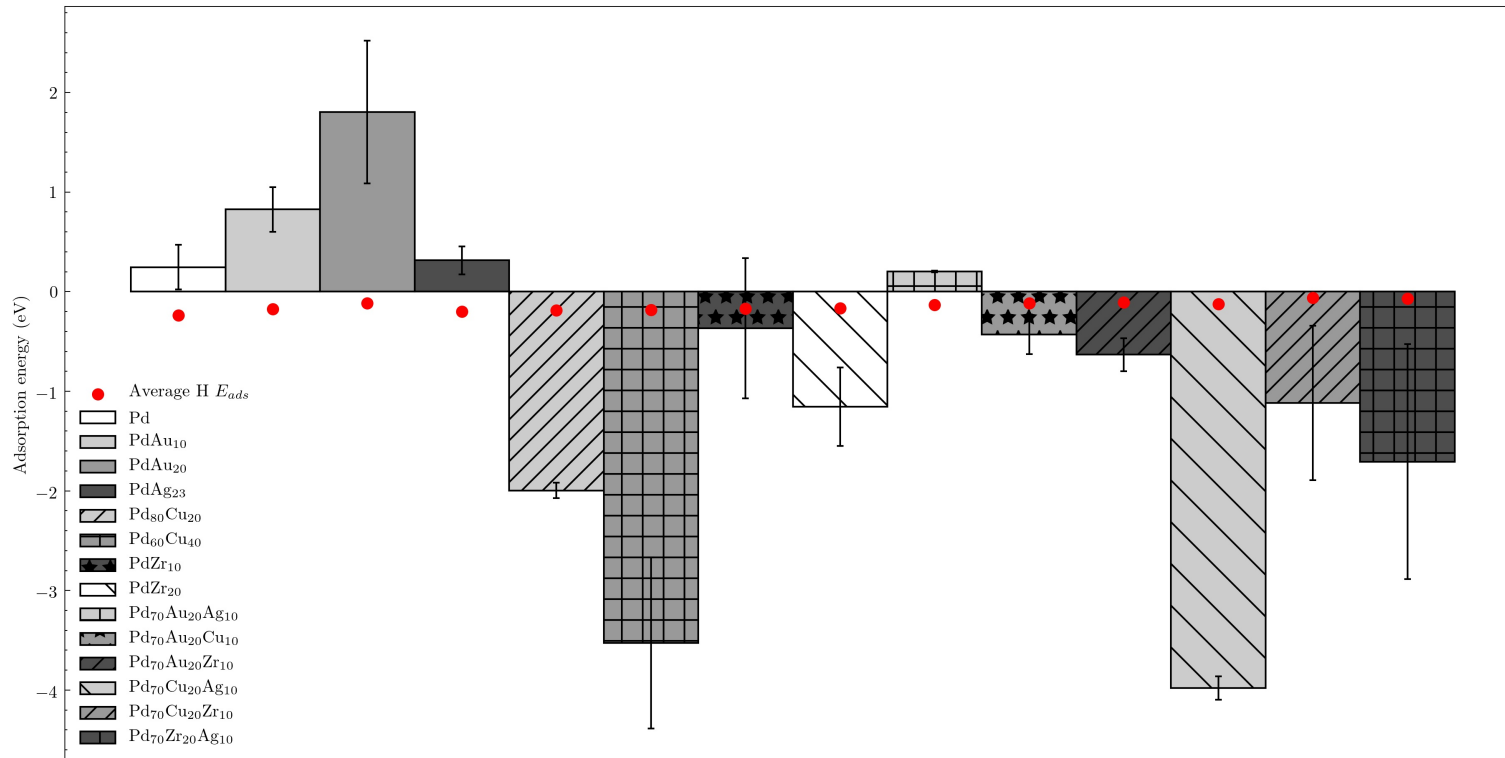
Oxygen and Water

Since O₂ is a symmetrical molecule binding was performed similarly to H₂ in section 4.2.2, the results of which are shown in figure 4.10. Alloys consisting mainly of noble metals (Pd, Ag, Au) typically did not readily bind with oxygen. Whereas alloys containing non-noble metals (Zr and Cu) showed a preference towards oxygen binding. This can pose an issue during enrichment and will likely lead to either the formation of oxides on the surface of the membrane, or catalyse a reaction between either oxygen and hydrogen, or oxygen and one of the other gaseous impurities. In the former the formation of oxides creates a shift in the lattice parameter, similar to the $\alpha - \beta$ transition seen in pure palladium membranes (figure 2.5)[17] and cause membrane failure. In the latter results from hydrogen impurity can be thrown off. Therefore if oxygen is expected in the sample Zr and Cu containing alloys should be avoided.

Water adsorption was performed by attaching the O atom to each available site as per previous studies. [18] The results are shown in figure 4.11 and follow the same trend as the O₂ results discussed above. One important caveat when considering water binding on the surface of metals is the ability for H₂O molecule to form hydrogen bonds with neighbouring molecules.[19] While this study only considered the influence of a single water molecule, in real tests the system will likely have a number of water molecules present. The effect of the hydrogen bond would likely result in the further stabilisation of future water molecules onto the surface, creating an exponential increase in adsorbed H₂O. [19] Care should also be taken, as previous studies on other metallic systems have shown that the binding of water often leads to subsequent dissociation, and formation of a metal oxide and hydrogen. Leading to the same problems with oxidation as previously discussed. [20]

In conclusion noble metals appear to be the best alloying compounds to protect against the influence of H₂O and O₂. This is to be expected as these metals are tradi-

tionally resistant to oxidation. It should be noted however that while this study focused on binding of water on the membrane, it does not take into account adsorption on any other components and fittings on a system. Water in particular is notoriously difficult to remove from a system due to its availability for binding on metal surfaces.[21] Therefore while reducing its effect on the membrane solves one problem, its effect on the overall system still has to be considered.

O_2 adsorptionFigure 4.10: Average binding energy of O₂ on the surface of palladium and palladium alloy slabs

H₂O adsorption

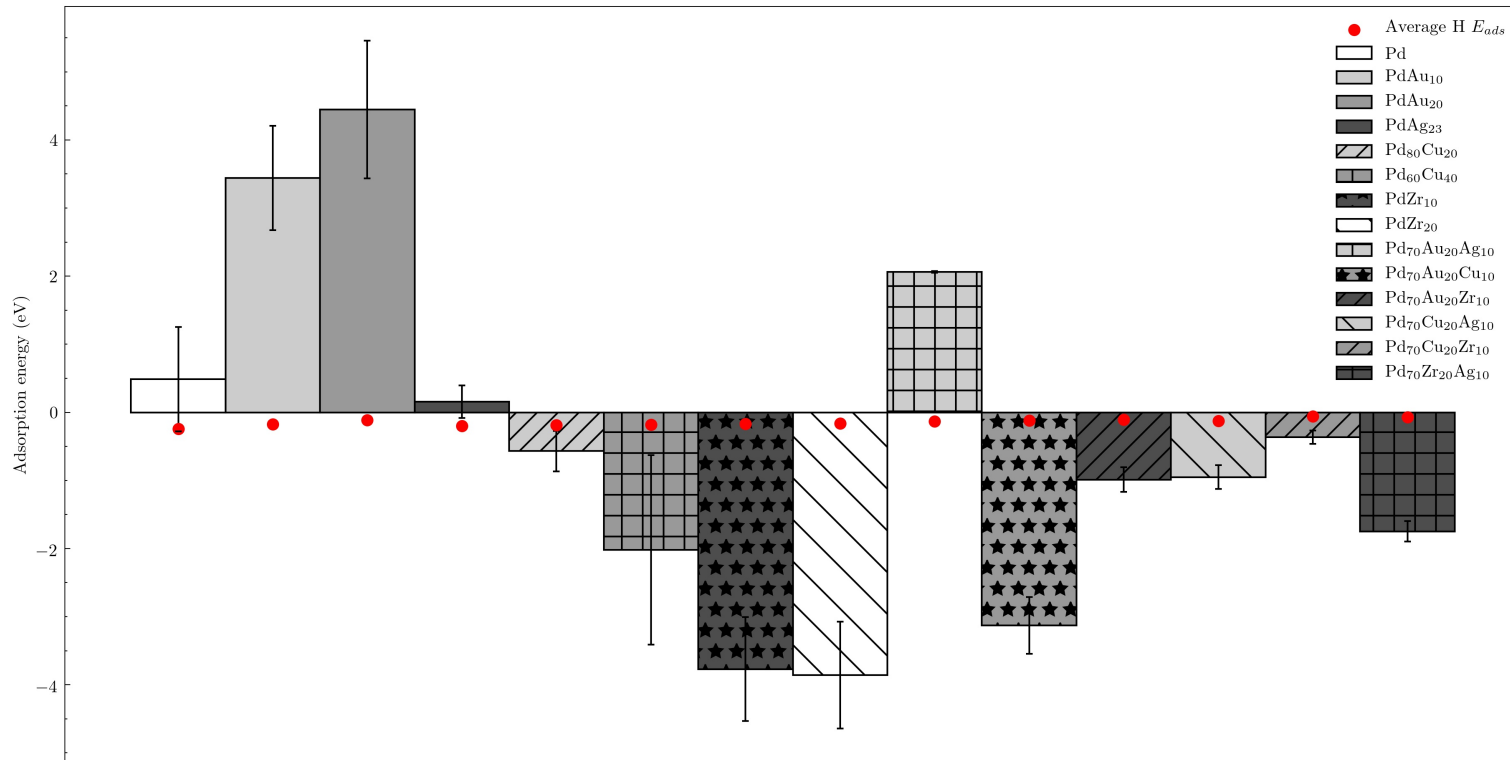


Figure 4.11: Average binding energy of H₂O on the surface of palladium and palladium alloy slabs

Methane

Methane was adsorbed onto the surface of the Pd slab systems using one of the hydrogen molecules as has previously been performed in literature. [22] The results of the simulations are shown in figure 4.13.

All simulated metals seem to have the ability to bind CH₄ to its surface. Intuitively this seems reasonable since the atom binding to the surface is H₂, which we have already proven has the ability to bind to all Pd alloy models. The molecule also features a carbon molecule which from our CO simulations in figure 4.8 will also preferentially bind to the surface of the Pd slab models, at a higher preference than hydrogen. The results of the CH₄ simulations seem to follow the general trend of it's sister CO results, however at a weaker level. All simulations were unstable which is shown by the large error values showing large swings in the results from each simulation. Therefore it is likely that in many simulations, while CH₄ is stable on the surface, could not find the most stable coordination due to competing forces acting from the hydrogen atoms, and the carbon atom.

The binding energies of CH₄ on each site in the Pd system are shown in figure 4.12. Similarly to CO, the CH₄ molecule has a higher preference to the FCC and HCP sites than H. Unlike CO, CH₄ does not bind as strongly to the TOP site as CO. The reason for the strong binding preference to the FCC and HCP sites is likely due to the fact that while the H atom is bound within the HCP and FCC sites, the C atom and other H atoms will bind to the surrounding metallic atoms in the crystalline lattice, stabilising the molecule in those sites. On the TOP and BRIDGE sites this does not happen, and since the H atom is bound more strongly to C through a covalent bond, the resulting energy available for binding on these sites is lower than it would be if the molecule was pure hydrogen.

In terms of resistance to CH₄ binding, the conclusions reached in the section dis-

cussing the results of CO still hold true. All alloy compositions with high percentages of Au and Ag showed higher resistance to CH₄ binding, whereas Cu and Zr containing molecules performed worse.

Past studies performing CH₄ binding on metallic surfaces found that in some cases the H atom could dissociate from the molecule, creating CH₃ and H. [23] In this particular application such a reaction would result in the liberated H atom permeating through the membrane, leaving CH₃ on the retentate side. While this changes the composition of the retentate gas, from a measurement perspective it should not pose much of an issue. The ISO 14687-2[24] standard specifies a total hydrocarbon level and therefore any CH₃ that is produced should be detected using previously outlined techniques. [25]

What may pose a larger issue is that in the study performed by Herron [16], it was found that similar to Ammonia, CH₄ based radicals will bind more strongly to the surface than CH₄ resulting in an increasing poisoning effect. It is unknown whether the hydrogen dissociation effect previously discussed would continue to occur with these radicals, but in the case it does, the result would eventually be carbon deposition on the surface of the membrane. Eventually deactivating the membrane entirely, and throwing off all results due to removal of carbon from the gas.

CH_4 adsorption sites on Pd compared to H

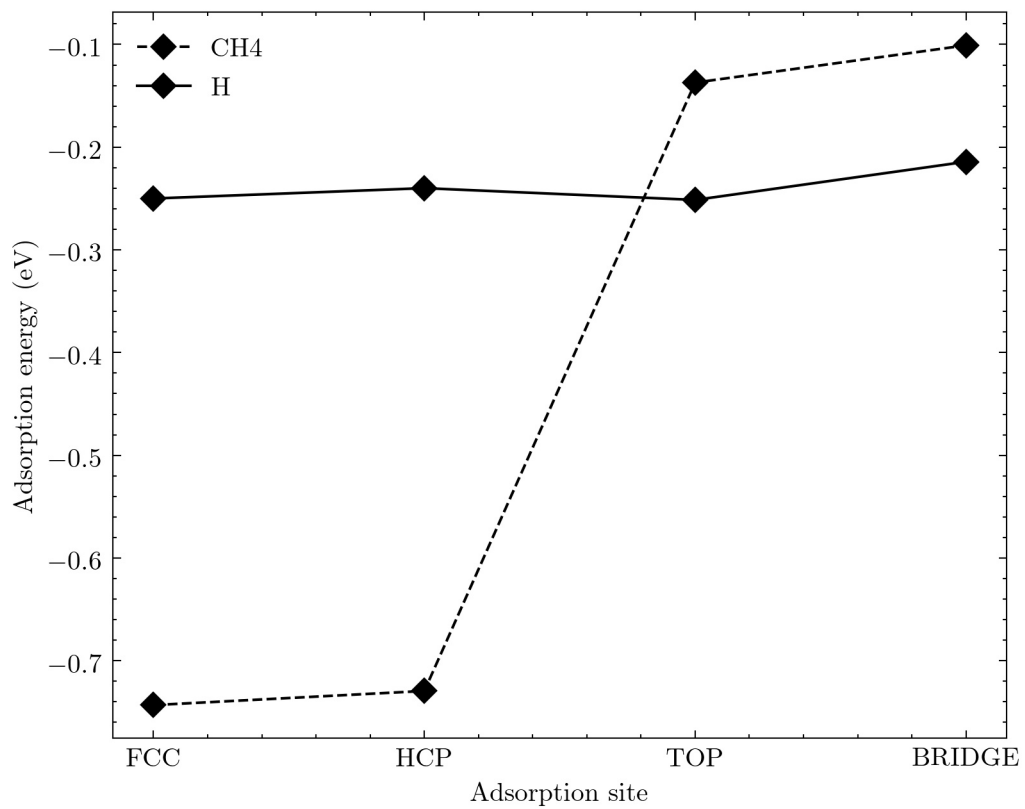


Figure 4.12: binding energy of H and CH_4 for each site on a $2\times 2\times 5$ Pd slab

CH₄ adsorption

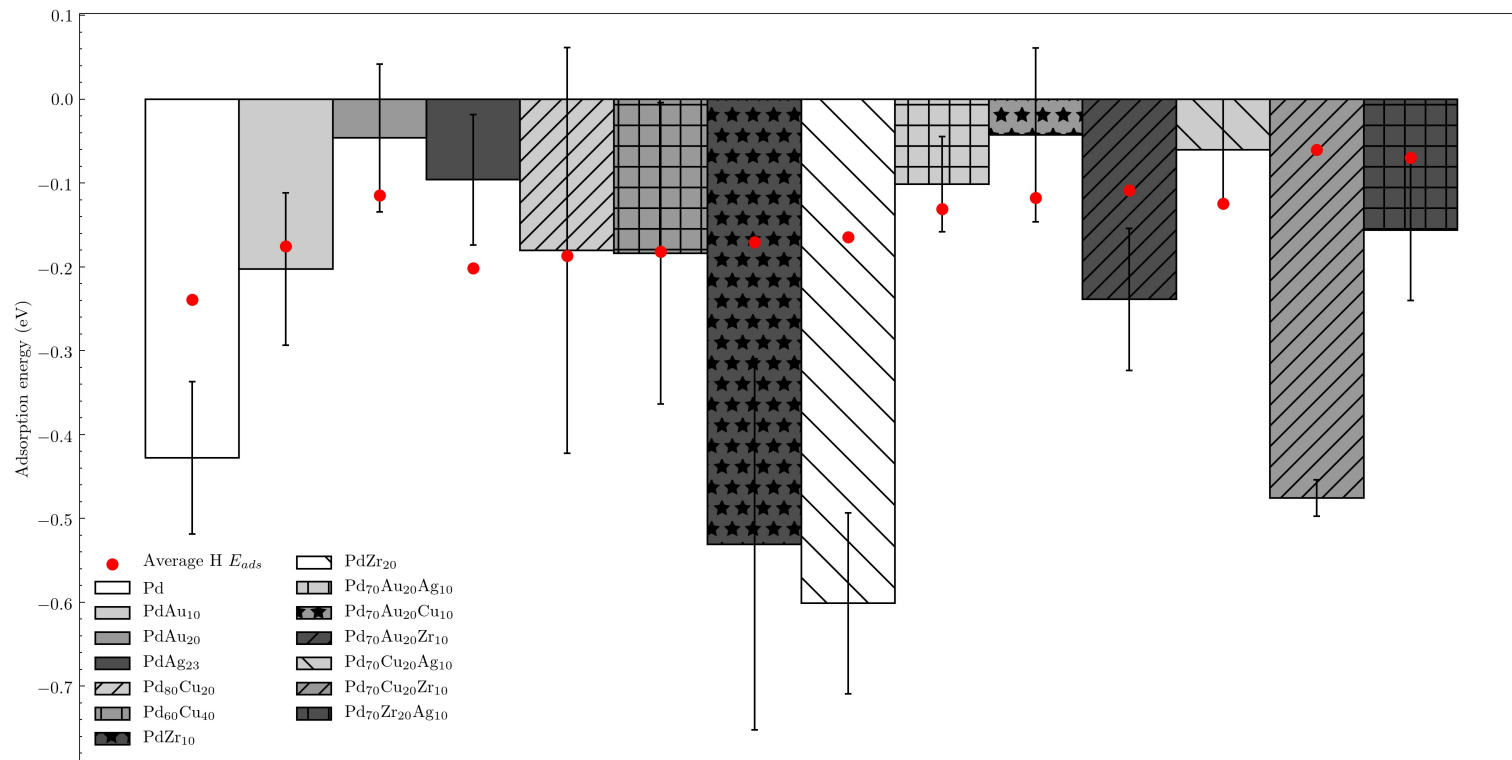


Figure 4.13: Average binding energy of Methane on the surface of palladium and palladium alloy slabs

Formaldehyde and Formic acid

Formaldehyde and Formic acid are similar molecules, with the only difference being one of the hydrogen atoms being replaced with an OH group on formic acid. Both molecules were adsorbed onto the surface using the double bonded O atom perpendicular to the surface of the slab model.[26] The results for the simulations are shown in both figure 4.14 for formaldehyde and figure 4.15 for formic acid.

The results of these simulations vary widely, with formaldehyde showing strong binding ability with Pd and Pd alloy surfaces, while Formic acid appears to reject binding completely. The systems were also largely unstable as indicated by the large error values, which indicates that there are a number of forces acting on each atom on the molecule and therefore multiple stable arrangements other than the one chosen.

This result for formaldehyde is not surprising as formaldehyde is widely known to be effective catalyst for oxidation of formaldehyde, being able to oxidise formaldehyde under the presence of sunlight alone. [27] Therefore it is likely that any mixture containing both formaldehyde and oxygen under the presence of a palladium membrane will likely react, forming carbon dioxide and hydrogen. Additionally palladium alone may be powerful enough to dissociate the formaldehyde molecule, and depending on the coordination of the molecule from H₂ and CO, or hydrocarbon compounds ranging from CH₂ to C₄ and oxygen,[26] the ramifications of which have been discussed previously. Unfortunately out of the tested alloys there does not appear to be a solution to this and further membrane compositions should be screened in order to determine an appropriate material to suppress the effect of formaldehyde.

Past research evaluating Pd surfaces for formic acid oxidation found that Pd surfaces typically reject COH bindings which lines up well with these results. [28]

Formaldehyde adsorption

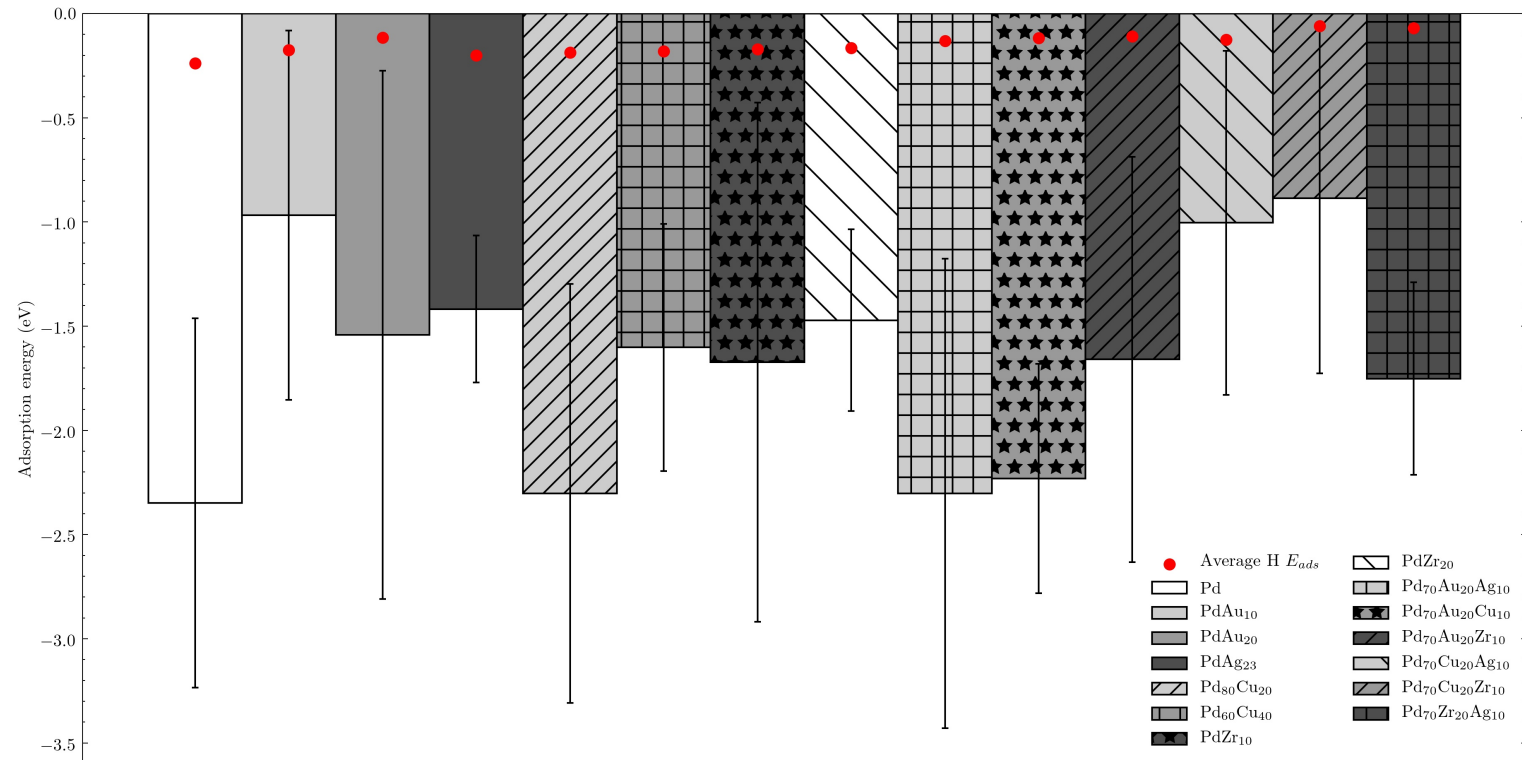


Figure 4.14: Average binding energy of formaldehyde on the surface of palladium and palladium alloy slabs

Formic Acid adsorption

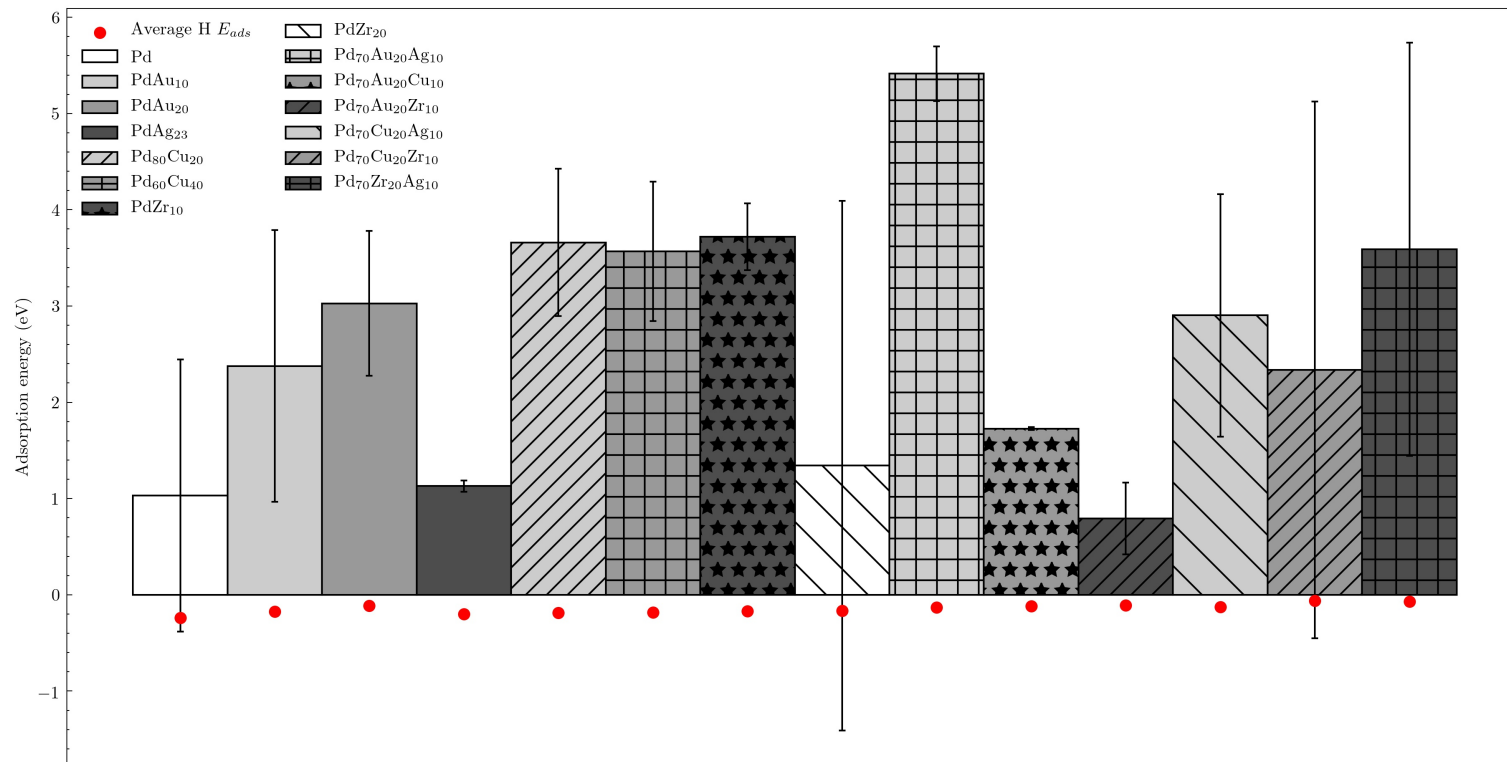


Figure 4.15: Average binding energy of Formic Acid on the surface of palladium and palladium alloy slabs

Hydrogen sulphide

The final molecule that was simulated was H₂S. This molecule was adsorbed using the sulphur atom as this is the known mechanism for H₂S binding on a metallic surface. [29] The results are shown in figure 4.17. As expected all metals showed the ability to bind with the sulphur atom at least as strongly as hydrogen. Additionally the S atom will bind stronger to all active sites for hydrogen dissociation as shown by figure 4.16.

It appears that alloying with most metals will do little to halt the binding of sulphur, except for gold and Zr. Alloying with these metals brings the binding energy to a level where it is around equal to that of hydrogen, and is therefore more manageable. Additionally while alloying with silver on its own appears to infact increase the ability for sulphur to bind onto the surface, the effect is completely negated when gold is present.

Of the alloys tested PdAu₂₀, both Zr binary alloys, PdAuZr, PdCuAu, and PdZrCu appear to be the most suitable for mitigating the effects of H₂S. It should be noted that past studies have revealed that Pd₄S is in fact available for hydrogen permeation, albeit at a much slower rate.[29] This may indicate that it is possible to pretreat a palladium membrane with sulphur, to a point where it is no longer reactive to sulphur, but can still permeate hydrogen. Such studies are outside the scope of this thesis however

H₂S adsorption sites on Pd compared to H

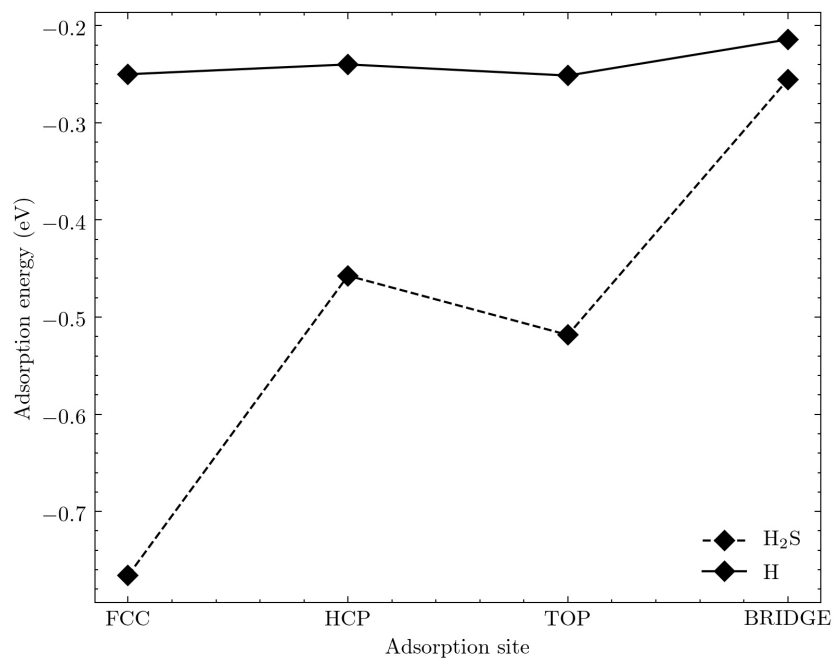


Figure 4.16: binding energy of H and H₂S for each site on a 2x2x5 Pd slab

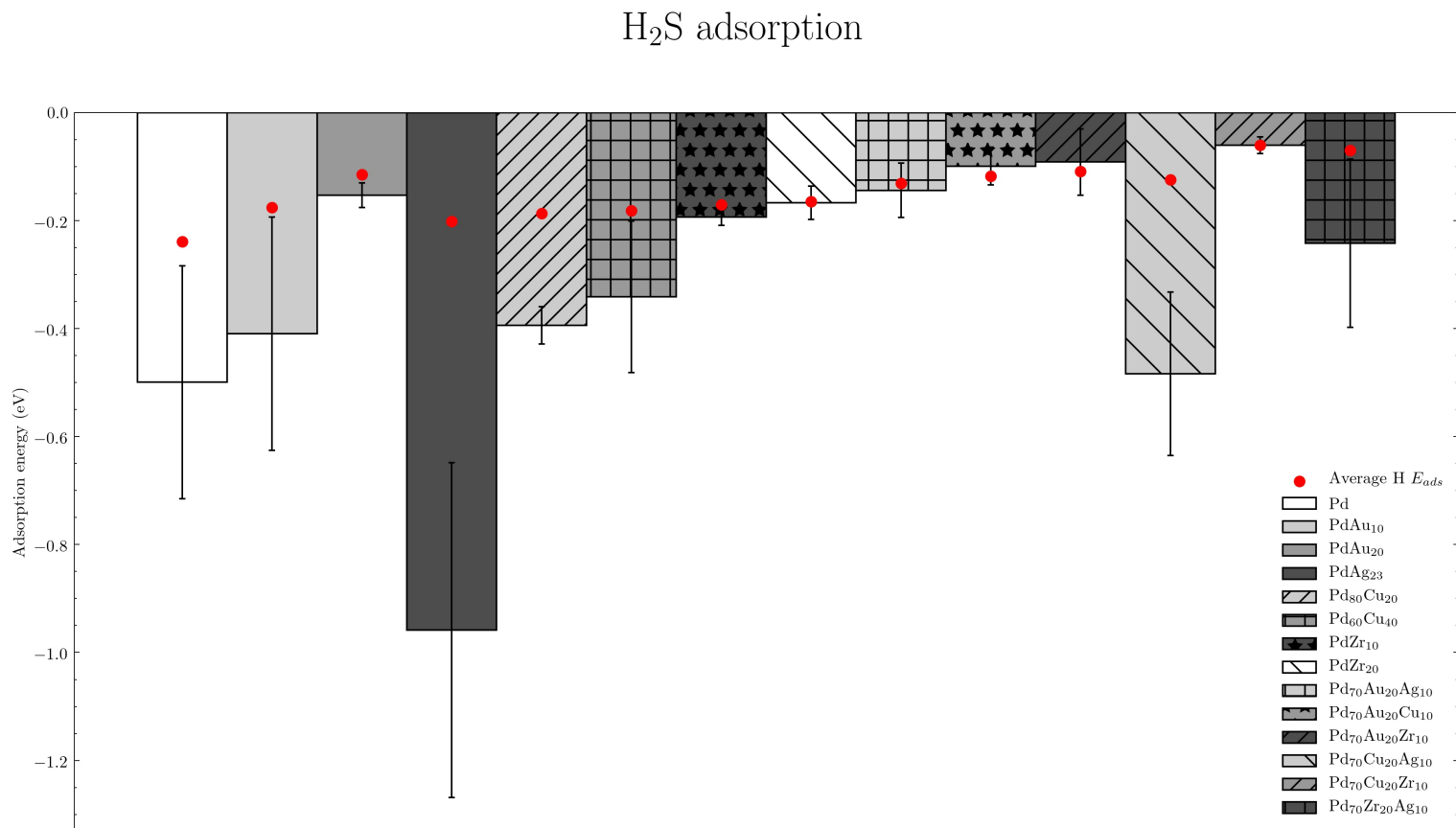


Figure 4.17: Average binding energy of H_2S on the surface of palladium and palladium alloy slabs

Table 4.4: Best performing alloys for each environment with respect to the different between the binding energies with relevant impurities, and the binding energy of hydrogen

Environment	Best performing alloy(s)	$E_{i_{ads}}/E_{H_{ads}}$ ($i=$ impurity)
Oxidising	PdAu20	-38.73 (H ₂ O), -7.18 (O ₂)
Carbonaceous	PdAu ₂₀	0.50(CO) 0.40 (CH ₄)
	PdAuCu	0.70(CO) 0.36(CH ₄)
	PdAuCu	0.84
Sulphurous	PdCuZr	0.92
	PdAuZr	0.98

4.3 Conclusion

DFT simulations were carried out investigating the binding energies of ISO 14687-2 impurities on the surface of palladium and palladium alloy membranes. A number of metals were alloyed, either because they are commonly used in literature, or are known for their resistance to sulphur containing environments which were of key importance to this thesis. Most alloys were found to be stable except for Cr containing alloys, which were eliminated from the study.

After testing the impurities it was clear that the binding of CO, CH₄, O₂, H₂O and H₂S were affected most by the alloy composition. Ar, He, N₂, NH₃, CO₂, and Formic acid were found to be completely inert to all compositions. Formaldehyde strongly adsorbed to all alloys regardless of composition and further research will have to be taken to find a suitable composition to mitigate this.

These impurities can be split into 3 broad groups, oxidising (O₂ and H₂O) carbonaceous (CH₄ and CO) and sulphurous (H₂). The best performing alloys for each of these impurities were decided by comparing the calculated binding energy to that of the same alloy binding with Hydrogen. The most suitable alloys for each class of material is shown in table 4.4.

In the following chapter these membranes will be manufactured and tested under carbonaceous and sulphur containing environments in order to validate the results of this study. Oxygen containing environments will not be tested due to the dangers of heating oxygen in a hydrogen matrix.

References

- [1] Paolo Giannozzi, Stefano Baroni, Nicola Bonini, Matteo Calandra, Roberto Car, Carlo Cavazzoni, Davide Ceresoli, Guido L Chiarotti, Matteo Cococcioni, Ismaila Dabo, Andrea Dal Corso, Stefano de Gironcoli, Stefano Fabris, Guido Fratesi, Ralph Gebauer, Uwe Gerstmann, Christos Goucoussis, Anton Kokalj, Michele Lazzeri, Layla Martin-Samos, Nicola Marzari, Francesco Mauri, Riccardo Mazzarello, Stefano Paolini, Alfredo Pasquarello, Lorenzo Paulatto, Carlo Sbraccia, Sandro Scandolo, Gabriele Sclauzero, Ari P Seitsonen, Alexander Smogunov, Paolo Umari, and Renata M Wentzcovitch. Quantum espresso: a modular and open-source software project for quantum simulations of materials. *Journal of Physics: Condensed Matter*, 21(39):395502 (19pp), 2009. URL <http://www.quantum-espresso.org>.
- [2] P Giannozzi, O Andreussi, T Brumme, O Bunau, M Buongiorno Nardelli, M Calandra, R Car, C Cavazzoni, D Ceresoli, M Cococcioni, N Colonna, I Carnimeo, A Dal Corso, S de Gironcoli, P Delugas, R A DiStasio Jr, A Ferretti, A Floris, G Fratesi, G Fugallo, R Gebauer, U Gerstmann, F Giustino, T Gorni, J Jia, M Kawamura, H-Y Ko, A Kokalj, E Küçükbenli, M Lazzeri, M Marsili, N Marzari, F Mauri, N L Nguyen, H-V Nguyen, A Otero de-la Roza, L Paulatto, S Poncé, D Rocca, R Sabatini, B Santra, M Schlipf, A P Seitsonen, A Smogunov, I Timrov, T Thonhauser, P Umari, N Vast, X Wu, and S Baroni. Advanced capabilities for materials modelling with quantum espresso. *Journal of Physics: Condensed Matter*, 29(46):

465901, 2017. URL <http://stacks.iop.org/0953-8984/29/i=46/a=465901>.

- [3] Paolo Giannozzi, Oscar Baseggio, Pietro Bonfà, Davide Brunato, Roberto Car, Ivan Carnimeo, Carlo Cavazzoni, Stefano de Gironcoli, Pietro Delugas, Fabrizio Ferrari Ruffino, Andrea Ferretti, Nicola Marzari, Iurii Timrov, Andrea Urru, and Stefano Baroni. Quantum espresso toward the exascale. *The Journal of Chemical Physics*, 152(15):154105, 2020. doi: 10.1063/5.0005082. URL <https://doi.org/10.1063/5.0005082>.
- [4] Haebin Shin, Minsung Baek, Youngsoo Ro, Changyeol Song, Kwan-Young Lee, and In Kyu Song. Improvement of sulfur resistance of pd/ce-zr-al-o catalysts for co oxidation. *Applied Surface Science*, 429:102 – 107, 2018. ISSN 0169-4332. doi: <https://doi.org/10.1016/j.apsusc.2017.05.198>. URL <http://www.sciencedirect.com/science/article/pii/S0169433217315519>. Materials Challenges in Alternative and Renewable Energy 2017(MCARE 2017).
- [5] P. Marcus and J.M. Grimal. The antagonistic roles of chromium and sulphur in the passivation of nicrfe alloys studied by xps and radiochemical techniques. *Corrosion Science*, 31:377 – 382, 1990. ISSN 0010-938X. doi: [https://doi.org/10.1016/0010-938X\(90\)90134-Q](https://doi.org/10.1016/0010-938X(90)90134-Q). URL <http://www.sciencedirect.com/science/article/pii/0010938X9090134Q>. Passivation of metals and semiconductors.
- [6] G. T. Kasun Kalhara Gunasooriya and Mark Saeys. Co adsorption on pt(111): From isolated molecules to ordered high-coverage structures. *ACS Catalysis*, 8(11): 10225–10233, 2018. doi: 10.1021/acscatal.8b02371. URL <https://doi.org/10.1021/acscatal.8b02371>.
- [7] Nong Xu, Sung Su Kim, Anwu Li, John R Grace, C Jim Lim, and Tony Boyd. Investigation of the influence of tar-containing syngas from biomass gasification on

dense Pd and Pd–Ru membranes. *Powder Technology*, 290:132–140, 2016. doi: 10.1016/j.powtec.2015.08.037.

- [8] Lin Qin and Chao Jiang. First-principles based modeling of hydrogen permeation through Pd-Cu alloys. *International Journal of Hydrogen Energy*, 37(17):12760–12764, 2012. ISSN 03603199. doi: 10.1016/j.ijhydene.2012.06.029.
- [9] Ichiro Oda, Hirohito Ogasawara, and Masatoki Ito. Carbon monoxide adsorption on copper and silver electrodes during carbon dioxide electroreduction studied by infrared reflection absorption spectroscopy and surface-enhanced raman spectroscopy. *Langmuir*, 12(4):1094–1097, 1996. doi: 10.1021/la950167j. URL <https://doi.org/10.1021/la950167j>.
- [10] Sh.k. Shaikhutdinov, R. Meyer, M. Naschitzki, M. Baumer, and H.-J. Freund. Size and support effects for co adsorption on gold model catalysts. *Catalysis Letters*, 86(4):211–219, Mar 2003. doi: 10.1023/a:1022616102162.
- [11] A. MAUREEN ROUHI. Organozirconium chemistry arrives. *Chemical & Engineering News Archive*, 82(16):36–39, 2004. doi: 10.1021/cen-v082n016.p036. URL <https://doi.org/10.1021/cen-v082n016.p036>.
- [12] Dennis B. Malpass. *Commercially Available Metal Alkyls and Their Use in Polyolefin Catalysts*, chapter 1, pages 1–28. 2010. ISBN 9780470504437. doi: 10.1002/9780470504437.ch1. URL <https://onlinelibrary.wiley.com/doi/abs/10.1002/9780470504437.ch1>.
- [13] Ying She, Sean C Emerson, Neal J Magdefrau, Susanne M Opalka, Catherine Thibaud-Erkey, and Thomas H Vanderspurt. Hydrogen permeability of sulfur tolerant Pd–Cu alloy membranes. *Journal of Membrane Science*, 452:203–211, 2014. doi: 10.1016/j.memsci.2013.09.025.

- [14] Sang Chul Yeo, Sang Soo Han, and Hyuck Mo Lee. Adsorption, dissociation, penetration, and diffusion of n₂ on and in bcc fe: first-principles calculations. *Phys. Chem. Chem. Phys.*, 15:5186–5192, 2013. doi: 10.1039/C3CP44367A. URL <http://dx.doi.org/10.1039/C3CP44367A>.
- [15] Sean-Thomas B Lundin, Taichiro Yamaguchi, Colin A Wolden, S Ted Oyama, and J Douglas Way. The role (or lack thereof) of nitrogen or ammonia adsorption-induced hydrogen flux inhibition on palladium membrane performance. *Journal of Membrane Science*, 514:65–72, 2016. doi: 10.1016/j.memsci.2016.04.048.
- [16] Jeffrey A. Herron, Scott Tonelli, and Manos Mavrikakis. Atomic and molecular adsorption on pd(111). *Surface Science*, 606(21):1670 – 1679, 2012. ISSN 0039-6028. doi: <https://doi.org/10.1016/j.susc.2012.07.003>. URL <http://www.sciencedirect.com/science/article/pii/S0039602812002245>.
- [17] Hui Li, Hengyong Xu, and Wenzhao Li. Study of n value and α/β palladium hydride phase transition within the ultra-thin palladium composite membrane. *Journal of Membrane Science*, 324(1-2):44–49, 2008. doi: 10.1016/j.memsci.2008.06.053.
- [18] Jerome Roques, Edouard Veilly, and Eric Simoni. Periodic density functional theory investigation of the uranyl ion sorption on three mineral surfaces: A comparative study. *International journal of molecular sciences*, 10:2633–61, 07 2009. doi: 10.3390/ijms10062633.
- [19] Sheng Meng, E. G. Wang, and Shiwu Gao. Water adsorption on metal surfaces: A general picture from density functional theory studies. *Phys. Rev. B*, 69:195404, May 2004. doi: 10.1103/PhysRevB.69.195404. URL <https://link.aps.org/doi/10.1103/PhysRevB.69.195404>.
- [20] Jia Chen and Annabella Selloni. Water adsorption and oxidation at the co₃o₄

- (110) surface. *The Journal of Physical Chemistry Letters*, 3(19):2808–2814, 2012. doi: 10.1021/jz300994e. URL <https://doi.org/10.1021/jz300994e>.
- [21] Thomas Bacquart, Niamh Moore, Nick Hart, Abigail Morris, Thor A. Aarhaug, Ole Kjos, Fabien Aupretre, Thibault Colas, Frederique Haloua, Bruno Gozlan, and Arul Murugan. Hydrogen quality sampling at the hydrogen refuelling station – lessons learnt on sampling at the production and at the nozzle. *International Journal of Hydrogen Energy*, 45(8):5565 – 5576, 2020. ISSN 0360-3199. doi: <https://doi.org/10.1016/j.ijhydene.2019.10.178>. URL <http://www.sciencedirect.com/science/article/pii/S0360319919340510>. 22nd World Hydrogen Energy Conference.
- [22] Hao Cui, Xiaoxing Zhang, Jun Zhang, and Muhammad Ali Mehmood. Interaction of co and ch4 adsorption with noble metal (rh, pd, and pt)-decorated n3-cnts: A first-principles study. *ACS Omega*, 3(12):16892–16898, 2018. doi: 10.1021/acsomega.8b02578. URL <https://doi.org/10.1021/acsomega.8b02578>.
- [23] Yuta Tsuji and Kazunari Yoshizawa. Adsorption and activation of methane on the (110) surface of rutile-type metal dioxides. *The Journal of Physical Chemistry C*, 122(27):15359–15381, 2018. doi: 10.1021/acs.jpcc.8b03184. URL <https://doi.org/10.1021/acs.jpcc.8b03184>.
- [24] International Standard ISO 14687: 2019. Hydrogen Fuel - Product Specification, 2019.
- [25] Arul Murugan and Andrew S Brown. Review of purity analysis methods for performing quality assurance of fuel cell hydrogen. *International Journal of Hydrogen Energy*, 40(11):4219–4233, 2015. doi: 10.1016/j.ijhydene.2015.01.041.
- [26] Dandan Wang, Yingying Fan, Zhonghui Sun, Dongxue Han, and Li Niu. A theoretical study of formaldehyde adsorption and decomposition on a wc (0001)

surface. *RSC Adv.*, 8:32481–32489, 2018. doi: 10.1039/C8RA04983A. URL <http://dx.doi.org/10.1039/C8RA04983A>.

- [27] Longhui Nie, Jiaguo Yu, Mietek Jaroniec, and Franklin Feng Tao. Room-temperature catalytic oxidation of formaldehyde on catalysts. *Catal. Sci. Technol.*, 6:3649–3669, 2016. doi: 10.1039/C6CY00062B. URL <http://dx.doi.org/10.1039/C6CY00062B>.
- [28] Andrew Capon and Roger Parsons. The oxidation of formic acid on noble metal electrodes: II. a comparison of the behaviour of pure electrodes. *Journal of Electroanalytical Chemistry and Interfacial Electrochemistry*, 44(2):239 – 254, 1973. ISSN 0022-0728. doi: [https://doi.org/10.1016/S0022-0728\(73\)80250-5](https://doi.org/10.1016/S0022-0728(73)80250-5). URL <http://www.sciencedirect.com/science/article/pii/S0022072873802505>.
- [29] Bryan D Morreale, Bret H Howard, Osemwengie Iyoha, Robert M Enick, Chen Ling, and David S Sholl. Experimental and Computational Prediction of the Hydrogen Transport Properties of Pd 4 S. *Ind. Eng. Chem. Res.*, 46:6313–6319, 2007.

Chapter 5

Impurity resistance of dense metal membranes under hydrogen impurities

Abstract

In this chapter a number of dense palladium alloy membranes were synthesised on a YSZ substrate using a combination of electroless plating and magnetron sputtering in order to determine which membrane compositions resisted impurities.

The permeability of the synthesised membranes, in addition to a commercial membrane were tested under a variety of ISO 14687-2 impurities in order to determine which alloy composition was most suitable for use as a membrane material for hydrogen impurity enrichment, where low reactivity with impurities present in hydrogen samples are required. Of the tested membranes the best performing compositions were PdAuAg, PdAuCu and PdCuZr which only showed a 27%, 25% and 26% drop in permeability under atmospheres containing 10 ppm of non-sulphurous, and 2 ppm of sulphurous impurities typically expected to be found in hydrogen derived from steam methane re-

forming. The commercial membrane for comparison did not lose any permeability when exposed to samples containing carbonaceous samples, however became completely impermeable when exposed to sulphur. This indicates that these alloys are most suitable for metrology purposes due to their low reactivity.

5.1 Introduction

In order to improve the accuracy and reduce the cost of hydrogen impurity enrichment a suitable membrane composition must be found. In addition to this all previous studies used a commercial palladium-based membrane and in all cases it was noted that certain impurities reacted with the membrane. This interaction had the result of changing the composition of the enriched gas mixture and therefore reducing the final accuracy of the measurement. [1, 2] The self-supported commercial membranes used in both studies are also generally between 20-100 μm in order to provide sufficient mechanical strength for a membrane. However, for palladium membranes to be economical this thickness must be reduced to about 1-5 μm giving the added benefit of greater flux and therefore lower enrichment times.

Palladium alloy membranes are generally created by forming an alloy with silver, copper or gold. By doing this the hydrogen embrittlement effect can be effectively mitigated. Using alloys has the added benefits of decreasing the overall amount of palladium required in the film, driving up their cost effectiveness, and in some cases increasing the flux of the membrane to higher levels achievable than a pure palladium membrane. In the previous chapter a number of membrane compositions were simulated using DFT which predicted their ability to resist certain classes of ISO 14687-2 impurities. The best membranes being identified as PdAu₂₀ and PdAu₂₀Cu₁₀ for carbonaceous impurities. For sulphur containing impurities PdCu₂₀Zr₁₀, PdAu₂₀Zr₁₀, and PdAu₂₀Cu₁₀ were the most resistant to binding with H₂S. In this chapter these membranes will be manu-

factured and tested under environments containing these gases in order to verify these results, and quantify the level of reactivity. In addition to these alloys, PdCu₂₀Ag₁₀ and PdAu₂₀Ag₁₀ will be synthesised due to their strong performance in the previous chapter. PdAg₂₃, PdCu₂₀ and PdCu₄₀ will also be synthesised as these are popular membrane compositions in literature and act as a good benchmark in addition to the commercial membrane. Due to the high cost of sputtering gold a decision was made to not manufacture the PdAuZr composition

Palladium alloy membranes will be deposited onto porous YSZ supports using both electroless plating and closed field unbalanced magnetron sputter ion plating as described in sections 3.4.2 and 3.4.2. This will have the combined effect of reducing the amount of palladium used, driving down their cost, and increasing the flux, and therefore reducing the time taken to enrich a hydrogen sample. The degree of interaction of impurities with the surface of the membrane will be quantified using a three-step experimental procedure. The pure hydrogen flux of each membrane composition will be measured and the membranes hydrogen permeability calculated as a base line. The following two permeation tests will measure the change in permeability resulting from introducing part-per-million level impurities into the gas sample. The change in permeability which results from this will act as a measure for the membranes tendency to interact with different impurity types. Additionally, at all three testing stages, X-ray photoelectron spectroscopy (XPS) will be performed on the surface of the membranes to investigate how the composition on the surface of the membrane changes when exposed to each impurity environment. This will allow the alloy segregation behaviour to be observed, and more importantly, quantify the amount of sulphur which has reacted with the surface of the membrane.

Table 5.1: Membrane compositions analysed by EDS and their thickness measured using FIB-SEM

Membrane ID	Manufacturing technique	Composition (wt%) (+- 1% Relative)					Thickness (μm)
		Pd	Cu	Ag	Au	Zr	
PdCu (fcc)	Magnetron Sputtering	76.24	23.76	-	-	-	1.68
PdCu (bcc)	Magnetron Sputtering	43.24	56.64	-	-	-	1.66
PdCuZr	Magnetron Sputtering	72.10	14.46	-	-	13.54	1.54
PdAg	Electroless Plating	65.55	-	34.45	-	-	0.57
PdAu	Electroless Plating	74.7	-	-	25.3	-	1.17
PdCuAg	Electroless Plating	72.1	-	8.27	19.58	-	0.87
PdCuAu	Electroless Plating	63.90	13.6	-	22.1	-	1.55
PdAuAg	Electroless Plating	60	-	11.2	28.3	-	0.74

5.2 Results and Discussion

5.2.1 Membrane characterisation

Figure 5.1 (a)-(g) shows the cross-sectional SEM images of the manufactured membranes. The thickness of the fabricated membranes are shown in 5.1 and ranged from 573 nm to 1.579 μm . In general thinner layers were achieved using electroless plating although theoretically sub-micron layers are possible through magnetron sputtering, examples of this being SINTEF's patented sputtering process.[3] The integrity of the manufactured membranes was measured using the procedure laid out in section 3.4.3. All membranes showed no leakage when pressurised to 10 bar indicating that all membranes were uniform, pinhole free and therefore suitable for hydrogen separation. [4]

The surface composition of each membrane was measured by XPS and is shown in Table 5.1. A wide range of compositions were fabricated. From phase data on the PdCu system [5, 6] both varieties of PdCu membranes (bcc phase and fcc phase) were successfully fabricated.

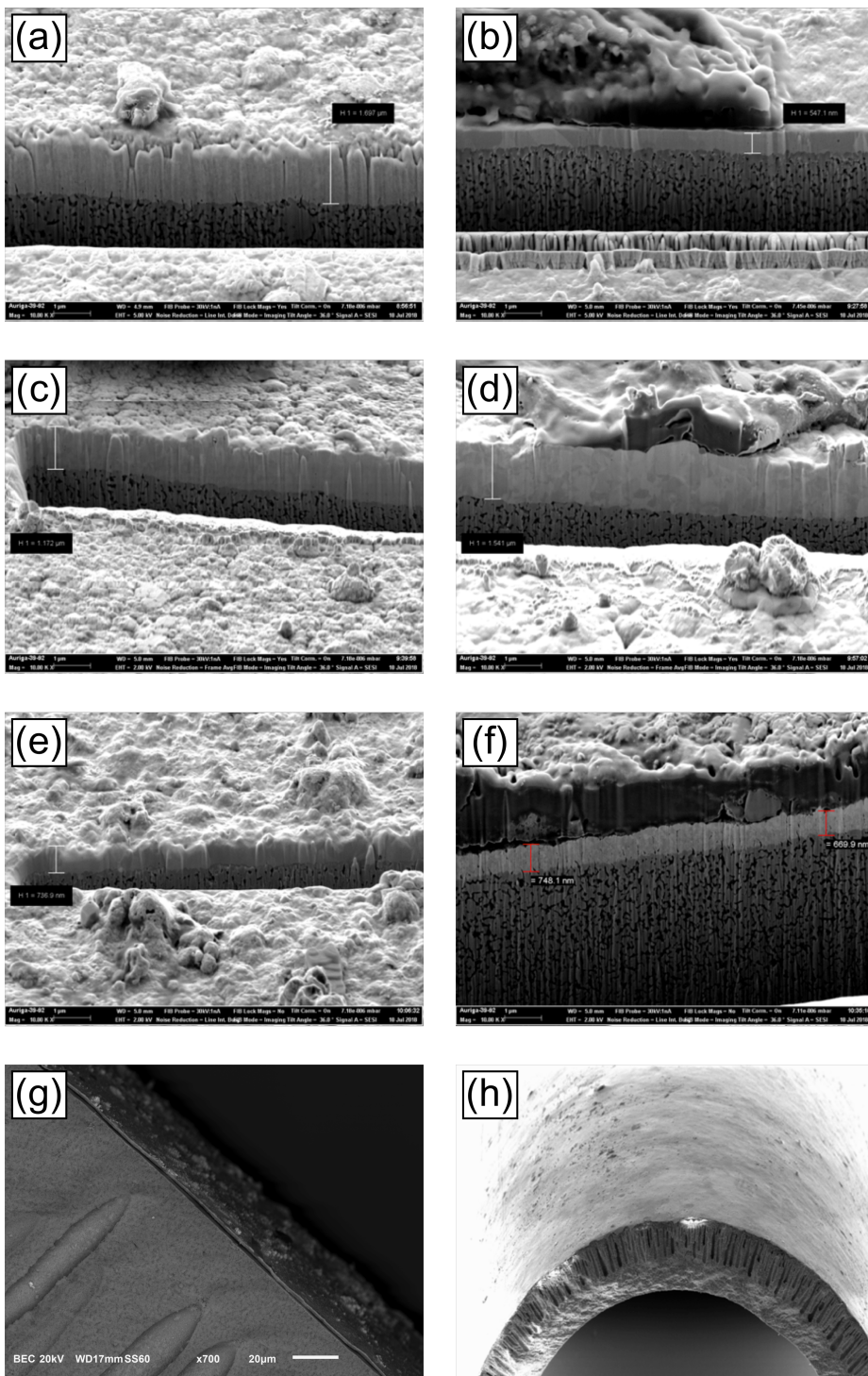


Figure 5.1: SEM images of fabricated membranes (a) PdCu (fcc) (Sputtering) (b) PdAg (ELP) (c) PdAu (ELP) (d) PdCuZr (Sputtering) (e) PdAgAu (ELP) (f) PdCuAg (ELP) (g) PdCu (bcc) (Sputtering) (h) typical cross section

5.2.2 Hydrogen permeation

Table 5.2 shows the hydrogen permeation through the 9 tested membranes at steady state after 12 hours of operation. As expected, hydrogen permeation flux increases with the elevated temperatures. Moreover, the mass transfer resistance of the substrate will not represent major limitations since its gas transport resistance is negligible compared to that of the dense palladium alloy layer [4]. Deposited layers were all on the scale of 0.5-2 μm which from previous research indicates the main rate limiting step in hydrogen permeation being the thickness of the membrane layer. [7] The palladium copper alloy which was in the bcc phase showed the highest hydrogen permeability of all the synthesised membranes which was expected as discussed in section 2.5.1. The membrane which showed the lowest hydrogen permeability was the PdCuZr membrane, this is likely due to the combined effects of the alloy having the lowest concentration of palladium compared to the other synthesised membrane, increasing the transport resistance of the membrane, and this composition having a lower preference to hydrogen binding as all other palladium alloys as predicted in the simulations performed in section 4.2.2 and shown in figure 4.2. The PdAu and PdAuAg membranes both showed low permeabilities. Gold as an alloying material traditionally does not show much increase in permeability [8] but is instead used to suppress the effects of impurities on the membrane, [8] which is the main goal of this study. Despite the fact that the commercial membrane is also based on PdAgAu, the membrane manufactured through electroless plating has a lower permeability due to the high gold concentration. It is likely that the concentration of silver in the commercial membrane is closer to 23%, which is the optimal value for hydrogen permeation, and it's gold concentration is much lower than the electroless plated membrane. Both PdCuAg and PdCuAu had reasonably high hydrogen permeabilities. While none of these membranes showed a hydrogen permeability as high as the commercial alloy, it should be noted that the commercial membrane had

Table 5.2: Pure hydrogen permeability of studied alloy membranes under pure hydrogen at 300°C and 1 bar pressure differential

Membrane ID	Permeability (mol m ⁻¹ s ⁻¹ Pa ^{1/2} × 10 ⁻⁸)
PdCu (fcc)	1.30
PdCu (bcc)	1.68
PdCuZr	0.14
PdAg	0.94
PdAu	0.33
PdCuAg	1.22
PdCuAu	1.43
PdAuAg	0.19
Commercial (REB)	5.71

Table 5.3: Permeability results for all membranes under both impurity conditions

Membrane ID	Permeability (mol m ⁻¹ s ⁻¹ Pa ^{1/2} × 10 ⁻⁸)			% Drop	
	Pure H ₂	Non-Sulphur	Sulphur	Non-sulphur	Sulphur
PdCu (Fcc)	1.30	0.22	0.19	80%	86%
PdCu (Bcc)	1.68	0.72	2.47	55%	85%
PdCuZr	0.14	0.12	0.10	12%	26%
PdAg	0.94	0.12	0.01	88%	92%
PdAu	0.33	0.17	0.21	51%	35%
PdCuAg	1.22	0.48	0.30	61%	75%
PdCuAu	1.43	0.79	1.07	45%	25%
PdAuAg	0.19	0.16	0.14	16%	27%

a much larger thickness resulting in a much higher cost and lower flux values than the composite membranes.

5.2.3 Impurity reactivity

Table 5.3 shows the results of hydrogen permeation under the presence of the two different impurity conditions discussed in Table 5.3 compared to the pure hydrogen permeability values shown in Table 5.2. The permeability data was taken once the flux had reached steady state after 12 hours of operation. For all membranes there was a reduc-

tion in permeability when the membranes were exposed to impurities. The magnitude of this reduction compared to the pure hydrogen permeability is used as an indication of the degree of interaction between the membrane and the impurities. Table 5.4 shows the composition of each membrane in between each test in order to measure permanent surface reactions and segregation behaviour of the alloys under the chosen impurities.

Binary alloys

In non-sulphur tests the PdAg binary alloy was the worst performing, with the permeability dropping by 88% of its original value. This was expected as the addition of silver to a palladium system, while effective at increasing the permeability, does not contribute much to impurity resistance. [9] This was further supported by the results of the sulphur tests where the permeability dropped by 92% and composition analysis in Table 5.4 showing that sulphur was present in 42% of the surface. The PdAg alloy also showed a large degree of segregation behaviour under non-sulphur impurities which likely contributed to the large reduction in flux, with silver concentration increasing to 75% at the top 10 nm of the sample, resulting in a large drop in permeability.

Interestingly the PdCu membrane with a composition in the bcc phase showed higher resistance to non-sulphurous impurities than the fcc phase, with the former only experiencing a 55% drop in permeability compared to an 80% drop in permeability in the latter. This again seems to be a result of the segregation behaviour of the alloy, with the PdCu alloy in the fcc phase experiencing a large amount of segregation, with the palladium concentration increasing to around 90% on the retentate side. Conversely the PdCu composition in the bcc phase membrane only changed slightly. The XPS analysis showed that while the reactivity of sulphur on the surface of both copper based binary membranes was of a similar magnitude, the bcc phase had a slightly lower resistance, with 29% of the surface containing sulphur after exposure to sulphurous impurities as opposed to the 25% shown by the fcc phase alloy.

The PdAu alloy showed the best impurity resistance out of the binary alloys tested under both impurity conditions, with only a 51% and 35% drop in permeability under non-sulphur and sulphur conditions respectively and only a 12% concentration of sulphur was observed on the surface after XPS analysis. The alloy showed slight segregation of gold away from the permeate surface under non-sulphur impurity conditions likely due to the fact the difference in interaction strength between gold and palladium with the components of the gas mixture varies widely, with many gases preferentially adsorbing on palladium [10].

Table 5.4: XPS composition analysis of the palladium alloy membrane surfaces after impurity tests

Membrane ID	Pure Hydrogen Exposure					Non-Sulphur Exposure					Sulphur Exposure					
	Pd	Ag	Au	Cu	Zr	Pd	Ag	Au	Cu	Zr	Pd	Ag	Au	Cu	Zr	S
PdCu (Fcc)	65.5	-	-	35.5	-	92.5	-	-	7.5	-	67.5	-	-	7.5	-	25.0
PdCu (Bcc)	44.0	-	-	66.0	-	54.9	-	-	45.2	-	40.0	-	-	31.0	-	29.0
PdCuZr	63.6	-	-	22.6	13.8	64.4	-	-	27.5	8.5	54.2	-	-	27.0	8.0	10.8
PdAg	65.5	34.5	-	-	-	25.0	75.0	-	-	-	29.0	29.0	-	-	-	42.0
PdAu	75.0	-	25.0	-	-	82.9	-	17.1	-	-	71.0	-	16.0	-	-	13.0
PdCuAg	64.6	9.1	-	26.3	-	8.6	8.9	-	82.5	-	6.0	5.0	-	64.0	-	25.0
PdCuAu	63.9	-	22.5	13.6	-	84.9	-	1.5	13.6	-	65.3	-	1.0	18.5	-	15.2
PdAuAg	60.0	11.7	28.3	-	-	47.2	49.8	3.0	-	-	52.0	35.0	1.0	-	-	12.0

Ternary alloys

Five ternary alloy compositions were tested including the commercial alloy. The commercial alloy had the highest permeability of all ternary alloys with a value of $5.71 \text{ mol m}^{-1} \text{ s}^{-1} \text{ Pa}^{-0.5} \times 10^{-8}$ under pure hydrogen and $4.28 \text{ mol m}^{-1} \text{ s}^{-1} \text{ Pa}^{-0.5} \times 10^{-8}$ under non-sulphur conditions, a drop in permeability of 25%. However, the commercial membrane nearly lost all of its permeability under sulphurous conditions. The PdAuAg membrane manufactured through electroless plating performed better under both impurity conditions than the commercial alloy despite being based on the same composition, only seeing a 16% and 27% drop in hydrogen permeability under non-sulphur and sulphur conditions respectively compared to a 25% and 96% drop shown by the commercial alloy. The high levels of gold likely contributed to the low levels of sulphur on the surface of the electroless plated PdAuAg membrane. These results indicate that the composition of the commercial membrane, while ideal for separation, does not contain enough gold to withstand the levels of sulphur impurities expected for analytical purposes.

The worst performing ternary alloy was the PdCuAg alloy which showed large permeability drops under all conditions, 61% under non-sulphur and 75% under sulphurous conditions. In addition to these, large degrees of segregation were observed under non-sulphur impurities, with the palladium concentration at the surface dropping to 8.5 wt%, showing that the alloy is not completely stable under the varying conditions expected during analytical purposes.

Both gold containing ternary alloys, PdAuAg and PdCuAu, performed well under sulphur conditions, with the PdCuAu alloy only reducing in permeability by 25% and the PdAgAu membrane by 27%. The PdCuAu membrane however had a stronger interaction with non-sulphur impurities, indicated by the permeability drop of 45% when exposed to the non-sulphur containing gas sample. This drop is likely due to the segregation of palladium to the surface with the XPS data indicating an increase of palladium to

the surface to 84.9 wt% from 63.9%. The best performing ternary membrane was the PdCuZr membrane which showed the smallest drop in permeability of only 12% non-sulphur conditions, and a permeability percentage drop of 26% under sulphur conditions which on a similar magnitude to that of the gold containing alloys.

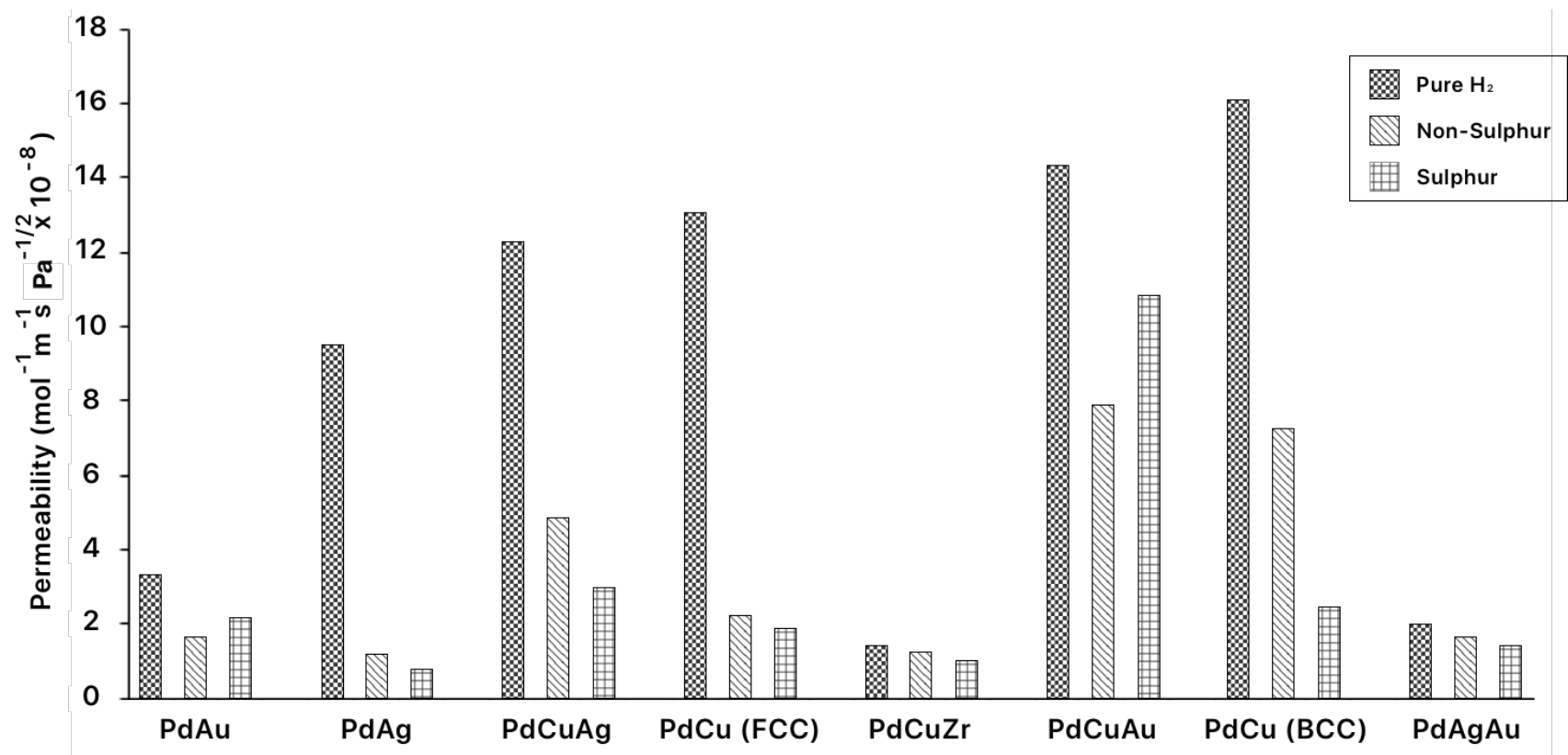


Figure 5.2: Permeability data for pure hydrogen, non-sulphur, and sulphur permeation tests

Segregation behaviour

All membranes tested showed some degree of segregation with the two thinnest membrane samples, PdAg (0.573 micron), PdAuAg (0.736 micron) and PdCuAg (0.873 micron) all showing the highest degrees of segregation. While this may still be a property of the alloy compositions it may also indicate that sub-micron palladium alloys layers are unstable and there may be a minimum thickness for alloys, below which the membrane layer is unstable and frequently varies during operation.

5.2.4 Relationship to DFT results

The previous chapter attempted to use DFT generated binding energies to predict the performance of alloy compositions in environments containing ISO 14687-2 impurities. While a useful analysis it appears in some cases that these results were not completely correct and could be improved in further studies.

For carbonaceous environments the model predicted that PdAu₂₀ and PdAuCu would be the best performing alloys. PdAuCu experienced a 45% drop in permeability under carbonaceous environments while PdAu₂₀ experienced a 51% drop. Which while showing reasonable resistance, were inferior to both the PdCuZr and PdAuAg alloys which only experienced a 12% and 16% drop respectively. For the PdAuAg alloy the model did indeed predict that it would resist adsorption to these impurities, and agrees with the conclusion of this analysis that the addition of gold and silver improves the alloys resistance to carbonaceous impurities. However these results appear to be completely incorrect, with all models predicting that the alloy would be more susceptible to poisoning.

The model fared better when predicting the influence of sulphurous impurities on the surface of the membrane. The model successfully predicted that both PdCuAu and PdCuZr alloys would be the most resistant to sulphurous environments. The model

appears to be accurate in predicting how the other alloys would react in the environment, indicating the PdAg, PdCuAg, and both FCC and BCC PdCu alloys would perform poorly and see severe levels of sulphur poisoning. It should be noted that many of the results in this section were close and other alloys which performed reasonably well against sulphur poisoning (PdAu₂₀ and PdAuAg) could be as a result of the error between simulations.

The DFT simulations were a useful tool in predicting the sulphur resistance of the alloys, however when used to predict the behaviour of weaker adsorbing compounds, such as the carbonaceous impurities, it appears to break down. This is likely due to the fact that DFT is not as effective at simulating the behaviour of weaker bonds as discussed in section 2.6.2. Alternative methods should be explored if these interactions are to be predicted.

5.3 Conclusion

In order to identify a suitable palladium alloy composition for hydrogen impurity enrichment, eight different membrane compositions were manufactured and tested under three different hydrogen conditions against a commercial palladium membrane. Two different measures were used to compare the membrane compositions suitability for hydrogen impurity enrichment, the permeability deviation from the pure hydrogen permeability was used as an initial indicator of interaction between the alloy and impurities, and the surface composition was measured to detect any impurities which had permanently reacted with the membrane.

The best performing membrane, and therefore the most suitable for hydrogen impurity enrichment was the PdCuZr alloy, which only showed a 12% and 26% drop in permeability under non-sulphur, and sulphur conditions, and low levels of sulphur on the surface. The permeability of this alloy was low, however, surface areas could eas-

ily be scaled up to increase the speed of hydrogen enrichment. For the purpose of our application reducing reactivity with the surface is more important due to the results of an accurate enrichment being dependent on the gas composition not changing. While higher permeability will result in higher fluxes and therefore faster enrichment times, it should not be increased at the expense of using a more reactive membrane composition.

In the following chapter this membrane will be used in the design of the hydrogen impurity enrichment device and it's performance measured when tested with a real hydrogen fuel sample.

References

- [1] Arul Murugan and Andrew S Brown. Advancing the analysis of impurities in hydrogen by use of a novel tracer enrichment method. *Analytical Methods*, 6(15):5472, 2014. doi: 10.1039/c3ay42174k.
- [2] Shabbir Ahmed, Sheldon H D Lee, and Dionissios D Papadias. Analysis of trace impurities in hydrogen: Enrichment of impurities using a H₂ selective permeation membrane . *International Journal of Hydrogen Energy*, 35(22):12480–12490, 2010. doi: 10.1016/j.ijhydene.2010.08.042.
- [3] T. A. Peters, T. Kaleta, M. Stange, and R. Bredesen. Development of thin binary and ternary Pd-based alloy membranes for use in hydrogen production. *Journal of Membrane Science*, 383(1-2):124–134, 2011. ISSN 03767388. doi: 10.1016/j.memsci.2011.08.050. URL <http://dx.doi.org/10.1016/j.memsci.2011.08.050>.
- [4] Ana Gouveia Gil, Miria Hespanhol M Reis, David Chadwick, Zhentao Wu, and K Li. A highly permeable hollow fibre substrate for Pd/Al₂O₃ composite membranes in hydrogen permeation. *International Journal of Hydrogen Energy*, 40(8):3249–3258, 2015. ISSN 0360-3199. doi: <https://doi.org/10.1016/j.ijhydene.2015.01.021>. URL <http://www.sciencedirect.com/science/article/pii/S0360319915000580>.
- [5] Fernando Roa and J Douglas Way. Influence of Alloy Composition and Membrane Fabrication on the Pressure Dependence of the Hydrogen Flux of Palladium-Copper

Membranes. *Ind. Eng. Chem. Res*, 42(23):5827–5835, 2003. ISSN 08885885. doi: 10.1021/ie030426x.

- [6] Shahrouz Nayebossadri, John Speight, and David Book. Development of Pd – Cu Membranes for Hydrogen Separation Why Hydrogen Separation ? 2013.
- [7] Tina M Nenoff Nathan W. Ockwig. Membranes for Hydrogen Separation. *Chemical Reviews*, 107:4078–4110, 2007.
- [8] Chao-Huang Chen and Yi Hua Ma. The effect of H₂S on the performance of Pd and Pd/Au composite membrane. *Journal of Membrane Science*, 362(1-2):535–544, 2010. doi: 10.1016/j.memsci.2010.07.002.
- [9] T A Peters, J M Polfus, M Stange, P Veenstra, A Nijmeijer, and R Bredesen. H₂ flux inhibition and stability of Pd-Ag membranes under exposure to trace amounts of NH₃. *Fuel Processing Technology*, 152:259–265, 2016. doi: 10.1016/j.fuproc.2016.06.012.
- [10] Sabina K. Gade, Sarah J. DeVoss, Kent E. Coulter, Stephen N. Paglieri, Gökhan O. Alptekin, and J. Douglas Way. Palladium-gold membranes in mixed gas streams with hydrogen sulfide: Effect of alloy content and fabrication technique. *Journal of Membrane Science*, 378(1-2):35–41, 2011. ISSN 03767388. doi: 10.1016/j.memsci.2010.11.044. URL <http://dx.doi.org/10.1016/j.memsci.2010.11.044>.

Chapter 6

Designing an improved hydrogen impurity measurement device for measuring ISO 14687 impurities

Abstract

In this chapter, the NPL Hydrogen Impurity Enrichment Device previously reported in [1] was modified and improved to:

- Develop a method to add krypton trace to sampling cylinder before hydrogen sampling
- Provide new design that is inherently safer and automated
- Provide automated calculation of enrichment factor

Through the use of automation and optimisation of parameters the design of the enrichment device was improved to create a more efficient, safer, and user friendly device to meet the requirements of hydrogen impurity laboratories. PID temperature control

was implemented, allowing greater control of the heating rate and temperature within the enrichment device, preventing damage to the membrane which earlier designs were lacking. Temperature and pressure monitoring was also implemented and fed into a microcontroller which allows the operator to continuously monitor the process paraments, and calculated enrichment factor in real time.

6.1 Introduction

Now that appropriate membrane compositions have been found, a number of improvements must be made to the hydrogen impurity enrichment device in order to make it suitable as a commercial process and product for measurement of ISO 14687-2 impurities. All previous devices used were extremely manual and required close operator attention to ensure the experiment performed correctly. All enrichment factor calculations discussed in section 3.6 must also be calculated by hand, after the experiment has been performed, limiting the ability for the operator to plan the experiment in advance. In addition to this the krypton enrichment method which was identified as the best method for calculating the enrichment factor in section 2.4 but no procedure is in place to instruct operators on how to add this krypton to their sampling vessel.

This chapter will provide a method for taking krypton spiked samples from a hydrogen refuelling station, improve the hydrogen impurity enrichment device through automation to improve the usability of the device, while providing real time results for the user.

6.2 Addition of krypton for tracer enrichment

Past studies using tracer enrichment have simply added the krypton required when making a gas mixture through loop addition [1], allowing for a known quantity of krypton

to be added prior to any test. While this is appropriate when making a mixture from scratch, it is unsuitable for sampling from a hydrogen refuelling station, as the low pressure krypton cannot be added to a sample already taken. While there are some studies that have succeeded in adding low pressure gas to a high pressure sample using cryoegnics [2], these tests were on a small scale and were deemed unsuitable for HRS sampling. The only available option for spiking of the hydrogen samples was to add a known quantity of krypton to the already empty vessel, and analyse the final concentration of krypton afterwards to use in the enrichment factor calculations. The disadvantage of this method is that it adds an extra, higher uncertainty associated with the GC used to measure the krypton concentration. There are three variables which will effect the final krypton concentration added to the cylinder to allow for tracer enrichment; the sampling vessel volume, the sample fill pressure from the hydrogen refuelling station, and the mass of krypton added.

It is standard for hydrogen samples to be taken using a 10L vessel, although in the future operators may wish to take larger samples using a 50L cylinder, or smaller samples using a 1L cylinder. Although theoretically any sample size could be taken, these are generally the standard sample sizes used for metrology purposes and will be the only ones considered. The fill pressure of the sample has previously found to be unpredictable since it relies on sampling in line with a FCEV. Because of this, the final fill pressure of the sample cylinder be proportional to the amount of fuel remaining in the car. Despite this samples are generally not taken above 10 MPa for safety reasons.

It was decided that the best procedure is to add a set mass of krypton to the desired sampling vessel prior to sampling taking place. The krypton is added to the evacuated sample cylinder using the procedure outlined in section 3.2. The sample can then be filled from the HRS using the procedure outlined in section 3.3 and the mole fraction of krypton measured using the gas analysis procedure outlined in section 3.2. 16ENG01 MetroHyVe

states that hydrogen samples should contain 1-10 $\mu\text{mol/mol}$ of krypton. Using the ideal gas law the mass of krypton required to ensure the krypton concentration stayed within these bounds was calculated. It was found that for samples below 10bar it was not possible to keep the concentration of krypton within the bounds of 1-10 $\mu\text{mol/mol}$ and therefore it is recommended to ensure a sample higher than this is taken in order to ensure a reasonably high enrichment factor can be achieved during the subsequent experiments. The predicted concentrations of krypton compared to fill pressures at an assumed temperature of 20°C were calculated and shown in figure 6.1. The results show that for a 1L cylinder 30.8 mg Kr should be added, for a 10L cylinder 300.79mg, and for a 50L cylinder 1484mg. This is enough to ensure concentrations between 1-10 $\mu\text{mol/mol}$ are achieved in pressures between 10-100 bar.

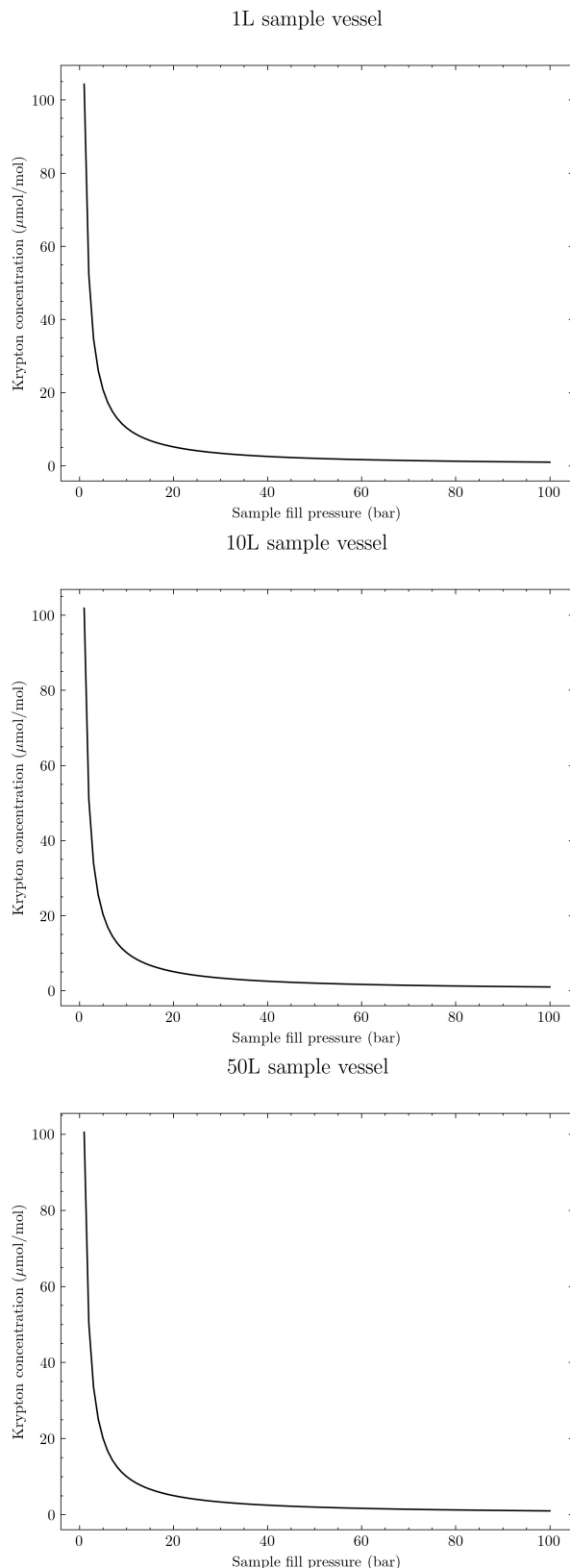


Figure 6.1: Predicted concentration of krypton within hydrogen samples in; 1L cylinder (30.8 mg Kr), 10L cylinder (300.79 mg Kr), 50L cylinder (1484 mg Kr)

6.3 Improvements

The aim of this section is to design an improved hydrogen impurity enrichment device which balances cost, accuracy and is operator-friendly. Automation will be taken into account in anticipation of the larger number of samples for analysis in the future and to improve the overall user experience. The goals of this section are to:

- Improve reliability by providing greater control over process parameters
- Improve safety by adding additional interlocks
- Improve user experience through in-situ process monitoring and data analysis

Previous enrichment devices in literature can be described as early prototypes.[3] [1] In order to make the enrichment device commercially viable it must first be made more reliable. Greater control must be implemented over the pressures and temperatures within the device in order to ensure the membrane is not damaged inadvertently. Since the enrichment device operates by heating hydrogen to 300°C, adequate safety is of high concern. Previous enrichment devices in literature were lab scale, with the only safety measures in place being those in the lab. Further safety and interlocks must be added to the enrichment device to ensure in the event of equipment failure the system can shut down safely. Finally all past devices involved the user manually recording important process values by hand, which is unintuitive, susceptible to errors, and does not allow easy monitoring system. An intuitive interface between the operator and the system will be added in order to automatically calculate output values such as the CEF, delivering this to the operator along with other important process parameters.

The redesigned HIED is shown in figure 6.2. All tubing and pressure fittings were supplied by Swagelok [4] and the system was manufactured by Strata Technology London. [5]

The system is split into two units, the stationary unit and the transportable unit. The stationary unit is the bulk of the system, and contains piping to transport the gases to the enrichment device, connections for two gas cylinders for nitrogen (Q1) and the hydrogen sample to be tested (Q2), pressure relief valves (PSV001 & PSV002), and connections to the vacuum system and gas vents.

The transportable unit contains the enrichment vessel, heating and temperature control equipment, and the membrane. The enrichment vessel is a 300 cm³ sulfurnert [6] treated vessel. The membrane is connected to one end of the vessel and operates in dead end mode.

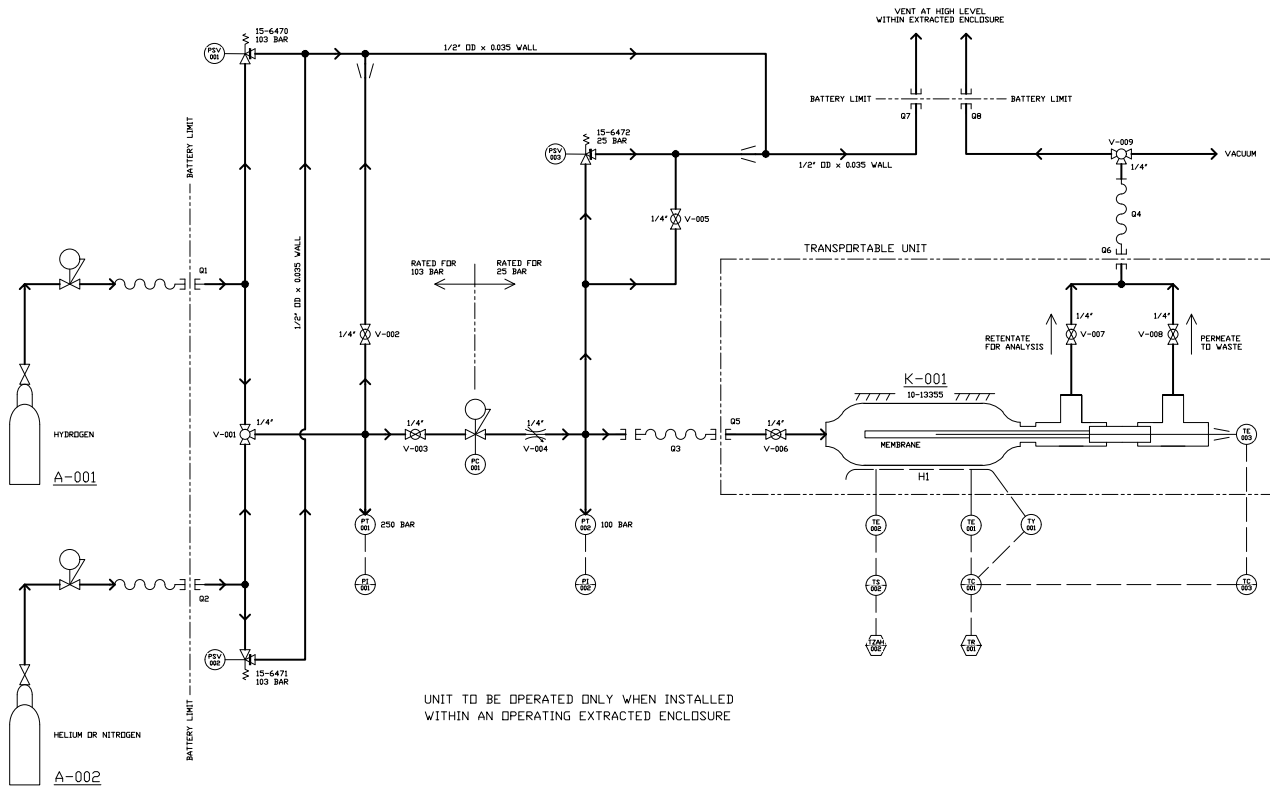


Figure 6.2: P&ID for the redesigned hydrogen impurity enrichment device

6.3.1 Safety

It was decided that a nitrogen cylinder should be added to the system in order to ensure safety. Prior to evacuating the enrichment device the system should be purged 7 times with nitrogen as this is adequate to reduce the concentration of gases remaining in the vessel, in particular the oxygen in air and any leftover hydrogen from previous tests, to a low enough level where it is not dangerous. [7] The enrichment device must be evacuated to a high vacuum before testing in order to ensure integrity of the results. Many commercially available vacuum systems are not safe for use in explosive environments, therefore purging with nitrogen is a requirement before any procedures are to take place in the system.

Two pressure relief valves were added to the system. PSV001 is the safety interlock on the stationary unit and is set at 103 bar bar ensuring that in the event a higher pressure cylinder is connected to the system, there are sufficient safety measures in place. PSV002 is the pressure relief valve for the transportable unit, although is only in operation when it is connected to the stationary unit. PSV002 is set to 25 bar in order to prevent overpressurisation of the membrane. This pressure relief valve is critical when operating the enrichment device as the pressure initially in the enrichment vessel is at ambient temperature. As the enrichment vessel heats to the desired operating temperature, this pressure will increase, and since the enrichment vessel operates in dead end mode it is the only way out the system. This will cause the pressure within the enrichment vessel to potentially increase above the temperature rating of the membrane, resulting in failure. The pressure within the enrichment vessel is set using pressure controller PC001, effectivley creating two safety interlocks for the enrichment vessel. In the event of a pressure relief valve being triggered the gas will be automatically purged from the system through the vent.

A temperature shutoff was also added to the enrichment vessel to act as an interlock

in the event temperature control breaks down. There are three thermocouples (TE001, TE002 and TE003) on the enrichment vessel. TE003 is for controlling and monitoring the temperature of the membrane, while TE002 is for monitoring the temperature outside the vessel. TE003, which also measured the temperature outside the vessel, is connected to a temperature cut off, which is set 25°C above the setpoint temperature of the enrichment vessel. If the recorded temperature outside of the enrichment vessel passes this threshold the heater will activate a trip, cutting off electricity until the device is checked by the operator.

6.3.2 Usability

The main improvement to the usability is through the segmentation of the system into the stationary unit and transportable unit which is shown in figure 6.3. Bench space in a lab is often limited so often it is not always possible to place the enrichment device next to the analyser that will be used following enrichment. Previous iterations of the enrichment device required either transporting the whole device, which is a difficult and potentially dangerous task, or disconnecting the swagelok fittings and transporting the vessel this way. While swagelok fittings can technically be disconnected and reconnected, it is not recommended since they are designed to be permanent pressure fittings, and the more times this operation is repeated, the faster components will have to be replaced.

The transportable unit replaces the swagelok fittings which are most often disconnected with VCR fittings, which are designed for disconnection and reconnection. The transportable unit also contains connections for the thermocouples connected to the temperature monitoring and control system, and the electrician connection to the system which are all designed for easy removal and reconnection. Finally the ergonomics of transporting the device have been improved through addition of a handle, allowing for easy transportation without unintentionally placing any strain on the pressure fittings.

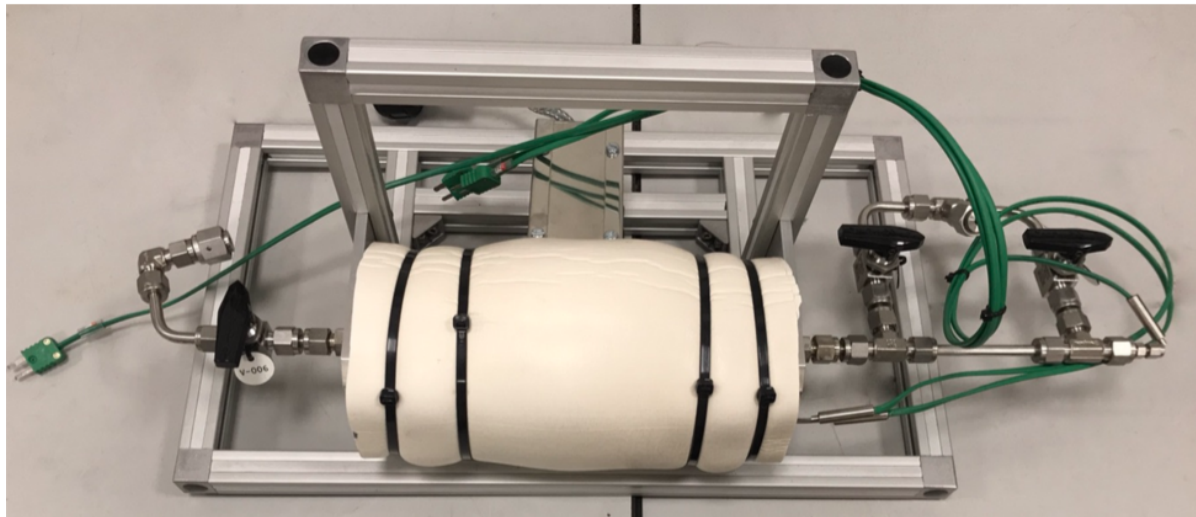


Figure 6.3: Disconnected transportable unit

The result of this is less instances of breaking and reconnecting fittings. As the system has been split into the stationary unit and transportable unit, the pressure fittings will gain an increased lifespan. Since the system is stationary it can benefit from being permanently connected to an evacuation rig and nitrogen supply. In the event of leakage multiple valves are implemented to allow the user to isolate different parts of the system in order to identify and replace the leaking component.

Finally the new system gives the the ability to easily control the temperature of the system. Previously the temperature controller was hardwired in, giving the user little control over the setpoint and temperature ramp of the device. With the new system these values can be controlled easily directly through the temperature controller, or using a microcontroller connected to the temperature controller, allowing more options for the operator.

6.3.3 Automation

There are two main factors to control for the enrichment device, the temperature and pressure. In past iterations of these systems control and measurement was done manually

and hardwired into the system. By implementing adequate systems to measure and control these values operation of the system becomes easier, safer and more reliable

The temperature of the enrichment vessel is changed using heating tape wrapped around the heating tape, and then covered in several layers of insulation. Pressure is controlled using a tamper proof temperature controller.

The original system used an On/Off temperature controller, which simply measured the temperature using a thermocouple placed inside the membrane (TE003, figure 6.2), when the temperature rises above the setpoint the heater is switched off, when it drops below the heater is switched back on. The solution was unreliable, for example when the temperature setpoint was set at 300°C, the average value recorded was 302.7°C, with a standard deviation of 5°C. This is shown in figure 6.4.

The system was upgraded with a PID temperature controller (OMRON), which continuously calculates an error value as the difference between a desired setpoint (SP) and a measured process variable (PV) and applies a correction based on proportional, integral, and derivative terms. This change in control loop mechanism improved the overall control of the system, bringing the average temperature recorded over 1 hour down to 302.7°C and the standard deviation down to 1.78°C.

The pressure controller (PC001, figure 6.2) is considered reliable, as it can be set at a fixed pressure, which cannot be changed accidentally by the user. The issue with reliability came from the measurement of pressure. Originally only one pressure sensor was used to measure the pressure inside the enrichment vessel (K-001), with the pressure of the sample cylinder used to calculate the enrichment factor only being measured once before and after the test. Two high resolution pressure sensors (Balluff) were added before and after the pressure controller so that both of these values could be monitored during the experiments.

Data collection and processing was done manually and no automation was involved.

Comparison of control methods for enrichment temperature

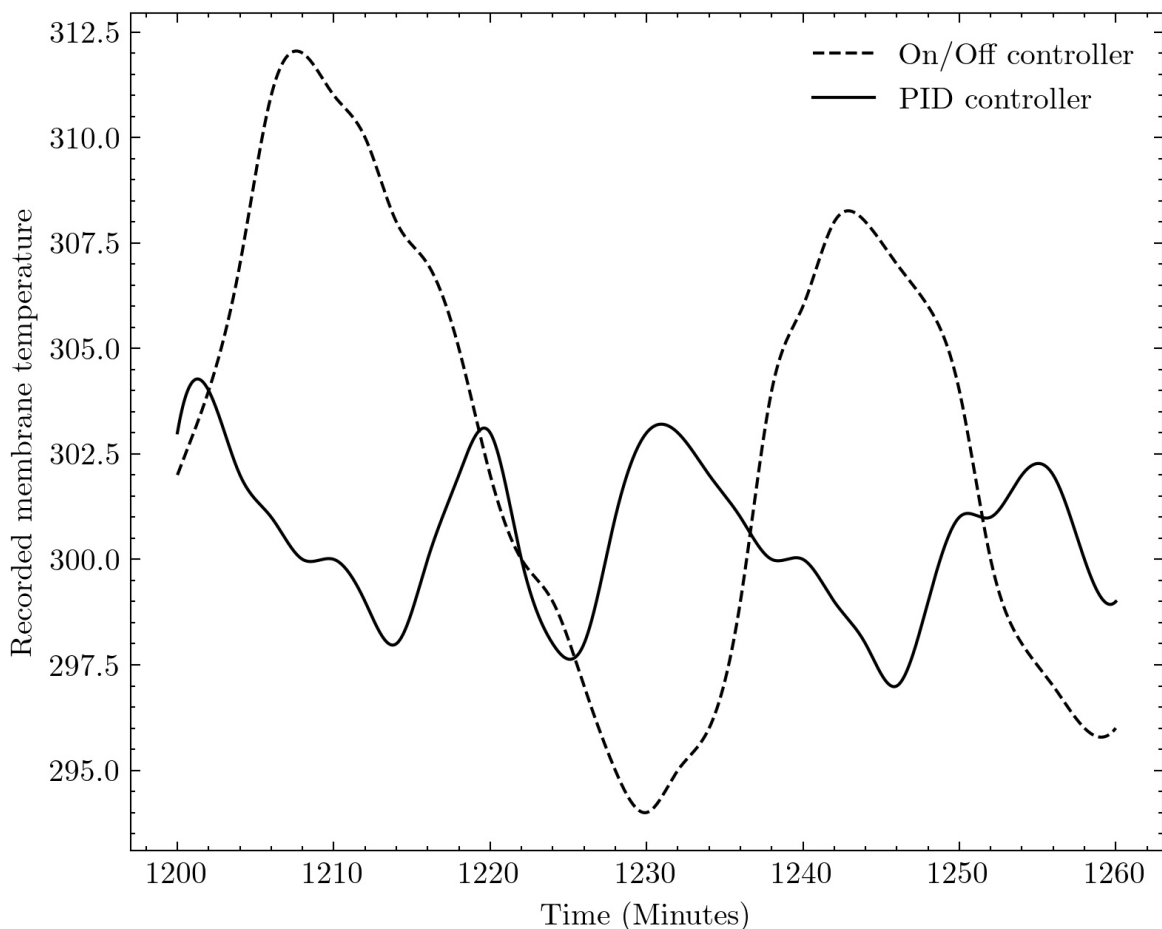


Figure 6.4: Comparison of the On/Off temperature controller and PID temperature controller over a 1 hour period

The main improvement in the new system involved the use of a microcontroller to automatically log process variables. These values were stored for later processing by the user. A data analysis script was also prepared in order to estimate the time remaining for the experiment to reach the desired enrichment factor, and the current enrichment factor achieved. At the beginning of the experiment the user had the option of entering their desired enrichment factor. If entered this would be stored and the experiment would start. The system would then automatically log the initial pressures of the, hydrogen cylinder and enrichment vessel as $P_{1,a}$ and $P_{2,a}$, and the initial temperature of the enrichment vessel as $T_{1,a}$ and $T_{2,a}$ for the non ideal gas law enrichment factor (equation 2.18). The script would then continuously measure values for $P_{1,b}$, $P_{2,b}$, and $T_{2,b}$ and use them to calculate the current non-ideal gas law enrichment factor in real time. Note it was assumed the temperature of the sample cylinder ($T_{2,a}$) would remain constant at ambient temperature. This process is shown in pseudocode in figure 6.5. It should be noted that it was only possible to calculate the non-ideal gas law enrichment factor in real time as it is not possible to continuously monitor the concentration of the inert tracer molecule in the enrichment vessel.

It has already been concluded in section 2.4 that the tracer enrichment method is the best method for calculating the enrichment factor and therefore this method will still be used going forward. Calculating the non-ideal gas law enrichment factor in this manner however acts as a useful safety measure to ensure the user has a rough estimate of what gas is within the vessel at any given time. It is also useful to store this information to identify when leaks have occurred as discussed in section 2.4.

6.4 Conclusion

The enrichment device was successfully upgraded in order to improve its reliability, safety, and the user interface for performing enrichment. This was done by changing the

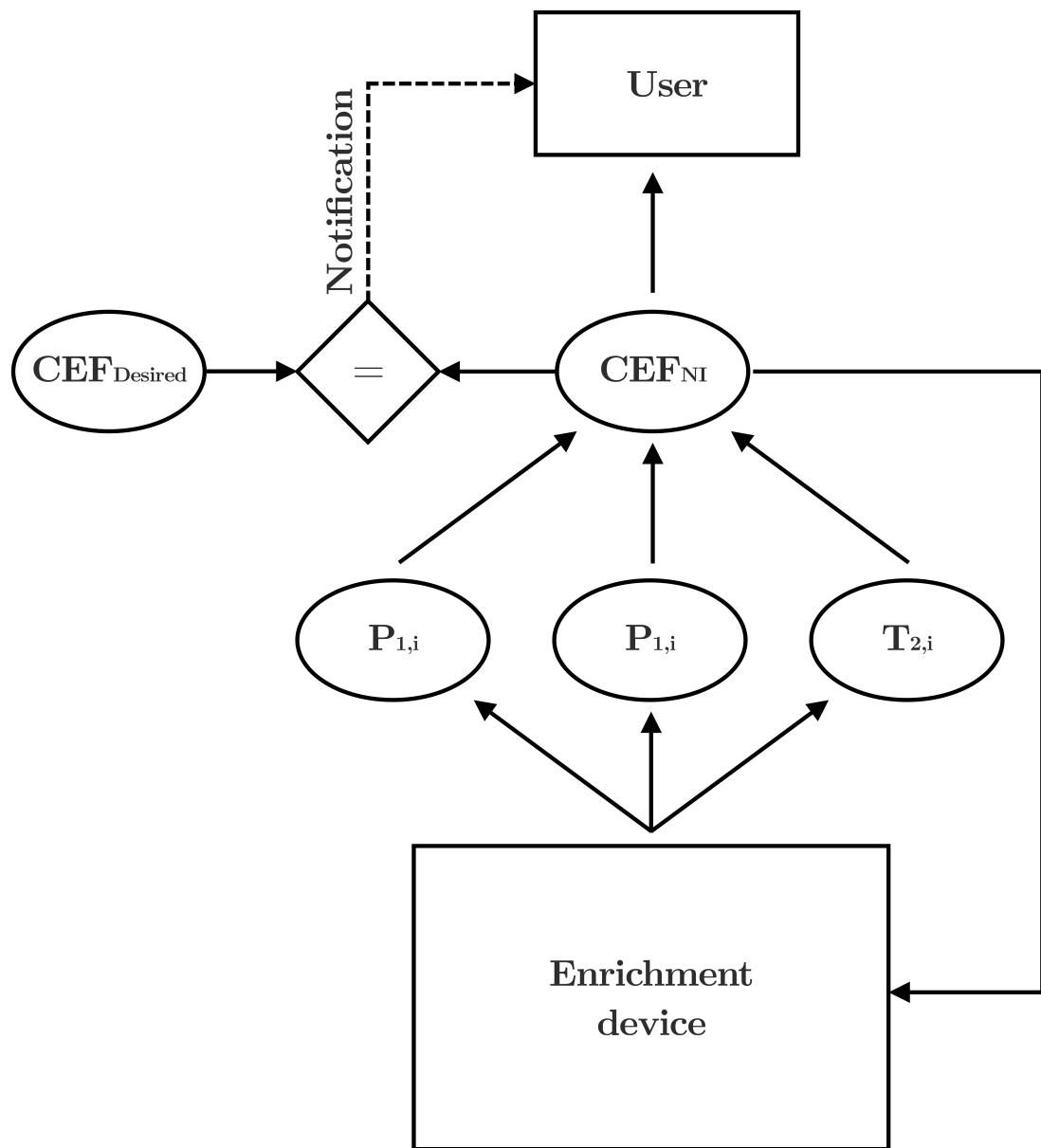


Figure 6.5: Diagrammatic representation of the data processing algorithm used to provide real time enrichment factor

temperature controller to a PID control system which reduced the standard deviation of the temperature while at setpoint to 1.78°C. The safety and usability of the device were improved by splitting the device into two sections, the stationary unit, where majority of the piping, electronics, and safety interlocks are in place, and the transportable unit, which contained the enrichment vessel containing the membrane, and the gas to be analysed.

References

- [1] Arul Murugan and Andrew S Brown. Advancing the analysis of impurities in hydrogen by use of a novel tracer enrichment method. *Analytical Methods*, 6(15):5472, 2014. doi: 10.1039/c3ay42174k.
- [2] Michael Podesta, Darren Mark, Ross Dymock, Robin Underwood, Thomas Bacquart, Gavin Sutton, Stuart Davidson, and Graham Machin. Re-estimation of argon isotope ratios leading to a revised estimate of the boltzmann constant. *Metrologia*, 54, 06 2017. doi: 10.1088/1681-7575/aa7880.
- [3] Shabbir Ahmed, Sheldon H D Lee, and Dionissios D Papadias. Analysis of trace impurities in hydrogen: Enrichment of impurities using a H₂ selective permeation membrane . *International Journal of Hydrogen Energy*, 35(22):12480–12490, 2010. doi: 10.1016/j.ijhydene.2010.08.042.
- [4] Product catalog. URL <https://www.swagelok.com/en/toolbox/product-catalog>.
- [5] Skid mounted rigs: Pilot plants: Nuclear engineering decommissioning. URL <https://www.strata tec.co.uk/>.
- [6] Sulfinert-treated sample cylinders. URL https://www.restek.com/Technical-Resources/Technical-Library/Petroleum-Petrochemical/petro_A005.

[7] Thomas Bacquart, Niamh Moore, Nick Hart, Abigail Morris, Thor A. Aarhaug, Ole Kjos, Fabien Aupretre, Thibault Colas, Frederique Haloua, Bruno Gozlan, and Arul Murugan. Hydrogen quality sampling at the hydrogen refuelling station – lessons learnt on sampling at the production and at the nozzle. *International Journal of Hydrogen Energy*, 45(8):5565 – 5576, 2020. ISSN 0360-3199. doi: <https://doi.org/10.1016/j.ijhydene.2019.10.178>. URL <http://www.sciencedirect.com/science/article/pii/S0360319919340510>. 22nd World Hydrogen Energy Conference.

Chapter 7

Enriching impurities in hydrogen refuelling station samples

Abstract

In this chapter the HIED was tested under a number of conditions using a commercial membrane compared against the best performing fabricated membranes in chapter 5.

Enrichment was performed using a number of synthetic hydrogen samples created using the procedure outlined in section 3.2, and a hydrogen sample taken from a hydrogen refuelling station. The device was capable of enriching samples to 85 times. Theoretically higher enrichment factors were possible but these tests were limited for safety reasons. The commercial membrane took 7 days to perform this measurement and provided the final value of within 2% of the gravimetrically calculated value using the tracer enrichment method which was deemed sufficient for a commercial device. The device was also tested using a sulphur containing sample which resulted in failure of all membranes. The PdCuZr membrane while identified as being a strong candidate for enriching sulphurous impurities, failed in all tests due to poor thermal stability of the support. The commercial membrane on the other hand reacted with the gases in the

mixture and became completely inactive.

For the first time a sample was taken directly from a hydrogen refuelling station and enriched. The sample was enriched 46 times and was found to have 22 ppm of nitrogen, and a small amount of argon which was not visible during other tests, further showing that the method can be used to quantify impurities past the limit of detection normally achievable.

7.1 Introduction

Now that appropriate membrane compositions have been found, a number of improvements must be made to the hydrogen impurity enrichment device in order to make it suitable as a commercial process and product for measurement of ISO 14687-2 impurities. All previous devices used were extremely manual and required close operator attention to ensure the experiment performed correctly. All enrichment factor calculations discussed in section 3.6 must also be calculated by hand, after the experiment has been performed, limiting the ability for the operator to plan the experiment in advance. In addition to this the krypton enrichment method which was identified as the best method for calculating the enrichment factor in section 2.4 but no procedure is in place to instruct operators on how to add this krypton to their sampling vessel.

This chapter will provide a method for taking krypton spiked samples from a hydrogen refuelling station, improve the hydrogen impurity enrichment device through automation to improve the usability of the device, while providing real time results for the user, and quantify how the enrichment device performs when tested using a real sample from a hydrogen refuelling station.

Table 7.1: Gas mixture composition of the inert sample used during enrichment tests

Impurity	Concentration ($\mu\text{mol/mol}$)
N ₂	6.67 ± 0.06
Kr	5.984 ± 0.06
H ₂	Balance

7.2 Enrichment of hydrogen samples

Enrichment of the hydrogen samples was performed using the set up shown in figure 6.2. An initial test was performed using a commercial membrane supplied by REB using an inert mixture created using the procedure in section 3.2 in order to calculate the uncertainty associated with the device. Both the commercial and PdCuZr membrane identified as the best performing membrane in chapter 5 were tested using a synthetic gas mixture containing sulphur containing compounds, and krypton. Finally both the commercial membrane and PdCuZr membrane were tested using a sample taken from the hydrogen refuelling station using the procedure outlined in section 3.3.

In each case the system was purged 7 times with the hydrogen sample to ensure there was no air present in the system. Enrichment was performed at a temperature of 300°C and a final enrichment pressure of 5 bar. Enrichment factors were calculated using both the tracer enrichment method (equation ??) calculated at the end of the test, and non-ideal gas law method (??) calculated using the data processing script described in section 6.3.3.

The gas mixtures used in the inert and sulphur tests are shown in table 7.1 and 3.2. Prior to testing the HRS sample was tested to verify the concentration of krypton, and ensure there was no oxygen present in the system to pose as a hazard. Enrichment factors were capped at 100 to ensure any residual oxygen would not reach a high enough concentration to create an explosive environment.

7.2.1 Inert components

The inert mixture in table 7.1 was enriched to a CEF value of approximately 85. The enrichment period was performed over a 7 day period due to the low flux value achieved by the commercial membrane supplied. The CEF_{NI} value was calculated using the algorithm described in section 6.3.3 and can it's progress over the 7 day period shown in figure 7.1. The CEF_{NI} slightly overshot the desired value of 85, stabilising at a value of 84.33 ± 9.24 , and as can be seen varied widely over the course of the experiment due to signal noise and interference. The value is still useful for keeping track of the progress of the experiment.

The system was not operated continuously for 180 hours, and was switched off at night when monitoring was not possible. This is why the CEF_{NI} value fluctuated over time.

Automatic CEF_{NI} calcutaions for inert enrichment test

241

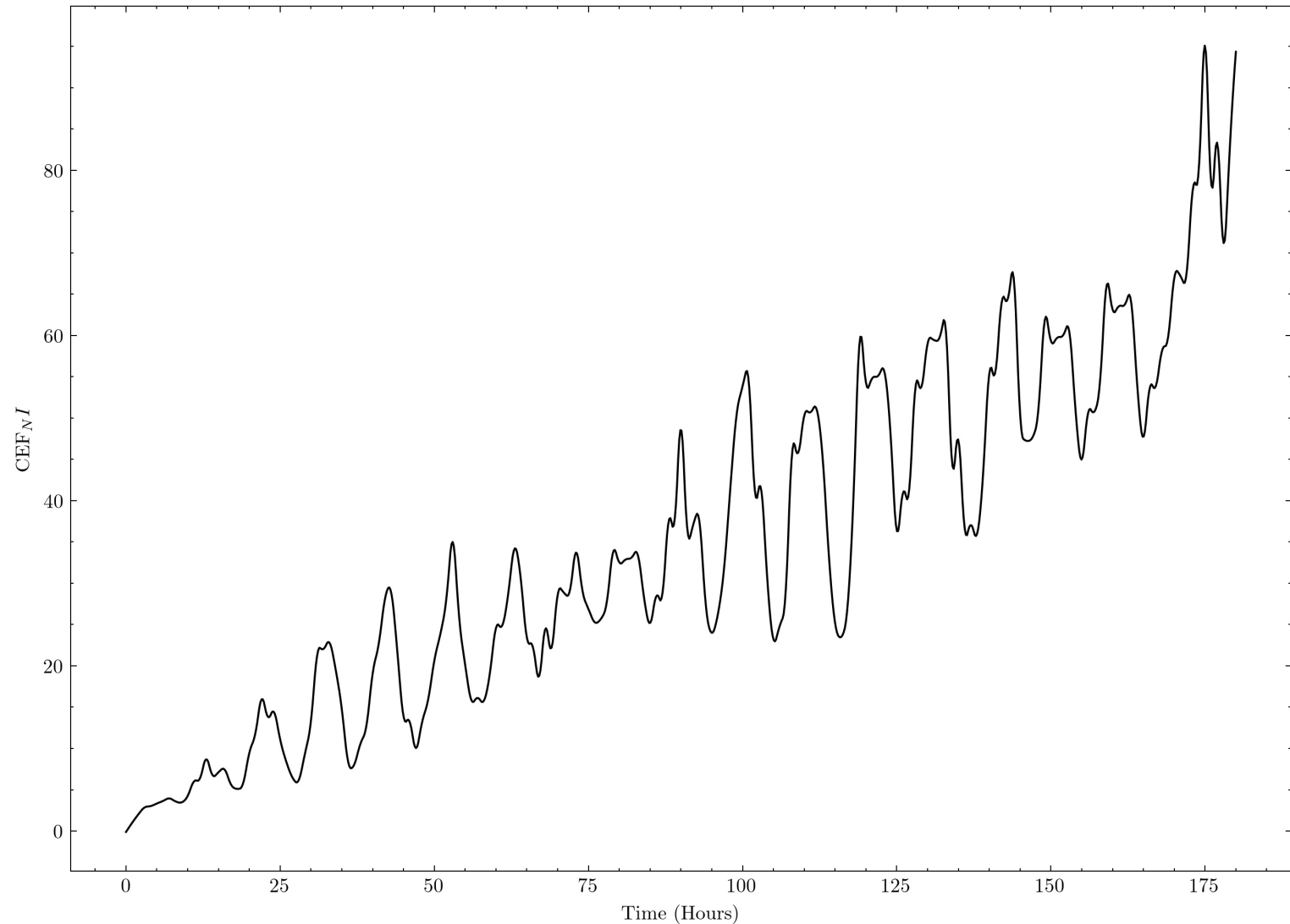


Figure 7.1: CEF_{NI} over the 180 hour enrichment of the inert hydrogen sample shown in table 7.1

Once the enrichment was complete, the system was isolated and left to cool. The transportable unit was then disconnected and it's composition measured and compared with it's original composition. Results were compared to nitrogen samples containing 251 nmol/mol, 500.77 nmol/mol, 1064 nmol/mol, 1437.37 nmol/mol using a derived calibration curve to account for non-linearity of the detector. The GC-PDHID data is shown in figure 7.2. This analysis found that the enriched gas contained 514.62 ± 52 $\mu\text{mol/mol}$ of krypton and $570 \pm 60 \mu\text{mol/mol}$ of Nitrogen. Calculating the CEF_T using the tracer enrichment method gave a value of 86 ± 9 .

The calculation using CEF_{NI} gave an initial Nitrogen concentration of $6.11 \mu\text{mol/mol}$ (-7%) N_2 . The tracer enrichment method calculated a value of $6.48 \mu\text{mol/mol}$ (-1.7%) further showing that the tracer enrichment method provides a more accurate result.

GC data of the inert sample before and after enrichment

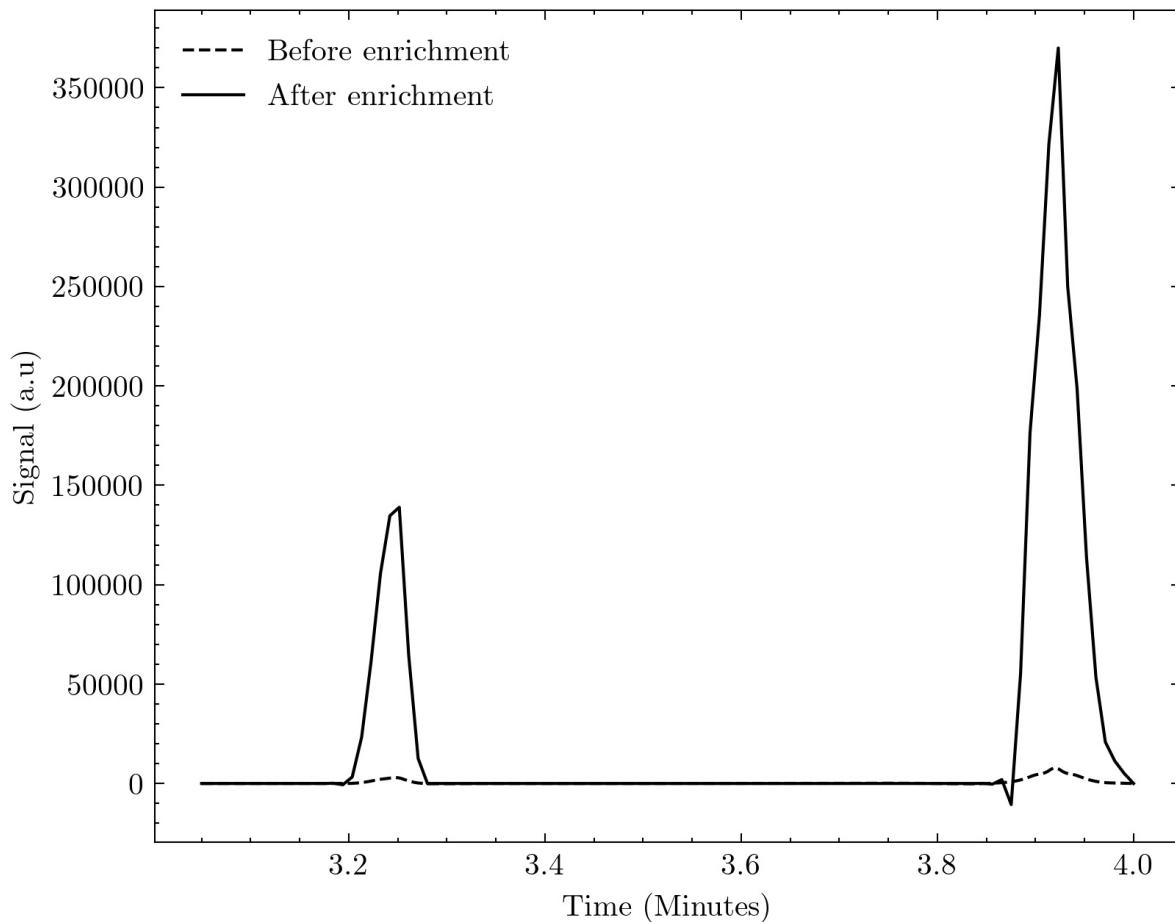


Figure 7.2: GC-PDHID data of the inert sample both before and after enrichment with N₂ peaks shown at Time=3.25, and Kr peaks shown at Time=3.92

7.2.2 Sulphur containing compounds

The sulphur containing samples were tested using the same set up as section 7.2.1, with the commercial PdAgAu membrane, and the PdCuZr alloy manufactured in chapter . The CEF_{NI} values calculated in line for the experiment are shown in figure 7.4.

The commercial membrane saw the same dramatic drop in permeability as observed in chapter 7.3. The experiment continued however it became clear that the permeability of the commercial membrane was dropping as the experiment went on, eventually be-

coming inactive to hydrogen permeability. The experiment was stopped. Upon analysis of the gas remaining within the enrichment vessel it was noted that the composition had significantly changed. This is shown in figure 7.3. The OCS, t-BuSH, THT and CS₂ in the gas mixture had reacted with the hydrogen to form H₂S. While this would not effect the results of analysis much, sine the ISO 14687-2 standard does not give a maximum level of a specific sulphur containing compound, only the total concentration, OCS, THT, T-BuSH and CS₂ all contain carbon molecules. The result of this could be the formation of hydrocarbons, CO, or solid carbon on the surface of the membrane. In the case of carbon deposition, this would explain the complete deactivation of the membrane as discussed previously in section 2.5.1. In order to prevent this the exact reactions should be determined and process parameters further optimised to inhibit them from taking place.

GC data of the sulphurous sample tested using the commercial membrane before and after enrichment

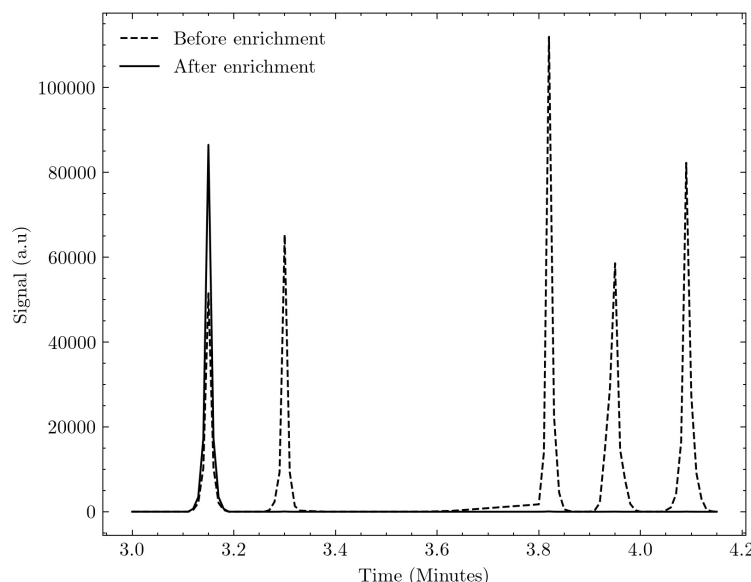


Figure 7.3: GC-SCD data of the sulphurous sample both before and after enrichment with commercial membrane

The PdCuZr membrane was tested twice, with both runs ending in failure due to delamination of the membrane after a number of temperature cycles. On the second

attempt the heating ramp was lowered to 1 °C/min in order to put less thermal strain on the membrane. This resulted in the membrane lasting one extra temperature cycle, however made no lasting difference to the result. The reason for this is likely to be the combined force of the extra pressure in the enrichment vessel during heating, and the multiple heating cooling cycles used over the course of the experiment causing the mismatch between the thermal expansion coefficient between the membrane and support to result in membrane failure.

Since all enrichment experiments failed for the sulphur sample a comparison of the enrichment factors in sulphur containing atmospheres cannot be performed.

Automatic CEF_{NI} calcutaions for inert enrichment test

246

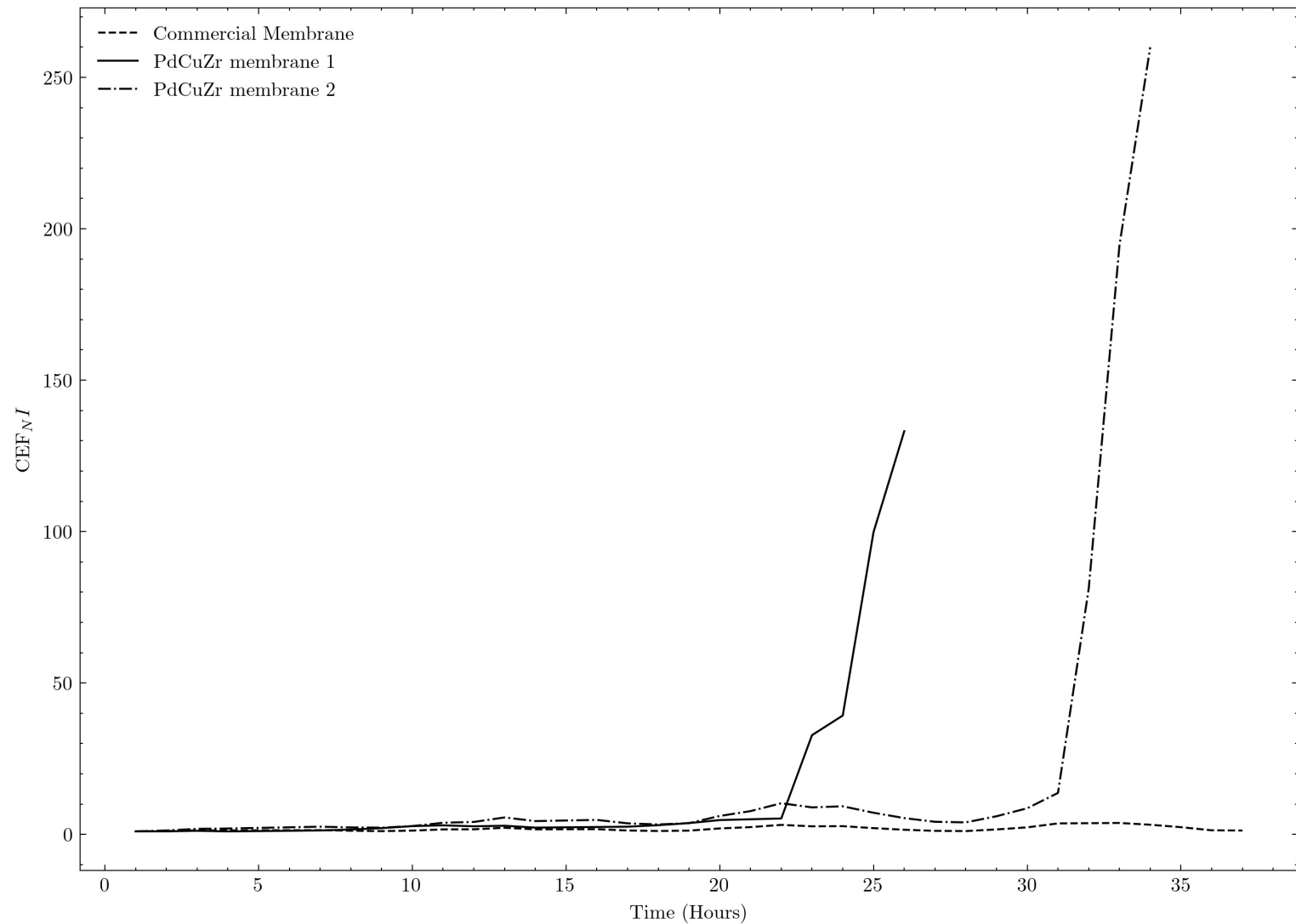


Figure 7.4: CEF_{NI} over the 40 hour enrichment of the sulphurous hydrogen sample shown in table 3.2

7.2.3 HRS sample

The sample taken from the hydrogen refuelling station spiked with krypton as described in 6.2 was enriched using the commercial PdAuAG membrane as this was the only composition able to withstand the conditions required for enrichment. The enrichment was performed over 120 hours. Initial analysis showed that the krypton concentration in the sample before enrichment was 80 $\mu\text{mol/mol}$ and that nitrogen was present in the sample likely due to dead volume within the H_2 qualitizer. The CEF_{NI} over the course of the experiment is shown in figure 7.5 and predicted that the sample was enriched 55.36 \pm 3.4 times using the non-ideal gas law method.

Automatic CEF_{NI} calculations for HRS enrichment test

248

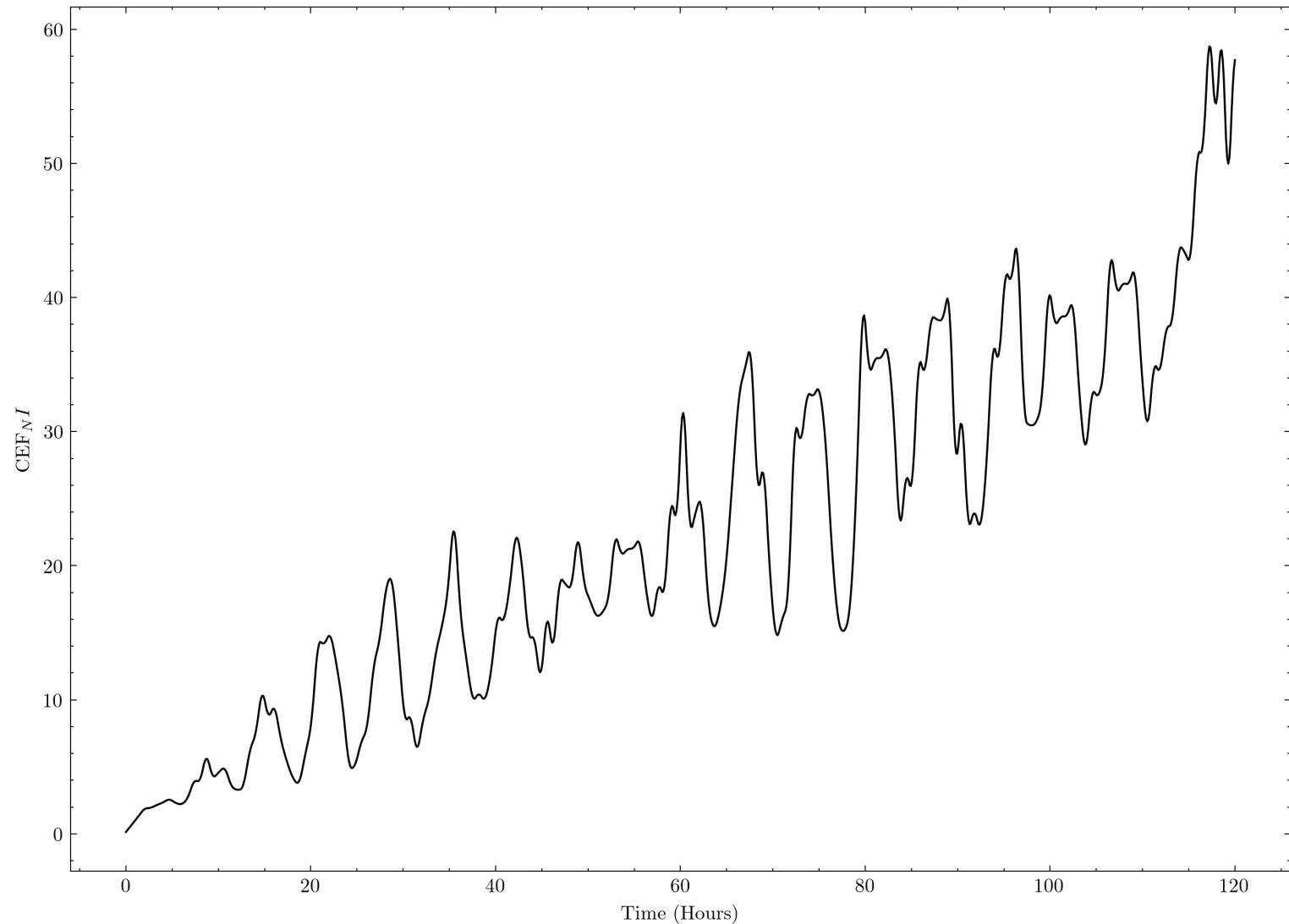


Figure 7.5: CEF_{NI} over the 120 hour enrichment of the HRS hydrogen sample

The sample was enriched to an enrichment factor of 41.76 ± 2.3 as shown by the increase of krypton and nitrogen concentrations shown in figure 7.6. These peaks corresponded to concentrations of $3374 \pm 32 \mu\text{mol/mol}$ of krypton and $957 \pm 10.6 \mu\text{mol/mol}$ of Nitrogen respectivley. Using the tracer enrichment factor this corresponds to an initial concentration of $22.91 \pm 3.2 \mu\text{mol/mol}$ of Nitrogen in the hydrogen sample. The results in the enriched sample also show a new peak at 2.4 minutes which corresponds to Argon, thereby proving that the method can be used to quantify impurities which were below the limit of detection of the detector in the initial sample. Due to the small size of the peak, quantifying the concentration was difficult and a higher enrichment factor would be required to accurately determine this. Unfortunately due to interruptions from COVID-19 adequate time was not available to perform this test.

GC data of the HRS sample before and after enrichment

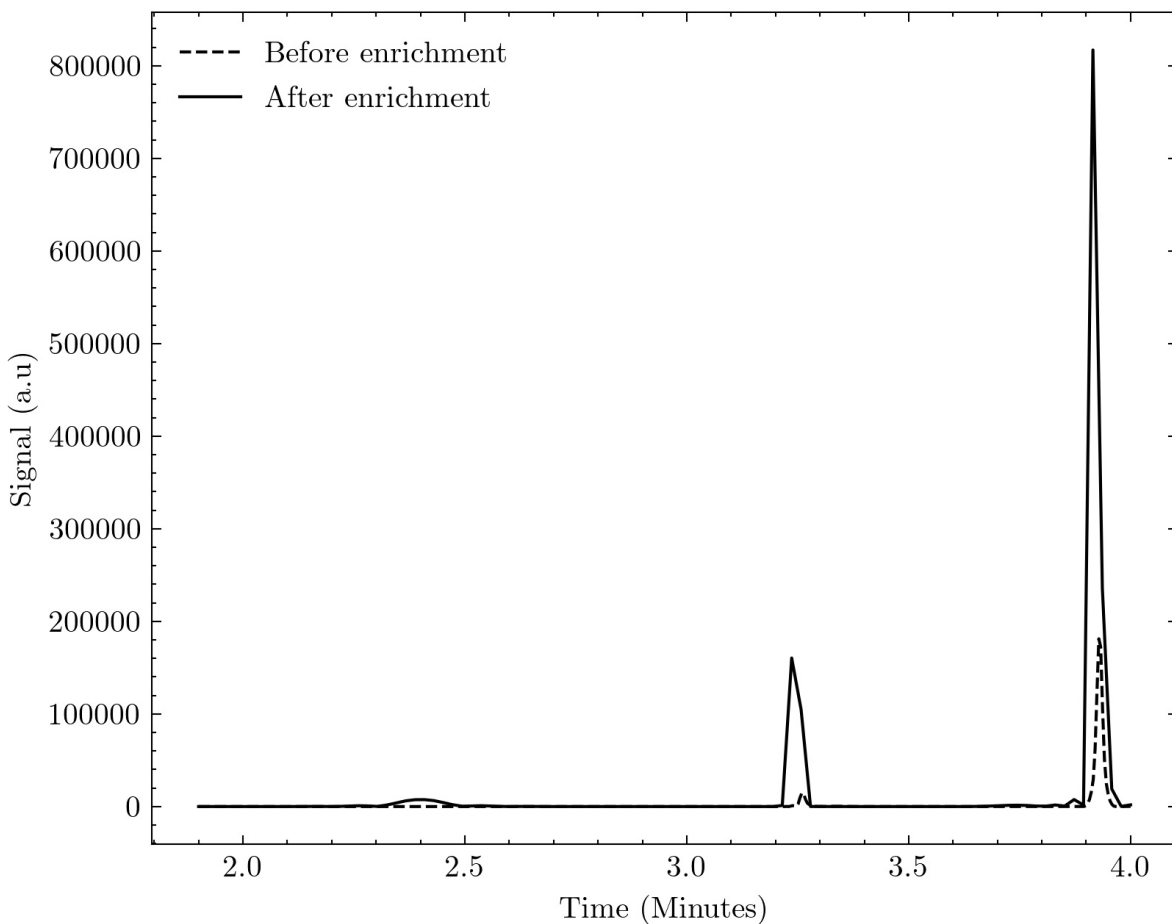


Figure 7.6: GC-PDHID data of the HRS sample both before and after enrichment with commercial membrane

7.3 Conclusion

The new enrichment device was tested using 3 hydrogen samples, a sample containing only inert impurities in order to test the device functions as required, a sulphur containing sample to test how the PdCuZr membrane identified as the best membrane in chapter , and a sample taken from a hydrogen refuelling station. The inert sample was successfully enriched to 50x and using the tracer enrichment method using krypton the

initial concentration of nitrogen was calculated to within 2% of it's original value.

The sulphur tests resulted in failure of all membranes used. For the commercial membrane this was due to high reactivity with the sulphur compounds which was also identified in chapter 5. For the PdCuZr membrane this was due to material instability and further work is required to manufacture the ceramic supported membrane to be able to withstand temperature cycling.

For the first time enrichment was performed on a real sample from a hydrogen refuelling station, proving both that the method is viable for analysis of real world hydrogen samples, and the protocol for spiking a hydrogen sample with krypton gas is appropriate. The sample was enriched 41 times and was able to accurately determine that the concentration of nitrogen in the sample before enrichment was 22.91 $\mu\text{mol/mol}$. Enrichment also revealed the presence of Argon in the sample, which would not have been present in the analysis otherwise, further proving that the technique can provide a more accurate composition analysis of fuel grade hydrogen, past what is possible with commercial analysers.

Chapter 8

Conclusions and future work

This chapter will bring together the results of this thesis, providing final thoughts on the theoretical and experimental work performed. The future of hydrogen separation membranes and their use in the hydrogen economy will be discussed. Finally future applications and further improvements for the HIED will be described.

8.1 Membranes for hydrogen separation

8.1.1 DFT for screening impurity resistant alloys

This thesis presented a methodology for fast screening of palladium alloy membrane compositions for resistance of impurities. The simulations involving sulphur samples were relatively accurate, and were able to successfully predict which membranes would perform the best when tested in chapter 5. The model however broke down for other impurities and this is due to the fact that the chosen simulation method is not accurate for weak interactions. [1] Further development of the models should be performed in order to accurately predict the impact of these impurities. The model can also be expanded to predict the solubility of hydrogen within the palladium alloy membranes by

combining monte carlo simulation techniques with cluster expansion simulations as has been performed by Scholl et al. [2] Future work could take combine these simulation methods to predict everything from the impurity interactions, to permeability and performance of the membranes. If such a system was developed it could greatly reduce the time taken to discover new alloy compositions.

There is also scope for testing more membrane compositions. This thesis tested a limited number of alloy composition due to lack of computing power and time available. With HPC networks becoming more and more available [3] a great number of alloys can be simulated quickly, allowing bespoke membrane compositions to be potentially found for any application.

8.1.2 Use for dense metal membranes in the hydrogen economy

In this work we presented a use case for dense metal membranes as a material to perform hydrogen impurity enrichment to measure ISO 14687-2 impurities. As the hydrogen economy grows there will be other potential uses for such technology.

There are already examples of industry capturing waste hydrogen from their processes and using it as a power source either through a fuel cell, or other means.[4] It is estimated that there are 100,000MW of waste hydrogen produced each year and therefore could result in a meaningful resource. [5] As more processes turn to this there is potential for a highly personalised market for dense metal membranes. Dense metal membranes provide ultrapure hydrogen suitable for use in fuel cells, therefore protecting the investment in any new type of energy utilization technology and this will become especially true as the cost of such membranes decreases through the development of stable ceramic supported membranes.

If combined with the simulation research discussed in section 8.1.1 there could be potential for an highly linked membrane ecosystem. Where a plant owner can define the

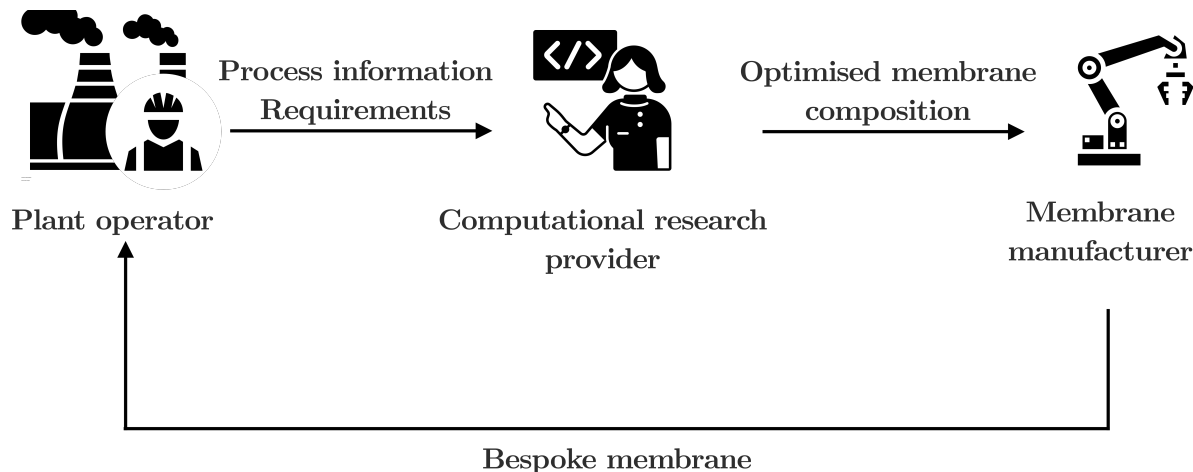


Figure 8.1: Theoretical manufacturing process for a bespoke dense metal membrane with optimal composition calculated by a research provider, manufactured to specification, and delivered to the customer

requirements for their hydrogen separation process, the optimal membrane can be found by a computational research provider, and finally manufactured into a module. This process is visualised in figure 8.1. While palladium membranes will likely not replace PSA in the SMR process, due to the high levels of impurities found in these processes, however may be suitable for processes where hydrogen is often a byproduct such as ammonia, or certain pharmaceutical processes.

Another potential use for dense metal membranes is in a potential hydrogen grid system. Projects such as HyGrid [6] aim to use the existing natural gas network in Europe as a storage medium for the hydrogen economy, mixing hydrogen with natural gas to improve its energy density and reduce the carbon footprint of the natural gas network. In addition to this there are several companies now offering hydrogen CHP systems for use in homes, which are powered using a fuel cell, to provide thermal energy for households.[7] There may soon be a need for a source of ultrapure hydrogen. Palladium membranes could be used to provide this, separating the hydrogen out from the natural gas network at the point of use. The challenge with this is that there are a number of impurities present in the natural gas network, potentially varying even by

region. There is an opportunity to develop bespoke membranes for such a purpose using the system described in figure 8.1.

Ultimately most large scale hydrogen production processes will continue to use polymer membranes or PSA to provide purified hydrogen, however this thesis proves that there are a number of niche applications where palladium membranes could be used in the future hydrogen economy.

Ceramic supported dense metal membranes

This work used YSZ supported membranes in order to improve the flux and cost of the dense metal membranes. The techniques used in this thesis were able to deposit membranes within the range of 0.5-2 µm, allowing for high flux membranes to be manufactured from materials which contain lower concentrations of palladium, and are more resistant to impurities. The module consisted of a single membrane operating in dead end, however it can be easily expanded to contain a bundle of hollow fibre membranes. Through this even extremely low flux membranes can be used as long as there are enough in the bundle to produce a flux reasonable for the chosen process. The problem that was encountered with the use of ceramic supported dense metal membranes is that they lacked stability under temperature cycling, experiencing delamination after a low number of temperature cycles. In order to be commercially viable the product must be properly optimised with a reasonable lifespan in order to provide an attractive solution to buyers.

8.2 Impurity enrichment devices

In chapter 6 the hydrogen impurity enrichment device was greatly improved in terms of its safety, usability and reliability. Using a commercial membrane it was shown to be capable of providing the concentration of nitrogen impurities in a hydrogen sample

to within 2% of its real value, which is adequate for metrology purposes. [8] For the first time a real sample taken from a hydrogen refuelling station was also enriched and was able to quantify the level of nitrogen in the sample to 22 $\mu\text{mol/mol}$. Enriching the sample was also able to show the presence of an additional impurity. Further work is required to quantify these impurities.

8.2.1 Commercialisation and optimisation

The device manufactured in chapter 6 has already been commercialised and sold to one customer at the time of writing, with other buyers currently in the pipeline. There are however further opportunities for commercialisation that arise as the device is automated further.

Since every hydrogen refuelling station must show that their hydrogen meets ISO 14687-2, there is potential for a hydrogen impurity device to be installed directly at every HRS to automatically provide this information. Such a system would involve four main components; a sample cylinder permanently connected to the HRS fixed upon a mass balance, a Krypton supply connected to the sample cylinder, the HIED, and an analyser. The process is shown in figure 8.2

The system could operate automatically through the use of automated valves. When a measurement is required the sample cylinder is evacuated and purged of any remaining gas, before a known mass of krypton defined in chapter 6, is spiked into the empty vessel, measured gravmetrically. The valve connecting the sample cylinder to the HRS is then opened, allowing a certain mass of hydrogen to enter the cylinder to be enriched and tested. Once enough gas has been sampled this valve can be closed, and the sample enriched. Once enrichment is complete the gas automatically passes through a dedicated analyser, tested against a standard, and the results delivered to an analyst off site. This would eliminate the costly and time consuming process of physically acquiring a sample,

Analyst

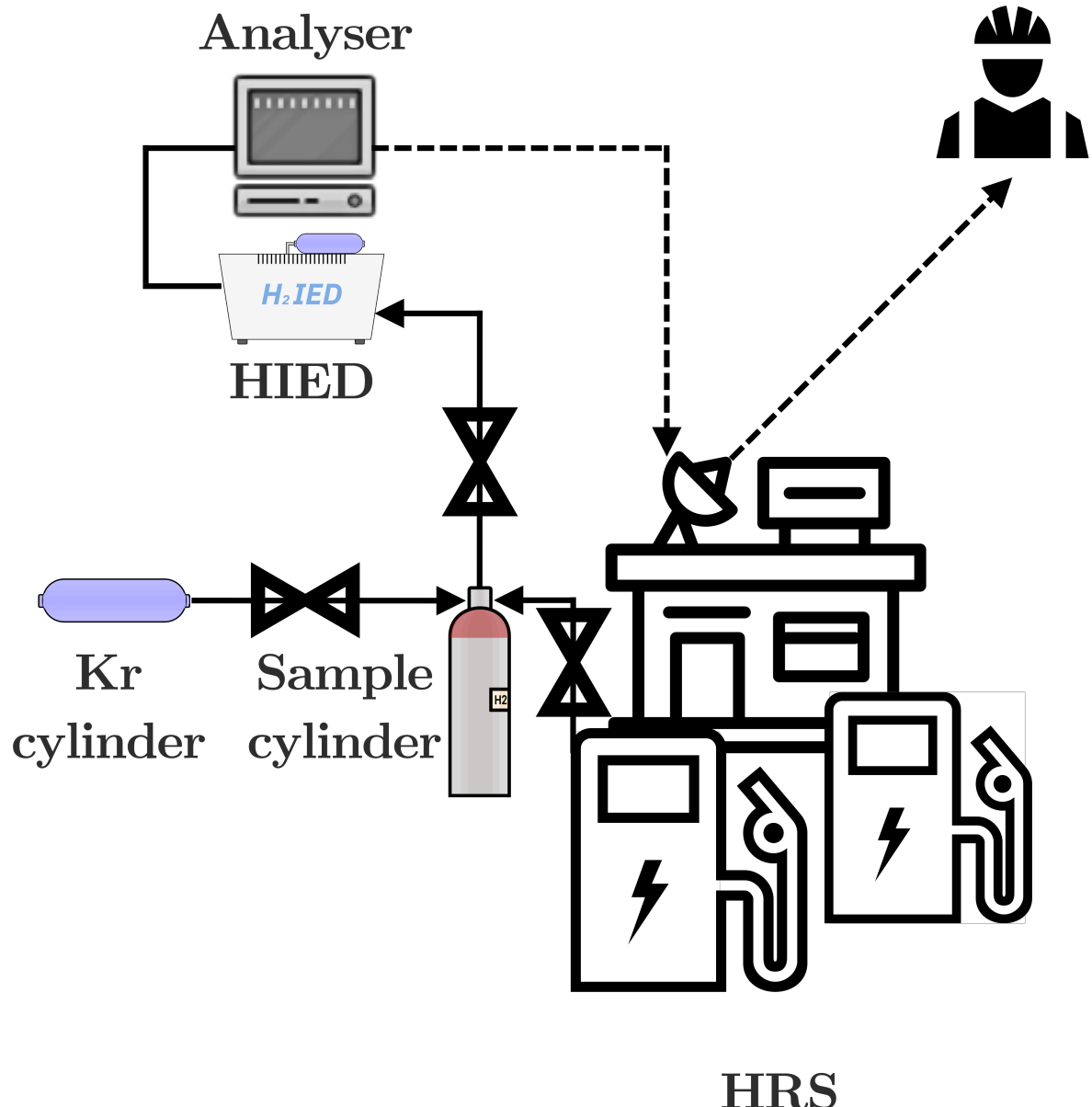


Figure 8.2: Proposed solution for automatic quality assurance of fuel cell hydrogen at HRS's

and transporting it to be tested, allow testing to be performed off site, and allow more flexibility for testing schedules. As the process for performing a hydrogen sample has already been defined [9] and could be automated with existing technology this could be the next step for impurity enrichment devices. As the market for hydrogen technology increases, modern solutions which greatly improve upon existing processes such as these will appear increasingly viable.

NPL has recently designed a Hydrogen Purity Van, which travels to hydrogen refuelling stations and performs analysis to ISO 14687 standard on-site. Similarly to analytical labs the equipment is expensive and takes up a large amount of space due to the number of instruments required. If the HIED was integrated into the Hydrogen Purity Van then it would lower the CAPEX and make such an initiative more viable.

One issue in the operation of the HIED is the resulting pressure of the enriched sample. Once the enriched sample has cooled the resulting pressure is normally < 5 bar, which may cause some issues when performing analysis on certain instrumentation. On the flipside if the pressure is too high then the pressure relief valves will activate during the run due to the high pressure created during heating, throwing off the results in the same way as if a leak had formed. A solution to this would be to manufacture a membrane at a higher pressure rating in order to allow higher enrichment pressures and therefore give greater allowance for pressure drops during cooling.

Finally it may be possible to perform in-situ measurement of some impurities within the enrichment device by incorporating chemical sensors into the enrichment vessel. Such a system would be able to automatically calculate the concentration of the impurity when it reaches the limit of detection of the sensor, combined with the non-ideal gas law enrichment factor. It would not be possible to use this type of system in conjunction with the tracer enrichment method due to there not being chemical sensors available for krypton. A similar system could be created by connecting the enrichment device to a gas

analyser and sampling throughout the enrichment, for example with a GC-PDHID this could be done at 10 minute intervals. This has the advantage of being able to measure all impurities in situ, not just ones that have available chemical sensors, however has the disadvantage of taking up an expensive piece of equipment for potentially days at a time.

8.2.2 Additional use cases

There is scope for using the impurity enrichment technique for gases other than hydrogen. Dense ceramic membranes which are permaselective to oxygen are in the research stage, [10] and could potentially be inserted into the enrichment device as is to provide this analysis if needed. Another alternative could be to enrich impurities in water to provide a similar analysis. As evidence that pollutants in water are increasing at alarming levels, and are increasingly dangerous to our health, there may be increased scope for water impurity analysis in the future. [11]

8.3 Other hydrogen impurity measurement challenges

This thesis mainly focused on a technique which is used for off-line analysis of impurities in fuel cell hydrogen. There is still a need for on-line monitoring of impurities at HRS's as stated by ISO 19880-8:2019. In a report performed for the MetroHyve project they concluded that no such devices capable of performing on-line sensing exist. Some of the methods used in this thesis, in particular the use of simulations to predict the suitability of a material for a given purpose, could prove useful when researching in this area.

8.4 Closing remarks

This thesis explored the use of a number of experimental and computational methods to find and test the best membrane for enriching hydrogen impurites to enable testing at a low cost, making the process accessable to a larger number of measurement providers. A commercialised device was designed and has been sold, able to provide purity analysis to within 2% of the original value. An appropriate membrane composition was found although further work is required to manufacture a palladium coated ceramic hollow fibre which is able to withstand the conditions required for enrichment. DFT proved to be a useful tool in screening of allows, in particular those resistent to sulphur impurities, however further work must be done to define an appropriate model for the interaction of the alloy surfaces and carbonaceous impurities which the model was not able to accurately predict. More impurities which are not included in the ISO standard, such as siloxanes, are also worthwhile investigating due to the increasing number of sources for hydrogen production processes increasing the liklihood of new impurities coming into contact with palladium membrane systems.

References

- [1] *What is Density Functional Theory?*, chapter 1, pages 1–33. John Wiley & Sons, Ltd, 2009. ISBN 9780470447710. doi: 10.1002/9780470447710.ch1. URL <https://onlinelibrary.wiley.com/doi/abs/10.1002/9780470447710.ch1>.
- [2] David S. Sholl. Using density functional theory to study hydrogen diffusion in metals: A brief overview. *Journal of Alloys and Compounds*, 446-447:462 – 468, 2007. ISSN 0925-8388. doi: <https://doi.org/10.1016/j.jallcom.2006.10.136>. URL <http://www.sciencedirect.com/science/article/pii/S0925838806017439>. Proceedings of the International Symposium on Metal-Hydrogen Systems, Fundamentals and Applications (MH2006).
- [3] Timothy Prickett Morgan, Jeffrey Burt, and Michael Feldman. A new era in high performance computing, Jun 2020. URL <https://www.nextplatform.com/2020/06/09/a-new-era-in-high-performance-computing/>.
- [4] Hussam Khasawneh, Motasem N Saidan, and Mohammad Al-Addous. Utilization of hydrogen as clean energy resource in chlor-alkali process. *Energy Exploration & Exploitation*, 37(3):1053–1072, 2019. doi: 10.1177/0144598719839767. URL <https://doi.org/10.1177/0144598719839767>.
- [5] Ruth Cox. Waste/by-product hydrogen. URL https://www.energy.gov/sites/prod/files/2014/03/f12/waste_cox.pdf.

- [6] Hydrogen recovery from natural gas. URL <https://www.hygrid-h2.eu/>.
- [7] H2ydropem, the hydrogen boiler by giacomini. URL <https://www.giacomini.com/en/hydrogen-systems/h2ydropem-hydrogen-boiler-giacomini>.
- [8] Arul Murugan and Andrew S Brown. Review of purity analysis methods for performing quality assurance of fuel cell hydrogen. *International Journal of Hydrogen Energy*, 40(11):4219–4233, 2015. doi: 10.1016/j.ijhydene.2015.01.041.
- [9] Thomas Bacquart, Niamh Moore, Nick Hart, Abigail Morris, Thor A. Aarhaug, Ole Kjos, Fabien Aupretre, Thibault Colas, Frederique Haloua, Bruno Gozlan, and Arul Murugan. Hydrogen quality sampling at the hydrogen refuelling station – lessons learnt on sampling at the production and at the nozzle. *International Journal of Hydrogen Energy*, 45(8):5565 – 5576, 2020. ISSN 0360-3199. doi: <https://doi.org/10.1016/j.ijhydene.2019.10.178>. URL <http://www.sciencedirect.com/science/article/pii/S0360319919340510>. 22nd World Hydrogen Energy Conference.
- [10] Shaomin Liu and George R. Gavalas. Oxygen selective ceramic hollow fiber membranes. *Journal of Membrane Science*, 246(1):103 – 108, 2005. ISSN 0376-7388. doi: <https://doi.org/10.1016/j.memsci.2004.09.028>. URL <http://www.sciencedirect.com/science/article/pii/S0376738804006416>.
- [11] Water testing & analysis market. URL <https://www.marketsandmarkets.com/Market-Reports/water-testing-analysis-market-152624587.html>.

Appendices

Uncertainties

The uncertainties used for gravimetric calculation of gas standard is the quadrature sum of the weighing uncertainties before and after the transfer of the component into the vessel.

Balance	Standard uncertainty
Mettler Toledo XPE26003LC	20.0 mg
Satorius 1475 MP8	1.4 mg
Mettler Toledo PR2004	0.3 mg
Mettler Toledo XP2004S	0.3 mg
Mettler Toledo XP205	0.1 mg
Sartorius R160P	0.1 mg

Standard uncertainties ($k=1$) of the balances used for gravimetric preparation of gas standards

Metallic Phase Diagrams

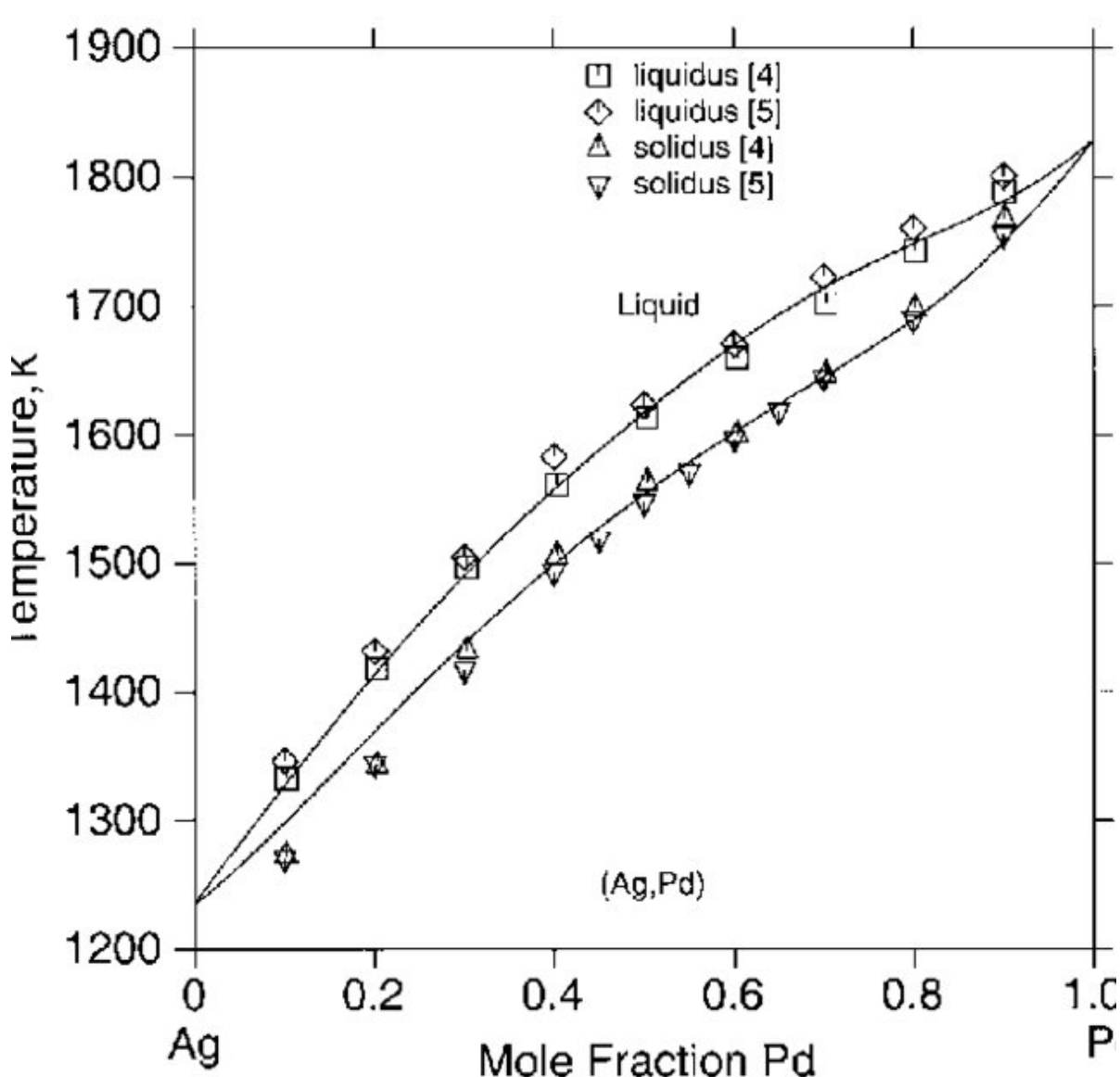


Figure 8.3: The calculated Ag-Pd phase diagram with experimental points [1]

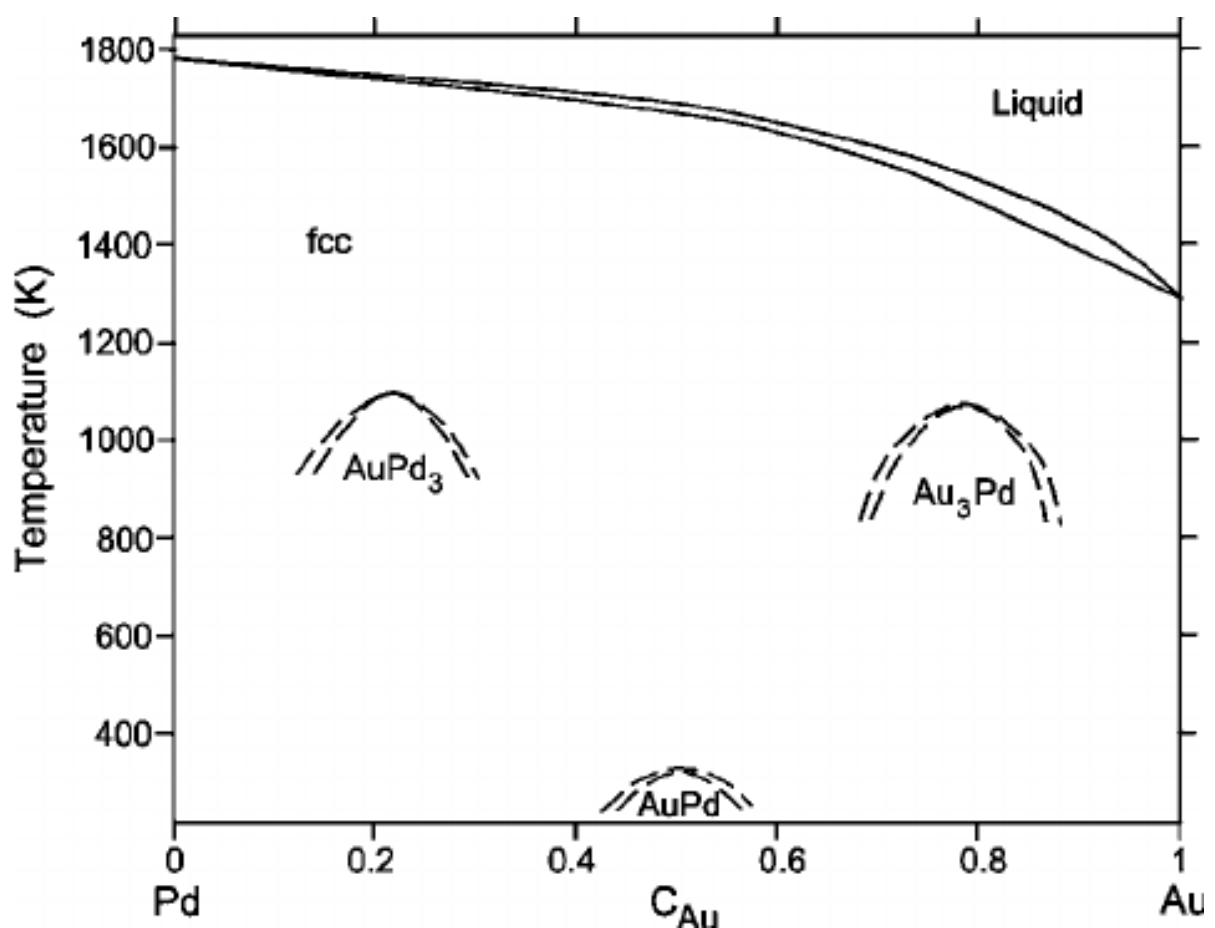


Figure 8.4: The calculated (dashed) Au-Pd phase diagram with experimental points [2]

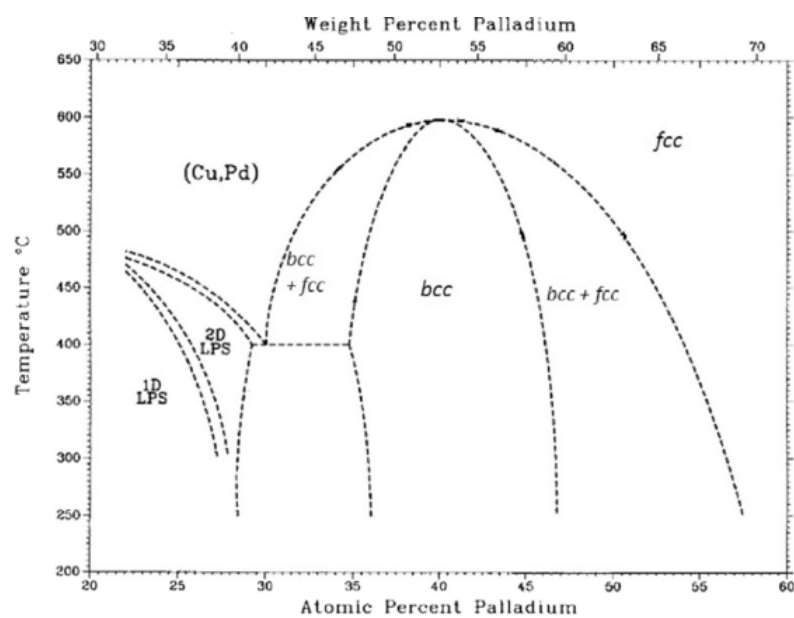


Figure 8.5: Cu-Pd phase diagram

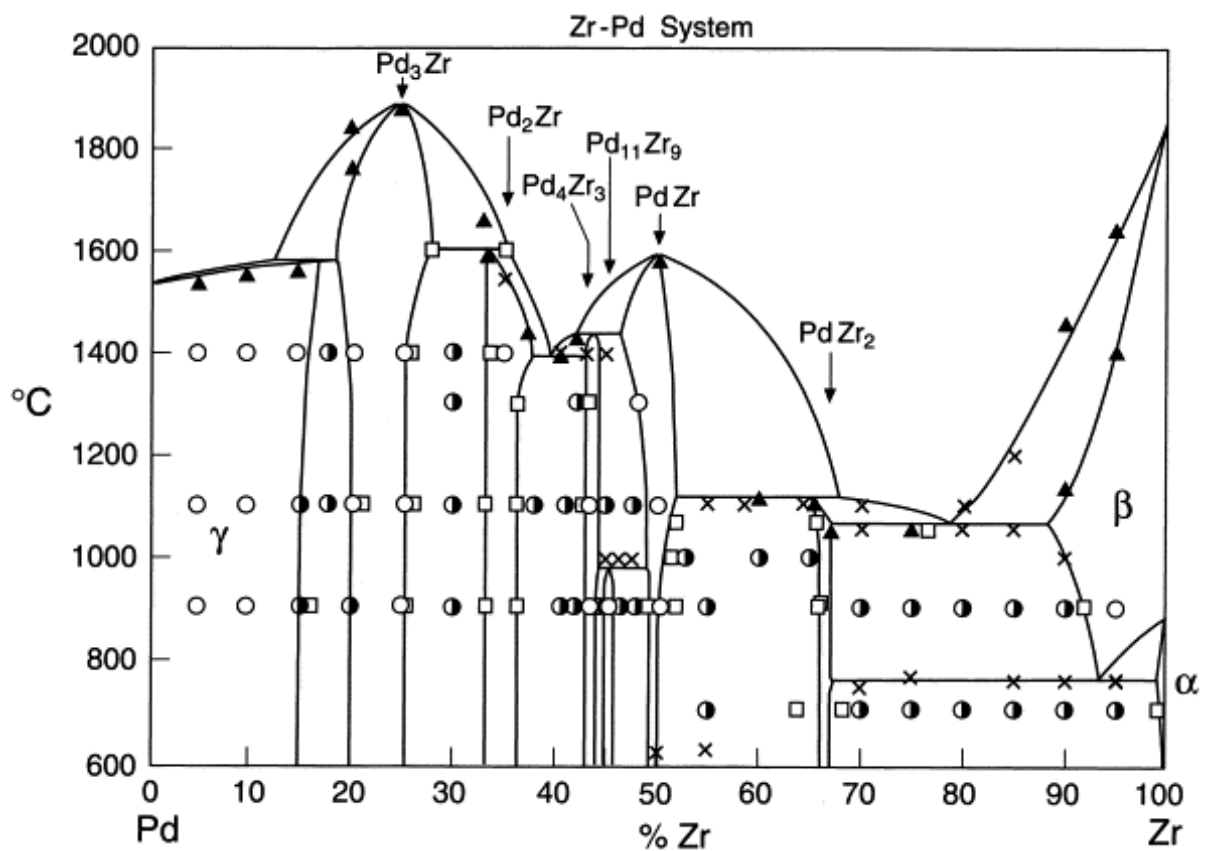


Figure 8.6: Zr-Pd phase diagram [3]

Simulation files

Hydrogen impurities

Ammonia

```
&CONTROL
  calculation='relax',
  outdir='./tmp/',
  prefix='Ammonia',
  pseudo_dir='/home/mp916/Simulations/qe/qe-6.1/Simulationpdpaper/Pseudo',
  verbosity='high',
  forc_conv_thr = 0.000583,
  tprnfor = .TRUE.

/
&SYSTEM
  ibrav=0,
  celldm(1)=15.1474115563d0,
  nat=4,
  ntyp=2,
  ecutwfc=30,
  ecutrho=120,
  occupations='smearing',
  degauss=0.005d0,
/
&ELECTRONS
  mixing_ndim = 20
```

```

mixing_beta = 0.8
conv_thr=1d-05,
/
&IONS
/
ATOMIC_SPECIES
H 1.007940d0 H.pw91-kjpaw_psl.1.0.0.UPF
N 14.006700d0 N.pw91-n-kjpaw_psl.1.0.0.UPF
ATOMIC_POSITIONS {crystal}
N 0.5042649612d0 0.4816814914d0 0.5185608552d0
H 0.5858110338d0 0.5710210191d0 0.4807806443d0
H 0.4526766026d0 0.4289789809d0 0.4165818655d0
H 0.4141889662d0 0.5407708619d0 0.5834181345d0
K_POINTS {automatic}
8 8 8 0 0 0
CELL_PARAMETERS {alat}
1.000000000000d0 0.000000000000d0 0.000000000000d0
0.000000000000d0 0.968552952250d0 0.000000000000d0
0.000000000000d0 0.000000000000d0 0.994255872719d0

```

Argon

```

&CONTROL
calculation='scf',
outdir='./tmp/',
prefix='Ar',
pseudo_dir='/home/mp916/Simulations/qe/qe-6.1/Simulationpdpaper/Pseudo',
verbosity='high',

```

```

forc_conv_thr = 0.000583,
tprnfor = .TRUE.

/
&SYSTEM
ibrav=0,
celldm(1)=15.0422199515d0,
nat=1,
ntyp=1,
ecutwfc=30,
ecutrho=120,
occupations='smearing',
smearing='mv',
degauss=0.005d0,
/
&ELECTRONS
mixing_mode = 'local-TF'
mixing_ndim = 20
mixing_beta = 0.3
conv_thr=1d-05,
/
ATOMIC_SPECIES
Ar 39.948000d0 Ar.pw91-nl-kjpaw_psl.1.0.0.UPF

```

```

ATOMIC_POSITIONS {crystal}
Ar    0.5000000000d0    0.5000000000d0    0.5000000000d0

K_POINTS {automatic}
8 8 8 0 0 0

CELL_PARAMETERS {alat}
1.000000000000d0 0.000000000000d0 0.000000000000d0
0.000000000000d0 1.000000000000d0 0.000000000000d0
0.000000000000d0 0.000000000000d0 1.000000000000d0

```

Carbon Dioxide

```

&CONTROL
calculation='relax',
outdir='./tmp/',
prefix='CO2',
pseudo_dir='/home/mp916/Simulations/qe/qe-6.1/Simulationpdpaper/Pseudo',
verbosity='high',
forc_conv_thr = 0.000583,
tprnfor = .TRUE.
/

```

```

&SYSTEM
ibrav=0,
celldm(1)=15.5625245542d0,
```

```
nat=3,  
ntyp=2,  
ecutwfc=30,  
ecutrho=120,  
occupations='smearing',  
smearing='mv',  
degauss=0.005d0,  
/  
  
/
```

&ELECTRONS

```
mixing_mode = 'local-TF'  
mixing_ndim = 20  
mixing_beta = 0.3  
conv_thr=1d-05,  
/  
  
/
```

&IONS

/

ATOMIC_SPECIES

```
C 12.010700d0 C.pw91-n-kjpaw_psl.1.0.0.UPF  
O 15.999400d0 O.pw91-n-kjpaw_psl.1.0.0.UPF
```

ATOMIC_POSITIONS {crystal}

```
C 0.5000000007d0 0.5000000008d0 0.4999999998d0
```

```
0    0.4529264144d0    0.4999999999d0    0.3864094181d0
0    0.5470735856d0    0.4999999992d0    0.6135905819d0
```

K_POINTS {automatic}

```
8 8 8 0 0 0
```

CELL_PARAMETERS {alat}

```
1.000000000000d0  0.000000000000d0  0.000000000000d0
0.000000000000d0  0.915567068158d0  0.000000000000d0
0.000000000000d0  0.000000000000d0  1.172141239726d0
```

Carbon Monoxide

&CONTROL

```
calculation='relax',
outdir='./tmp/',
prefix='CO',
pseudo_dir='/home/mp916/Simulations/qe/qe-6.1/Simulationpdpaper/Pseudo',
verbosity='high',
forc_conv_thr = 0.000583,
tprnfor = .TRUE.
/
```

&SYSTEM

```
ibrav=0,
```

```
celldm(1)=14.2485349792d0,  
nat=2,  
ntyp=2,  
ecutwfc=30,  
ecutrho=120,  
occupations='smearing',  
smearing='mv',  
degauss=0.005d0,  
/  
 
```

&ELECTRONS

```
mixing_mode = 'local-TF'  
mixing_ndim = 20  
mixing_beta = 0.3  
conv_thr=1d-05,  
/  
 
```

&IONS

```
/
```

ATOMIC_SPECIES

```
C 12.010700d0 C.pw91-n-kjpaw_psl.1.0.0.UPF  
O 15.999400d0 O.pw91-n-kjpaw_psl.1.0.0.UPF
```

ATOMIC_POSITIONS {crystal}

```
0    0.5000270812d0    0.5738644516d0    0.5000000000d0
C    0.4999729188d0    0.4261355484d0    0.5000000000d0
```

K_POINTS {automatic}

```
8 8 8 0 0 0
```

CELL_PARAMETERS {alat}

```
1.000000000000d0  0.000000000000d0  0.000000000000d0
0.000000000000d0  1.167110986173d0  0.000000000000d0
0.000000000000d0  0.000000000000d0  1.000000000000d0
```

Formaldehyde

&CONTROL

```
calculation='relax',
outdir='./tmp/',
prefix='Formaldehyde',
pseudo_dir='/home/mp916/Simulations/qe/qe-6.1/Simulationpdpaper/Pseudo',
verbosity='high',
forc_conv_thr = 0.000583,
tprnfor = .TRUE.
/
```

&SYSTEM

```
ibrav=0,
celldm(1)=14.2485349792d0,
nat=4,
```

```

ntyp=3,
ecutwfc=30,
ecutrho=120,
occupations='smearing',
smearing='mv',
degauss=0.005d0,
/
&ELECTRONS
mixing_mode = 'local-TF'
mixing_ndim = 20
mixing_beta = 0.3
conv_thr=1d-05,
/
&IONS
/
ATOMIC_SPECIES
C 12.010700d0 C.pw91-n-kjpaw_psl.1.0.0.UPF
O 15.999400d0 O.pw91-n-kjpaw_psl.1.0.0.UPF
H 1.007940d0 H.pw91-kjpaw_psl.1.0.0.UPF
ATOMIC_POSITIONS {crystal}
H    0.5000032071d0    0.3993778194d0    0.6091900164d0

```

C	0.4999967927d0	0.4644674926d0	0.4999863532d0
H	0.5000032073d0	0.3993419309d0	0.3908099836d0
O	0.5000031360d0	0.6006580691d0	0.4999707562d0

K_POINTS {automatic}

8 8 8 0 0 0

CELL_PARAMETERS {alat}

1.000000000000d0	0.000000000000d0	0.000000000000d0
0.000000000000d0	1.170692569629d0	0.000000000000d0
0.000000000000d0	0.000000000000d0	1.126681305036d0

Formic acid

&CONTROL

```
calculation='relax',
outdir='./tmp/',
prefix='Formicacid',
pseudo_dir='/home/mp916/Simulations/qe/qe-6.1/Simulationpdpaper/Pseudo',
verbosity='high',
forc_conv_thr = 0.000583,
tprnfor = .TRUE.
/
```

&SYSTEM

```
ibrav=0,  
celldm(1)=17.2803095283d0,  
nat=5,  
ntyp=3,  
ecutwfc=30,  
ecutrho=120,  
occupations='smearing',  
smearing='mv',  
degauss=0.005d0,  
/  
/
```

&ELECTRONS

```
mixing_mode = 'local-TF'  
mixing_ndim = 20  
mixing_beta = 0.3  
conv_thr=1d-05,  
/
```

&IONS

/

ATOMIC_SPECIES

```
C 12.010700d0 C.pw91-n-kjpaw_psl.1.0.0.UPF  
O 15.999400d0 O.pw91-n-kjpaw_psl.1.0.0.UPF  
H 1.007940d0 H.pw91-kjpaw_psl.1.0.0.UPF
```

```
ATOMIC_POSITIONS {crystal}

H    0.6145158987d0    0.4838354467d0    0.3823127673d0
C    0.5065122208d0    0.4904111511d0    0.4330303046d0
O    0.3854841013d0    0.4782033285d0    0.3808877459d0
O    0.5145431942d0    0.5163076772d0    0.5762053140d0
H    0.4199060272d0    0.5217966715d0    0.6191122541d0
```

K_POINTS {automatic}

```
8 8 8 0 0 0
```

CELL_PARAMETERS {alat}

```
1.000000000000d0  0.000000000000d0  0.000000000000d0
0.000000000000d0  0.848121779294d0  0.000000000000d0
0.000000000000d0  0.000000000000d0  1.013821874194d0
```

Hydrogen

```
&CONTROL
calculation='relax',
outdir='./tmp/',
prefix='Hydrogen',
pseudo_dir='/home/mp916/Simulations/qe/qe-6.1/Simulationpdpaper/Pseudo',
verbosity='high',
forc_conv_thr = 0.000583,
```

```
tprnfor = .TRUE.  
/  
  
&SYSTEM  
  
ibrav=0,  
celldm(1)=12.6119438239d0,  
nat=2,  
ntyp=1,  
ecutwfc=30,  
ecutrho=120,  
occupations='smearing',  
smearing='mv',  
degauss=0.005d0,  
/  

```

```
&ELECTRONS  
  
mixing_mode = 'local-TF'  
mixing_ndim = 20  
mixing_beta = 0.3  
conv_thr=1d-05,  
/  

```

```
&IONS  
  
/  

```

ATOMIC_SPECIES

H 1.007940d0 H.pw91-kjpaw_psl.1.0.0.UPF

ATOMIC_POSITIONS {crystal}

H	0.5025437140d0	0.5504756643d0	0.4980656210d0
H	0.4974562860d0	0.4495243357d0	0.5019343790d0

K_POINTS {automatic}

8 8 8 0 0 0

CELL_PARAMETERS {alat}

1.000000000000d0	0.000000000000d0	0.000000000000d0
-0.500000000000d0	0.866025403784d0	0.000000000000d0
0.000000000000d0	0.000000000000d0	3.858856497911d0

Helium

&CONTROL

```
calculation='scf',
outdir='./tmp/',
prefix='He',
pseudo_dir='/home/mp916/Simulations/qe/qe-6.1/Simulationpdpaper/Pseudo',
verbosity='high',
forc_conv_thr = 0.000583,
tprnfor = .TRUE.
/
```

```
&SYSTEM
ibrav=0,
celldm(1)=14.8532473391d0,
nat=1,
ntyp=1,
ecutwfc=30,
ecutrho=120,
occupations='smearing',
smearing='mv',
degauss=0.005d0,
/
```

```
&ELECTRONS
mixing_mode = 'local-TF'
mixing_ndim = 20
mixing_beta = 0.3
conv_thr=1d-05,
/
```

```
&IONS
```

```
/
```



```
ATOMIC_SPECIES
He 4.002600d0 He.pw91-kjpaw_psl.1.0.0.UPF
```

```

ATOMIC_POSITIONS {crystal}
He    0.5000000000d0    0.5000000000d0    0.5000000000d0

K_POINTS {automatic}
8 8 8 0 0 0

CELL_PARAMETERS {alat}
1.000000000000d0  0.000000000000d0  0.000000000000d0
0.000000000000d0  1.000000000000d0  0.000000000000d0
0.000000000000d0  0.000000000000d0  1.000000000000d0

```

Hydrogen Sulphide

```

&CONTROL
calculation='relax',
outdir='./tmp/',
prefix='h2s',
pseudo_dir='/home/mp916/Simulations/qe/qe-6.1/Simulationpdpaper/Pseudo',
verbosity='high',
forc_conv_thr = 0.000583,
tprnfor = .TRUE.
/

```

&SYSTEM

```
ibrav=0,  
celldm(1)=16.0398870722d0,  
nat=3,  
ntyp=2,  
ecutwfc=30,  
ecutrho=120,  
occupations='smearing',  
smearing='mv',  
degauss=0.005d0,  
/  
 
```

&ELECTRONS

```
mixing_mode = 'local-TF'  
mixing_ndim = 20  
mixing_beta = 0.3  
conv_thr=1d-05,  
/  
 
```

&IONS

/

ATOMIC_SPECIES

```
H 1.007940d0 H.pw91-kjpaw_psl.1.0.0.UPF  
S 32.065000d0 S.pw91-nl-kjpaw_psl.1.0.0.UPF
```

```
ATOMIC_POSITIONS {crystal}
H    0.5676219636d0    0.4950645124d0    0.3911640247d0
S    0.4323780364d0    0.5049354876d0    0.4708913462d0
H    0.5069112201d0    0.4960181453d0    0.6088359753d0
```

```
K_POINTS {automatic}
```

```
8 8 8 0 0 0
```

```
CELL_PARAMETERS {alat}
```

```
1.000000000000d0  0.000000000000d0  0.000000000000d0
0.000000000000d0  0.947225998108d0  0.000000000000d0
0.000000000000d0  0.000000000000d0  1.003132863700d0
```

Methane

```
&CONTROL
calculation='relax',
outdir='./tmp/',
prefix='ch4',
pseudo_dir='/home/mp916/Simulations/qe/qe-6.1/Simulationpdpaper/Pseudo',
verbosity='high',
forc_conv_thr = 0.000583,
tprnfor = .TRUE.
/

```

```
&SYSTEM
ibrav=0,
celldm(1)=15.5988312226d0,
nat=5,
ntyp=2,
ecutwfc=30,
ecutrho=120,
occupations='smearing',
smearing='mv',
degauss=0.005d0,
/
```

```
&ELECTRONS
mixing_mode = 'local-TF'
mixing_ndim = 20
mixing_beta = 0.3
conv_thr=1d-05,
/
```

```
&IONS
```

```
/
```

```
ATOMIC_SPECIES
C 12.010700d0 C.pw91-n-kjpaw_psl.1.0.0.UPF
H 1.007940d0 H.pw91-kjpaw_psl.1.0.0.UPF
```

```
ATOMIC_POSITIONS {crystal}

H    0.5977973834d0    0.5255779311d0    0.4030437573d0
C    0.4844150120d0    0.5064005724d0    0.4672387946d0
H    0.4022026166d0    0.6045463354d0    0.4423372459d0
H    0.4299497513d0    0.3954536646d0    0.4266264303d0
H    0.5076890964d0    0.4999969626d0    0.5969562427d0
```

K_POINTS {automatic}

```
8 8 8 0 0 0
```

CELL_PARAMETERS {alat}

```
1.000000000000d0  0.000000000000d0  0.000000000000d0
0.000000000000d0  1.017066353498d0  0.000000000000d0
0.000000000000d0  0.000000000000d0  0.997913028772d0
```

Nitrogen

```
&CONTROL
calculation='relax',
outdir='./tmp/',
prefix='n2',
pseudo_dir='/home/mp916/Simulations/qe/qe-6.1/Simulationpdpaper/Pseudo',
verbosity='high',
forc_conv_thr = 0.000583,
```

```
tprnfor = .TRUE.  
/  
  
&SYSTEM  
  
ibrav=0,  
celldm(1)=14.1735975053d0,  
nat=2,  
ntyp=1,  
ecutwfc=30,  
ecutrho=120,  
occupations='smearing',  
smearing='mv',  
degauss=0.005d0,  
/  

```

```
&ELECTRONS  
  
mixing_mode = 'local-TF'  
mixing_ndim = 20  
mixing_beta = 0.3  
conv_thr=1d-05,  
/  

```

```
&IONS  
  
/  

```

ATOMIC_SPECIES

N 14.006700d0 N.pw91-n-kjpaw_psl.1.0.0.UPF

ATOMIC_POSITIONS {crystal}

N	0.5000229854d0	0.5638317643d0	0.5000000000d0
N	0.4999770146d0	0.4361682357d0	0.5000000000d0

K_POINTS {automatic}

8 8 8 0 0 0

CELL_PARAMETERS {alat}

1.000000000000d0	0.000000000000d0	0.000000000000d0
0.000000000000d0	1.146293961020d0	0.000000000000d0
0.000000000000d0	0.000000000000d0	0.999954029241d0

Oxygen

&CONTROL

```
calculation='relax',
outdir='./tmp/',
prefix='O2',
pseudo_dir='/home/mp916/Simulations/qe/qe-6.1/Simulationpdpaper/Pseudo',
verbosity='high',
forc_conv_thr = 0.000583,
tprnfor = .TRUE.
```

/

&SYSTEM

ibrav=0,
celldm(1)=14.0980751846d0,
nat=2,
ntyp=1,
ecutwfc=30,
ecutrho=120,
occupations='smearing',
smearing='mv',
degauss=0.005d0,

/

&ELECTRONS

mixing_mode = 'local-TF'
mixing_ndim = 20
mixing_beta = 0.3
conv_thr=1d-05,

/

&IONS

/

ATOMIC_SPECIES

0 15.999400d0 0.pw91-n-kjpaw_psl.1.0.0.UPF

ATOMIC_POSITIONS {crystal}

0	0.5000254749d0	0.5697808506d0	0.5000000000d0
0	0.4999745251d0	0.4302191494d0	0.5000000000d0

K_POINTS {automatic}

8 8 8 0 0 0

CELL_PARAMETERS {alat}

1.000000000000d0	0.000000000000d0	0.000000000000d0
0.000000000000d0	1.162139169543d0	0.000000000000d0
0.000000000000d0	0.000000000000d0	0.999949050114d0

Water

&CONTROL

```
calculation='relax',
outdir='./tmp/',
prefix='Water',
pseudo_dir='/home/mp916/Simulations/qe/qe-6.1/Simulationpdpaper/Pseudo',
verbosity='high',
forc_conv_thr = 0.000583,
tprnfor = .TRUE.
/
```

```
&SYSTEM
ibrav=0,
celldm(1)=14.8665566802d0,
nat=3,
ntyp=2,
ecutwfc=30,
ecutrho=120,
occupations='smearing',
smearing='mv',
degauss=0.005d0,
/
```

```
&ELECTRONS
mixing_mode = 'local-TF'
mixing_ndim = 20
mixing_beta = 0.3
conv_thr=1d-05,
/
```

```
&IONS
```

```
/
```



```
ATOMIC_SPECIES
0 15.999400d0 0.pw91-n-kjpaw_psl.1.0.0.UPF
```

H 1.007940d0 H.pw91-kjpaw_psl.1.0.0.UPF

ATOMIC_POSITIONS {crystal}

H	0.5519282150d0	0.4962140751d0	0.4124172883d0
O	0.4480717850d0	0.5037859249d0	0.4724366744d0
H	0.4747052991d0	0.4993010724d0	0.5875827117d0

K_POINTS {automatic}

8 8 8 0 0 0

CELL_PARAMETERS {alat}

1.000000000000d0	0.000000000000d0	0.000000000000d0
0.000000000000d0	0.948259720965d0	0.000000000000d0
0.000000000000d0	0.000000000000d0	1.023268717357d0

Palladium system

Example system adsorbing Hydrogen on the surface of PdAg

```
&CONTROL
  calculation='scf',
  outdir='./tmp/',
  prefix='pdh2sfcc',
  pseudo_dir='/media/mp916/0A6296CF6296BF3F/MembraneDFTscript/Simulationpdpaper/Pseud
  verbosity='high',
  forc_conv_thr = 0.000583,
  tprnfor = .TRUE.
/

```

&SYSTEM

```
ibrav=0,  
celldm(1)=10.3967346064d0,  
nat=23,  
ntyp=4,  
ecutwfc=30,  
ecutrho=120,  
occupations='smearing',  
degauss=0.005d0,
```

/

&ELECTRONS

```
mixing_mode = 'local-TF'  
mixing_ndim = 21  
mixing_beta = 0.1  
conv_thr=1d-03,
```

/

&IONS

/

ATOMIC_SPECIES

```
H 1.007940d0 H.pw91-kjpaw_psl.1.0.0.UPF  
Pd 106.420000d0 Pd.pw91-n-kjpaw_psl.1.0.0.UPF
```

S 32.065000d0 S.pw91-nl-kjpaw_psl.1.0.0.UPF

Ag 107.868000d0 Ag.pw91-n-kjpaw_psl.1.0.0.UPF

ATOMIC_POSITIONS {crystal}

Pd	0.1666669970d0	0.3333339940d0	0.0991198960d0	0	0	0
Pd	0.6666666670d0	0.3333333330d0	0.0991197760d0	0	0	0
Pd	0.1666669970d0	0.8333330030d0	0.0991198960d0	0	0	0
Ag	0.6666660060d0	0.8333330030d0	0.0991198960d0	0	0	0
Pd	0.0000000000d0	0.0000000000d0	0.2084872330d0	0	0	0
Ag	0.4999994680d0	-0.0000010630d0	0.2084882210d0	0	0	0
Pd	0.0000010630d0	0.5000005320d0	0.2084882210d0	0	0	0
Ag	0.4999994680d0	0.5000005320d0	0.2084882210d0	0	0	0
Pd	0.3333331390d0	0.1666665700d0	0.3175525410d0	1	1	1
Pd	0.8333334300d0	0.1666665700d0	0.3175525410d0	1	1	1
Pd	0.3333333330d0	0.6666666670d0	0.3175526140d0	1	1	1
Pd	0.8333334300d0	0.6666668610d0	0.3175525410d0	1	1	1
Pd	0.1666668260d0	0.3333336520d0	0.4262792350d0	1	1	1
Ag	0.6666666670d0	0.3333333330d0	0.4262800040d0	1	1	1
Pd	0.1666668260d0	0.8333331740d0	0.4262792350d0	1	1	1
Pd	0.6666663480d0	0.8333331740d0	0.4262792350d0	1	1	1
Pd	0.0000000000d0	0.0000000000d0	0.5354872520d0	1	1	1
Ag	0.4999992870d0	-0.0000014260d0	0.5354874210d0	1	1	1
Pd	0.0000014260d0	0.5000007130d0	0.5354874210d0	1	1	1
Pd	0.4999987651d0	0.5000007130d0	0.5354874210d0	1	1	1
S	0.8333338900d0	0.1666664227d0	0.5595108834d0	1	1	1

```
H    0.8415731417d0    0.1791808477d0    0.6225635207d0 1 1 1  
H    1.1011049065d0    0.3005523705d0    0.5788091707d0 1 1 1
```

```
K_POINTS {automatic}
```

```
4 4 4 1 1 0
```

```
CELL_PARAMETERS {alat}
```

```
1.000000000000d0 0.000000000000d0 0.000000000000d0  
-0.500000000000d0 0.866025403784d0 0.000000000000d0  
0.000000000000d0 0.000000000000d0 3.858856497911d0
```

Pictures of commercial enrichment device



Figure 8.7: Enrichment device control panel



Figure 8.8: Enrichment device chassis layout

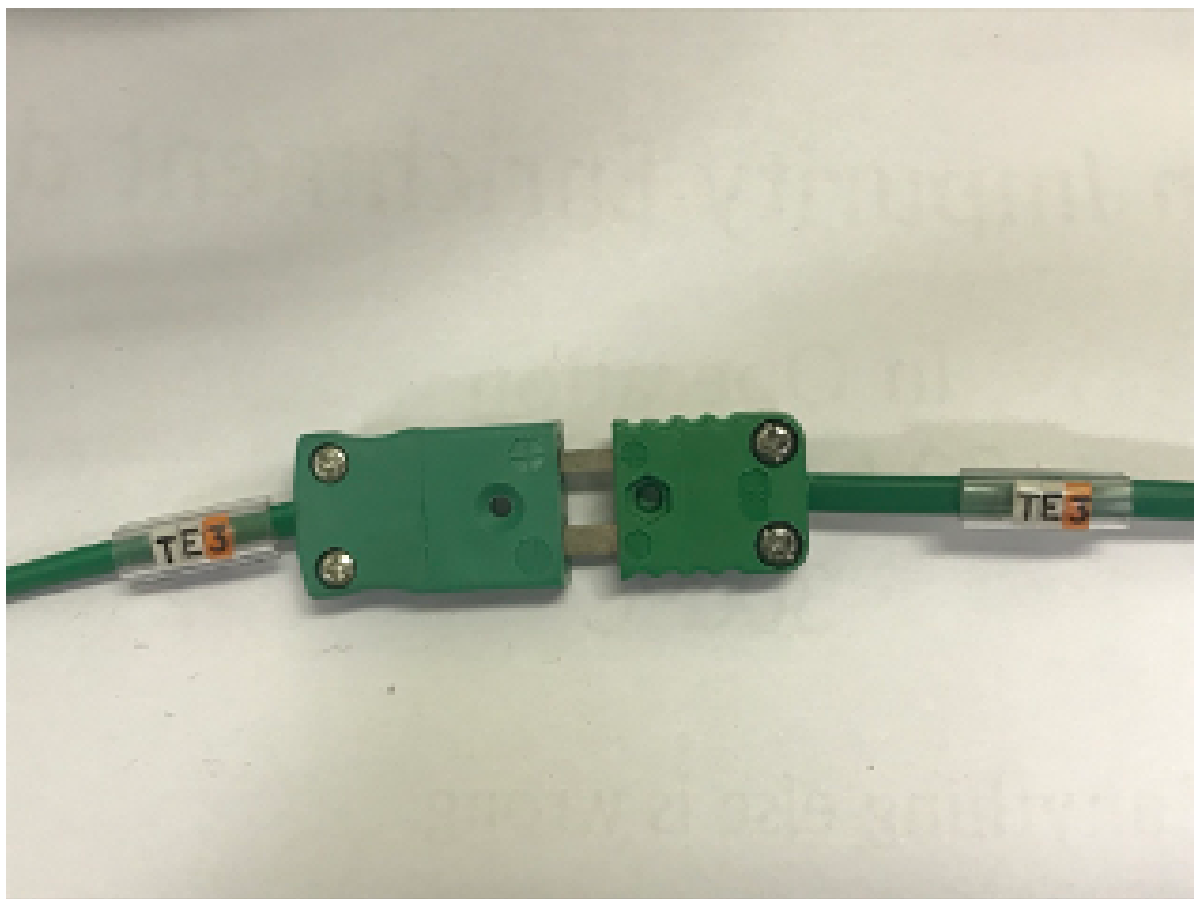


Figure 8.9: Example of connecting thermocouples using TE3

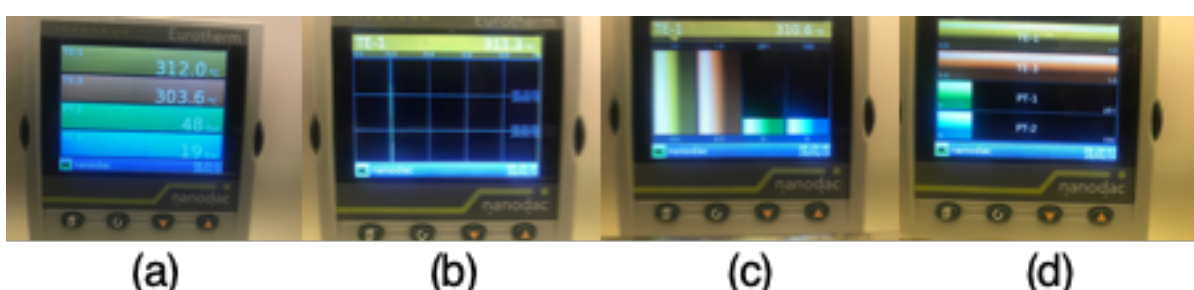


Figure 8.10: Information based views on eurotherm control panel
(a) System Summary
(b) Vertical trend over time (c) Vertical bar chart (d) Horizontal bar chart



(a)



(b)

Figure 8.11: Temperature control views



Position 0: off



Position 1: on

Figure 8.12: Heating switch

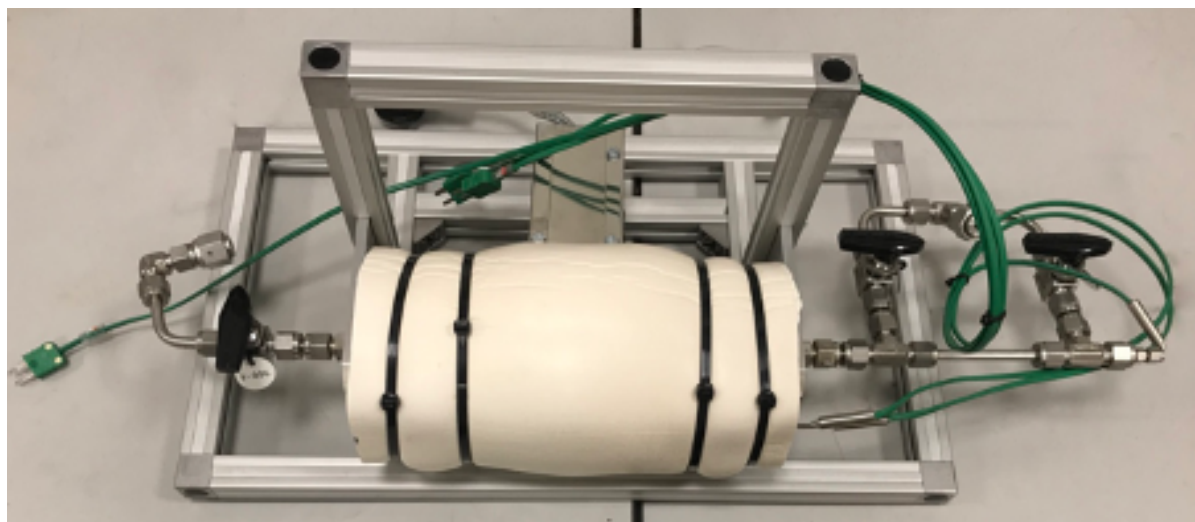


Figure 8.13: Disconnected transportable unit

References

- [1] Gautam Ghosh, C. Kantner, and G. Olson. Thermodynamic modeling of the pd-x ($x=ag$, co , fe , ni) systems. *Journal of Phase Equilibria*, 20:295–308, 05 1999. doi: 10.1361/105497199770335811.
- [2] Marcel Sluiter, Catherine Colinet, and Alain Pasturel. Ab initio calculation of the phase stability in au-pd and ag-pt alloys. *Physical Review B*, 73, 05 2006. doi: 10.1103/PhysRevB.73.174204.
- [3] R.M Waterstrat, A Shapiro, and A Jeremie. The palladium–zirconium phase diagram. *Journal of Alloys and Compounds*, 290(1):63 – 70, 1999. ISSN 0925-8388. doi: [https://doi.org/10.1016/S0925-8388\(99\)00127-9](https://doi.org/10.1016/S0925-8388(99)00127-9). URL <http://www.sciencedirect.com/science/article/pii/S0925838899001279>.

List of Publications and Presentations

Publications

1. **M. Plunkett**, K.Li, A. Murugan; Review of membrane technologies for hydrogen impurity enrichment (To be resubmitted)
2. **M. Plunkett**, A. Morris, S. Nayebossardi, T. Bacquart, B. Wang, S. Spencer, K. Mingard, K. Li, A. Murugan ; Determining impurity resistant palladium alloy membrane compositions for enrichment of hydrogen fuel samples with low level contaminants (In final preparation)
3. **M. Plunkett**, N. Moore, T. Bacquart, K.Li, A. Murugan; Analysing low level impurities in hydrogen refuelling station hydrogen using hydrogen impurity enrichment; (In preparation)

Oral Presentations

1. **M. Plunkett**, A. Murugan, K. Li; A hydrogen impurity enrichment device using Pd-Alloy membranes to support the hydrogen economy. Presented at International Conference for Membrane and Electromembrane Processes 2018, 13th – 16th May

2018, Prague, Czech Republic.

2. **M. Plunkett**, A. Murugan, K. Li; A hydrogen impurity enrichment device using Pd-Alloy membranes to support the hydrogen economy. Presented at 15th International Conference on Inorganic Membranes, 18th – 22nd June 2018, Dresden, Germany.
3. **M. Plunkett**; Determining impurity resistant palladium alloy membrane compositions for enrichment of hydrogen fuel samples with low level ISO 14687-2 contaminants. Presented at 2nd bi-annual Gas and Particle Metrology symposium, 14th August, 2018, Teddington, United Kingdom
4. **M. Plunkett**; Developing suitable palladium alloy membranes for enrichment of hydrogen fuel samples to satisfy growing analytical demand. Presented at H2FC Research Conference University of Birmingham, 14th August, 2018, Birmingham, United Kingdom
5. **M. Plunkett**; Hydrogen Quality Assurance Work Package 2, Task 2.4: Optimisation of impurity enrichment devices. EMPIR MetroHyVe M39 meeting, 25th August, 2020, Online